SECURITY CLASSIFICATION OF THIS PAGE (When Data Entered)

READ INSTRUCTIONS
BEFORE COMPLETING FORM

REPORT DOCUMENTATION PAGE

1. REPORT NUMBER	2. GOVT ACCESSION NO.	3. RECIPIENT'S CATALOG NUMBER
79-268D	AD-A091 408	

4. TITLE (and Subtitle)	5. TYPE OF REPORT & PERIOD COVERED
Latent Heat Induced Divergence and the Ultra-Long Waves of the Subtropics and Midlatitudes	THESIS/DISSERTATION
	6. PERFORMING ORG. REPORT NUMBER

7. AUTHOR(s)	8. CONTRACT OR GRANT NUMBER(s)
Fred Parker Lewis	Doctoral thesis

9. PERFORMING ORGANIZATION NAME AND ADDRESS	10. PROGRAM ELEMENT, PROJECT, TASK AREA & WORK UNIT NUMBERS
AFIT STUDENT AT: The University of Utah	AFIT-CI-79-268D

11. CONTROLLING OFFICE NAME AND ADDRESS	12. REPORT DATE
AFIT/NR	Dec 1979
WPAFB OH 45433	13. NUMBER OF PAGES
	240

14. MONITORING AGENCY NAME & ADDRESS(If different from Controlling Office)	15. SECURITY CLASS. (of this report)
LEVEL	UNCLASS
	15a. DECLASSIFICATION/DOWNGRADING SCHEDULE

16. DISTRIBUTION STATEMENT (of this Report)

APPROVED FOR PUBLIC RELEASE; DISTRIBUTION UNLIMITED

DTIC
ELECTE
NOV 6 1980

C

17. DISTRIBUTION STATEMENT (of the abstract entered in Block 20, if different from Report)

18. SUPPLEMENTARY NOTES

APPROVED FOR PUBLIC RELEASE: IAW AFR 190-17

25 SEP 1980

FREDRIC C. LYNCH, Major, USAF
Director of Public Affairs
Air Force Institute of Technology (ATC)
Wright-Patterson AFB, OH 45433

19. KEY WORDS (Continue on reverse side if necessary and identify by block number)

20. ABSTRACT (Continue on reverse side if necessary and identify by block number)

ATTACHED

DD FORM 1473 EDITION OF 1 NOV 65 IS OBSOLETE

UNCLASS 012200

80 10 14 20

THE UNIVERSITY OF UTAH GRADUATE SCHOOL

SUPERVISORY COMMITTEE APPROVAL

of a dissertation submitted by

Fred Parker Lewis

I have read this dissertation and have found it to be of satisfactory quality for a doctoral degree.

June 18, 1979
_____
Date

_____
Jan Paegle
Chairman, Supervisory Committee

I have read this dissertation and have found it to be of satisfactory quality for a doctoral degree.

June 18, 1979
_____
Date

Elford G. Astling
_____
Elford G. Astling
Member, Supervisory Committee

I have read this dissertation and have found it to be of satisfactory quality for a doctoral degree.

June 18, 1979
_____
Date

_____
S. K. Kao
Member, Supervisory Committee

I have read this dissertation and have found it to be of satisfactory quality for a doctoral degree.

June 18, 1979
_____
Date

_____
Julia N. Paegle
Member, Supervisory Committee

I have read this dissertation and have found it to be of satisfactory quality for a doctoral degree.

June 18, 1979
_____
Date

_____
Frank Stenger
Member, Supervisory Committee

THE UNIVERSITY OF UTAH GRADUATE SCHOOL

FINAL READING APPROVAL

To the Graduate Council of The University of Utah:

I have read the thesis of _____ Fred Parker Lewis _____ in its
final form and have found that (1) its format, citations, and bibliographic style are
consistent and acceptable; (2) its illustrative materials including figures, tables, and
charts are in place; and (3) the final manuscript is satisfactory to the Supervisory
Committee and is ready for submission to the Graduate School.

NOV. 9, 1979
Date

Jan Paegle
Member, Supervisory Committee

Approved for the Major Department

S. K. Kao
Chairman/Dean

Approved for the Graduate Council

James L. Clayton
Dean of The Graduate School

LATENT HEAT INDUCED DIVERGENCE AND THE ULTRA-LONG WAVES

OF THE SUBTROPICS AND MIDLATITUDES

by

Fred Parker Lewis

A dissertation submitted to the faculty of The
University of Utah in partial fulfillment of the requirements
for the degree of

Doctor of Philosophy

Department of Meteorology

The University of Utah

December 1979

ABSTRACT

Winter and summer Goddard Institute of Space Studies (GISS)
Data System Test (DST) (prototype Global Atmospheric Research Proj-
ect (GARP) data) time average fields are compared with several
average data sets. An analysis of the GISS DST data involving kine-
matically and noneliptically computed divergent flow fields suggests
that the positioning of the subtropical jets and ultra-long waves
(wavenumbers 1-3) may be partially in response to strong longitudi-
nal variations in tropical convective heating.

Experiments with divergent barotropic and two-level primitive
equation models are used to test the short (1-3 days) and long (15-
30 days) range effects of large scale tropical heating patterns upon
the subtropical and midlatitude long and ultra-long waves and flow
patterns. The barotropic model experiments suggest that forcing in
the tropics of one hemisphere can significantly accelerate (by means
of gravity wave energy propagation) the opposite hemisphere subtrop-
ical jet in a matter of one to three day's time, regardless of east-
erly or westerly tropical flow. The maximum subtropical jets due to
forcing in one hemisphere are shown to exist in the opposite hemi-
sphere.

Two-level primitive equation model experiments are conducted
for the spherical earth with uniform mid and high latitude net
diabatic forcing. Long and short range tropical heating experiments

with and without orography for mean northern hemisphere winter conditions are performed. Mountains are found to play a major role in the positioning of the jet streams and ultra-long waves. Short range large scale intensifications ("pulsing") and reductions ("unpulsing") of localized southern hemisphere tropical heatings are imposed to study effects upon the midlatitude northern hemisphere ultra-long wave structure. In the presence of mountains there are changes that may explain from 1/3 to 1/2 of the ultra-long wave error differences between the GISS General Circulation Model (GCM) forecasts and the National Meteorological Center (NMC) forecasts.

Long and short range two-level model tropical heating tests for the southern hemisphere winter in the presence of mountains are also conducted. Mountains appear to play a surprisingly important role in the long term placement of the preferred southern hemisphere jet positions. The wintertime ultra-long wave model amplitudes forced by the southern hemisphere mountains are found to be about 3/4 of the wintertime ultra-long wave amplitudes forced by the northern hemisphere mountains. Short range amplification and reduction of localized large scale northern hemisphere tropical heating areas do significantly affect the ultra-long wave structure in the midlatitudes of the southern hemisphere. These changes represent about 2/3 of the ultra-long wave northern hemisphere winter error amplitude differences that have been given between GISS GCM forecasts and NMC model forecasts.

TABLE OF CONTENTS

Table of Contents (continued)

LIST OF FIGURES

List of Figures (continued)

List of Figures (continued)

List of Figures (continued)

List of Figures (continued)

List of Figures (continued)

List of Figures (continued)

List of Figures (continued)

List of Figures (continued)

List of Figures (continued)

List of Figures (continued)

List of Figures (continued)

List of Figures (continued)

List of Figures (continued)

List of Figures (continued)

List of Figures (continued)

List of Figures (continued)

List of Figures (continued)

List of Figures (continued)

List of Figures (continued)

List of Figures (continued)

LIST OF TABLES

ACKNOWLEDGMENTS

models used in this research. I would like to thank Mr. Max Peterson, Mr. Earl Rose, Mr. Parley Jeffs, and the many computer operators for their assistance in providing only the highest quality computer support. I would also like to thank Major Jim Hatch for his assistance with the Cyber 70 operating system and countless programming problems.

CHAPTER 1

INTRODUCTION

The science of numerical weather prediction has advanced tre-
mendously since its original conception by Bjerknes (1919) and
Richardson (1922). Many scientists have made significant contribu-
tions in both the physical and numerical aspects of the problem.
The early work of Rossby (1938-1940) and the invention of the elec-
tronic computer allowed Charney, et al. (1950) to first forecast
the rotational part of the midlatitude flow with a barotropic model.
Since the early 1950's numerical techniques, computer hardware, and
data quality and quantity have improved considerably. Along with
the improvement in the numerics, atmospheric physical processes are
becoming better understood through real data studies with more com-
plete data sets.

With all of the advances that have been made in the past 30
years, the surprising fact is that our ability to forecast the short
range (1-3 days) midlatitude storm pattern has not drastically im-
proved since the early barotropic forecast experiments. This is
suggested by the fact that the National Meteorological Center (NMC)
barotropic model is still one of the main forecasting tools used by
most operational forecasters.

Since the shorter weather producing waves are essentially
steered by the long and ultra-long waves, it is of paramount

importance in any operational forecast model to forecast the long
and ultra-long waves well. Leith (1974) has suggested that a large
portion of the error in the NMC primitive equation model forecasts
is due to incorrectly forecasted ultra-long waves. Baumhefner and
Downey (1977) studied the short range forecasts of three state of
the art forecast models. The NMC, the National Center for Atmos-
pheric Research (NCAR), and Goddard Institute of Space Studies
(GISS) operational model forecasts were compared from 20° to 90°
north for several different initial conditions. The ultra-long
waves (wavenumbers 1, 2, 3) were incorrectly forecasted by all
three models, but the GISS model was significantly more skillful
than the NCAR or NMC models. The overall forecasting ability of the
GISS model was also superior to the other two models even though the
short wave phenomena were forecasted with more skill in the NMC and
NCAR models. This suggests that a correct ultra-long wave forecast
is essential if a model is to verify well.

The differing forecasting skill for the ultra-long waves could
be due to the differing physics of the models. One difference be-
tween the three is that the GISS model is the only one to include
parameterized convective latent heating. The NMC model has a rigid
boundary at 20^ON, while the NCAR model only includes stable latent
heating. The influence of tropical convective latent heating upon
the subtropical and midlatitude ultra-long wave flow patterns will
be dealt with at length in the following sections.

Smagorinsky (1953) performed one of the first studies in which
the effect of diabatic heating on planetary scale waves was

discussed. His heating sources and sinks were confined to the mid-latitudes. The heat sources to be studied here are situated in the equatorial regions and are driven by the latent heat release in intertropical convergence zones or monsoon type circulations. The tropical and subtropical oceans are heated over vast areas by the sun. Evaporation occurs and the heat from the sun is stored in the water vapor as latent heat. This heat is finally realized in the equatorial regions, generally to the south of the equator during the northern hemisphere winter and to the north of the equator during the southern hemisphere winter, when the water vapor is precipitated out of the atmosphere. This heating induces divergent flows which drive both the Hadley and Walker type circulations. Data to substantiate this conclusion will be presented in Chapter 2 and can be seen in the studies of Sadler (1975), Krishnamurti (1971a,b) and Newell et al. (1972).

Since the subtropical jet maxima of both winter hemispheres in Newell et al. (1972) and in Chapter 2 tend to align themselves with these strongly precipitating areas, one might consider the resulting thermally driven divergent outflows as local sources of energy for the subtropical jet streams.

From scale analysis it can be shown that for the ultra-long waves in a stable atmosphere the order of magnitude of the divergence and vorticity are both approximately $10^{-6}s^{-1}$. Using Helmholtz's theorem in two dimensions

$$\mathbf{V} = \mathbf{V}_{\psi} + \mathbf{V}_{\chi}, \tag{1}$$

where $\mathbf{V}$ is the horizontal wind component, $\mathbf{V}_\psi = \mathbf{k} \times \nabla\psi$ is the rotational part of the horizontal wind, $\mathbf{V}_\chi = \nabla\chi$ is the divergent component of the horizontal wind and ψ and χ are the respective stream functions, it can be shown that

$$\left| \frac{\mathbf{V}_\psi}{\mathbf{V}_\chi} \right| \sim 0(1) \tag{2}$$

for the ultra-long waves.

Thus it is of interest to investigate the divergent component of the wind to see if (1) the ultra-long wave flow patterns align themselves in any fashion with the divergent components of the wind and (2) the divergent wind components align themselves with tropical precipitation areas. If this alignment does exist then some further consideration must be given to any numerical model initialization technique which utilizes only the rotational part of the wind field.

Another reason for studying the divergent wind component in the regions of the subtropical jet may be inferred from a study by Blackmon et al. (1977). This study used NMC analyses from 20°N to 90°N over a period of several winters. Blackmon et al. (1977) found that areas of acceleration/deceleration in the mean subtropical jet streams were positively correlated with areas of positive/negative ageostrophic flow. The zonal component of the mean horizontal momentum equation is

$$\frac{d\bar{u}}{dt} = f(\bar{v} - \bar{v}_g) + \text{transient eddy effects} + \text{friction} \tag{3}$$

f is the Coriolis parameter, $(\bar{}) = \frac{1}{T} \int_0^T () \, dt$, u and v are the zonal

and meridional components of the wind and v_g is the meridional geo-
strophic wind. Blackmon's results suggest that, on a local basis,
the subtropical jet streams are sustained by directly overturning
circulations rather than transient eddies. Equation (3) represents
the total change in the zonal wind following a given parcel of air.
Thus an area of ageostrophic flow of magnitude 1 m/sec for a period
of one day at 30^ON would lead to an increase of 6 m/sec in the zonal
wind component of the parcel.

Since the geostrophic wind is also divergent, one cannot
exactly relate the meridional divergent flow, v_χ, to the ageostrophic
flow, v_g. But areas of strongly divergent flow should be areas
where the flow is also to some degree ageostrophic. Thus careful
examination of both the ageostrophic and divergent wind components
seems to be warranted to reach a further understanding of the nature
of planetary scale waves. In Chapter 2 a detailed data study is
carried out with special emphasis on the divergent and ageostrophic
flow components. It is found that striking longitudinal correla-
tions exist between the westerly jets of both hemispheres, the
cross isobaric flow patterns, and divergent meridional outflows
from the tropics.

In light of the results of Chapter 2, the conjecture set forth
by Paegle et al. (1979) that long and short term low latitude con-
vective heating may significantly impact the intensity and posi-
tioning of the ultra-long waves by generating cross isobaric flow
fields far from the actual sources of heating will be further exam-
ined in modeling experiments detailed in Chapters 4 and 5.

This conjecture is not new. One of the early relevant data studies was made by Ramage (1969) who suggested that the large local differences in the jet stream strengths between the northern winters of 1962 and 1963 were related to large precipitation differences over Indonesia. Webster (1972) has also studied the relative roles of mountains and monsoons upon the stationary wave patterns of the tropics and subtropics. Since then, there have been numerous data studies of long term teleconnections between the tropics and mid-latitudes (e.g. Hastenrath, 1976, 1978; Murakami, 1978 and others). There are also many numerical modeling studies (e.g. Rowntree, 1976a,b; Julian et al., 1978 and others).

Although some understanding of the sensitivity of model results to tropical heating is emerging, the relative roles of midlatitudes and low latitudes in shaping the circulation are still not entirely clear. Additionally, hemispheric interactions and short term energy fluxes remain to be carefully delineated. Indeed, one purpose of the GARP experiment and its subprograms, such as GATE and MONEX, is to provide a good data base for such studies. The DST data studies presented here represent preliminary conclusions from such data. In order to test the possible short term importance of tropical heating upon the subtropical and midlatitude ultra-long waves, a divergent primitive barotropic model and a two-level primitive equation model are also developed (Chapter 3).

The barotropic model was used solely to discern the effect of forced tropical divergent outflows on the subtropical jet stream, (Chapter 4). This work was performed to test the sensitivity of

Paegle's (1978) conclusions to the beta effect and the sensitivity
of Hoskins et al. (1977) conclusions to gravity waves.

Hoskins et al. (1977), using the barotropic vorticity equation,
have shown that Rossby-Haurwitz waves do not efficiently propagate
energy from one hemisphere to the other when equatorial easterlies
exist. This result is in agreement with the Eliassen-Palm relation-
ship for such waves,

$$\overline{\Phi'v'} = - (\overline{u}-c) \overline{u'v'}, \qquad (4)$$

where the bar operator is defined as $(\overline{}) = \frac{1}{2\pi} \int_{0}^{2\pi} ( ) \, d\lambda$ the prime is
defined as $( )' = ( ) - (\overline{})$, Φ is the geopotential height, u and v
are the zonal and meridional horizontal velocity components and c is
the phase speed of the wave in question. This relationship predicts
that westerly propagating waves will be trapped by critical lines
where $\overline{u} - c = 0$, as shown in Figure 1. If $\overline{u} - c = 0$ at some lati-
tude ϕ_{c_1}, then $\overline{\Phi'v'} = 0$, and $\overline{\Phi'v'}$ represents the meridional energy
flux at latitude ϕ_{c_1}. Thus Rossby wave energy should not propagate
beyond the critical latitude ϕ_{c_1}, and the energy of the propagating
wave must be trapped below latitude ϕ_{c_1}.

The derivation of this result is based upon assumptions that
may not hold in more complex models and indeed it is found in Chap-
ter 4 that the gravity wave modes are not trapped by areas of east-
erly flow.

In Chapter 5, the two-level primitive equation model experi-
ments are discussed. These experiments were designed to test the
effects of realistic zonal average radiation fields along with
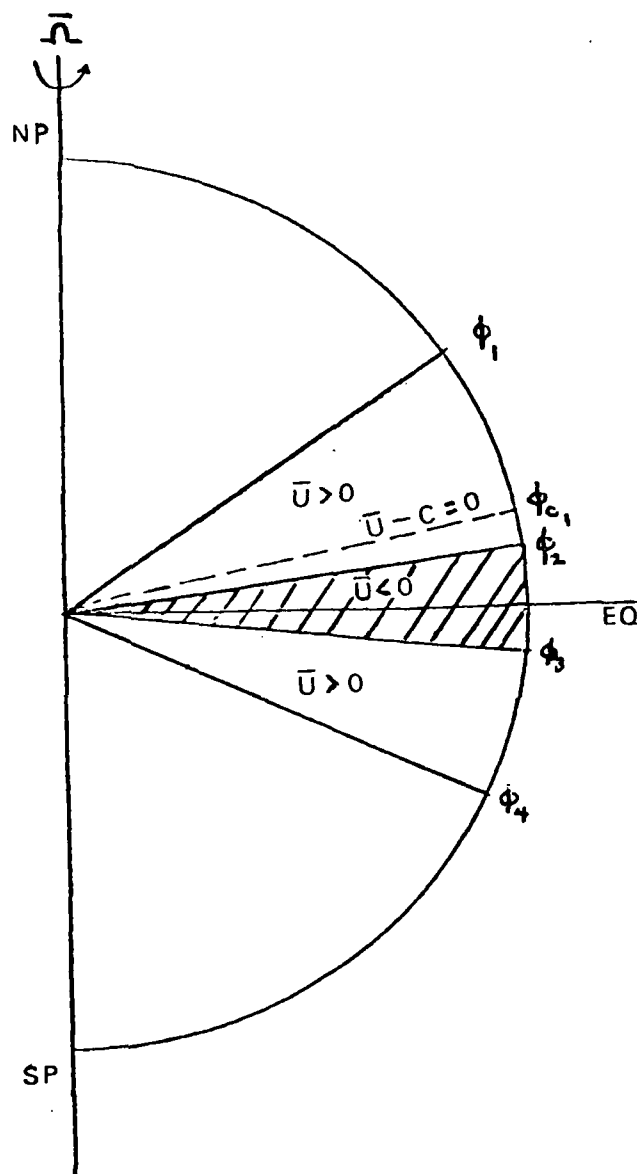
Figure 1. Idealized cross-section of the earth showing the
critical latitude ϕ_c in relation to the mean zonal
flow, $\bar{u}$.

variable tropical heating patterns for both mean northern and southern hemisphere wintertime situations. Since mountains have been shown by several authors to be of great importance in forcing the ultra-long waves, (e.g. Charney and Eliassen, 1974), experiments using the same heating patterns were carried out both with and without orography. The primitive equation model physics, which is discussed in Chapter 3, is kept as simple as possible to model the real atmosphere, but to also enable interpretation of the various forcing experiments in a pseudo cause and effect manner. Finally, the conclusions drawn from the data study and numerical experiments are summarized in Chapter 6.

CHAPTER 2

THE GISS DST DATA STUDY

2.1 Data Description

The data used in this study was obtained from the Goddard
Institute of Space Studies (GISS). The GISS data systems test
(DST) data set is a prototype data set for those which will be
provided during the Global Atmosphere Research Project (GARP). Thus
it represents one of the most consistent global data sets available
today. Two time periods of the GISS DST data are studied. One
period consists of northern hemisphere winter (NHW) data from 29 Jan
1976 to 3 Mar 1976, while the other is southern hemisphere winter
(SHW) data from 21 Aug 1976 to 4 Sep 1976. These data sets both
contain all available sonde data along with commercial aircraft
winds. The raw data is analyzed by a four dimensional assimilation
with the 9 level, 4° latitude by 5° longitude GISS GCM. Data at a
given time is inserted into the model at that time by modifying the
8 closest grid points to the given observation. Thus this data
should be well suited for studying the ultra-long waves considering
the GISS model's skill in forecasting these waves. A detailed sur-
vey of the GISS GCM can be found in Sommerville et al. (1974). Some
parts of the NHW data presented here have been previously presented
in McGlasson (1977) and in Paegle et al. (1979).

2.2 Data Analysis Techniques

The temperatures, horizontal wind components, and specific humidity GISS DST data were used in this study. The original data was on a nine level sigma coordinate system with levels between the surface and 10 mb. The data was first converted from the nine sigma coordinate surfaces to seven pressure surfaces in equal increments of 100 mb from 700 to 100 mb. This was done both to reduce the truncation errors in computation near the terrain features and to allow easier comparisons of our results with those of several other authors. A cubic spline interpolation technique following McGlasson (1977) was used here to transform the data from the sigma to the pressure coordinates system. After the interpolation of the temperature data to the pressure system, the hydrostatic equation was integrated to produce fields of geopotential height, Φ. These fields compared favorably in every comparison with NMC northern hemisphere facsimile charts.

Since the maxima of the subtropical jet and divergent wind fields tend to be focused near the 200 mb layer, the main thrust of this data study will be concerned with this level. Also, commercial aircraft flights increase data input near this level. Some mean height, temperature, and wind fields from other levels are shown for data consistency comparisons with other authors.

The data study will be presented in two parts. Part one contains the time averaged and standard deviation fields for both the SHW and the NHW data. Part two contains the divergent and ageostrophic wind computations.

2.3 Time Averaged Data Fields

The averages were computed using Eq. (5),

$$\overline{A}_{ij} = \frac{1}{N} \sum_{n=1}^{N} A_{ij}^{n} \ , \tag{5}$$

where N=70, 12-hour analysis periods for the NHW data and N=30, 12-hour analysis times for the SHW data.

The time average NHW and SHW fields show reasonable agreement with Newell et al. (1972), van Loon et al. (1971), and Sadler (1975). Some examples of these mean fields are presented in Figures 2-31. The area near the Himalayan Mountains should be ignored in the 700 mb charts since the lowest sigma surface is at approximately 600 mb in this region.

Figures 2, 3 and 4 are the mean NHW height fields at 700, 500 and 200 mb, respectively. They show a long wave ridge over the northern Rocky Mountains at all levels, while the flow pattern does not seem to reflect the Himalayan Mountain range. This is consistent with previous data studies that suggest that the air parcels flow around instead of over the Himalayan Mountain chain. In the southern hemisphere the height fields do not appreciably reflect the Andes Mountain range.

The two strong NHW natural baroclinic zones off the coasts of North America and Asia are visible in the height (Figures 2, 3 and 4) and temperature fields (Figures 5, 6 and 7). At 700 mb the main temperature gradient seems to be north of 40°N (Figure 5) while at 500 mb the temperature gradient lies between 30° and 50°N (Figure 6)
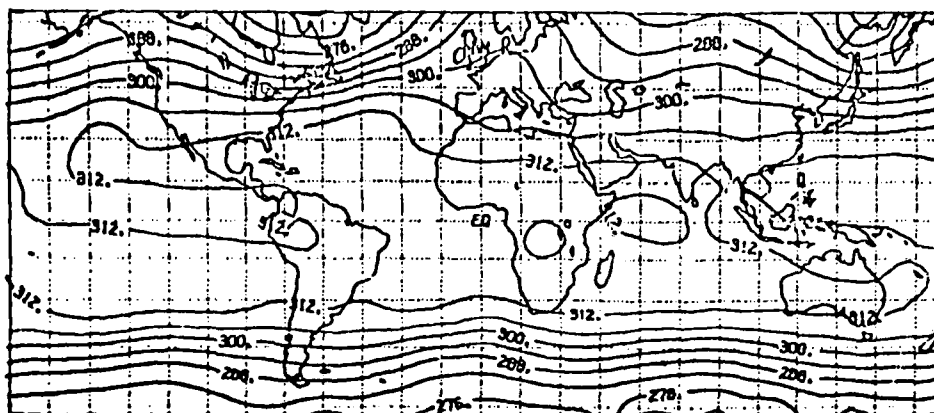
Figure 2. Time-average height field at 700 mb for the NHW (dm). The contour interval is 6 dm.
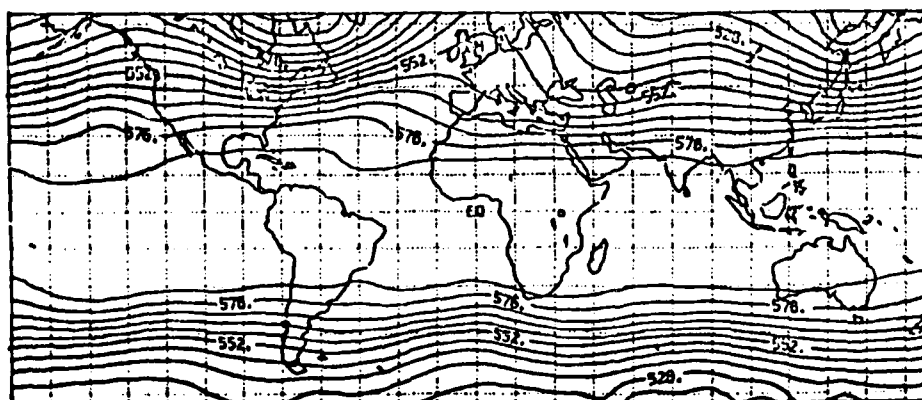
Figure 3. Time-average height field at 500 mb for the NHW (dm). The contour interval is 6 dm.
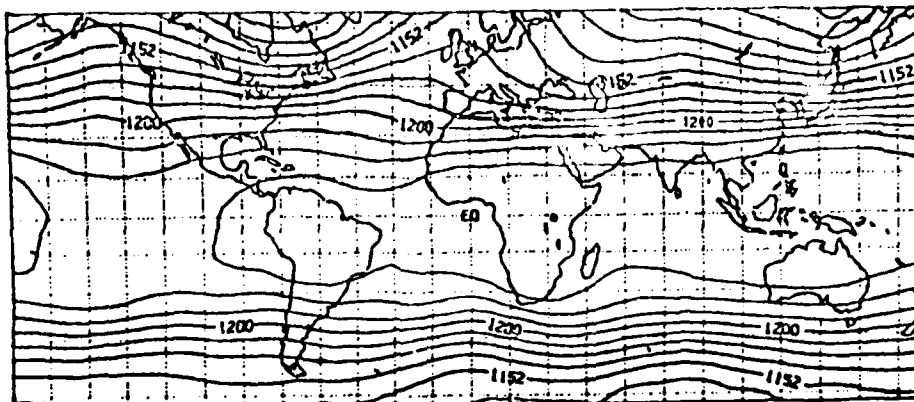
Figure 4. Time-average height field at 200 mb for the NHW (dm). The contour interval is 12 dm.
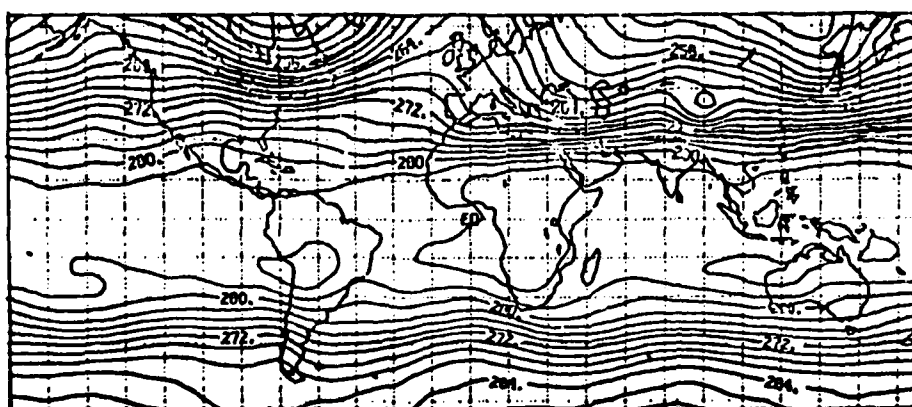
Figure 5. Time-average temperature field at 700 mb for the NHW (°K). The contour interval is 2°K.
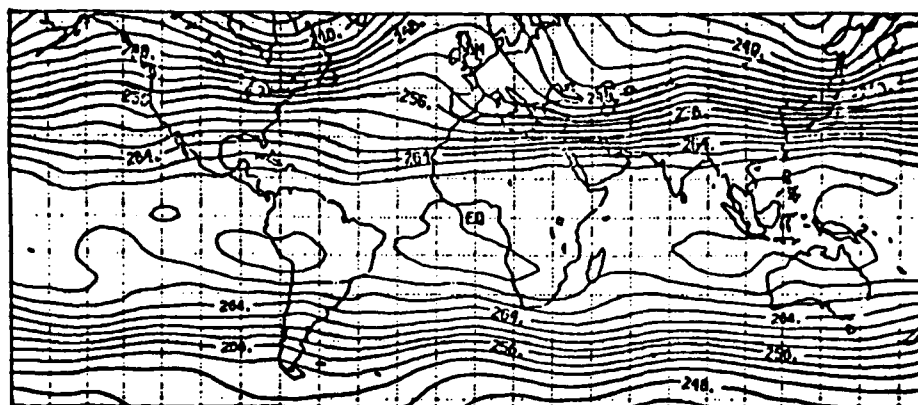
Figure 6.   Time-average temperature field at 500 mb for the
            NHW (°K). The contour interval is 2°K.
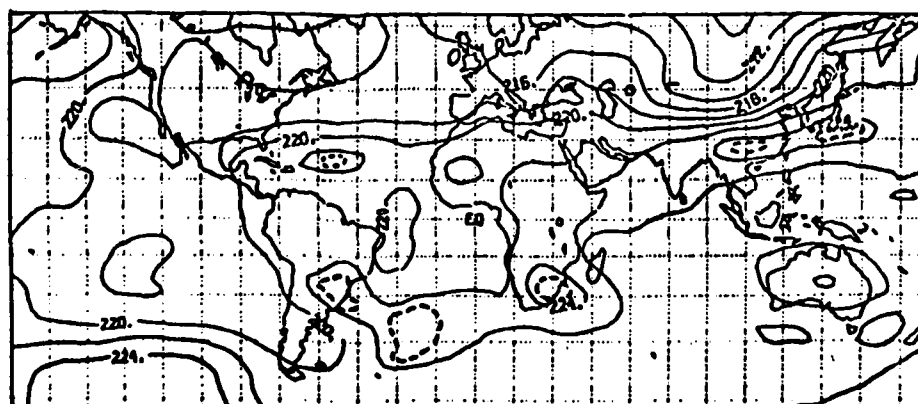
Figure 7.   Time-average temperature field at 200 mb for the
            NHW (°K). The contour interval is 2°K. Dashed
            lines represent intermediate values.

and at 200 mb the strongest temperature gradient is near 30° north
(Figure 7). These are consistent with the polar and subtropical jet
placements for the NHW as seen in Figures 8, 9 and 10.

The midlatitude or polar jet has its maximum between 400 and
300 mb (not shown) while the subtropical jet has a maximum at 200 mb
(Figure 10) in the northern hemisphere with two distinct centers.
The "subtropical" jet off the east coast of the United States is
much farther north here than in most other data studies. The 200 mb
jets in the southern hemisphere are located near 50° south and have
a definite zonal orientation which is in contrast to the southwest/
northeast orientation of the jets of the northern hemisphere. Fig-
ure 11 shows the 200 mb time averaged meridional wind field. This
field is rather cellular, but does show several areas where south-
erly and northerly flow exists in the average.

The column averaged relative humidity is given in Figure 12.
Values greater than 40% are analyzed and can be used to infer pre-
cipitation. Values between 80 and 100% should represent areas with
heavy precipitation. These inferred areas of heaviest precipita-
tion in the tropics compare quite well with Newell et al. (1972)
and Shutz and Gates (1972).

Figures 13 and 14 are the standing (KE_s) and transient (KE_t)
kinetic energies at 200 mb. The standing kinetic energy was com-
puted using Eq. (6), while the transient kinetic energy was computed
using Eq. (8).

$$KE_s = \frac{1}{2} (\overline{u}^2 + \overline{v}^2),$$
(6)
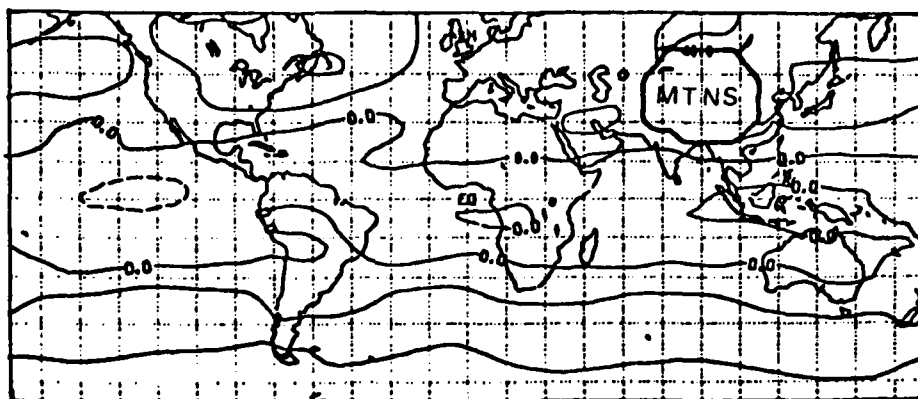
Figure 8. Time-average zonal component of the wind at 700 mb
for the NHW (ms^{-1}). The contour interval is 10 ms^{-1}.
Dashed lines represent negative values.
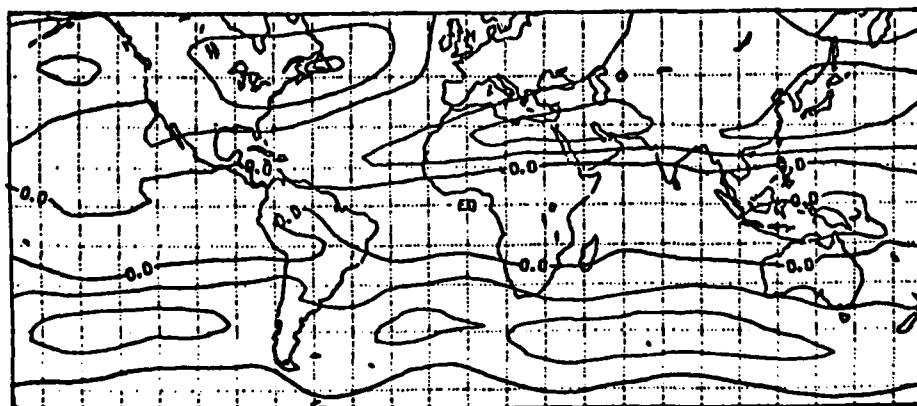
Figure 9. Time-average zonal component of the wind at 500 mb
for the NHW (ms^{-1}). The contour interval is 10 ms^{-1}.
Dashed lines represent negative values.
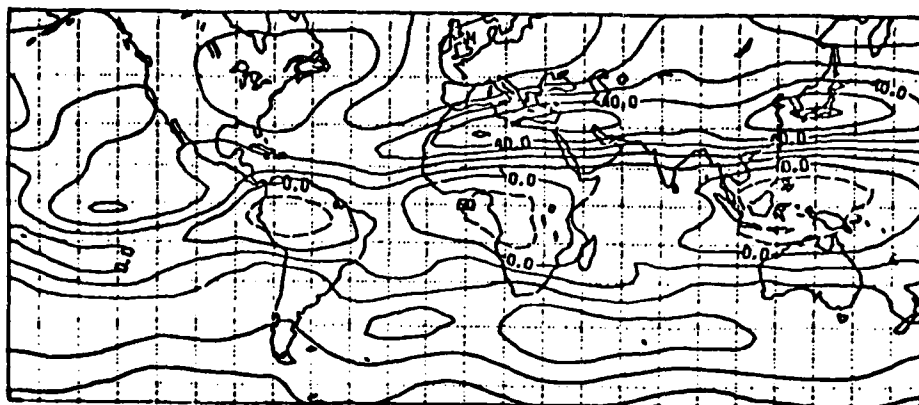
Figure 10. Time-average zonal component of the wind at 200 mb for the NHW (ms^{-1}). The contour interval is 10 ms^{-1}. Dashed lines represent negative values.
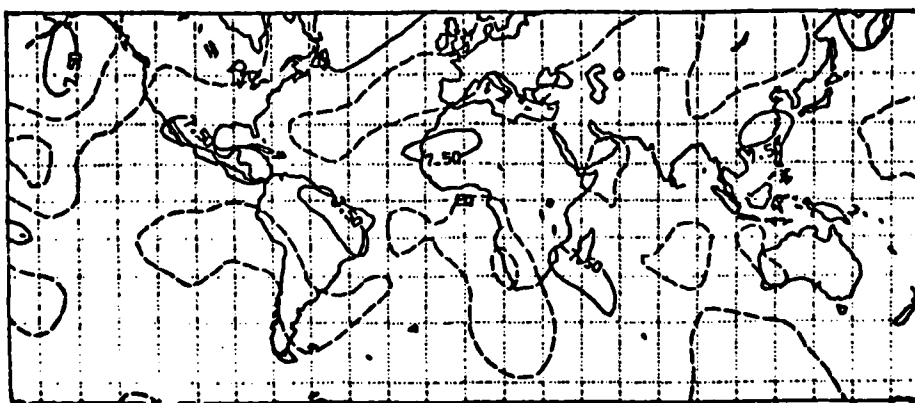
Figure 11. Time-average meridional component of the wind at 200 mb for the NHW (ms^{-1}). The contour interval is 10 ms^{-1}. Dashed lines represent negative values.
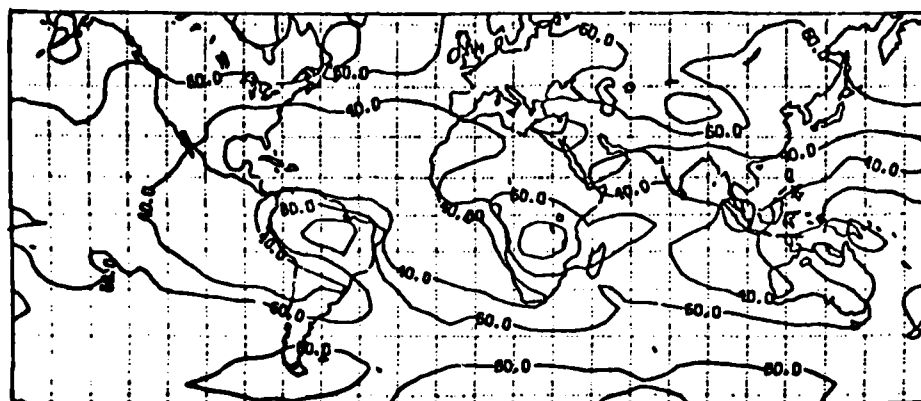
Figure 12. Time-average column average relative humidities for
the NHW (%). The contour interval is 20% with
values greater than 40% analyzed.
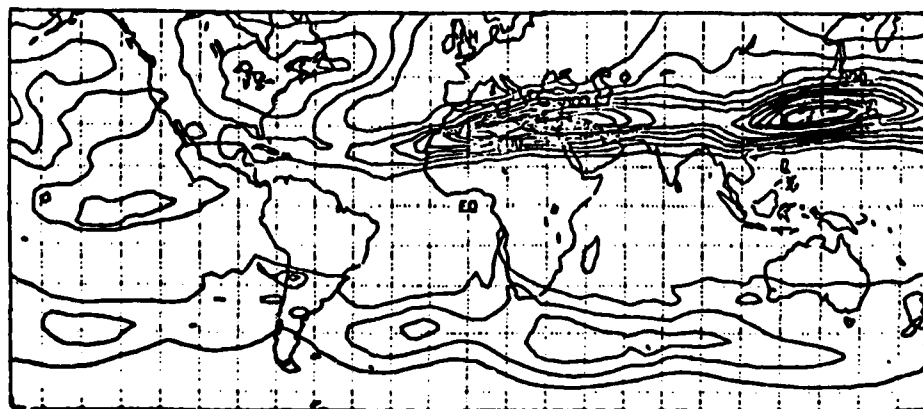
Figure 13. Time-average standing kinetic energy (KE_s) at 200 mb
for the NHW (m^2s^{-2}). The contour interval is 200
m^2s^{-2}.
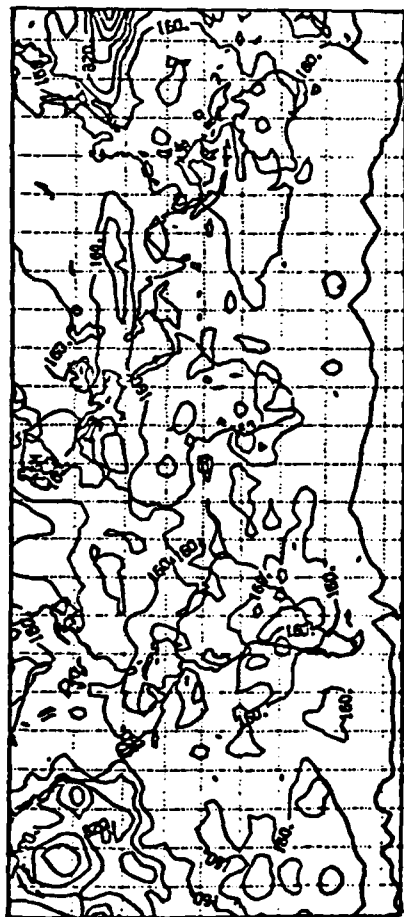
Figure 14. Time-average transient kinetic energy (KE_t) at 200 mb for the NHW (m^2s^{-2}). The contour interval is 80 m^2s^{-2}.
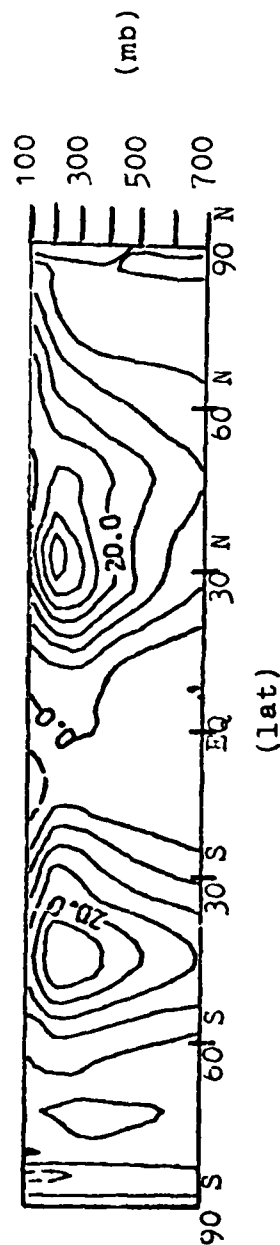
Figure 15. A latitude-height cross section of the time-longitude average zonal wind component (ms^{-1}) for the NHW. Contour interval is 5 ms^{-1}. Dashed lines represent negative values.

and

$$\sigma_u = \left[\frac{1}{N} \sum_{n=1}^{N} u^{n^2} - N\bar{u}^2\right]^{1/2} \tag{7}$$

where σ_u is the standard deviation of u, then KE_t is computed from

$$KE_t = \frac{1}{2} (\sigma_u^2 + \sigma_v^2). \tag{8}$$

The standard deviations (not shown) are in reasonable agreement with the fields given in Newell et al. (1972), with the variability in v being much greater than the variability in u. The KE_s fields agree closely with the time average zonal wind field (Figure 10) as is expected, while the KE_t fields show much more variability, with the highest values across the Northern Pacific Ocean.

The time-zonal average u and v components are presented in Figures 15 and 16, respectively. These values were computed using

$$[\bar{u}]_j = \frac{1}{MN} \sum_{i=1}^{72} \sum_{n=1}^{N} u^n_{ij} \tag{9}$$

where M=72 (5° longitude increment) and N=70 for the NHW data. The NHW zonal jet is located near 30°N with a maximum value of 38 m/sec at 200 mb. A secondary maximum occurs near 500 mb at 44°N with a value of 17 m/sec. The southern hemisphere zonal average jet is located at 48°S at all levels. The average meridional velocity component, [$\bar{v}$], shows the upper part of the northern Hadley cell with a maximum of southerly flow of about 2 m/sec between 200 and

(mb)

100
300
500
700

90 S   60 S   30 S   EQ   30 N   60 N   90 N
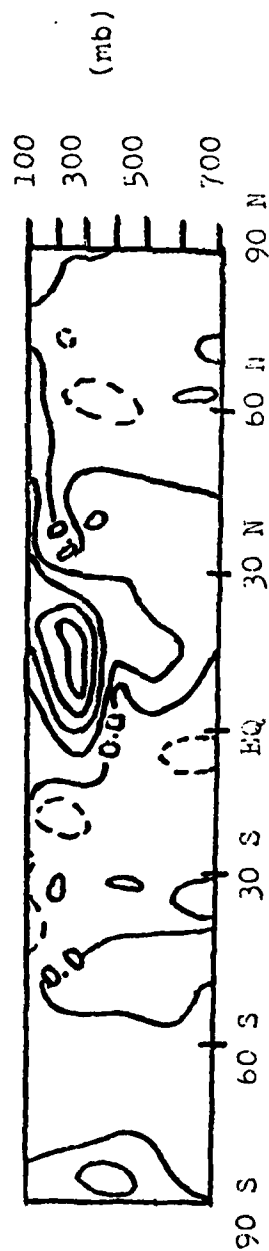
Figure 16. A latitude-height cross section of the time-longitude average meridional wind component (ms^{-1}) for the NHW. Contour interval is (.4 ms^{-1}). Dashed lines represent negative values.
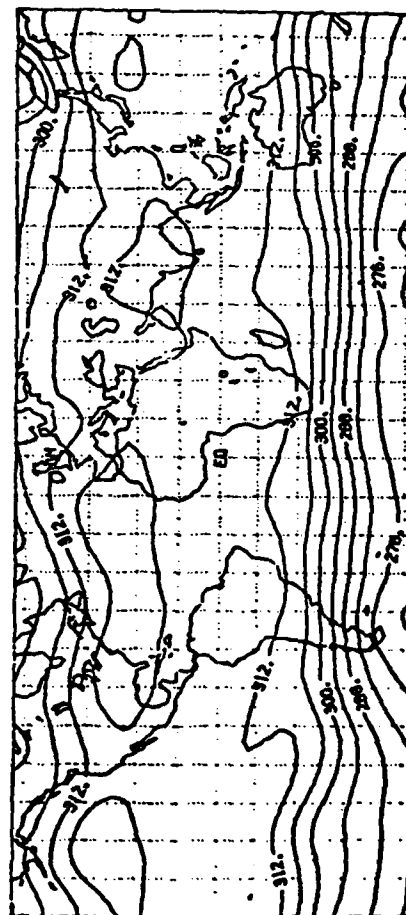
Figure 17. Time-average height field at 700 mb for the SHW (dm). The contour interval is 6 dm.

300 mb and around 12°N. The 850 mb level was not included in this study, but was shown in McGlasson (1977). Table 2 of McGlasson (1977) shows a negative [$\bar{v}$] between 24°S and 16°N which completes the lower portion of the northern Hadley cell. The maximum tropical [$\bar{v}$] northerly flow at 850 mb occurs at 4°S with a value of -1 m/sec. These time-zonal average fields are similar to those presented in Newell et al. (1972) and Oort et al. (1970).

The SHW data set is presented next. The SHW data consists of 15 days of 12-hour data, thus N=30 for this case. The mean fields are derived from a relatively short period of time and may be less representative than the previously presented NHW case. The 700, 500 and 200 mb height fields are shown in Figures 17, 18 and 19, respectively. The northern hemisphere height patterns seem to show much less dependence on mountain forcing. The long wave ridge is centered more over the central United States instead of the Rocky Mountains. This could be a function of the shortness of the data set and may not be representative. The southern hemisphere pattern is mainly one of zonal flow. There is a ridge near 40°S and slightly to the east of the Andes with a trough near 40°S and slightly to the west. These features appear weak in the mean fields during this time period. The lack of definite average ridge and trough positions could be due to the few mountain barriers in the southern hemisphere.

The mean 700, 500, 300 and 200 mb temperature fields are given in Figures 20-23, respectively. These temperature fields again correspond to the various polar and subtropical jets which can be seen
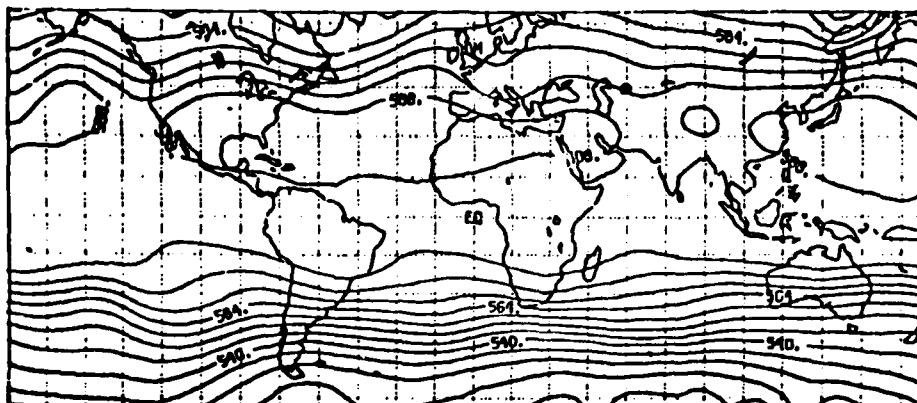
Figure 18.   Time-average height field at 500 mb for the SHW (dm).
             The contour interval is 6 dm.
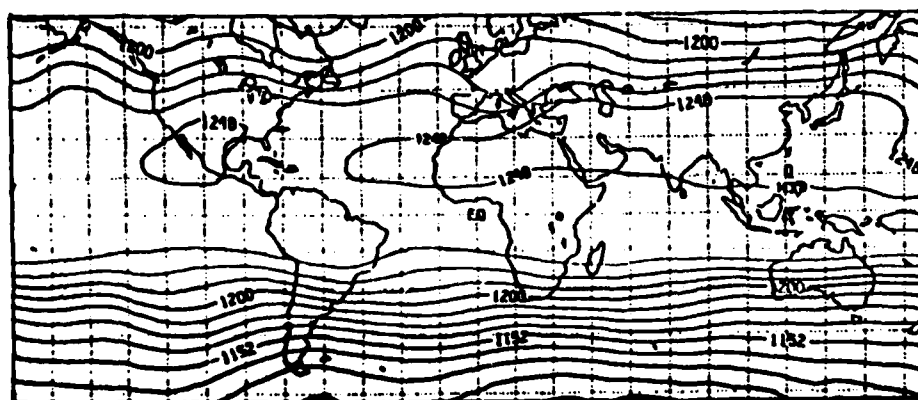
Figure 19.   Time-average height field at 200 mb for the SHW (dm).
             The contour interval is 12 dm.
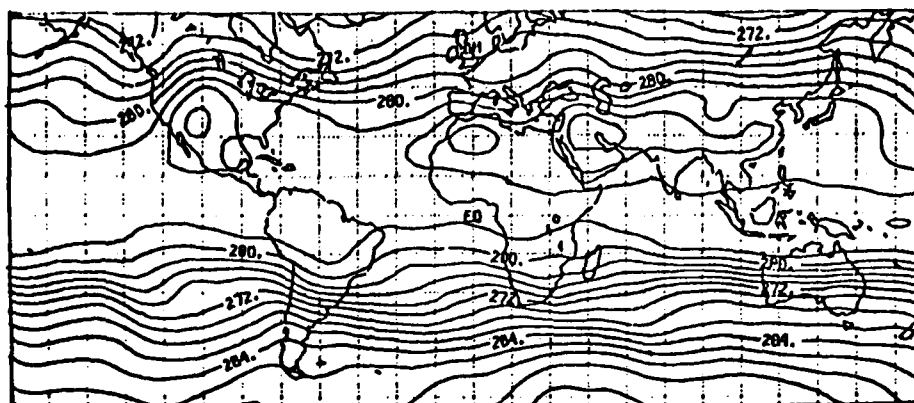
Figure 20. Time-average temperature field at 700 mb for the SHW (°K). The contour interval is 2°K.
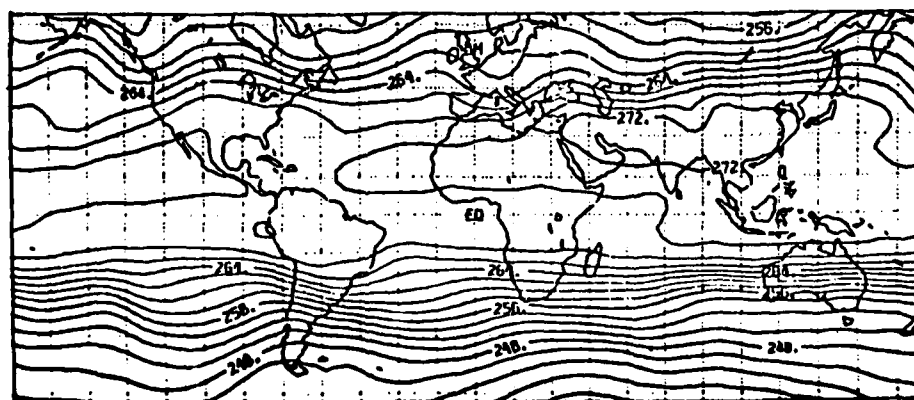
Figure 21. Time-average temperature field at 500 mb for the SHW (°K). The contour interval is 2°K.
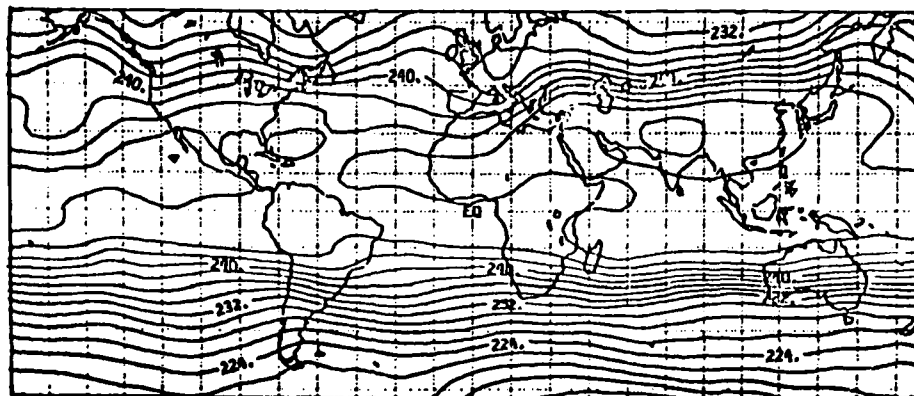
Figure 22. Time-average temperature field at 300 mb for the SHW
(°K). The contour interval is 2°K.
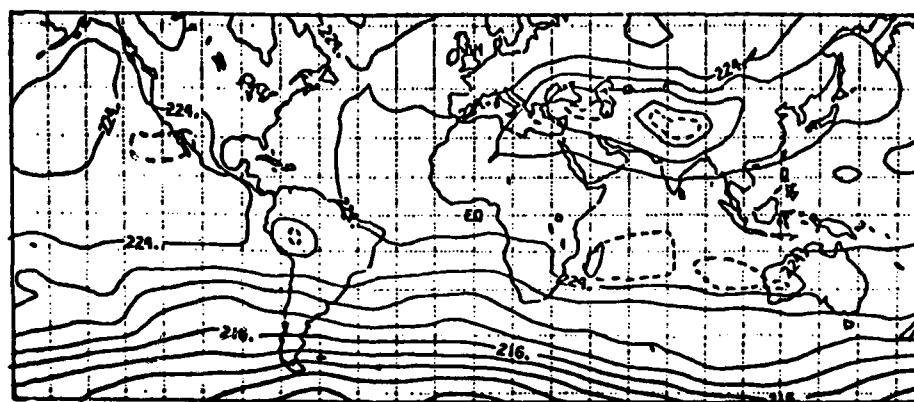
Figure 23. Time-average temperature field at 200 mb for the SHW
(°K). The contour interval is 2°K. Dashed lines
represent intermediate values.

in Figures 24-26.

The strongest jet during the SHW period occurs at 200 mb (Figure 26) near 30°S and across Australia. This jet positioning is in agreement with Newell et al. (1972). The 200 mb temperature field (Figure 23) does not strongly reflect this jet, but the 500 and 300 mb temperature fields (Figures 21 and 22) show a strong temperature gradient in this area.

In the northern hemisphere there is a relatively strong temperature gradient at 200 mb both to the north and the south of the Himalayan Mountain range. This strongly heated area corresponds with the area of the summer monsoon. To the north of this region there is a strong westerly 200 mb jet of magnitude 30 m/sec while to the south there is an easterly jet which has a maximum negative value near -20 m/sec. These jets are in agreement with similar jets presented in Newell et al. (1972) and Krishnamurti (1971b).

Figure 27 shows the 200 mb average meridional component of the horizontal wind. One interesting feature about the SHW data is that the horizontal velocity vector is almost completely nondivergent, unlike the NHW data. Thus, the analysis techniques used for the NHW data and the SHW data appear to be different. This subject will be further discussed in the next subsection.

The highest values of column averaged relative humidity (Figure 28) again correspond with the areas of heaviest precipitation given in Newell et al. (1972) with the exception that the area over Africa is slightly displaced to the west. Slight disagreements are to be expected since the intensity and placement of the tropical
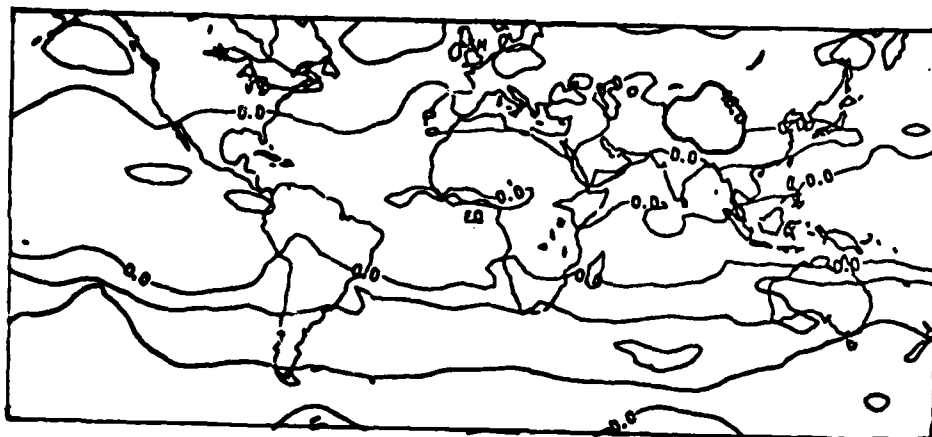
Figure 24. Time-average zonal component of the wind at 700 mb for the SHW (ms^{-1}). The contour interval is 10 ms^{-1}.
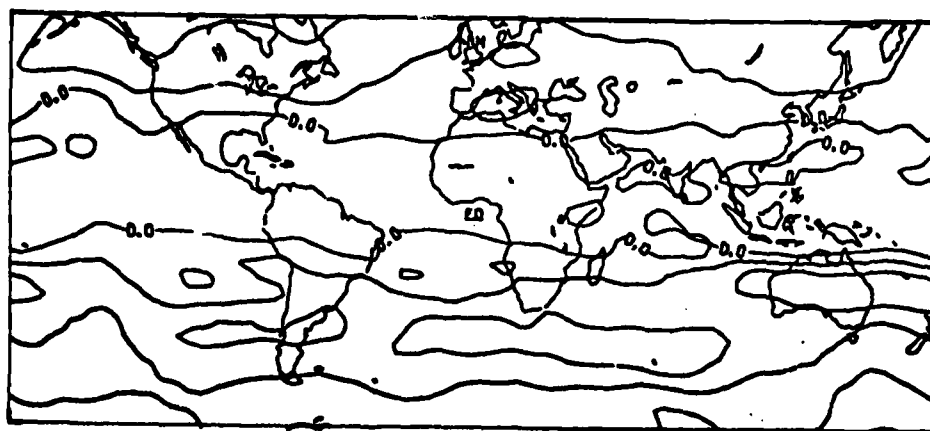
Figure 25. Time-average zonal component of the wind at 500 mb for the SHW (ms^{-1}). The contour interval is 10 ms^{-1}.
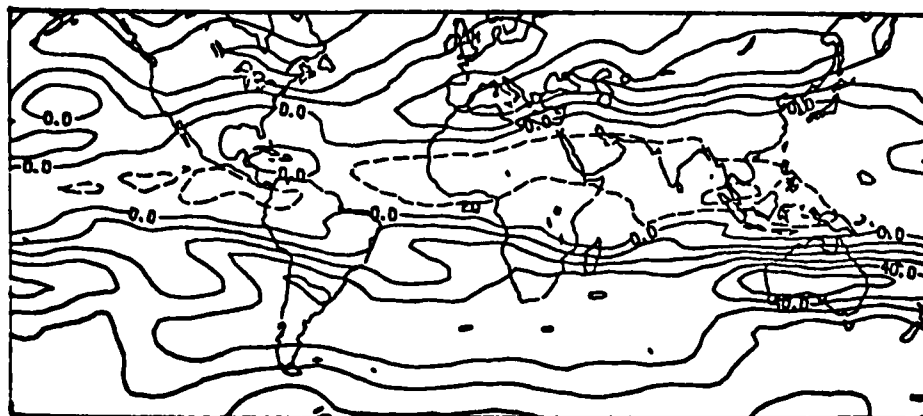
Figure 26. Time-average zonal component of the wind at 200 mb
for the SHW (ms^{-1}). The contour interval is 10 ms^{-1}.
Dashed lines represent negative values.
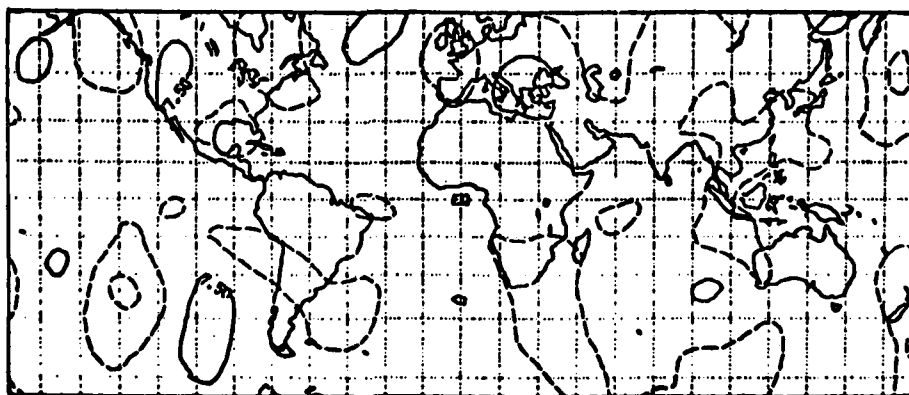
Figure 27. Time-average meridional component of the wind at
200 mb for the SHW (ms^{-1}). The contour interval is
10 ms^{-1}. Dashed lines represent negative values.
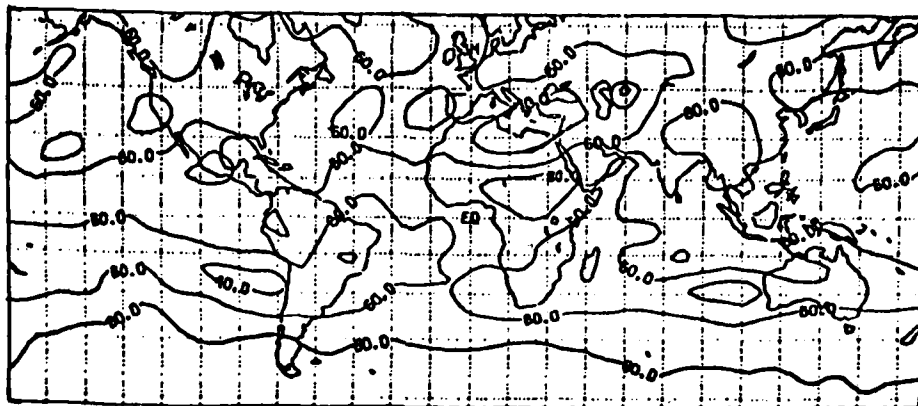
Figure 28. Time-average column average relative humidities for the SHW (%). The contour interval is 20% with values greater than 40% analyzed.
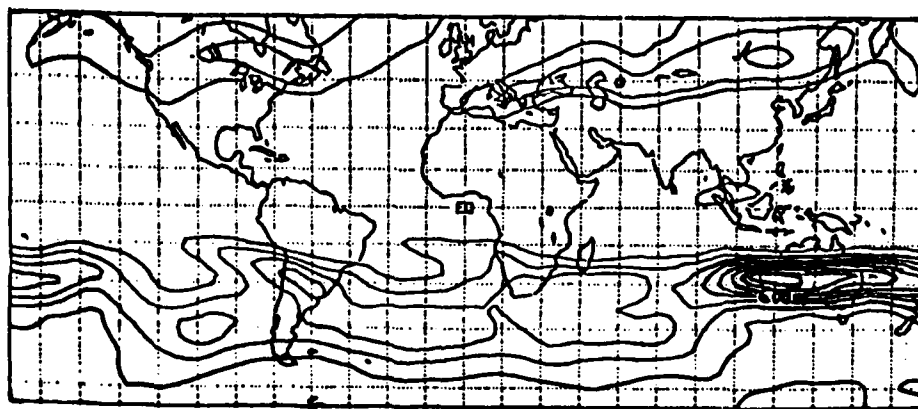
Figure 29. Time-average standing kinetic energy (KE_s) at 200 mb for the SHW (m^2s^{-2}). The contour interval is 200 m^2s^{-2}.

precipitation patterns are not completely known due to the sparsity of measurements in these areas.

The 200 mb standing kinetic energy field (Figure 29) is again much larger than the 200 mb transient kinetic energy field (Figure 30). The KE_s field corresponds quite well to 200 mb zonal wind component (Figure 26) and shows that the jet maximum across Australia has the highest average kinetic energy. The KE_t field is much less active for this data set as compared to the corresponding NHW KE_t field. The reason for this is not entirely obvious; but it could be due to the lack of data measurements in the southern hemisphere or the shortness of the data set.

The time-zonal average wind field (Figure 31) has a 200 mb, 36 m/sec jet maximum at 32^OS and a 22 m/sec maximum at 48^ON. The tropical easterlies are maximum at 100 mb with a value of -15 m/sec at 18^ON. These features are in agreement with Newell et al. (1972). The $[\bar{v}]$ field is not shown here since its order of magnitude is 10^{-2} m/sec, which again shows that this data set is remarkably non-divergent.

Before concluding this subsection, it is of interest to point out some relevant areas concerning the ultra-long waves that can be seen in this and other data studies. First, in the NHW average 200 mb northern hemisphere height field (Figure 5) there is a definite three wave pattern which appears to be anchored with a ridge over the Rocky Mountains. This three wave pattern is also visible in the average zonal wind fields of Newell et al. (1972), Plate 3.17, Krishnamurti (1960), and elsewhere. Also in the NHW data
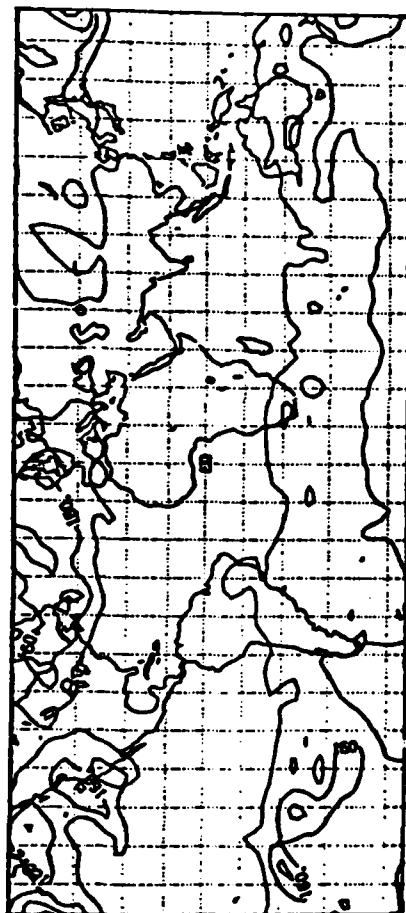
Figure 30. Time-average transient kinetic energy (KE_t) at 200 mb for the SHW (m^2s^{-2}). The contour interval is 80 m^2s^{-2}.
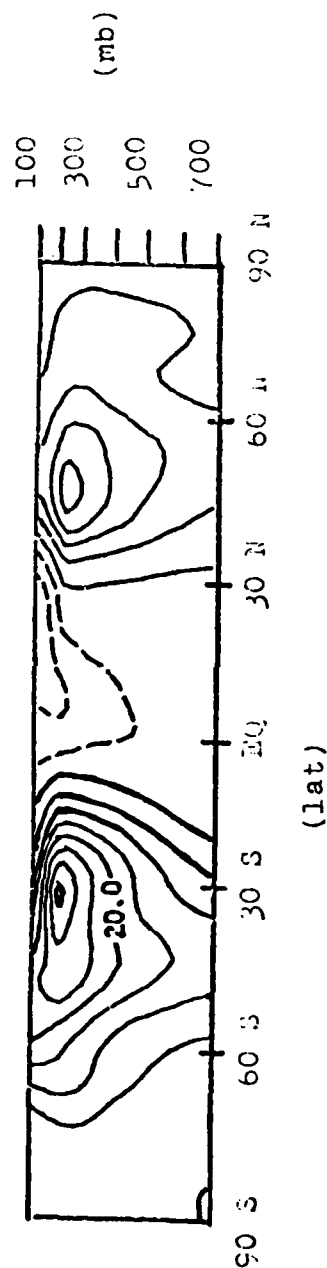
Figure 31. A latitude-height cross section of the time-longitude average zonal wind component (ms^{-1}) for the SHW. The contour interval is 5 ms^{-1}. Dashed lines represent negative values.

the heavy tropical precipitation areas given in Newell et al. (1972), Shutz and Gates (1972), and Figure 12 are located almost due south of the northern hemisphere mean jet positions given in Newell et al. (1972) and Figure 10. In the average 200 mb temperature field, Figure 7, there are also relatively warm areas at the southern fringes of the mean 200 mb jets.

From the SHW data similar analogies can be drawn between the most humid areas (Figure 28) and the positions of the southern hemisphere jet maxima (Figure 26). In this case, the Andes Mountains do not appear to appreciably affect the flow pattern, see Figure 19. The most active area of precipitation in the SHW is near the southern base of the Himalayan Mountains as is shown in Plate 9.3 from Newell et al. (1972). Looking to the south and slightly downwind of this region, one also finds the strongest SHW jet across Australia in Figure 26 and Plate 3.19 Newell et al. (1972). The other weaker jet maxima are also due south and slightly downwind of the other maxima in the tropical precipitation. Again, in the SHW 200 mb mean temperature field, Figure 23, there appear to be relatively heated areas near 30°S and in the regions of the subtropical jets. These areas do appear weaker here than in the NHW case and this may be due to the lack of data in these regions.

The locally heated areas near 30°N and 30°S, which are far from the sources of actual heating, are theorized here to be induced as follows. The monsoon areas average near 1 cm/day of rain which equates to an average vertical column heating of about 3°C/day. This heating occurs in areas of rising motion where the air is being

cooled adiabatically. Thus, the heating is not realized locally, but stored in the induced divergent motion field. A large portion of this heating is then released at approximately $30^\circ N$ or $30^\circ S$, depending on the season, when the air converges and is forced to subside, thus heating adiabatically. This is one mechanism that at least partially provides the strong temperature gradient needed for the maintenance of the subtropical jet streams. If the above hypothesis is valid, then one should find strong divergent outflows emanating from the heaviest precipitating areas and flowing into the regions of the subtropical jet streams. These divergent flows are carefully examined in the next subsection using the GISS NHW and SHW DST data sets.

Another instructive application of the time average data, in order to determine some measure of the effects of different types of forcing on the ultra-long waves has been carried out in Paegle et al. (1979). Using the fact that the divergence and vorticity are both 0 (10^{-6}) for the ultra-long waves, the vorticity equation, after Burger (1958), reduces to a very good approximation to $-f\nabla\cdot\mathbf{V}=\beta v$ and since $\frac{\partial\omega}{\partial p}=-\nabla\cdot v$ in pressure coordinates,

$$f \frac{\partial\omega}{\partial p} = \beta v . \tag{10}$$

Here f is the coriolis parameter, ω is the vertical motion, β is $\frac{1}{a}\frac{\partial f}{\partial\phi}$, and v is the meridional horizontal velocity component. Integrating Eq. (10) from the surface to the top of the atmosphere yields

$$\omega(p_{sfc}) = \int_0^{p_{sfc}} \frac{\beta v}{f} \, dp. \qquad (11)$$

For equivalently barotropic ultra-long waves with v varying slowly with height, Eq. (11) reduces to $\omega(p_{sfc}) \cong \frac{\beta v}{f} \sim$ 100 mb/day if v is order 10m/sec.

Since a pressure change of 100 mb/day for a parcel of air on the earth's surface following an ultra-long wave trajectory is only observed in the presence of high mountains that have a significant projection on the long waves, truly barotropic ultra-long waves should only exist in the presence of high mountains. Elsewhere, v must have some reversal in height to reduce the value of the integral in Eq. (11). The monsoonal type circulations do exhibit this reversal in the meridional flow with height. This also suggests that the subtropical ultra-long waves are at least in part forced by the monsoonal circulations.

The NHW mean meridional velocity component at 850 and 200 mb were decomposed with a fast Fourier transform (FFT) into its respective wavenumber components. Wavenumbers 0, 1, 2, and 3 were then reconstituted using the inverse FFT to produce ultra-long wave meridional velocity components. The results of these computations at 40^0S, 28^0S, 28^0N and 40^0N are given in Figure 1 of Paegle et al. (1979). Barotropic ultra-long wave flows only appear to exist at 40^0N, while in the areas of the subtropical jet, 28^0N and 28^0S, the flow demonstrates definite reversals in height. The reversal in v with height is the strongest at 28^0S. This result is in agreement

with the data previously presented, which tends to indicate that the
Andes Mountains do not appreciably affect the flow pattern of the
southern hemisphere in the NHW data. Future data studies with even
more complete data sets in the southern hemisphere should be carried
out to further check this result.

2.4 Divergent Flow Analysis

The divergent flow components are theorized to emanate from the
tropical areas with heaviest precipitation and flow toward the sub-
tropical jets of the winter hemisphere. To investigate this idea
more closely, the divergence was computed from the individual data
times for the NHW and SHW data using a centered difference approxi-
mation following McGlasson (1977). These divergence fields were
then averaged for the respective data sets. Figure 32 gives the
200 mb NHW positive time averaged divergence. The 200 mb NHW nega-
tive divergences less than -5 x 10^{-6} are analyzed in Figure 33.
These figures are hard to interpret beyond noting that areas of
strong average positive divergence do correspond to the areas of
heaviest tropical precipitation.

The average divergent horizontal velocity components were com-
puted from

$$\nabla^2 \chi = \nabla \cdot \mathbf{V} , \tag{12}$$

$$\mathbf{V}_\chi = \nabla \chi , \tag{13}$$

where ∇ is the horizontal gradient operator on a sphere, $\mathbf{V}$ is hori-
zontal velocity vector, $\mathbf{V}_\chi$ is the horizontal divergent wind, and χ is

Figure 32. Time-average positive divergence at 200 mb for the NHW (s^{-1}). The contour interval is $5 \times 10^{-6} s^{-1}$ with values of 5×10^{-6} or greater analyzed.
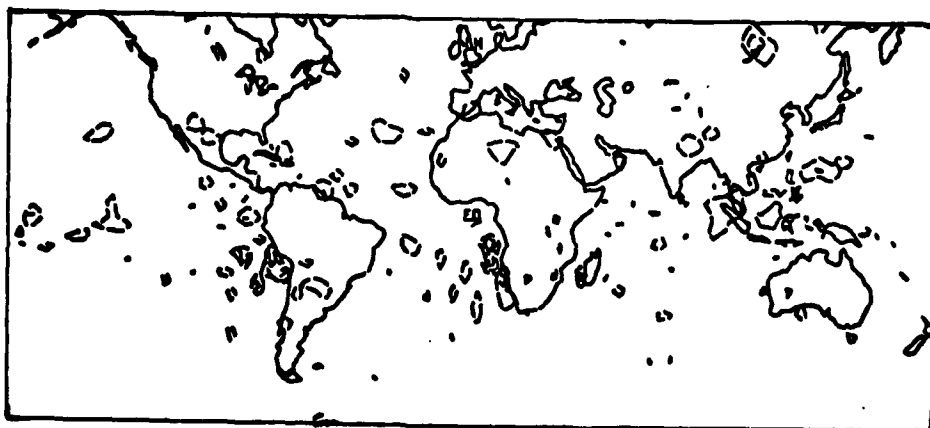
Figure 33. Time-average negative divergence at 200 mb for the NHW (s^{-1}). The contour interval is $5 \times 10^{-6} s^{-1}$ with values -5×10^{-6} or less analyzed.

the divergent velocity potential. Equation (12) was solved for χ

using a relaxation technique. Then the divergent velocity compo-

nents v_χ and u_χ were computed from Eq. (13) using a centered dif-

ference approximation. The results of these computations for the

200 mb NHW data are given in Figures 34, 35 and 36.

Figure 37 displays the 200 mb NHW meridional ageostrophic flow

field. Because the geostrophic wind becomes quite large near the

equator, the values of the ageostrophic wind between 6°S and 6°N

were scaled by 1 x 10^{-5}. The ageostrophic flows were computed by

applying a centered difference approximation to

$$\bar{v} - \bar{v}_g = \bar{v} - \frac{1}{f}\frac{1}{a\cos\phi}\frac{\partial\bar{\Phi}}{\partial\lambda} , \tag{14}$$

where Φ is the geopotential height, a is the radius of the earth and

the bar operator represents the time average.

Comparing the NHW average zonal wind (Figure 10) and the NHW

average meridional ageostrophic wind (Figure 37) one can see that

the jet streams are accelerating in areas of positive ageostrophic

flow in the northern hemisphere and negative ageostrophic flow in

the southern hemisphere. Also, areas of deceleration correspond to

negative/positive ageostrophic flows in the northern/southern hemi-

sphere.

These results are in agreement with those found by Blackmon

et al. (1977). Next, comparing NHW meridional divergent wind (Fig-

ure 35) with the meridional ageostrophic flow pattern (Figure 37)

and the column averaged relative humidity field (Figure 12), one
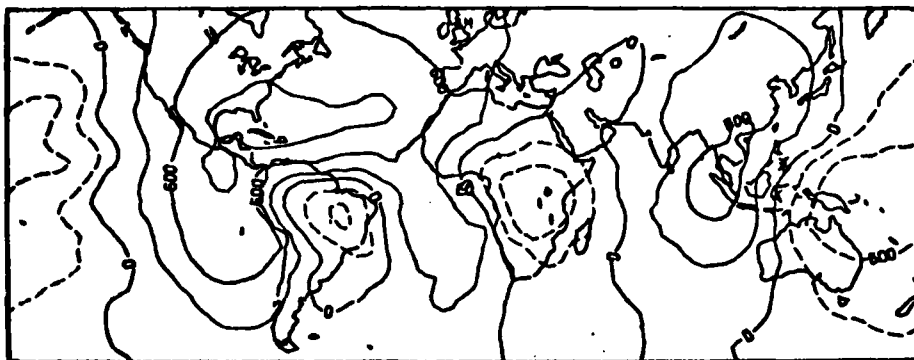
Figure 34. NHW divergent velocity potential (m2sec-1) computed from the 200 mb time-average divergence. The contour interval is $3 \times 10^6 m^2 s^{-1}$ and the labels are scaled by 1×10^{-4}. Dashed lines represent negative values.
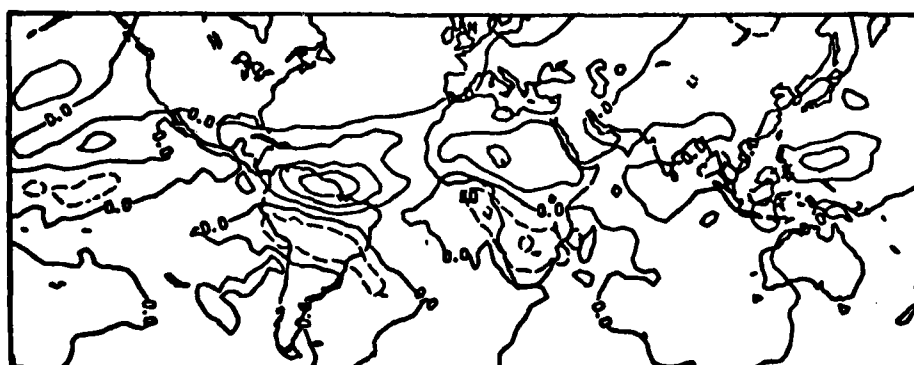
Figure 35. The 200 mb NHW time average meridional divergent component of the wind ($m\ sec^{-1}$). The contour interval is $2\ ms^{-1}$ with the negative contours dashed.
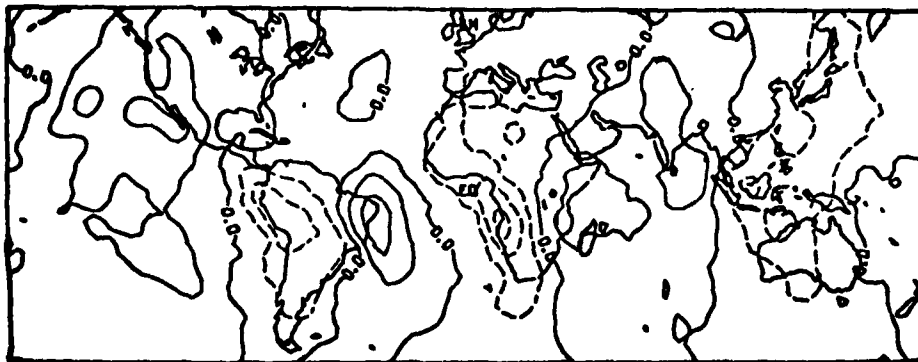
Figure 36. The 200 mb NHW time-average zonal divergent component of the wind (m s^{-1}). The contour interval is 2 m s^{-1} with the negative contours dashed.
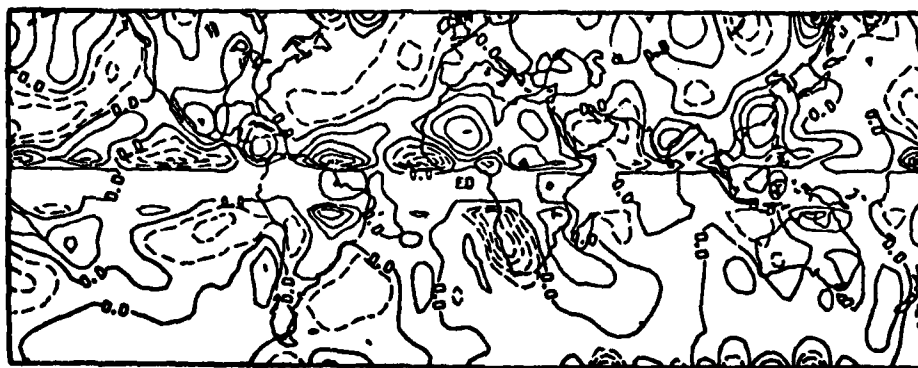
Figure 37. The 200 mb NHW time-average meridional ageostrophic flow field with contour interval of 2 m s^{-1} and negative contours dashed.

can see that, as postulated in the introduction, the divergent flows
originate in the areas of strongest precipitation and flow into
areas of the northern hemisphere where the ageostrophic flow is
positive.

The divergent flows into the southern hemisphere are much
weaker, as compared to the flows into the northern hemisphere. The
northern extent of the divergent outflows corresponds quite well to
the pockets of warm air at 200 mb located near 30^ON in Figure 7.
This also helps to substantiate the conjecture that the latent heat
release occurring in the tropics is not realized locally but carried
in the divergent part of the motion field to near 30^ON where the
heating occurs due to subsidence. One peculiarity in the NHW diver-
gent flow fields is that the strongest area of outflow occurs over the
Amazon basin, while the strongest precipitation given by Shutz and
Gates (1972) and Newell et al. (1972) occurs in the winter monsoon
to the north of Australia.

In similar computations with the SHW data, it was found that
the wind fields were essentially nondivergent at all levels, so it
was necessary to utilize another means of computing some measure of
the divergence for these fields. Paegle and Paegle (1976a) have
devised such a measure when the balance equation becomes nonelliptic
Houghton (1968) gives the condition for nonellipticity as

$$f^2 + 2\nabla^2 \phi + 2\beta u < 0. \tag{15}$$

But in this study, following the arguments of Paegle and Paegle
(1976a), Eq. (16) below is used for the ellipticity condition.

$$(f^2 + \nabla^2\Phi - G) - |f\{(\nabla^2\Phi - G)^2/f^2 - (A^2_g + B^2_g)\}^{\frac{1}{2}}| < 0 \qquad (16)$$

where

$$G = -\beta u_g - (v^2_g + u^2_g)/a^2 - (2\tan\phi/a^2) \cdot$$

$$\left[u_g \frac{\partial u_g}{\partial\phi} + v_g \frac{\partial v_g}{\partial\phi} + (u_g \frac{\partial v_g}{\partial\lambda} - v_g \frac{\partial u_g}{\partial\lambda} / \cos\phi \right] \qquad (17)$$

$$A_g = -\{\frac{\partial}{\partial\phi}[(u^2_g + v^2_g)\sin\phi/a] + 2\frac{\partial}{\partial\lambda}(u_g v_g \tan\phi/a)\}/af\cos\phi -$$

$$\left\{ \frac{\partial}{\partial\phi}(\frac{1}{a}\frac{\partial\Phi}{\partial\phi}\cos\phi) - \frac{\partial}{\partial\lambda}\left[\frac{\partial\Phi}{\partial\lambda}/(a\cos\phi)\right] \right\}/(af\cos\phi) - \beta u_g/f \qquad (18)$$

$$B_g = \left\{ -\beta v_g + 4u_g \frac{\partial u_g}{\partial\lambda}\tan\phi / (a^2\cos\phi) - \right.$$

$$\left. \left[\frac{\partial}{\partial\lambda}(\frac{\partial\Phi}{\partial\phi}) + \frac{\partial}{\partial\phi}(\frac{\partial\Phi}{\partial\lambda}) \right] / (a^2\cos\phi) \right\} / f. \qquad (19)$$

u_g/v_g are the zonal/meridional components of geostrophic wind, a is the radius of the earth, and ϕ and λ are latitude and longitude, respectively. Equation (16) actually leads to a slight underestimate of the actual nonelliptic areas (Paegle and Paegle, 1976a).

In areas where the balance equation is nonelliptic, divergence can be computed as follows. The absolute vorticity is assumed to be zero and then the nonelliptic divergence (NED) is calculated using either Eq. (20) or (22).

$$NED = [-(f^2 + \nabla^2\Phi - G) + |f\{(\nabla^2\Phi - G)^2/ f^2 -$$

$$(A^2_g + B^2_g)\}^{\frac{1}{2}}|]^{\frac{1}{2}}. \qquad (20)$$

If the radical in (16) is negative, then (21) is used as the condition for nonellipticity and the NED is computed from the condition

$$f^2 + 2\nabla^2\Phi - 2G + A_g^{\ 2} + B_g^{\ 2} < 0 \qquad (21)$$

and

$$NED = \{-(f^2 + 2\nabla^2\Phi - 2G + A_g^{\ 2} + B_g^{\ 2})\}^{\frac{1}{2}}. \qquad (22)$$

Figure 38 gives the time average NHW 200 mb nonelliptic divergence computed using a centered difference approximation on the above equations. The largest values of the divergence appear to be in the tropics and correspond to the areas of heaviest precipitation. This field is much larger than the actual kinematic average divergence field, but one must consider that this technique has no compensating convergence to reduce the average value.

To correct this problem, the values of the 200 mb nonelliptic divergence at each individual time were sorted into clusters. The weighted center of each cluster was then computed. The area average divergence of the cluster was compensated by adding an equal amount of area average convergence. The convergence was added outward from the cluster center between radii of 1000 to 3000 km in the tropics (30°N to 30°S). The compensation elsewhere extended from 1000 to 2000 km. These compensation distances were inferred from Paegle (1978). The individual divergence fields were then averaged. From this average 200 mb compensated nonelliptic field, the velocity potential χ (Figure 39), and the divergent velocity field, $\mathbf{V}_\chi$, (Figures 40 and 41) were computed.
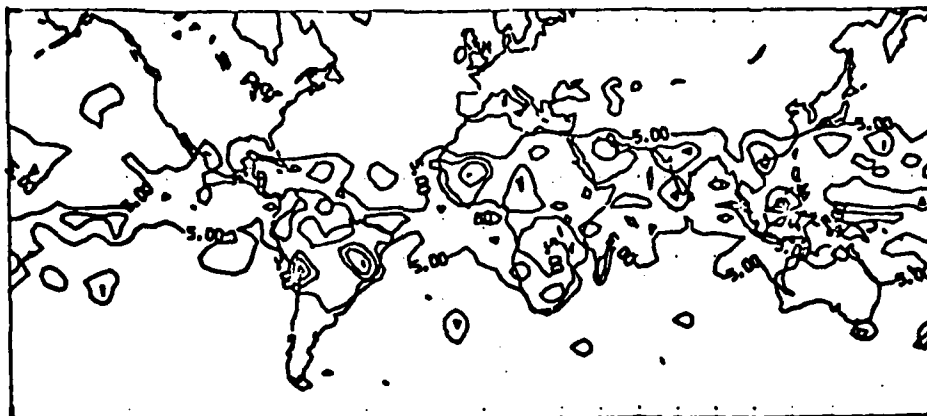
Figure 38. Time-average NHW 200 mb non-elliptic divergence. Contour interval of $10 \times 10^{-6} s^{-1}$. Labels are in units of $10^{-6} s^{-1}$. Values greater than $5 \times 10^{-6} s^{-1}$ are analyzed.

Figure 39. 200 mb compensated NHW time-average non-elliptic computed velocity potential in units of $m^2 s^{-1}$. Labels are scaled by 10^{-5}. Contour interval is 4×10^6.

The divergent velocity field computed by this method bears certain similarities to those computed from the actual wind fields. The main difference between Figures 35 and 41 are in the magnitudes of the divergent flows. The nonelliptically computed meridional velocity component (Figure 41) has its maxima flowing into but slightly upwind of the average 200 mb NHW jets (Figure 10). In all areas where the jet is accelerating there are NED flows with the strongest flows corresponding to areas of greatest acceleration. These flows also have some agreement with the areas of average ageostrophy. Since the NHW divergent flow pattern computed by this technique shows some agreement with the kinematic divergence flow fields, this measure of the divergence will be used in the SHW data where the velocity is nondivergent.

Figure 43 is the SHW divergent velocity potential, χ, computed from the nonelliptic divergence (Figure 42) using the above compensation technique. Figures 44 and 45 are the divergent zonal and meridional components, u_χ and v_χ, respectively. The meridional divergent velocity component shows a strong area of northerly flow into the area off the west coast of South America where the average jet undergoes an approximate acceleration of 30 m/sec (Figure 26). The southern hemisphere average jet pattern is also accelerated off the west coast of Australia where another area of northerly divergent flow exists. A weaker area of northerly divergent flow off the west coast of southern Africa flows into an area of weak acceleration of the mean zonal flow. The SHW mean meridional ageostrophic flow is given in Figure 46.
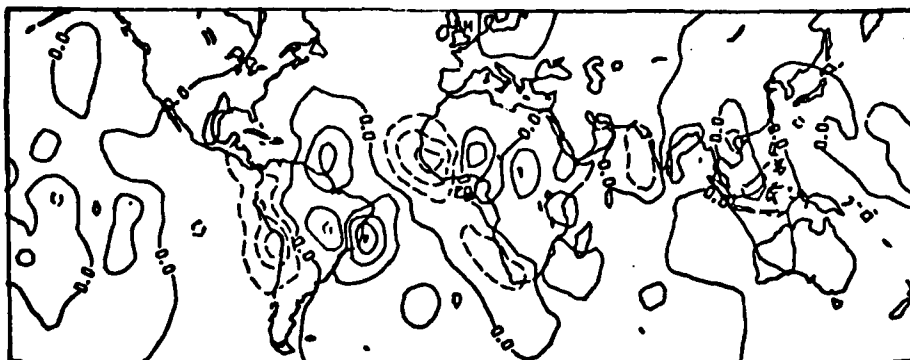
Figure 40. NHW 200 mb zonal non-elliptic divergent velocity component (m s^{-1}). Contour interval of 2 m s^{-1}. Dashed lines represent negative values.
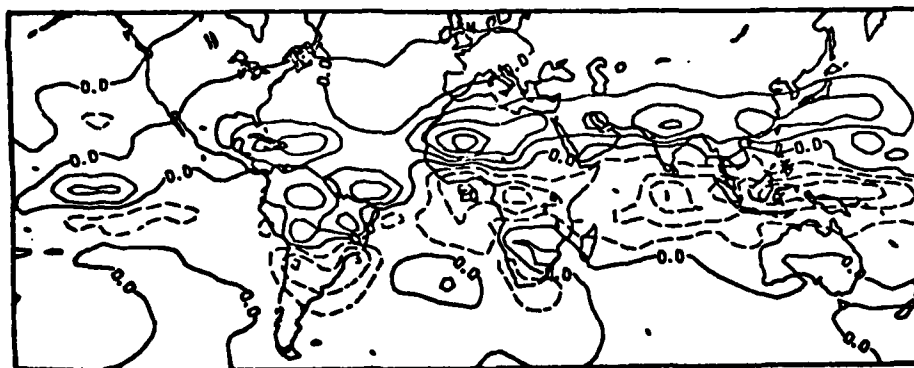
Figure 41. NHW 200 mb meridional non-elliptic divergent velocity component (m s^{-1}). Contour interval of 2 m s^{-1}. Dashed lines represent negative values.
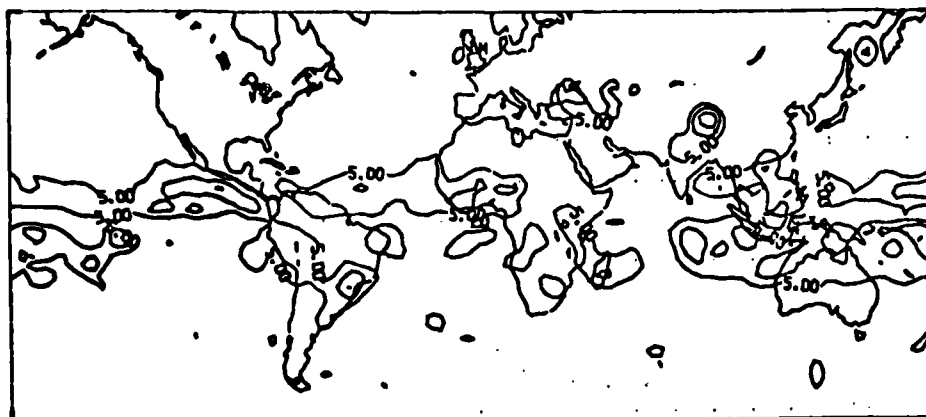
Figure 42. Time-average SHW 200 mb non-elliptic divergence.
Contour interval of $10^{-5} s^{-1}$. Labels are in units
of $10^{-6} s^{-1}$.
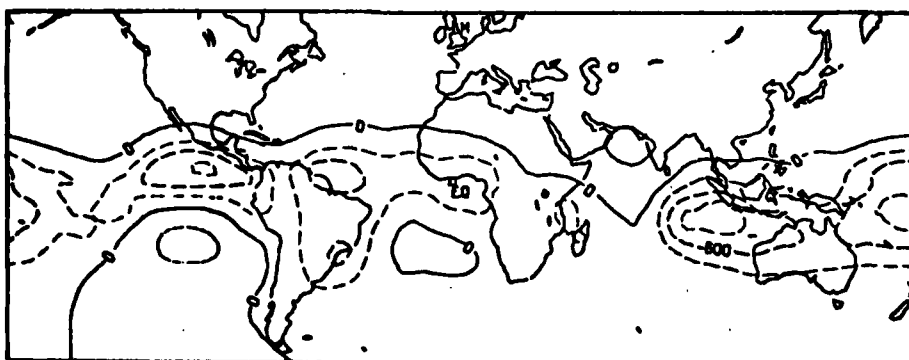
Figure 43. 200 mb compensated SHW time-average non-elliptic
computed velocity potential in units of $m^2 s^{-1}$.
Labels are scaled by 10^{-4}.
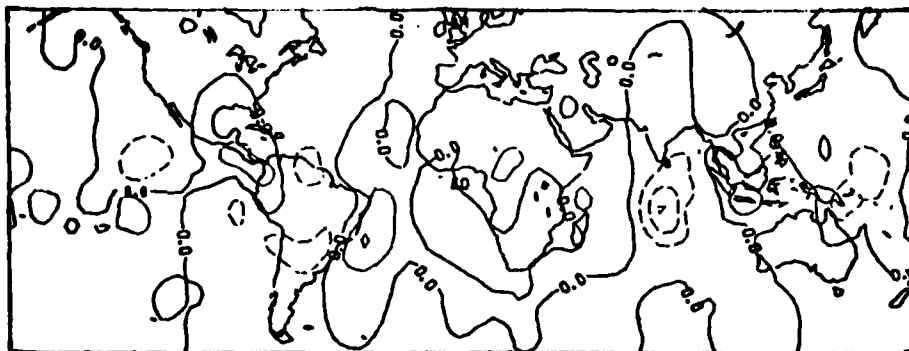
Figure 44. SHW 200 mb zonal non-elliptic divergent velocity component $(m\ s^{-1})$. Contour interval is $2\ m\ s^{-1}$. Dashed lines represent negative values.
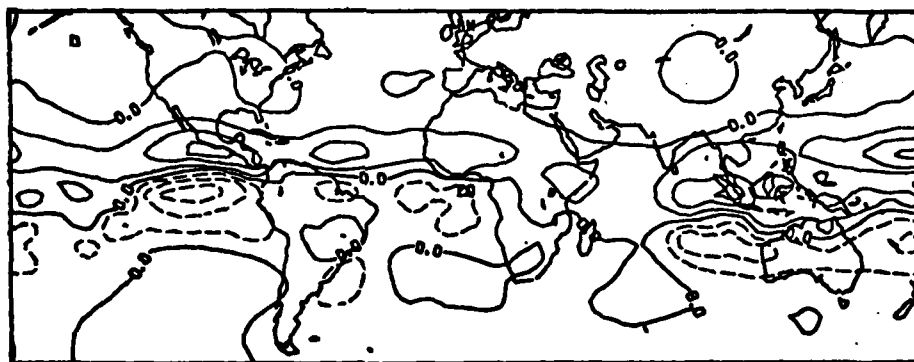
Figure 45. SHW 200 mb meridional non-elliptic divergent velocity component $(m\ s^{-1})$. Contour interval is $2\ m\ s^{-1}$. Dashed lines represent negative values.
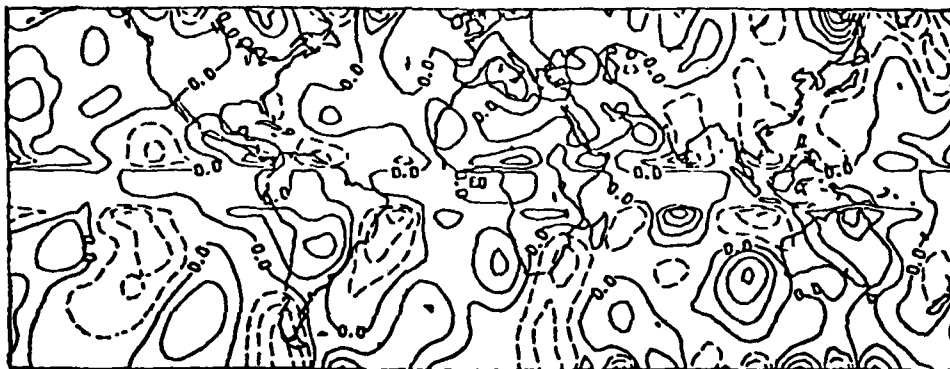
Figure 46.   The 200 mb SHW time-average meridional ageostrophic
flow field with contour interval of 2 m sec^{-1} and
negative contours dashed.

The NED flow patterns seem to originate in the areas of heaviest tropical precipitation near southern Mexico and western Africa, but the strongest precipitation area near the base of the Himalayan Mountains is not reflected locally in the NED flows. The area of strongest northerly flow is far from what one would believe to be the actual source, the summer Indian monsoon. The strongest non-elliptic divergences for the SHW data (Figure 42) did occur at 30°N near the Himalayan Mountains, but this area was very localized and was not reflected in the relaxed divergent fields. This may not reflect the actual kinematic fields, but might be a consequence of the technique used in computing the NED values or the compensation method, since the resulting flows are only an indirect estimate of the true divergent flows.

The next three chapters will describe several numerical experiments designed to check observational inferences made in this chapter. The next chapter details the experimental models, while chapters 4 and 5 present the experiments.

CHAPTER 3

THE TEST MODELS

Both a primitive equation divergent barotropic model and a two-level baroclinic primitive equation model were written using Arakawa's formulation given in Arawaka (1974) and Arakawa and Lamb (1977). The Arakawa finite difference schemes were chosen for the experiments described in Chapters 4 and 5 for several reasons. First, the consistent conservative properties of the Arakawa finite difference scheme closely match the real atmosphere. Next, the scheme is well understood and should be well suited for the simulation of the ultra-long waves as can be deduced from Baumhefner (1978). Finally, the scheme is affordable for 4° x 5° global resolution required to test the current hypotheses.

3.1 The Barotropic Model

The governing equations in flux form for the forced divergent barotropic model used in the study described in Chapter 4 are given below. The divergent forcing functions are on the right-hand sides of Eqs. (23), (24) and (25).

$$\frac{\partial}{\partial t}\left(\frac{u\Phi}{mn}\right) + \frac{\partial}{\partial \lambda}\left(\frac{\Phi u}{n} u\right) + \frac{\partial}{\partial \phi}\left(\frac{\Phi v}{m} u\right) - \left(\frac{f}{mn} - u\frac{\partial}{\partial \phi}\left(\frac{1}{m}\right)\right)\Phi v +$$

$$\frac{\Phi}{n}\frac{\partial \Phi}{\partial \lambda} = \frac{\tilde{\Phi}u}{mn}\Delta_f \,, \tag{23}$$

$$\frac{\partial}{\partial t} \left(\frac{\Phi v}{mn}\right) + \frac{\partial}{\partial \lambda} \left(\frac{\Phi u}{n} v\right) + \frac{\partial}{\partial \phi} \left(\frac{\Phi v}{m} v\right) + \left(\frac{f}{mn} - u \frac{\partial}{\partial \phi} \left(\frac{1}{m}\right)\right) \Phi u$$

$$+ \frac{\Phi}{m} \frac{\partial \Phi}{\partial \phi} = \frac{\tilde{\Phi} v}{mn} \Delta_f \ , \tag{24}$$

$$\frac{\partial}{\partial t} \left(\frac{\Phi}{mn}\right) + \frac{\partial}{\partial \lambda} \left(\frac{\Phi u}{n}\right) + \frac{\partial}{\partial \phi} \left(\frac{\Phi v}{m}\right) = \frac{\tilde{\Phi}}{mn} \Delta_f \tag{25}$$

where ϕ = latitude

λ = longitude

Φ = gZ the geopotential height

$m = (a \cos \phi)^{-1}$

$n = a^{-1}$, a is the earth radius

f is the Coriolis parameter.

$$\Delta_f \equiv \begin{cases} 0 \text{ for the divergent barotropic model with no forcing} \\ DIV_f \text{ divergent forcing function (constant in time)} \end{cases}$$

and

$$\tilde{\Phi} = \frac{1}{2\pi} \int_0^{2\pi} \Phi(\lambda,\phi,t) \ d\lambda.$$

The finite difference forms of the barotropic model given below follow from Arakawa (1974) and Arakawa and Lamb (1977). The variables are defined on the "c" staggered grid as defined in Arakawa and Lamb (1977).

The finite difference form of the spherical barotropic model is presented here since sphericity is not included in the particular description of Arakawa and Lamb (1977).

Equation (26) in finite difference form is

$$\Delta\lambda\Delta\phi \, \frac{\partial}{\partial t}\left(\frac{\Phi_{ij}}{m_j n}\right) + F_{i+\frac{1}{2}j} - F_{i-\frac{1}{2}j} + G_{ij+\frac{1}{2}} - G_{ij-\frac{1}{2}}$$

$$= \frac{\tilde{\Phi}_j}{m_j n} \, \Delta_{fij} \, \Delta\lambda\Delta\phi \tag{26}$$

$$F_{i+\frac{1}{2}j} = \frac{1}{2} \, \bar{u}_{i+\frac{1}{2}j} \, \frac{\Delta\phi}{n} \, (\Phi_{i+1j} + \Phi_{ij}) \tag{27}$$

$$G_{ij+\frac{1}{2}} = \frac{1}{2} \, v_{ij+\frac{1}{2}} \, \frac{\Delta\lambda}{m_j} \, (\Phi_{ij+1} + \Phi_{ij}) \tag{28}$$

where the overbar operator is a Fourier smoother used to reduce the phase speed of gravity waves near the poles. The form of the smoother is

$$S_j(s) = \frac{\Delta\lambda}{\Delta\phi} \, \cos \, \phi_j / \sin \, \left(\frac{s\Delta\lambda}{2}\right) \tag{29}$$

where $\Delta\lambda = 5^O$ is the grid size in longitude, $\Delta\phi = 4^O$ is the grid size in latitude, and s is the Fourier wavenumber. The u component of the momentum flux equation is given by

$$\frac{\partial}{\partial t} \, (\phi^{(u)}u)_{ij} + \left[\delta_\lambda(\hat{F}^{(u)}\overline{u}^\lambda) + \delta_\phi(g^{(u)}\overline{u}^\phi) + \delta_{\lambda'}(\tilde{F}^{(u)}\overline{u}^{\lambda'})\right.$$

$$\left. + \, \delta_{\phi'}(\tilde{g}^{(u)}\overline{u}^{\phi'})\right]_{ij} - \overline{(\phi C \overline{v}^\phi)}^\lambda_{ij} + \frac{\Delta\phi}{n} \, \overline{[\overline{\Phi}^\lambda \delta_\lambda \Phi]}_{ij}$$

$$= \tilde{\Phi}_j \, u_{ij} \, \Delta_{ij}^{(u)} \tag{30}$$

where

$$\delta_\lambda(\,) \equiv (\,)_{i+\frac{1}{2}j} - (\,)_{i-\frac{1}{2}j}$$

$$\overline{(\,)}^\lambda \equiv \frac{1}{2} \, [(\,)_{i+\frac{1}{2}j} + (\,)_{i-\frac{1}{2}j}]$$

$$\delta_\phi(\ ) \equiv (\ )_{ij+\frac{1}{2}} - (\ )_{ij-\frac{1}{2}}$$

$$\overline{(\ )}^\phi \equiv \frac{1}{2}[(\ )_{ij+\frac{1}{2}} + (\ )_{ij-\frac{1}{2}}]$$

$$\delta_{\lambda'}(\ ) \equiv (\ )_{i+\frac{1}{2}j+\frac{1}{2}} - (\ )_{i-\frac{1}{2}j-\frac{1}{2}}$$

$$\overline{(\ )}^{\lambda'} \equiv \frac{1}{2}[(\ )_{i+\frac{1}{2}j+\frac{1}{2}} + (\ )_{i-\frac{1}{2}j-\frac{1}{2}}]$$

$$\delta_\phi'(\ ) \equiv (\ )_{i-\frac{1}{2}j+\frac{1}{2}} - (\ )_{i+\frac{1}{2}j-\frac{1}{2}}$$

$$\overline{(\ )}^{\phi'} \equiv \frac{1}{2}[(\ )_{i-\frac{1}{2}j+\frac{1}{2}} + (\ )_{i+\frac{1}{2}j-\frac{1}{2}}]$$

$$\hat{F}^{(u)}_{i+\frac{1}{2}j} = \frac{2}{3}\ (\overline{F*}^{\phi\phi})_{i+\frac{1}{2}j}$$

$$g^{(u)}_{ij+\frac{1}{2}} = \frac{2}{3}\ (\overline{G*}^{\phi\lambda})_{ij+\frac{1}{2}}$$

$$\tilde{F}^{(u)}_{i+\frac{1}{2}j+\frac{1}{2}} = \frac{1}{6}\ (\overline{G* + F*}^\phi)_{i+\frac{1}{2}j+\frac{1}{2}}$$

$$\tilde{g}^{(u)}_{i-\frac{1}{2}j+\frac{1}{2}} = \frac{1}{6}\ (\overline{G* - F*}^\phi)_{i-\frac{1}{2}j+\frac{1}{2}}$$

$$\phi^{(u)}_{ij} = \left(\overline{(\frac{\Phi}{m})}^{\lambda\phi\phi}\right)_{ij}\ \frac{\Delta\lambda\Delta\phi}{n} \tag{30a}$$

$$\Delta^{(u)}_{ij} = \left(\overline{(\frac{\Delta_f}{m})}^{\lambda\phi\phi}\right)_{ij}\ \frac{\Delta\lambda\Delta\phi}{n} \tag{30b}$$

$$C_{ij} = f_j\ \frac{\Delta\lambda\Delta\phi}{m_j n} - \Delta\lambda\ \overline{u}^\lambda_{ij}\ \delta_\phi(\frac{1}{m})_j$$

$$F*_{ij} = \overline{F}^\lambda_{ij}$$

$$G*_{ij} = \overline{G}^\phi_{ij}\ .$$

Now the v component of the momentum flux equation is given by

$$\frac{\partial}{\partial t}\left(\phi^{(v)}v\right)_{ij} + \left[\delta_\lambda(\hat{F}^{(v)}\,\overline{v}^\lambda) + \delta_\phi(g^{(v)}\,\overline{v}^\phi) + \delta_{\lambda'}(\tilde{F}^{(v)}\,\overline{v}^{\lambda'})\right.$$

$$\left. + \delta_{\phi'}(\tilde{g}^{(v)}\,\overline{v}^{\phi'})\right]_{ij} + \overline{(\phi C \overline{u}^\lambda)}^\phi_{ij} + \frac{\Delta\lambda}{m_j}\left[\overline{\phi}^\phi\delta_\phi\,\phi\right]_{ij} =$$

$$= \tilde{\phi}_j\,v_{ij}\,\Delta^{(v)}_{ij} \tag{31}$$

where

$$\hat{F}^{(v)}_{i+\frac{1}{2}j} = \frac{2}{3}\,(\overline{F^\star}^{\phi\lambda})_{i+\frac{1}{2}j}$$

$$g^{(v)}_{ij+\frac{1}{2}} = \frac{2}{3}\,(\overline{G^\star}^{\lambda\lambda})_{ij+\frac{1}{2}}$$

$$\tilde{F}^{(v)}_{i+\frac{1}{2}j+\frac{1}{2}} = \frac{1}{6}\,(\overline{G^\star + F^\star}^\lambda)_{i+\frac{1}{2}j+\frac{1}{2}}$$

$$\tilde{g}^{(v)}_{i-\frac{1}{2}j+\frac{1}{2}} = \frac{1}{6}\,(\overline{G^\star - F^\star}^\lambda)_{i-\frac{1}{2}j+\frac{1}{2}}$$

$$\phi^{(v)}_{ij} = \left(\overline{\left(\frac{\phi}{m}\right)}^{\lambda\lambda\phi}\right)_{ij}\frac{\Delta\lambda\Delta\phi}{n} \tag{31a}$$

$$\Delta^{(v)}_{ij} = \left(\overline{\left(\frac{\Delta_f}{m}\right)}^{\lambda\lambda\phi}\right)_{ij}\frac{\Delta\lambda\Delta\phi}{n}. \tag{31b}$$

When $\Delta_{ij}=0$ for all i, j the above model is designed to conserve

    i) the total energy integrated over the spherical domain,

    ii) the kinetic energy, integrated over the domain, under inertial processes,

    iii) the enstrophy, integrated over the domain, for the case of nondivergent flow.
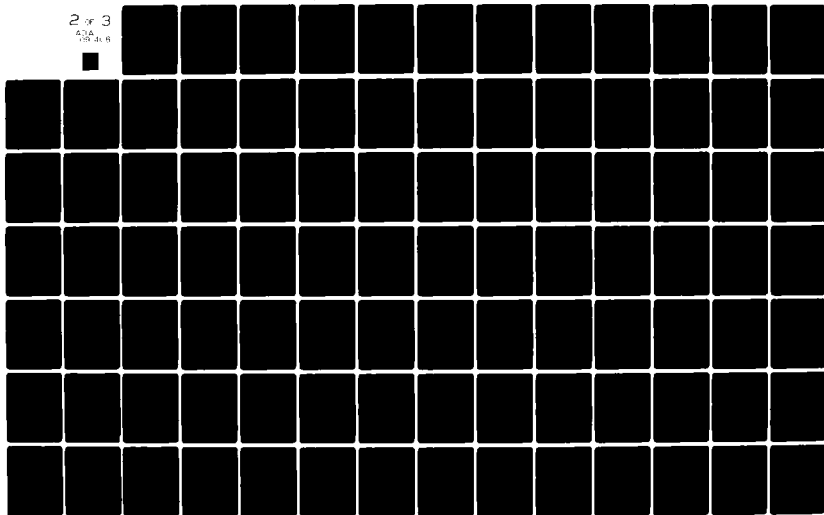
The time derivatives in Eqs. (26), (30), and (31) were discretized using a forward difference for the first time step and a centered difference for all future time steps. A Robert time filter after Robert (1965)

$$F^*(t+\Delta t) = F(t-\Delta t) + 2\Delta t \left(\frac{\partial F}{\partial t}\right)^* \qquad (32)$$

$$F(t) = F^*(t) + \alpha[F^*(t+\Delta t) + F(t-\Delta t) - 2F^*(t)] \qquad (33)$$
$$\alpha = .015$$

was applied after the second time step to avoid time splitting. The star represents the preliminary value and the absence of the star represents the final value.

For simplification, the special finite difference forms of Eqs. (23), (24), and (25) used at the grid points closest to the poles are not shown here. These special forms also preserve the conservative properties of the model.

3.2 The Global Primitive Equation Model (GPEM)

The GPEM utilizes the finite difference scheme given in Arakawa and Lamb (1977) with the following exceptions. The model does not use the continuity equations for water vapor and ozone. The complete physical treatments of radiation and convective adjustment used by Arakawa are not included. A planetary boundary layer is not included. The above simplifications are natural because the scope of the present research is to test the effects of various imposed tropical latent heating forcing patterns upon the ultra-long waves.

The vertical coordinate used in this model is a combination of the coordinate recommended by Phillips (1957) for the lower part of

the model. (See Figures (47a) and (47b) for a vertical depiction of the model.)

The σ coordinate is defined by:

$$\sigma = \frac{p - p_I}{\pi}$$

where

$$\pi = \begin{cases} \pi_u \equiv p_I - p_T & \text{for} & p_T \leq p < p_I \\ \pi_L \equiv p_s - p_I & \text{for} & p_I < p \leq p_s . \end{cases}$$

The model uses the following set of equations:

$$\alpha = RT/p \tag{34}$$

$$\delta\Phi = - \pi \alpha \delta \sigma \tag{35}$$

$$\frac{\partial \pi}{\partial t} + \nabla_\sigma \cdot (\pi \mathbf{V}) + \frac{\partial}{\partial \sigma} (\pi \dot{\sigma}) = 0 \tag{36}$$

$$\pi \dot{\sigma} = - \int_{-1}^{\sigma} \nabla \cdot (\pi \mathbf{V}) \, d\sigma \qquad \text{for } \sigma < 0 \tag{37}$$

$$\pi \dot{\sigma} = - \int_{-1}^{\sigma} \nabla \cdot (\pi \mathbf{V}) \, d\sigma - \sigma \frac{\partial \pi_L}{\partial t} \qquad \text{for } \sigma > 0 \tag{38}$$

$$\frac{\partial \pi_L}{\partial t} = \frac{\partial p_s}{\partial t} = - \int_{-1}^{1} \nabla \cdot (\pi \mathbf{V}) \, d\sigma \tag{39}$$

$$\frac{\partial}{\partial t} \left(\frac{\pi u}{mn}\right) + \frac{\partial}{\partial \lambda} \left(\frac{\pi u}{n} u\right) + \frac{\partial}{\partial \phi} \left(\frac{\pi v}{m} u\right) + \frac{\partial}{\partial \sigma} \left(\frac{\pi \dot{\sigma}}{mn} u\right)$$

$$- \left[\frac{f}{mn} - u \frac{\partial}{\partial \phi} \left(\frac{1}{m}\right)\right]\pi v + \frac{\pi}{n} \left[\frac{\partial \Phi}{\partial \lambda} + \sigma\alpha \frac{\partial \pi}{\partial \lambda}\right] = \frac{\pi}{mn} F_\lambda \tag{40}$$
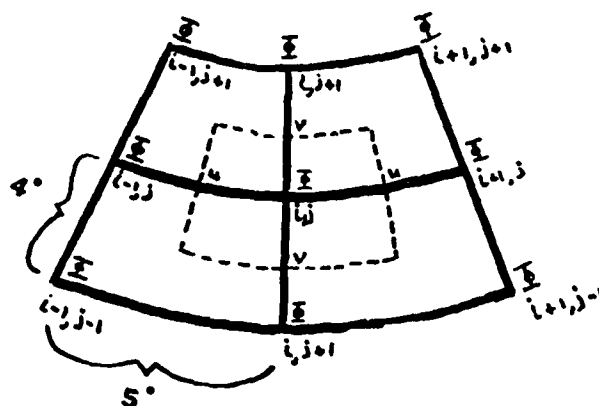
Figure 47a. The staggered grid used in the Arakawa barotropic
model, after Arakawa et al. (1977).
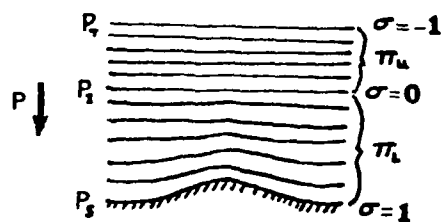
Figure 47b. The vertical depiction of the Arakawa GCM,
after Arakawa et al. (1977).

$$\frac{\partial}{\partial t} \left(\frac{\pi}{mn} v\right) + \frac{\partial}{\partial \lambda} \left(\frac{\pi u}{n} v\right) + \frac{\partial}{\partial \phi} \left(\frac{\pi v}{m} v\right) + \frac{\partial}{\partial \sigma} \left(\frac{\pi \dot{\sigma}}{mn} v\right)$$

$$+ \left[\frac{f}{mn} - u \frac{\partial}{\partial \phi} \left(\frac{1}{m}\right)\right] \pi u + \frac{\pi}{m} \left[\frac{\partial}{\partial \phi} \Phi + \sigma \alpha \frac{\partial \pi}{\partial \phi}\right] = \frac{\pi}{mn} F_\phi \quad (41)$$

$$\frac{\partial}{\partial t} \left(\frac{\pi}{mn} c_p T\right) + \frac{\partial}{\partial \lambda} \left(\frac{\pi u}{n} c_p T\right) + \frac{\partial}{\partial \phi} \left(\frac{\pi v}{m} c_p T\right) + P^K \frac{\partial}{\partial \sigma} \left(\frac{\pi \dot{\sigma}}{mn} c_p \theta\right) =$$

$$= \pi \sigma \alpha \left[\frac{\partial}{\partial t} \left(\frac{\pi}{mn}\right) + \frac{u}{n} \frac{\partial \pi}{\partial \lambda} + \frac{v}{n} \frac{\partial \pi}{\partial \phi}\right] + \frac{\pi}{mn} Q . \quad (42)$$

The variables ψ, T and Φ are defined at odd sigma levels as shown in Figure 47c. The variable $\pi\dot{\sigma}$ is defined at even sigma levels. In this model, as in the barotropic model, the "c" staggered system is used in the horizontal.
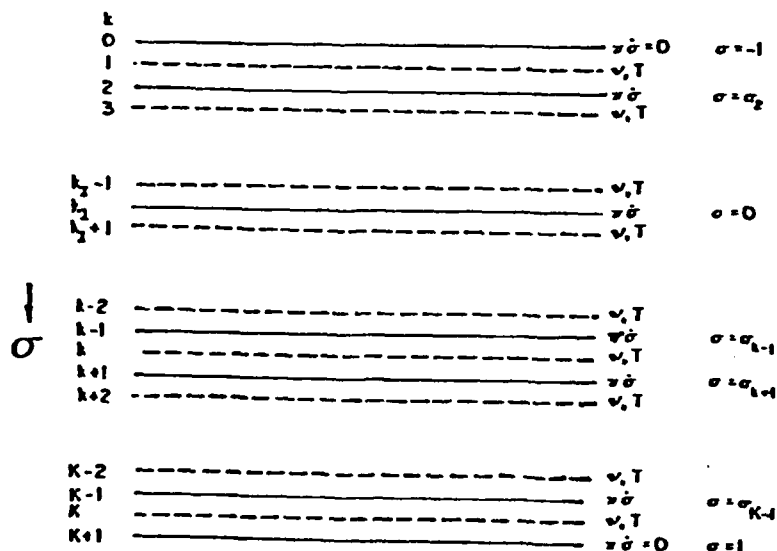
Figure 47c. The vertical staggered grid after Arakawa et al. (1977) showing the upper and lower boundary conditions.

The finite difference forms of Eqs. (34) through (42) are given in Arakawa and Lamb (1977) and will not be presented here.

The variables Q, F_λ, F_ϕ are the diabatic heating, and the vector components of horizontal friction, respectively. The simplified formulation of the diabatic heating is given in Chapter 5. F_λ and F_ϕ were assumed zero throughout this study.

The above model conserves the quantities listed below, when $Q = F_\lambda = F_\phi = 0$.

i) Total energy when integrated over the entire atmosphere.

ii) Total mass as far as advective processes are concerned and for the vertical differencing of the continuity equation.

iii) Total kinetic energy insofar as vertical and horizontal advection are concerned.

iv) Total potential enthalpy and total entropy under adiabatic processes.

v) Basic properties of the vertically integrated pressure gradient force.

vi) Correct conversion of available potential energy to kinetic energy.

vii) The total enstrophy during advection by the nondivergent component of the horizontal velocity.

The time derivative was discretized using the same technique as previously discussed in the barotropic version of the model with a time step of six minutes.

CHAPTER 4

BAROTROPIC MODEL EXPERIMENTS

4.1 Rossby-Haurwitz Wave Initialization

As a test of the accuracy of the divergent barotropic model, an initialization, after Phillips (1959), of a super-rotating flow plus a Rossby-Haurwitz wave was used. The initial velocity field is nondivergent and computed from the stream function

$$\psi = - a^2 \omega \sin \phi + a^2 K \cos^R \phi \sin \phi \cos R\lambda \qquad (43)$$

where

$a = 6.371 \times 10^6 m$ (radius of the earth)

$\omega = K = 7.848 \times 10^{-6}/sec$

$R = 4$ (wavenumber)

$\phi = $ latitude.

By solving for $\mathbf{V}$ in Eq. (44),

$$\mathbf{V} = \mathbf{K} \times \nabla\psi \qquad \text{where } \nabla \cdot \mathbf{V} = 0. \qquad (44)$$

The initial height field Φ was also taken from Phillips (1959) and is constrained to satisfy the balance equation,

$$\nabla \cdot \Psi\nabla\psi + \nabla \cdot \mathbf{A} = \nabla^2\Phi, \qquad (45)$$

where

$$\Psi = \sin \phi \ (2\overline{\Omega} - \frac{1}{a^2 \cos \phi} \frac{\partial\psi}{\partial\phi})$$

$$A_\lambda = a^{-3} \sec \phi \, J\left(\frac{\psi, \frac{\partial \psi}{\partial \phi}}{\lambda, \phi}\right) = - \mathbb{V} \cdot \nabla(a\dot{\lambda} \cos \phi)$$

$$A_\phi = - a^{-3} \sec \phi \, J\left(\frac{\psi, \sec \phi \frac{\partial \psi}{\partial \lambda}}{\lambda, \phi}\right) = - \mathbb{V} \cdot \nabla(a\dot{\phi})$$

$$(\dot{\ }) = \frac{d}{dt} (\ ) .$$

The solution is

$$\Phi = \Phi_s + a^2 A(\phi) + a^2 B(\phi) \cos R\lambda + a^2 C(\phi) \cos 2R\lambda \qquad (46)$$

where

$$A(\phi) = \frac{1}{2}\omega(2\overline{\Omega} + \omega)c^2 + \frac{1}{4} K^2 c^{2R}[(R+1)c^2 + (2R^2-R-2) - 2R^2 c^{-2}]$$

$$B(\phi) = 2\frac{(\overline{\Omega} + \omega)}{(R+1)(R+2)} K \, c^R[(R^2 + 2R + 2) - (R + 1)^2 c^2]$$

$$C(\phi) = \frac{1}{4} K^2 c^{2R}[(R+1)c^2 - (R+2)]$$

$$c = \cos \phi$$

and

$$\overline{\Omega} = 7.292 \times 10^{-5}/\text{sec}$$

$$\Phi_s = (8 \times 10^5 \text{m}) (9.81 \text{ m/sec}^2) .$$

The Rossby-Haurwitz waves should move from west to east without
change of shape and with angular velocity ν given by

$$\nu = \left(R(3+R)\omega - 2\overline{\Omega}\right)/[(R+1)(R+2)] .$$

$\nu = 2.4634 \times 10^{-6}$ Rad/sec or approximately 12.2°/day for the case
given above.

The Arakawa divergent barotropic model was then integrated with
the above Rossby-Haurwitz fields as initial data for a period of
11 days with a time step of five minutes. Figure 48 shows a plot of
the "available" total energy and mean square vorticity integrated

63
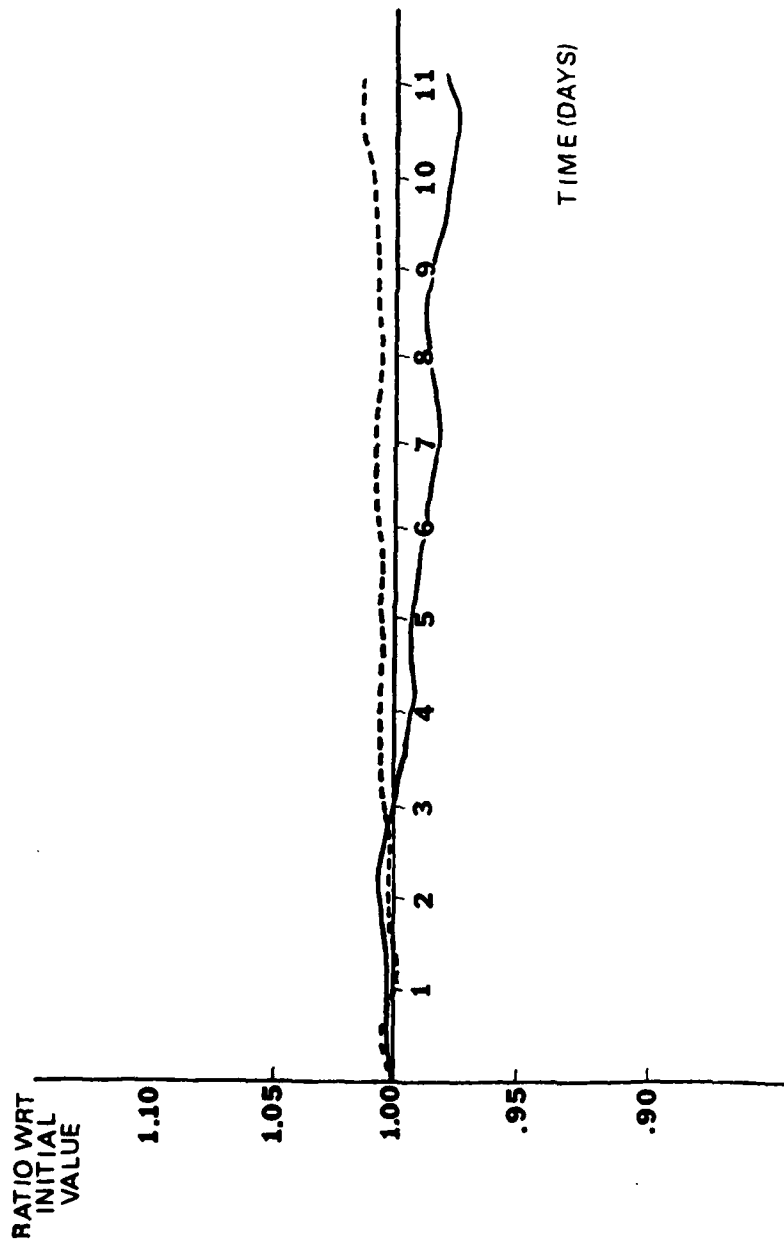
Figure 48. Total energy (TE) (solid line) and mean square vorticity (MSV) (dashed line) from a non-divergent barotropic model experiment.

over the spherical domain. They are defined as

$$ATE = \frac{1}{2g} \sum_{i=1}^{M} \sum_{j=1}^{N} \left\{ \Phi_{ij}^{(u)} u_{ij}^2 + \Phi_{ij}^{(v)} v_{ij}^2 + (\Phi_{ij} - gH)^2 \frac{\Delta\lambda\Delta\phi}{m_j n} \right\}$$

where $\Phi_{ij}^{(u)}$ is defined by (30a) and $\Phi_{ij}^{(v)}$ is defined by (31a).

$$H = \frac{1}{MN} \sum_{i=1}^{M} \sum_{j=1}^{N} \Phi_{ij}$$

$$MSV = \frac{1}{MN} \sum_{i=1}^{M} \sum_{j=1}^{N} \left\{ \left(f_{j-\frac{1}{2}} + m_j \left[(v_{ij-\frac{1}{2}} - v_{i-1j-\frac{1}{2}}) \frac{1}{\Delta\lambda} \right. \right. \right.$$

$$\left. \left. \left. + (u_{ij} \cos \phi_j - u_{ij-1} \cos \phi_{j-1}) \frac{1}{\Delta\phi} \right] \right)^2 \right\} \frac{\Delta\lambda\Delta\phi}{n \, m_{j-\frac{1}{2}}} \, .$$

The total energy at the end of the eleventh day decreases by 2.1% which may be partly due to the Robert time filter. The mean squared vorticity increases by 1%.

The phase error after three days of the integration is approximately 4.5^0 and is comparable to the phase error of $.3^0$ to 1.8^0 per day given by Hoskins (1973) where a spectral representation of the shallow water equation was integrated with the same initial conditions.

4.2 Divergent Forcing Tests

The form of the divergent forcing function $\Delta_{f_{ij}}$, was deduced from the time average positive divergence at 200 mb (Figure 32). This figure shows approximately three clusters of divergence in the tropics of the southern hemisphere. These clusters have a maximum magnitude of about 1×10^{-5}/sec surrounded by an area of divergence of 5×10^{-6}/sec. Based upon the above observations and Plates 5.3 -

5.5 of Newell et al. (1972) (not shown) as a key to the northern hemisphere summer forcing it was decided to use both a single and three source pattern of divergence for $\Delta_{f_{i_j}}$ in Eqs. (26), (30) and (31). Figure 49 shows the three forcing pattern and Figure 50 shows the single forcing function.

In the experiment with the single forcing function, the atmosphere is initially at rest with a constant height field of 250 m. This initial height field was chosen in order to have a gravity wave phase speed ($c=\sqrt{gH}$) of approximately 50 m/sec. This reduced phase speed for the external gravity waves should be close to that of the deep internal gravity waves of the troposphere. The single forcing function was turned on in what will be referred to as the summer hemisphere at time t=0 and remained constant for a 12-day integration using a 30 minute time step. The sixth and twelfth days of the integration are shown in Figures 51 through 57. As can be seen from Figures 51 and 53, the acceleration in the zonal wind occurs both to the north and south of the source of divergence. After the first day, the zonal flow is on the order of 5 m/sec as far north as 18^ON (not shown). At the twelfth day a westerly jet has developed with a NW to SE tilt from about 10^OS and 45^OE to 18^ON and 175^OW with the maximum flow of 23 m/sec around 6^ON and 75^OW.

The divergent wind fields for the barotropic experiments were computed using the relaxation technique and, as a check, a direct solver, NCAR system routine. These two routines produced almost identical results. The divergent wind reaches a steady state with the forcing very rapidly. Figure 58 shows the meridional divergent
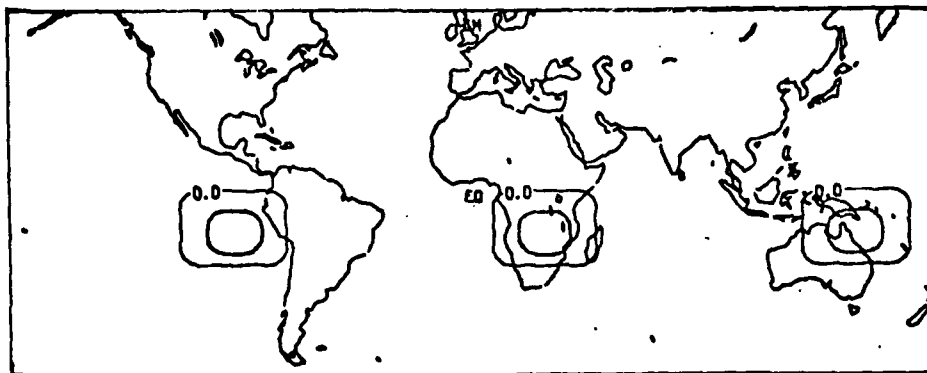
Figure 49. The three source divergent forcing function used in the barotropic model experiments. Isolines are every $1 \times 10^{-5} s^{-1}$.
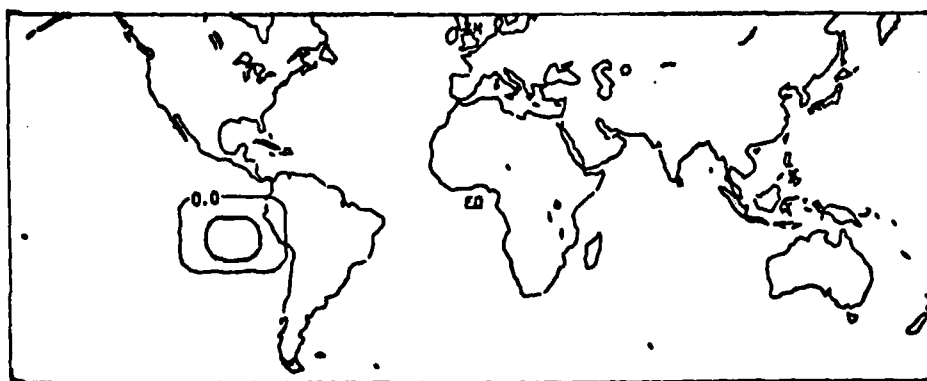
Figure 50. The single source divergent forcing function used in the barotropic model experiments. Isolines are every $1 \times 10^{-5} s^{-1}$.
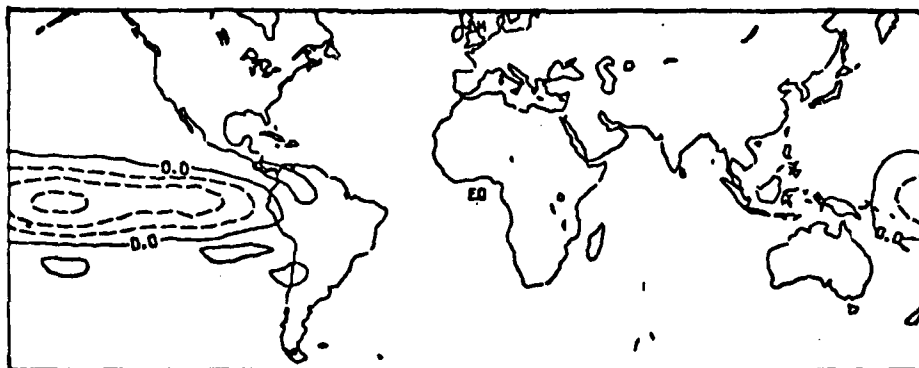
Figure 51. Barotropic experiment single forcing 6th day zonal
wind component (m s^{-1}). Isolines are every 10 m s^{-1}
with dashed lines representing negative values.
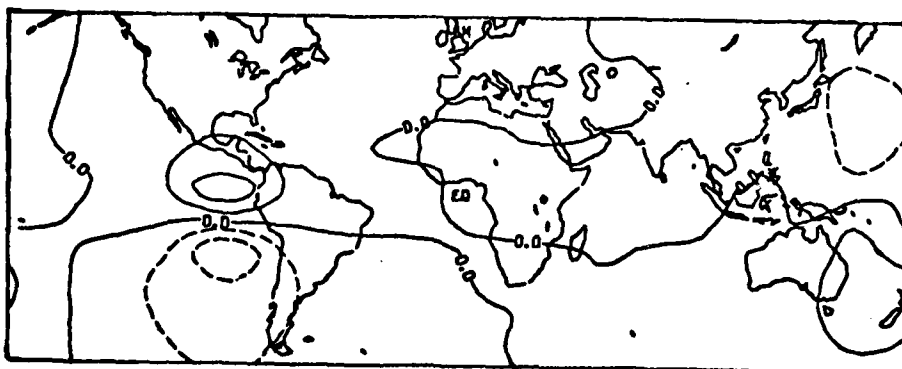
Figure 52. Barotropic experiment single forcing 6th day meridional
divergent velocity component (m s^{-1}). Isolines are
every 2 m s^{-1} with dashed lines representing negative
values.

Figure 53. Barotropic experiment single forcing 12th day zonal
wind component (m s^{-1}). Isolines are every 10 m s^{-1}
with dashed lines representing negative values.

Figure 54. Barotropic experiment single forcing 12th day meridional
wind component (m s^{-1}). Isolines are every 5 m s^{-1}
with dashed lines representing negative values.
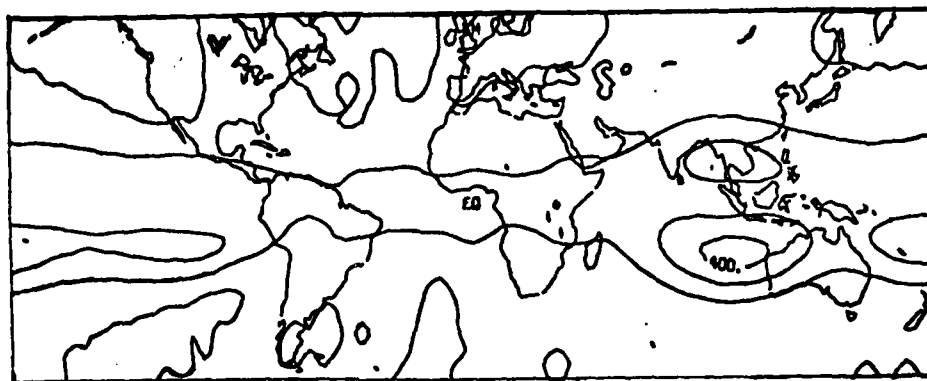
Figure 55. Barotropic single forcing experiment 12th day height field (m). Isolines are every 50 m.
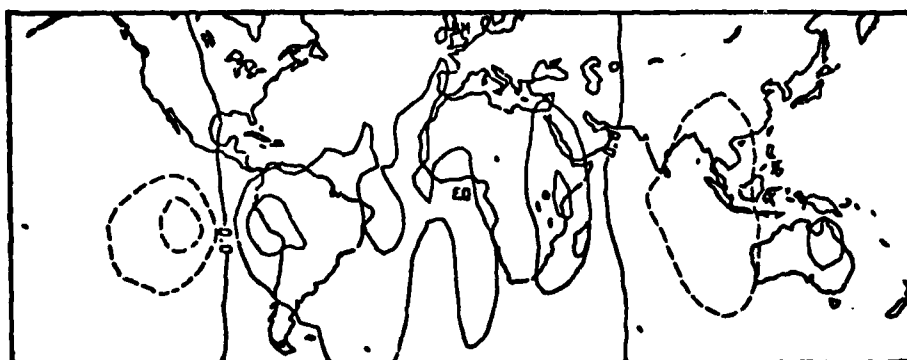
Figure 56. Barotropic single forcing experiment 12th day zonal divergent velocity component (m s^{-1}). Isolines are every 2 m s^{-1} with negative values dashed.
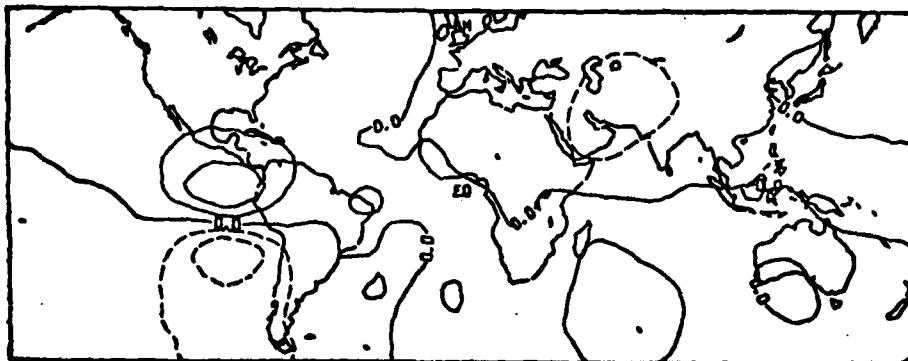
Figure 57. Barotropic single forcing experiment 12th day meridional divergent velocity component (m s^{-1}). Isolines are every 2 m s^{-1} with negative values dashed.
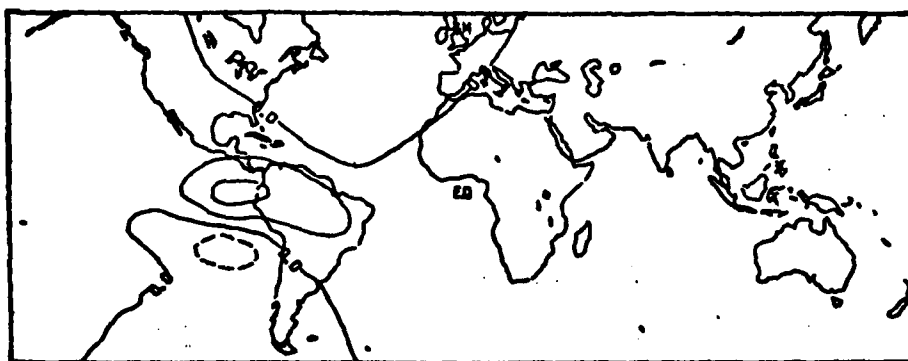
Figure 58. Barotropic experiment single forcing 1st day meridional divergent velocity component (m s^{-1}). Isolines are every 2 m s^{-1} with dashed lines representing negative values.

velocity component, v_x, after the first day of integration. Comparing this figure with the meridional divergent wind for the sixth (Figure 52) and twelfth (Figure 57) days of integration, one can see that indeed the divergent flow reaches a rapid steady state with the forcing. The divergent flow into the northern hemisphere is on the order of 1 m/sec greater than the flows into the southern hemisphere. It is postulated here that the rapid steady state is a consequence of gravity wave propagation. These gravity waves emanate from the forced area at phase speeds near 50 m/sec and provide the source of energy for the westerly jet maxima.

The single forcing experiment could be taken to represent, in a simplified fashion, the strong divergent outflows from the southeast monsoon over the Asian continent during the SHW. This strongly convectively heated area represents to a good approximation the most important source of divergence during the northern hemisphere summer. There is some similarity between Figure 26 and Figure 53 if one reverses hemispheres to account for the location of the heating.

The magnitude of the westerly jet produced by the 12-day integration is about half of the average northern summer time jet over Australia (Figure 53) and is located closer to the equator. But differences in magnitude are really meaningless, since this simulation only considers the forcing part of the problem with no frictional dissipation. Thus a steady state with respect to the wind field cannot be reached, and only relative magnitudes should be compared. There is an easterly jet westward from the divergent source position in both figures. There is also a weaker westerly

jet in the summer hemispheres of both figures.

The model used here is barotropic, thus it can only represent the growth of waves due to barotropic instability and baroclinically unstable waves do not exist. This is probably the main reason for the acceleration produced in the westerly jet at 18^ON that does not propagate further to the north as in the real atmosphere. The westerlies at the equator are unrealistic and are greatly reduced in the presence of more than a single source of divergence.

The second experiment is designed to test the effect of a stronger forcing function by multiplying the single forcing function by three. The experiment was then integrated using a time step of 30 minutes with the same initial conditions as the first experiment. After one day, the zonal wind component of this experiment (not shown) is about three times larger than the zonal wind in the previous experiment. The effect between the forcing and response in the zonal wind for short time periods appears to be almost linear. Thus if the original forcing used to produce Figure 53 was too small or too large, one could estimate the final result by simply computing the ratio of the new and previous divergent forcing function and then multiply the results of Figure 53 by this ratio.

The next experiments were the three source experiments. The first of these used the forcing function given by Figure 49. Again the initial atmosphere is at rest with a constant height field of 250 m. Figures 59, 60 and 61 give the 15th day zonal wind component, the meridional wind component and the height field, respectively. In this case, there are six distinct jet maxima of the
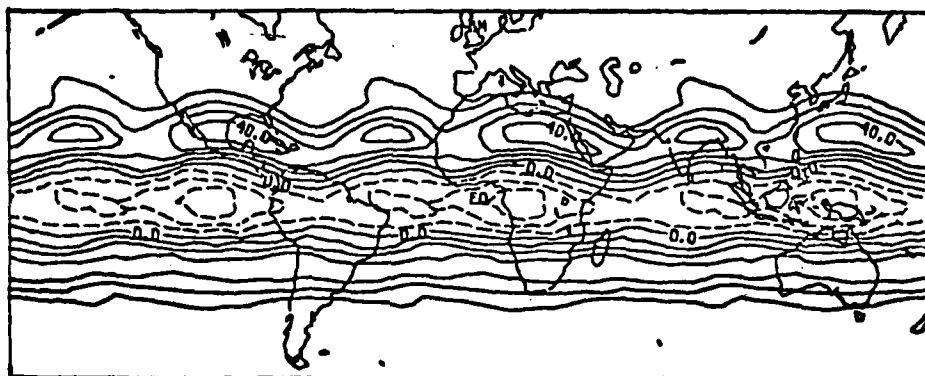
Figure 59. Barotropic three source experiment 15th day zonal velocity component (m s^{-1}). Isolines are every 10 m s^{-1} with negative values dashed.
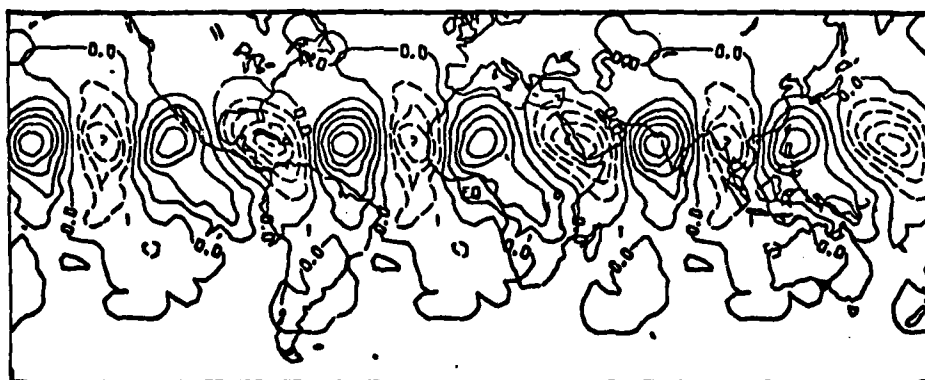
Figure 60. Barotropic three source experiment 15th day meridional velocity component (m s^{-1}). Isolines are every 5 m s^{-1} with negative values dashed.
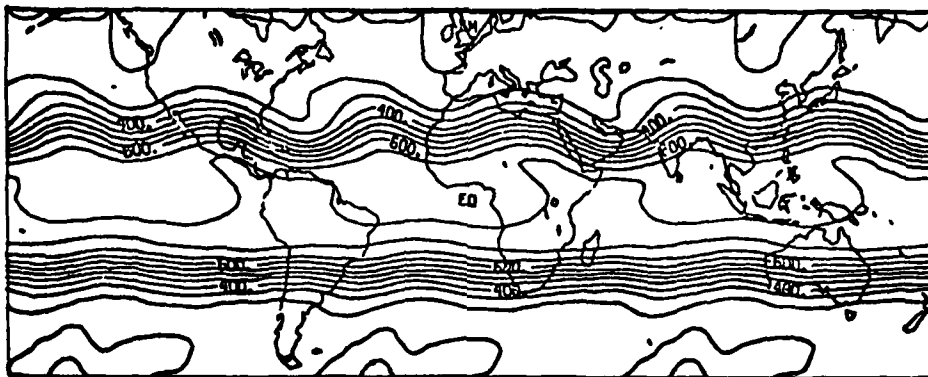
Figure 61. Barotropic three source experiment 15th day height field (m). Isolines are every 50 m.
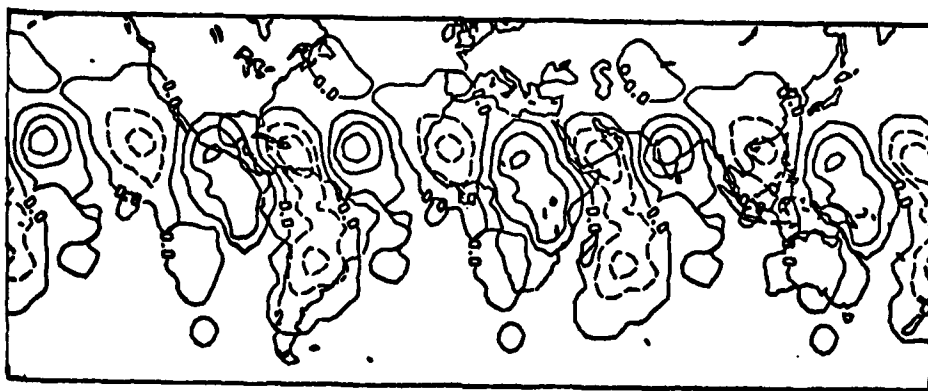
Figure 62. Barotropic three source experiment 13th day meridional velocity component (m s^{-1}). Isolines are every 5 m s^{-1} with negative values dashed.

zonal wind in the northern hemisphere. The six wave pattern in the northern hemisphere visible in Figure 60 appears to be barotropically unstable and growing at the expense of the mean flow. This can be seen by comparing the meridional components for the 13th and 15th days of integration (Figures 62 and 60, respectively). The wave activity also appears to be trapped in definite latitude belts (Figure 61). In the northern hemisphere the waves are confined to the region from $40^{O}N$ to $10^{O}N$, while in the southern hemisphere, the waves are between $15^{O}S$ and $45^{O}S$. This is consistent with the theory that barotropically unstable waves will tend to be trapped near sharp westerly jets.

At the end of the 15th day, the maximum value of the zonal wind in the northern hemisphere is 7 ms^{-1} greater than the maximum in the southern hemisphere with the maximum speeds of 47 ms^{-1} and 40 ms^{-1} at $26^{O}N$ and $26^{O}S$, respectively. The fact that higher speeds exist in the northern hemisphere is consistent with the properties of inertial gravity waves. The phase speed of the internal inertial gravity waves for the one dimensional case with zero mean flow of the model described in Paegle (1978) is given by

$$c = \pm \sqrt{c_G^2 k^2 + f^2} \Big/ k \qquad (47)$$

where

$$c_G^2 \equiv - \frac{\sigma' p_0}{4}$$

σ' is the static stability times the ideal gas constant, SR

p_0 is 1000 mb

k is the wavenumber

f is the coriolis parameter.

The phase speed of the energy propagation or group velocity is given by

$$c_g = \frac{\partial}{\partial k} (ck) = c_G^2 k \Big/ \sqrt{c_G^2 k^2 + f^2} . \tag{48}$$

Thus, from a non-equatorial tropical source of gravity waves, the maximum gravity wave propagation of energy should be into the opposite hemisphere. From Eq. (48) it can be seen that the coriolis force acts to decrease the energy density of the gravity wave; thus less energy will reach a given distance in the southern hemisphere forcing case to the south of the source than to the north of the source.

Note that with the three forcing experiments, a strong easterly flow develops about the equator by day 7.5, but in this case, unlike that of Hoskins et al. (1977), propagation of energy across the equator continues even after the easterly jet develops. In other words, the gravity wave modes are not trapped by easterly equatorial flows. Since Hoskins et al. (1977) dealt with Rossby-Haurwitz wave propagation, this would tend to support the statement of Paegle (1978), at least for the barotropic forcing case, that gravity waves propagate the energy away from strongly (heated) divergent areas.

For completeness, the 15th day divergent components of the wind (u_x, v_x) are shown in Figures 63 and 64. The v_x field (Figure 64) shows both northerly and southerly divergent flow out of the three sources of divergence, with the maximum flow to the north of the
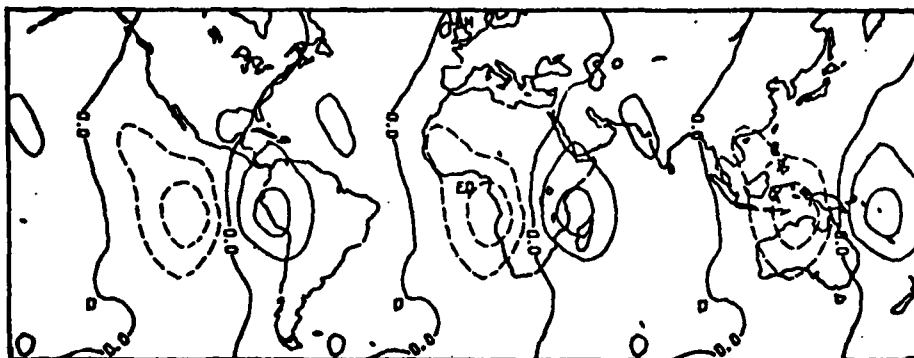
Figure 63. Barotropic three source experiment 15th day zonal divergent velocity component (m s^{-1}). Contour interval is 2 m s^{-1} with negative values dashed.
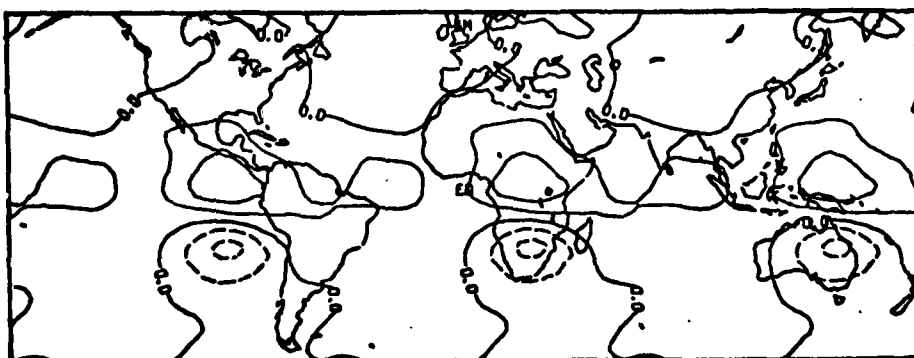
Figure 64. Barotropic three source experiment 15th day meridional divergent velocity component (m s^{-1}). Contour interval is 2 m s^{-1} with negative values dashed.

sources of divergence, possessing a magnitude of almost 6 ms^{-1}. In the northern hemisphere, an area of positive flow extends well north of 30°N.

The next experiment was used to provide a simple check on the influence of the gravity waves in propagating energy away from the three sources of divergence. The same three forcing case as in the last experiment was carried out with the exception that gravity for the test, g_T, was defined as $g_T=g/10$, where $g=9.81$ ms^{-2}. Thus the gravity wave propagation speed was cut to about 15 ms^{-2}. If gravity wave modes are important in propagating the divergent source of energy as postulated here and in Paegle (1978), then for the g_T case, 1) less energy should propagate away from the three sources into both hemispheres, and 2) the zonal wind speeds in the northern hemisphere need not be stronger than those of the southern hemisphere. From the experiments of Hoskins et al. (1977) one can also predict that if an easterly equatorial flow develops, then much of the energy should remain trapped in the southern hemisphere.

Figure 65 shows the zonal wind component at the 12th day of integration for the $g_T=g/10$ case, while Figure 66 is the 12th day zonal wind component for the $g_T=g$ case. When comparing the two experiments, points 1) and 2) above seem to be satisfied, since the maximum of the zonal component of the flow occurs in the southern hemisphere and is 7 ms^{-1} larger than the maximum flow in the northern hemisphere. Also, a very strong easterly flow develops about the equator with a maximum of -56 ms^{-1}. This seems to suggest that input energy goes into the easterly flow and is not

Figure 65. Barotropic three source (g/10) experiment 12th day zonal wind component (m s^{-1}). Contour interval 10 m s^{-1} with dashed lines for negative values.
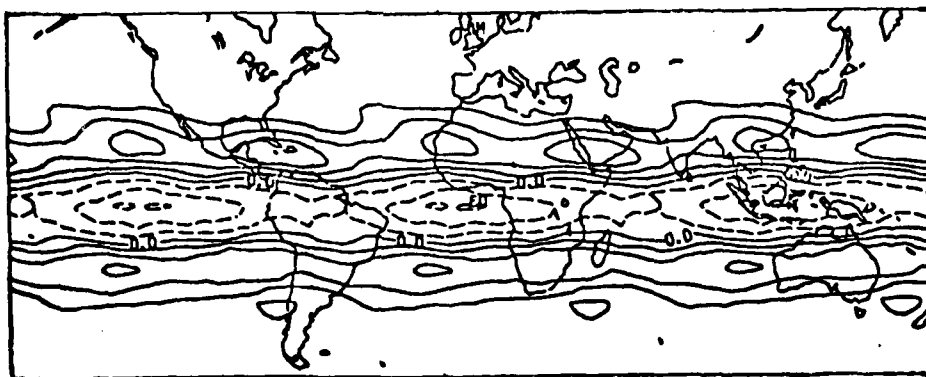
Figure 66. Barotropic three source experiment 12th day zonal wind component (m s^{-1}). Contour interval 10 m s^{-1} with dashed lines for negative values.

propagated away from the source as compared to the $g_T=g$ case of Figure 66, where the maximum easterly flow is only -32 ms^{-1}. These concepts cannot be completely tested by this formulation since the gravity wave speed is only reduced and some gravity wave propagation of energy still does exist.

The final experiment presented in this section consists of multiplying (or what will be termed "pulsing") the source of divergence centered at -92.5^O longitude by a constant factor of 2.5 (Figure 67). The pulsed forcing was turned on at the start of the 13th day of integration of the three forcing case with g=9.81 ms^{-2} and continued for three days. This was done to test the effect of enhanced divergence in one area of the globe. This enhanced divergence could represent an active outbreak of convection which is often observed in satellite data. In comparison with upper tropospheric data over the Amazon basin, the factor of 2.5 is found to be realistic.

Figures 68 through 73 show the results at the 15th day after three days of the steady pulsed forcing. Comparisons of Figures 68 and 59 (the zonal wind for the same period of integration without the pulsing) are instructive. The northern hemisphere zonal wind to the north of the pulsed source is about 10 ms^{-1} higher in the pulsed case than in the control case with the subtropical jet in this region at 30°N as compared to 26°N for the control case. The increased energy of the jet in the pulsed case has also propagated downstream to approximately 95°E. This is probably due to Rossby wave energy propagation and the beta effect.
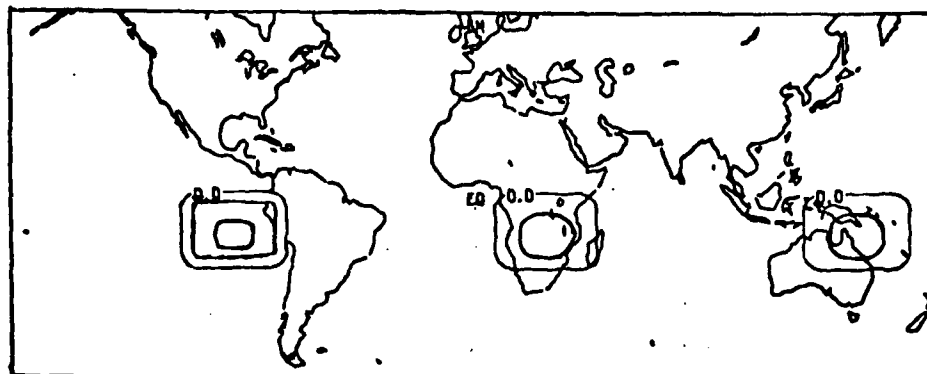
Figure 67. The three source pulsed divergent forcing function used in the barotropic model experiments. Isolines are every $1 \times 10^{-5} s^{-1}$.
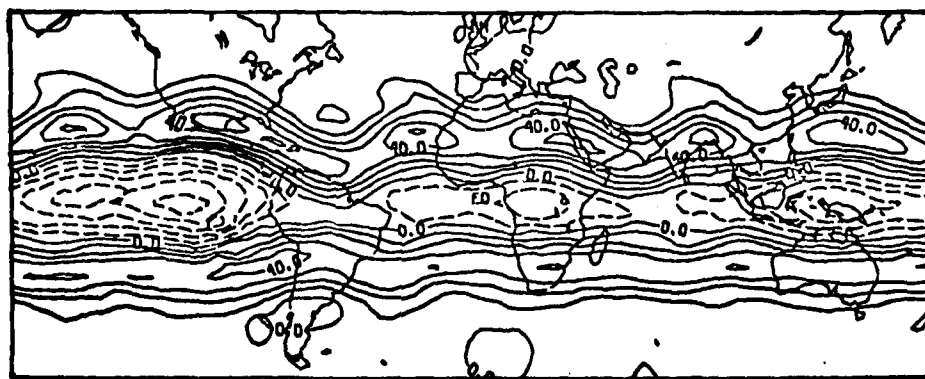
Figure 68. Barotropic pulsed three source experiment 15th day zonal wind component (m s^{-1}). Isolines are every 10 m s^{-1} with negative values dashed.
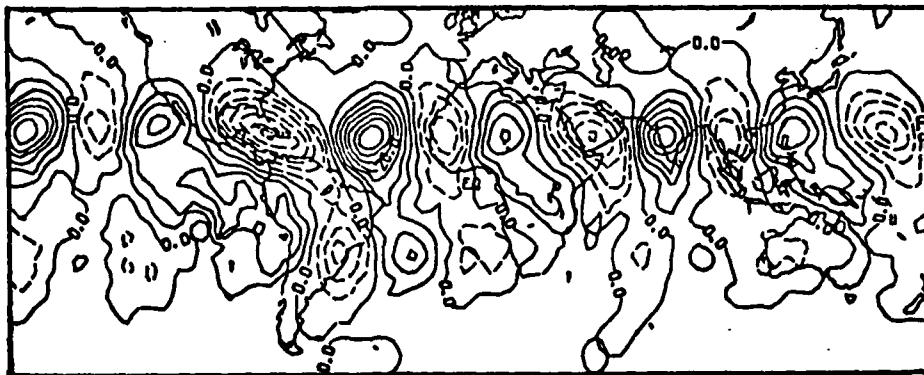
Figure 69. Barotropic pulsed three source experiment 15th day
            meridional wind component (m s^{-1}). Isolines are
            every 5 m s^{-1} with negative values dashed.
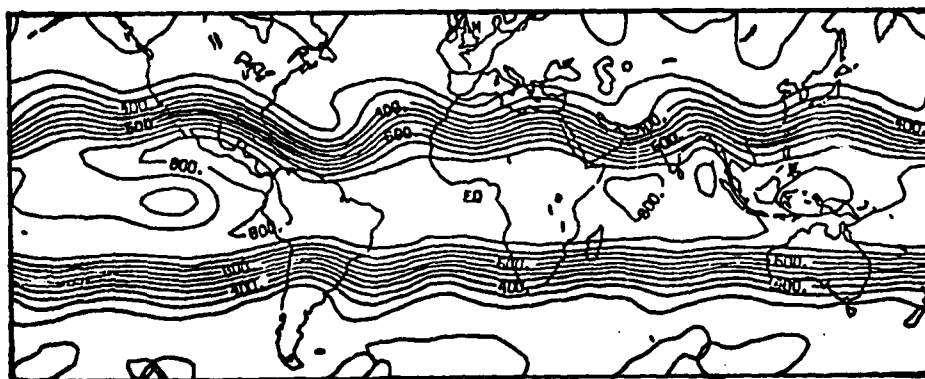
Figure 70. Barotropic pulsed three source experiment 15th day
            height field (m). Contour interval is 50 m.
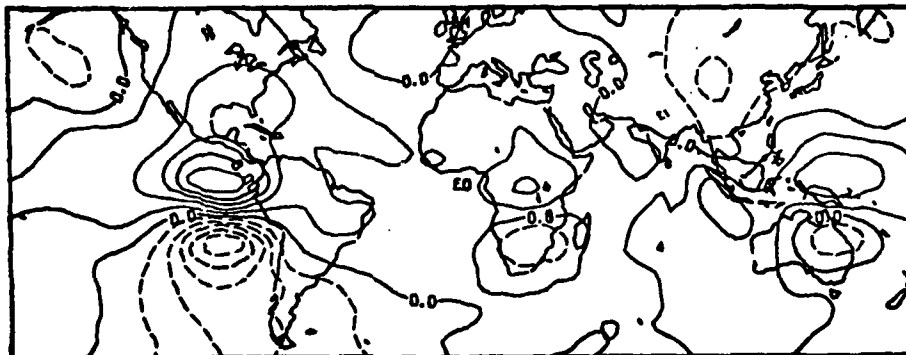
Figure 71. Barotropic pulsed three source experiment 15th day meridional divergent velocity component (m s^{-1}). Isolines are every 2 m s^{-1} with negative values dashed.
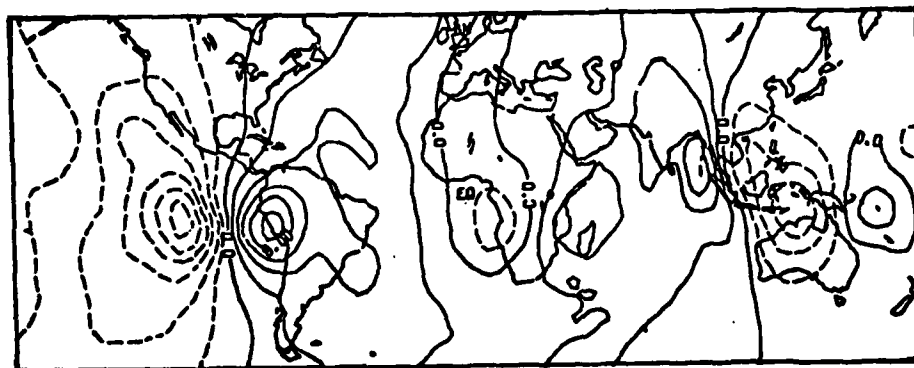
Figure 72. Barotropic pulsed three source experiment 15th day zonal divergent velocity component (m s^{-1}). Isolines are every 2 m s^{-1} with negative values dashed.

Figure 73. Barotropic pulsed three source experiment 13th day
meridional divergent velocity component (m s^{-1}).
Isolines are every 2 m s^{-1} with negative values
dashed.
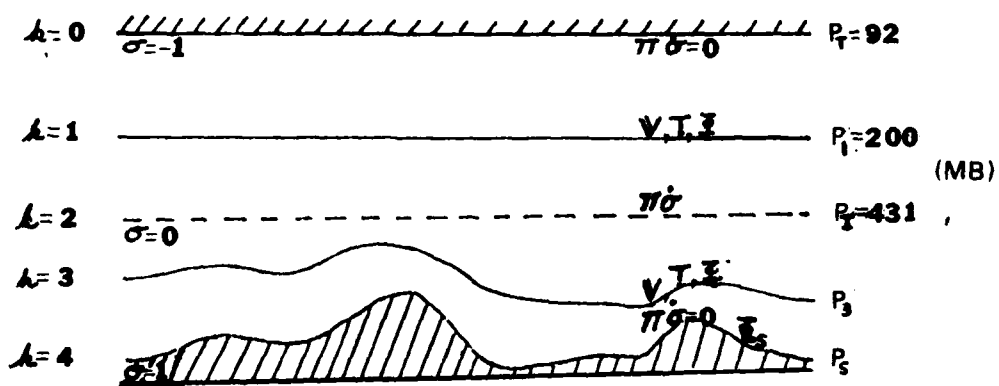
Figure 74. Two-level model depiction with sigma levels and
pressure levels given.

Next, comparing the meridional velocity components, it is clear
that the barotropic waves to the north and slightly east of the
pulsed region are much more active in the pulsed case (Figure 69)
than in the control case (Figure 60). This is to be expected since
these waves are probably barotropically unstable in this region and
growing at the expense of the mean flow which is stronger locally
in the pulsed case. The height fields (Figures 61 and 70) also show
large differences in the region of the pulse with a stronger ridge
and trough system to the north and east of the pulsed divergent
source.

The divergent winds, u_x and v_x, realize a nearly steady state
in the pulsed area very rapidly. The maximum values of near 11
ms^{-1} in the pulsed case (Figures 71 and 72) are about 2.5 times the
values given in the control case (Figures 63 and 64). Initially,
in the pulsed case, the divergent meridional flow (Figure 73) into
the northern hemisphere is much stronger (14 ms^{-1} as compared to
-10 ms^{-1} into the southern hemisphere). But after the three-day
integration, the respective flows into the northern and southern
hemispheres are nearly the same, approximately 11 ms^{-1}.

Comparing the 15-day integration of the $g_T = g$ case (see Figure
59) with observations of Figure 10 and Plate 3.19 of Newell et al.
(1972), one can detect some similarities in the overall patterns,
although conclusions drawn from a comparison of this type are specu-
lative. One can see that the strongest jets exist in the northern
hemisphere near $30°N$ in all three figures, with easterlies in the
tropical areas, and weaker westerly jet maxima in the southern

hemisphere. In Figure 59 the tropical easterlies are quite strong and not realistic when compared to the real atmosphere. Finally one must consider that Figure 10 and Plate 3.19 of Newell et al. (1972) represent the sum total of all effects including mountains, baroclinic instabilities, momentum fluxes, tropical convective heating, etc., and cannot be completely reproduced by a simple barotropic model.

In concluding this chapter, it appears from the various divergent forcing tests that large scale divergence clusters at tropical latitudes can affect the magnitude and positions of the opposite hemisphere jet stream. The gravity wave modes in these experiments provide the mechanism for the energy transfer from the tropics of the "summer hemisphere" to the subtropics of the "winter hemisphere." These modes are not trapped by strong equatorial easterlies as are the Rossby wave modes. From these results it is natural to postulate that the gravity modes provide an efficient energy link between the strongly forced tropical areas and the jet streams of both hemispheres, in agreement with the conjecture of Paegle (1978). One must remember that these conclusions are for a barotropic atmosphere and must be examined in at least a two-level baroclinic primitive equation model to see if large scale convective heating causes a similar response. In the next section, several baroclinic experiments with a two-level primitive equation model are reported.

CHAPTER 5

TWO-LEVEL PRIMITIVE EQUATION MODEL EXPERIMENTS

A simplified two-level version of the model discussed in
Arakawa and Lamb (1977) was used for these experiments. The deci-
sion to utilize the two-level version was based on several factors.
One, the model must include the entire globe and have at least a
horizontal resolution of 5^0 in latitude and longitude. Second, the
model must use the primitive equation physics to properly simulate
energy propagation and gravity wave modes on the spherical earth.
Third, the model must include thermal effects in order to determine
the relation between large scale tropical latent heat sources and
the subtropical and midlatitude ultra-long waves. Finally, the
model must be affordable for a large number of 25 to 30 day experi-
ments. The least expensive version of the model which could resolve
the thermal effects is the two-level primitive equation model
(TLPEM).

5.1 The Two-Level Primitive Equation Model Description

A vertical depiction of the TLPEM is given in Figure 74. The
intermediate or odd pressure levels P_1 and P_3 are computed in this
model from the even pressure levels P_T, P_I and P_S. For σ less than
zero the pressure (P_1) is computed from Eq. (49), below while for
σ greater than zero the pressure (P_3) is computed from Eq. (50),

below. These equations are given in Arakawa and Lamb (1977).

$$P_1 = (P_T \, P_I)^{\frac{1}{2}}$$

(49)

where P_T and P_I are chosen such that

$$P_I = P_T \, e^d; \qquad d = 1.54$$

$$P_3 = \left[\frac{1}{1+a} \frac{(P_S^{1+a} - P_I^{1+a})}{P_S - P_I} \right]^{1/a}$$

(50)

where a = .205.

The intermediate pressure level, P_1, in the upper portion of the model ($\sigma < 0$) is chosen as in Eq. (49) to prevent spurious computational reflection of wave energy in an isothermal atmosphere due to the vertical discretization of the model equations. Of course this does not completely prevent vertical reflection of wave energy at the top of the model since the assumption that $\pi\dot{\sigma} = 0$ acts as a lid on the top of the model. The intermediate pressure level, P_3, is computed from Eq. (50) in order to reduce discretization errors in the computation of the geopotential height field, Φ_3, from the discrete form of the hydrostatic equation. When the model is formulated in the vertical as given in Arakawa and Lamb (1977) the odd sigma level values need not be specified, since all vertical computations use only the even sigma values.

The two-level model has two distinct advantages with respect to its vertical structure. First, since the lower portion of the model

is in sigma coordinates, mountains can be included easily by simply making the surface height, Z_s, equal to the height of the given terrain field at that point. Consequently, mountains were included in this study with little difficulty.

The second advantage is that the upper level, P_1, of the model is a constant pressure surface. Thus, the results can be compared easily with the results of Chapter 2 and other data studies.

The horizontal resolution is 4^0 latitude by 5^0 longitude. The model uses the staggered grid shown in Figure 47a with the zonal (u) and meridional (v) components of the wind specified at separate grid points. The temperature (T), potential temperature (θ), geopotential height (Φ), vertical motion ($\pi\dot{\sigma}$), surface pressure (P_s), and dia-batic term (Q) are all defined at the same grid point which is cen-tered between the u and v grid points. The variable Φ has been used to represent the grid point location of Φ, T, θ, $\pi\dot{\sigma}$, P_s and Q in Figure 47a.

In simple terms, the time forecast sequence for the TLPEM is as follows. The prognostic variables u, v, T, and P_s, are forecasted every time step using a leapfrog finite difference scheme. Then the diagnostic variables $\pi\dot{\sigma}$, θ and Φ are computed from the forecasted values of u, v, P_s, and T. Next, the diagnostic variables are utilized in the next forecasts of u, v, P_s, and T, and so forth. As previously stated, a Robert time filter is applied after the second time step and a forward time step is used to start the model integration.

The treatment of pole points and near pole points in the

spherical coordinate finite difference formulation of the atmos-
pheric set of equations often proves difficult. The form of the
difference equations used here follows that of Arakawa and Lamb
(1977) as closely as possible.

Some interpretation of the form of the thermodynamic equation
near the poles was necessary since the finite difference form of
this equation was not given. An earlier version of the model
(Arakawa, 1974) was also used to determine the form of the thermo-
dynamic equation. One problem near the north pole did occur at the
31st day of integration in the no-mountain case and at the 22nd day
of the mountain case. The origin of this problem probably lies in
the numerical formulation of the near pole and pole points coupled
with the facts that there is no dissipation in the model and baro-
clinically unstable wave activity exists with zonal and meridional
speeds of order 15 to 20 ms^{-1} very near the poles (75^ON and 70^OS).
This problem was corrected by utilizing the total energy conserving
linear smoother, Eq. (29). The form of the smoother from day 20 in
the mountain cases and from day 27 in the no-mountain cases was re-
duced by one-half from 74^ON to 90^ON and 74^OS to 90^OS. With this
slight change, the stability of the two-level model was maintained
for all of the experiments.

5.2 Two-Level Model Forcing

The TLPEM forcing was designed to parameterize in a simple
fashion the typical net diabatic forcing fields for both the north-
ern and southern hemisphere winters and summers. The main emphasis
of this study is to investigate the response of the winter hemisphere

subtropical jet streams and ultra-long waves to several different tropical diabatic heat distributions. To accomplish this in a realistic but simple manner, a zonal average net diabatic heating is used at all latitudes with the exception of the tropics. Longitudinal variation of the net diabatic heating is retained in the tropical areas to parameterize the mean variability of precipitation from location to location. The diabatic forcing functions are constant in time. In preliminary experiments with the model it was found that in a three-day forecast the response in the subtropical jet was very nearly the same for either a time dependent or constant forcing as long as both forcings had the same time average values.

The actual diabatic heating fields (Q_{net}) were taken from both Hantel and Baader (1978) for the time average zonal diabatic heating ($Q_z(\phi,P)$) part and from precipitation data given in Shutz and Gates (1972) and Newell et al. (1972) for the tropically variable part of the diabatic heating ($Q_v(\lambda,\phi,P)$). The values of Q_z presented in Hantel and Baader (1978) were computed from the MIT Data Library using the thermodynamic equation in time-average zonal mean form and are given from $15^{O}S$ to $90^{O}N$. Since the data set used in Hantel and Baader (1978) does not resolve subsynoptic features, the computed Q_z values are actually the sum of the net diabatic heating and the subsynoptic diabatic heating. Thus, by using this zonal diabatic heating in the 4° by 5° resolution TLPEM, subsynoptic diabatic heating effects are partially parameterized.

Since the values of Q_z from $15^{O}S$ to $90^{O}S$ are not given by Hantel and Baader (1978), these values were obtained by another method. The

zonal diabatic heating for the NHW southern hemisphere below $15^{\circ}S$ were inferred from the northern hemisphere summer values from $15^{\circ}N$ to $90^{\circ}N$. This technique was also used for the SHW experiments where the values of the NHW from $15^{\circ}N$ to $90^{\circ}N$ were used for the southern hemisphere from $15^{\circ}S$ to $90^{\circ}S$. Since the purpose of the experiments presented in the following subsection is to test the effects of various tropical heating sources on the ultra-long waves of the sub-tropics of mainly the winter hemisphere, the actual values used for the adiabatic heating fields must be realistic, but need not be exact. In any case, values of Q_z in both hemispheres are not really known exactly.

The values of Q_z for the two levels (Q_{z1} and Q_{z3}) of the model were chosen to represent the layers implied by the respective levels. The upper layer represents approximately 90 to 430 mb, while the lower layer represents approximately 430 mb to 1000 mb in the ab-sence of mountains. The values were also chosen to satisfy two other constraints. First, the initial value of the integral of Q_z over the mass of the atmosphere was constrained to be zero:

$$\int_{-M} Q_z (\phi,\sigma) \, dM = 0 .$$ (51)

Equation (51) can be rewritten as

$$\int_{-1}^{1} \int_{0}^{2\pi} \int_{-\pi/2}^{\pi/2} Q_z(\phi,\sigma) \, \pi(\lambda,\phi,t) \, a^2 \cos \phi \, d\lambda \, d\phi \, d\sigma = R.$$ (52)

This can only be zero initially since π is a function of time. Both for the mountain and no-mountain cases, the residual, R, remained

small throughout the various periods of integration. Also, as long as the residual remains small, the average total energy is nearly a conservative quantity (see Eq. (53) below) when the frictional force is zero.

$$\frac{\partial}{\partial t}\left[\int_0^{2\pi}\int_{-\pi/2}^{\pi/2}\left\{P_s\ \Phi_s\ +\ \int_{-1}^1\pi(\tfrac{1}{2}\mathbb{V}\cdot\mathbb{V}\ +\ c_pT)\ d\sigma\right\}\right.$$
$$\left. -\ a^2\ \cos\phi\ d\lambda\ d\phi\right] = R. \tag{53}$$

The second constraint was designed to maintain a stable static stability throughout the period of integration. This was accomplished by keeping the values of Q_{z1} at a given point slightly greater than the values of Q_{z3} at that point. The only exception to this was for the SHW integration cases where the heating in the deep tropics was slightly greater in the lower level as dictated by Hantel and Baader (1978).

The values of the zonal heating Q_{z1} and Q_{z3} used for the NHW and SHW experiments are given in Figures 75 and 76, respectively. In comparison of these figures with those given in Hantel and Baader (1978), one should note that the area of heating near 40^ON in the winter hemisphere has been left out and that the tropical heating maxima are slightly larger in Figures 75 and 76 than in Hantel and Baader (1978). The heating near 40^ON was taken out since this is probably due to latent heat release from storm systems (baroclinic waves). Thus, this heating should not be included here since all the model experiments start from an initial atmosphere at rest and baroclinic waves do not exist in the model until after at least
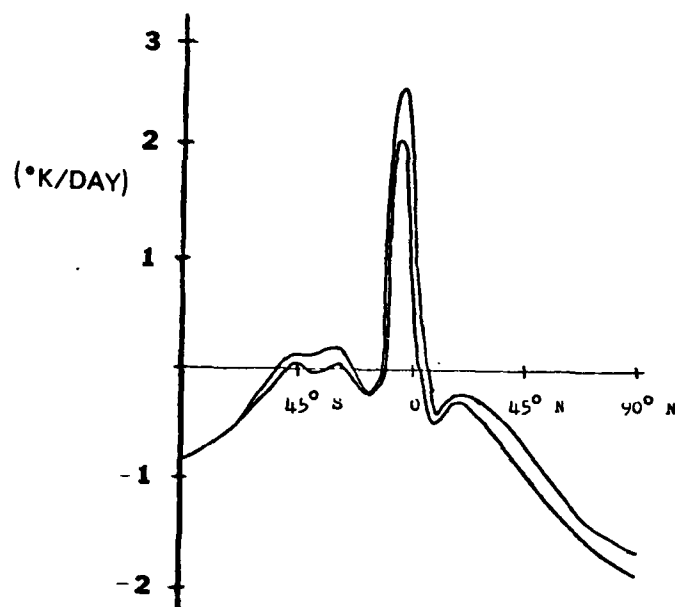
Figure 75. NHW zonal average heating Q_z ($°day^{-1}$). The upper line represents the model layer forcing function Q_{z1}, while the lower line represents lower level model forcing function Q_{z3}.
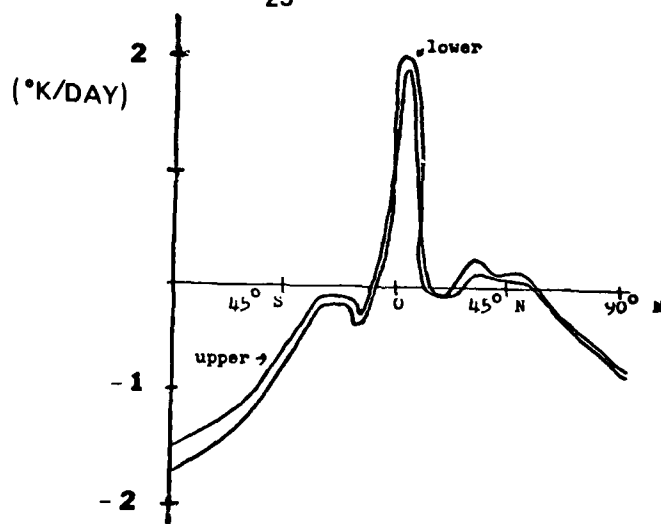
Figure 76. SHW zonal average heating Q_z ($°day^{-1}$) upper and lower level heating curves are labeled.

20 days of integration. The maxima in the tropics were made
slightly larger to reduce the number of days of integration required
to reach a realistic atmospheric state. This was solely to save
computer time. The values are only slightly larger and therefore
well within the amount of uncertainty in the measurements. Also,
by using slightly larger values, the maximum effect of tropical
latent heating can be estimated.

The longitudinally variable part of Q_{net} was inferred from the
mean precipitation data of Shutz and Gates (1972) for the NHW ex-
periments and Newell et al. (1972) for the SHW experiments. The
values of precipitation were converted to column average heating
rates by using the conversion that 1 cm/day of rain is approximately
2.5^OK/day column average heating. Values were read off of Figure 12
of Shutz and Gates (1972) for the NHW every 30° of longitude from
22^OS to 10^ON. The 30° interval values were then analyzed with a
Fast Fourier Transform (FFT). The mean was removed and an inverse
FFT was performed converting the data to the model resolution of 5°
longitude (Figure 77). This longitudinal varying part of the heat-
ing (Q_V) was then added to the zonal average heatings, Q_{z1} and Q_{z3}.
The vertical variation in the latent heating was inferred from
Newell et al. (1972) by taking the ratio of the average value of the
latent heating in the upper portion of the atmosphere to the average
value in the lower portion. Table I (page 97) gives a list of these
(r values) ratios.

The values of Q_V actually added to the two levels were deter-
mined from:
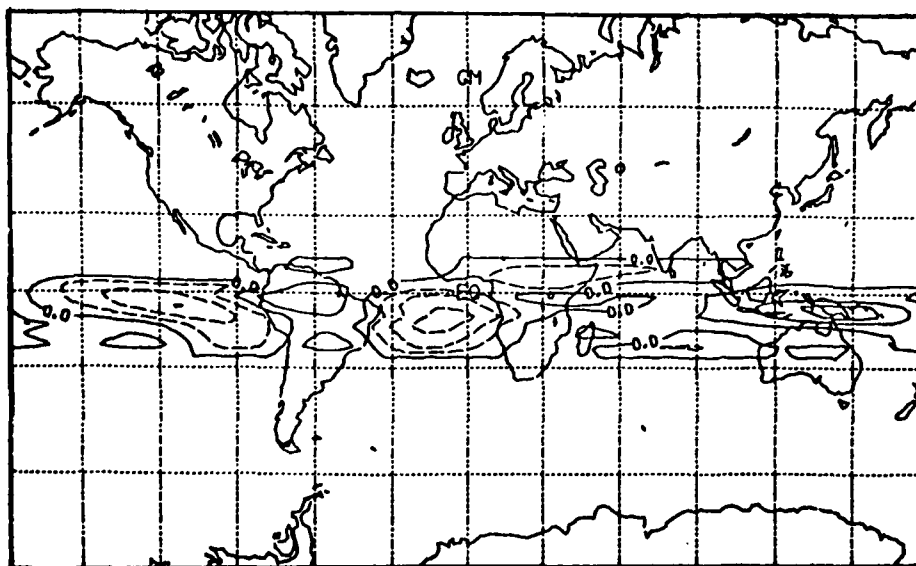
Figure 77. NHW longitudinally variable heating (Q_v) in units
of °K day^{-1}. Isoline labels scaled by 10 and
actual contour interval .5°K day^{-1}.
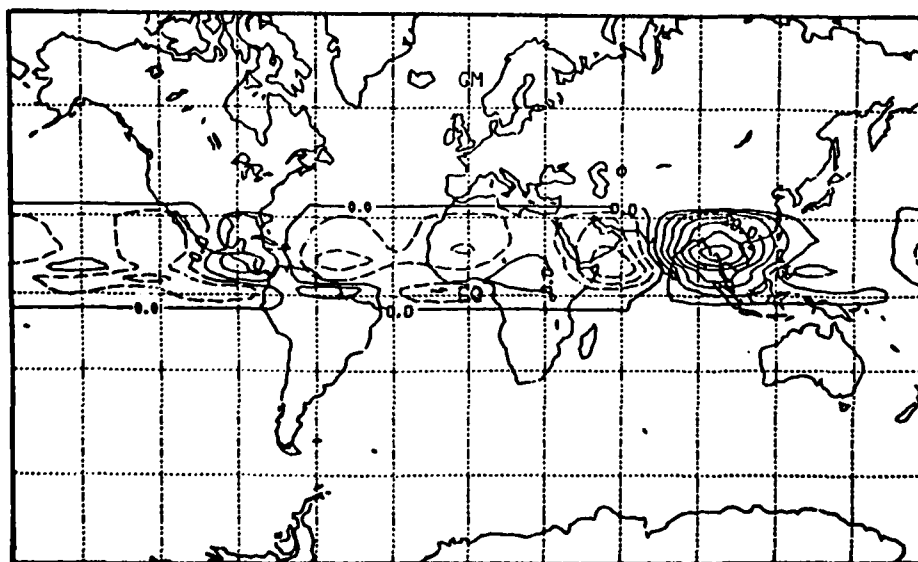
Figure 78. SHW longitudinally variable heating (Q_v) in units of
°K day^{-1}. Isoline labels scaled by 10 and actual
contour interval .5°K day^{-1}.

TABLE I

NHW r values used in Eqs. (56) and (57) to compute
the vertical variability of the tropical
diabatic forcing (Q_{v1} and Q_{v2})

Latitude	r Value
22^OS	.73
18^OS	.88
14^OS	1.16
10^OS	1.43
6^OS	1.43
2^OS	1.41
2^ON	1.44
6^ON	1.44
10^ON	.73

$$\pi_u \, Q_v + \pi_L \, Q_{v3} = \alpha(\pi_u + \pi_L) \, Q_v \qquad (54)$$

$$Q_{v1}/Q_{v3} = r \qquad (55)$$

Q_{v1} and Q_{v3} are the variable parts of the heating for the two layers,
while Q_v is the total variable part as computed above. r is the
ratio of the upper to the lower variable heating given in Table I
with π_u and π_L representing the thickness in millibars of the upper
and lower layers, respectively. Equations (54) and (55) were solved
for Q_{v1} and Q_{v3}

$$Q_{v1} = \alpha \, \frac{\pi_u + \pi_L}{r\pi_u + \pi_L} \, r \, Q_v \qquad (56)$$

$$Q_{v3} = \alpha \frac{\pi_u + \pi_L}{r\pi_u + \pi_L} \; Q_v \tag{57}$$

and these values were added to Q_{z1} and Q_{z3} from 22^oS to 10^oN for the NHW cases (Figure 75).

The factor α was set to 1, except during the course of one of the experiments where it was set to ½ inadvertently. A value of α of ½ would represent a case with half the variability in the precipitation as compared to the mean fields presented in Shutz and Gates (1972). This should still be an interesting case, since the limited observations available in the tropics seem to indicate that the intensity and positioning of tropical precipitation is highly variable. The final diabatic heating diagrams will be presented with each experiment in the following subsections.

The SHW Q_v field is given in Figure 78 and was computed from 2^oS to 30^oN following the same technique as above in the NHW case. The SHW precipitation data given in Newell et al. (1972) Plate 9.3 was used to determine the variability. The quantities Q_{v1} and Q_{v3} were computed using equations (56) and (57) with $\alpha = 1$ and an r value of 1.4. These values were then added to the zonal average fields (Figure 76) to produce the final diabatic forcing function for the SHW experiments. As before, the final diabatic forcing field will be presented with the SHW tests.

5.3 Rossby-Haurwitz Wave Initialization

To check the accuracy of the TLPEM an initialization of u and v on the sigma surface with a Rossby-Haurwitz wave number 4 was chosen.

The temperature on each sigma surface was initialized from the standard atmospheric temperature near that level, and was constant on each given sigma surface.

The initial field of the surface pressure P_s, was calculated by using Φ_s from Eq. (46) with $\Phi_0 = 1089 \ m^2 s^{-2}$. Then the hydrostatic equation was integrated assuming a constant temperature, $T_0 = 287^oK$ to get

$$P_{s_{ij}} = P_0 \ e^{-[(\Phi_{s_{ij}} - \Phi_0)/RT_0]} \quad ; \quad P_0 = 1000 \ mb$$

where R is the ideal gas constant for dry air.

The TLPEM was then integrated in time using a six-minute time step out to 10.3 days (2472 time steps). Since the above initialization is slightly baroclinic, one would not expect the Rossby-Haurwitz waves to propagate exactly as in a nondivergent barotropic model. Even so, the waves maintained their proper longitudinal and latitudinal structure with an average propagation rate of approximately $8.5^o \ day^{-1}$ for the integration period. The maximum changes in the u and v components of the velocity were about 10%. The temperature field, T, remained almost constant, deviating from the initial values by a maximum of 3^oC. The total energy in the model

$$TE = \int_0^{2\pi} \int_{-\pi/2}^{\pi/2} [P_s \Phi_s + \int_{-1}^{1} \pi (\frac{\underline{\Psi} \cdot \underline{\Psi}}{2} + c_p T) \ d\sigma] \ a^2 \cos \phi \ d\phi \ d\lambda$$

was reduced by about 1/3 of a percent at the end of the 10-day integration.

Several other two to five day integrations were carried out with zonal average wind and temperature fields taken from Newell et al. (1972). These experiments were used to further check the two-level model's conservative properties. It was found that the total potential enthalpy ($c_p \theta$), the total entropy ($c_p \ln \theta$), and the total mass ($\partial P_s / \partial t$) were also conserved with similar accuracy as the total energy. Sensitivity tests involving different diabatic heating functions, Q, were also carried out. The changes in the total potential enthalpy and the total entropy corresponded quite well to the predicted change that one would expect given a non-zero Q field. Finally, the total energy was closely monitored during all of the integrations, since it is a near conservative property as long as the residual in Eq. (52) is small. The ratio of the initial to final total energies will be given for the several experiments in the following subsections.

5.4 Experiment 1, NHW Forcing with No Mountains

The first experiment utilized the NHW diabatic forcing functions Q_1 and Q_3 given in Figures 79 and 80. These forcing functions were calculated using the techniques given in the last section with $\alpha = \frac{1}{2}$. This experiment is designed to check the effect of variable tropical heating in the absence of mountains in the two-level model. The basic experiment consisted of a 30-day integration of the model to quantify the long range response of the two-level model to the variable forcing. Several other short range (3-6 day) "pulse" experiments were also carried out to test the short range effect of enhanced or diminished convective activity.
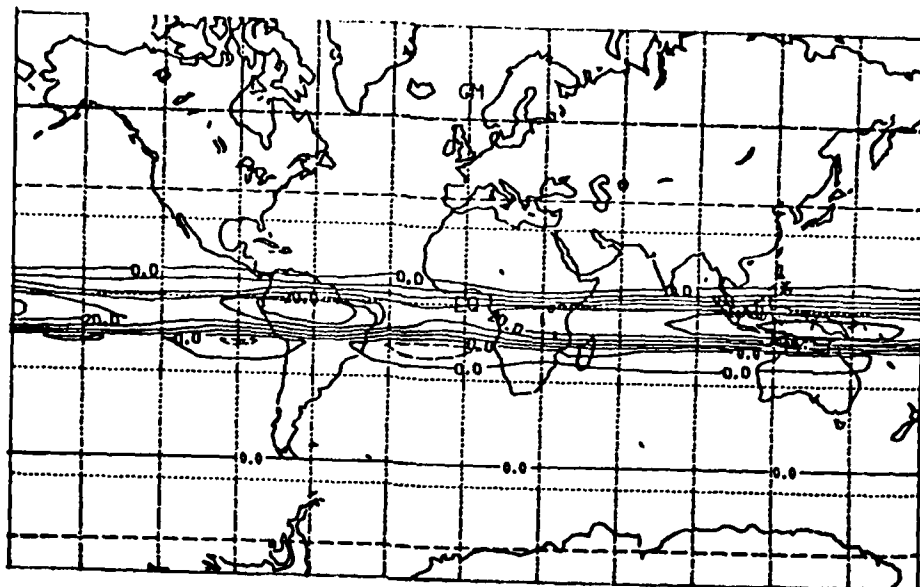
Figure 79. NHW total diabatic forcing function (Q) for upper
level with $\alpha = 1/2$. Isolines every $.5°$ day^{-1}.
Contour labels scaled by 10.
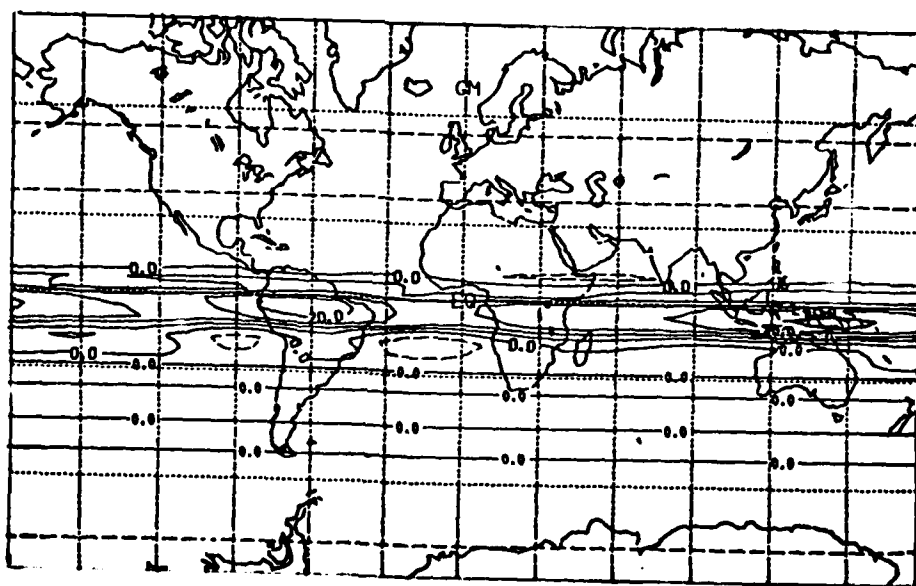
Figure 80. NHW total diabatic forcing function (Q) for lower
level with $\alpha = 1/2$. Isolines every $.5°$ day^{-1}.
Contour labels scaled by 10.

For the 30-day integration, the initial atmosphere is at rest with a constant temperature field on each sigma level ($T_1 = 230^\circ$K and $T_3 = 280^\circ$K). The surface pressure (P_s) and terrain height (Z_s) were also constant. P_s was set to 1000 mb initially which Z_s was kept constant at 111 m. The intermediate pressure levels, computed from Eqs. (49) and (50), were then $P_1 = 200$ mb and initially $P_3 = 700$ mb. The static stability

$$S = \frac{\partial T}{\partial p} - \frac{RT}{c_p P} \tag{58}$$

which was approximated as

$$S \approx (T_3 - T_1) / (P_3 - P_1) - R\overline{T}_2 / (c_p \overline{P}_2) \tag{59}$$

where $\overline{T}_2 = (T_1 + T_3)/2$ and $\overline{P}_2 = (P_1 + P_3)/2$ yields a value of $-.062^\circ$K/mb for the above initial conditions.

The zonal structure of the midlatitude forcing is reflected in the two-level model resultant fields until about day 24 when baroclinically unstable waves start to grow. Figure 81 (the 20th day 200 mb height field) gives an example of the zonal structure. The baroclinic waves seem to extract the momentum from the mean flow from days 24 to 30 and several 200 mb subtropical type jets are visible by the 30th day of integration (Figure 82).

The 200 mb height field after the 30th day of integration (Figure 83) shows that six days after the unstable baroclinic wave activity begins the zonal nature of the flow pattern has completely disappeared. Figure 84 shows the 30th day 200 mb meridional velocity
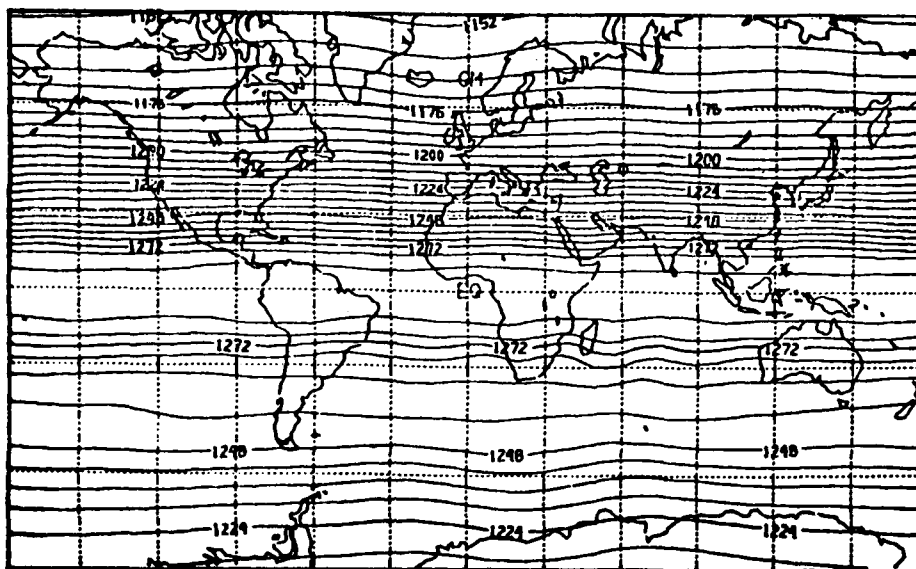
Figure 81. Two-level model no-mountain experiment 20th day
200 mb height field (dm). Contour interval is 6 dm.
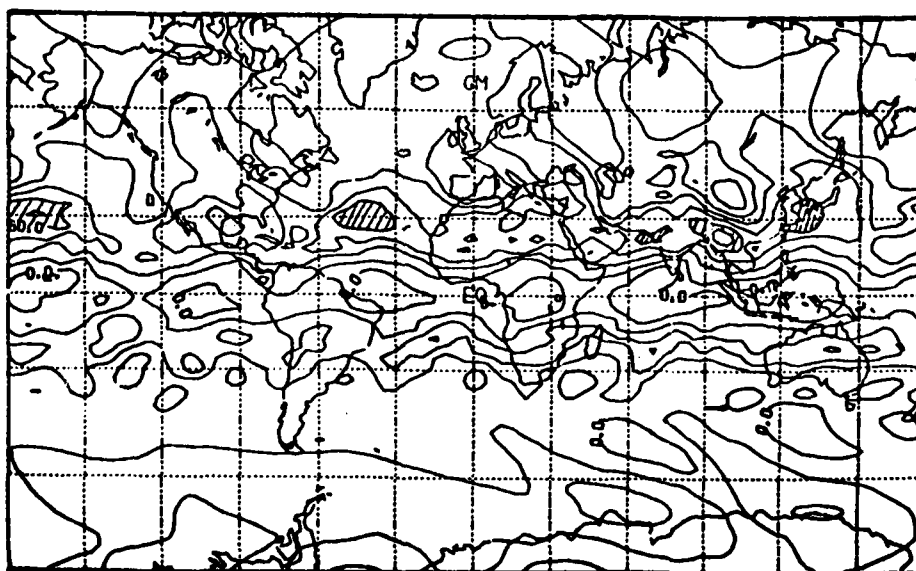
Figure 82. Two-level model no-mountain experiment 30th day 200 mb
zonal wind component (m s^{-1}). Isolines every 15 m s^{-1}.
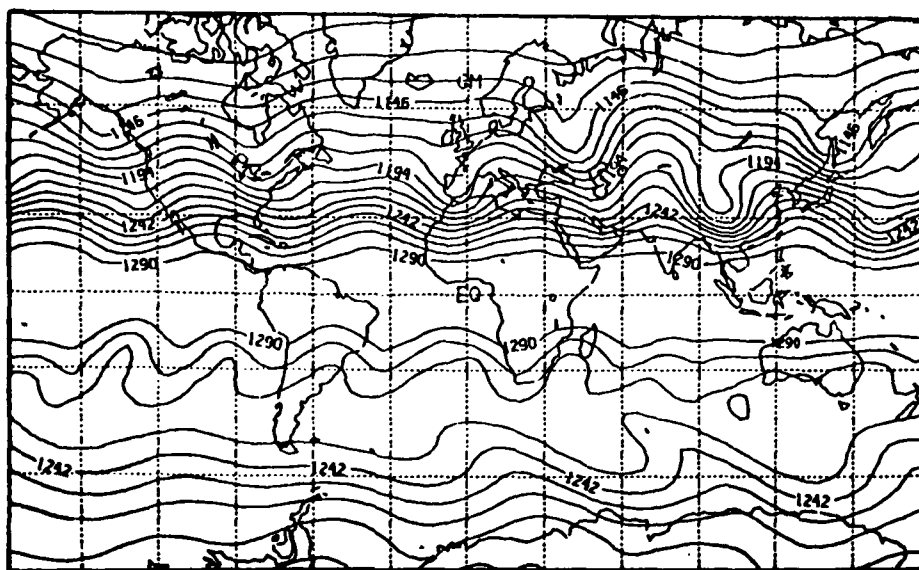
Figure 83.   Two-level model no-mountain experiment 30th day 200 mb
height field (dm).   Contour interval is 12 dm.
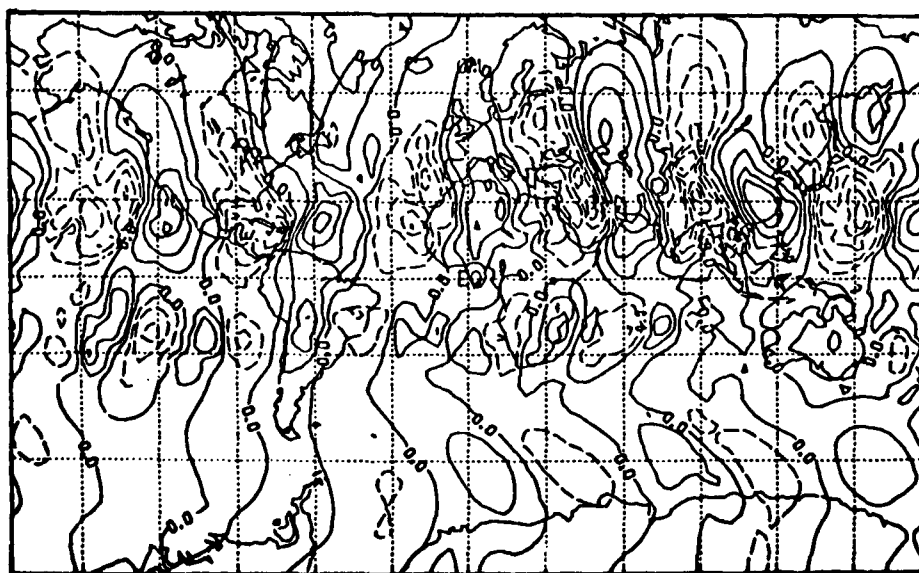
Figure 84.   Two-level model no-mountain experiment 30th day 200 mb
meridional velocity component (m s^{-1}).   The contour
interval is 10 m s^{-1}.   Dashed lines represent negative.

component and indicates the degree of wave activity at this time.
At day 24, this field had a maximum magnitude in the northern hemi-
sphere of only about 10 ms^{-1}. The 200 mb kinetic energy at the end
of the 30th day is given by Figure 85. As one would expect, the
local maxima in the kinetic energy corresponds to the subtropical
jet maxima.

To better determine the position of the subtropical jet streams
a three-day average (over six 12-hour fields) was performed for the
27 to 30 day zonal velocity components (Figure 86). This average by
no means represents the long term position of the subtropical jet
which cannot really be obtained from only a 30-day integration
starting from rest. But the areas of higher short term average
momentum can be compared with the meridional divergent flow field
v_x to see if any correspondence between these jets and positive v_x
can be seen.

Figure 87 shows the divergent meridional velocity component for
the 24th day of integration. In this experiment, as in the baro-
tropic model tests given in the last chapter, the divergent wind
field rapidly reaches a steady state with the forcing function. The
largest value of the divergence produced by the heating field (maxi-
mum near $3.2^{\circ}K$ day^{-1}) is located north of Australia and has an
approximate magnitude of $3 \times 10^{-6}s^{-1}$. This value is only about a
fourth of the 200 mb divergence found in the data study (Figure 32).
The reason for this is probably that in the real atmosphere the
divergent effect of tropical convective heating is focused near the
tropopause (approximately 200 mb in the tropics) in a shallow layer
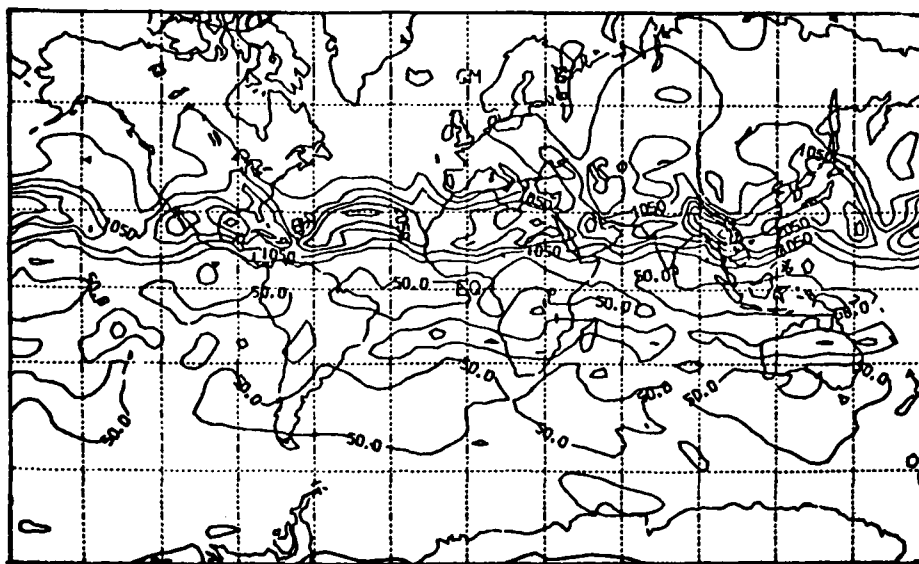
Figure 85. Two-level model no-mountain experiment 30th day 200 mb kinetic energy (m^2s^{-1}). Contour interval is 500 m^2s^{-2} starting at 50 m^2s^{-2}.
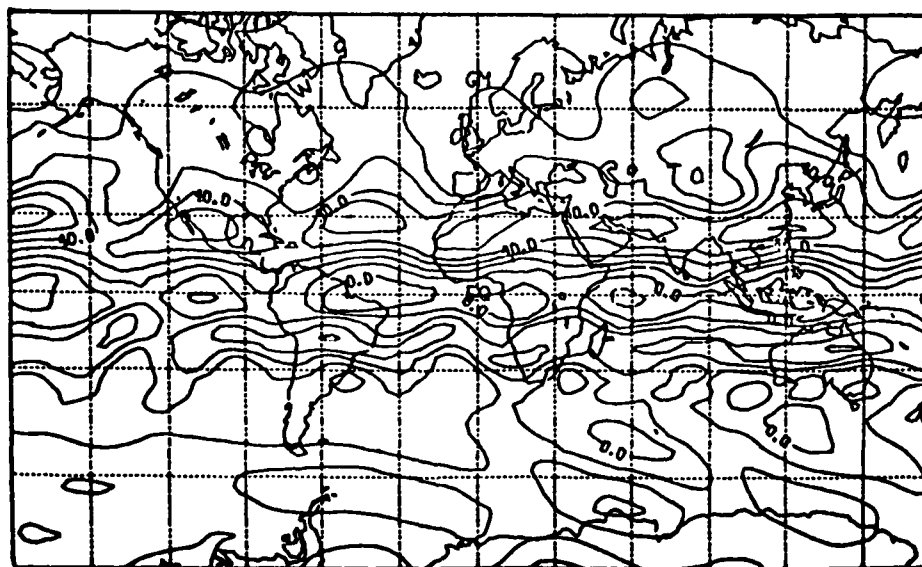
Figure 86. Two-level model no-mountain three-day average (days 27-30) 200 mb zonal wind component $(m\ s^{-1})$. Contour interval 10 $m\ s^{-1}$. Dashed lines represent negative values.
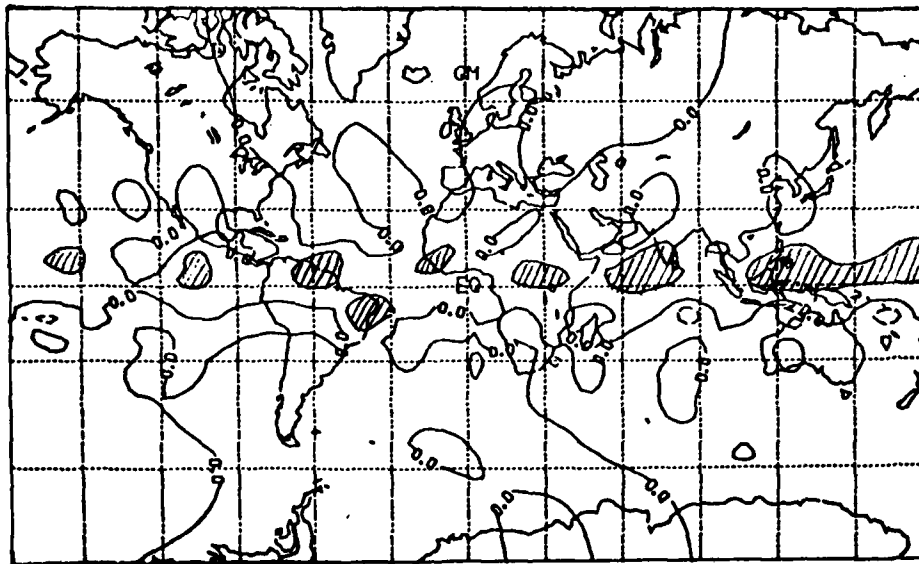
Figure 87. Two-level model no-mountain 24th day 200 mb
            meridional divergent velocity component (m s^{-1}).
            Contour interval is 1 m s^{-1}.
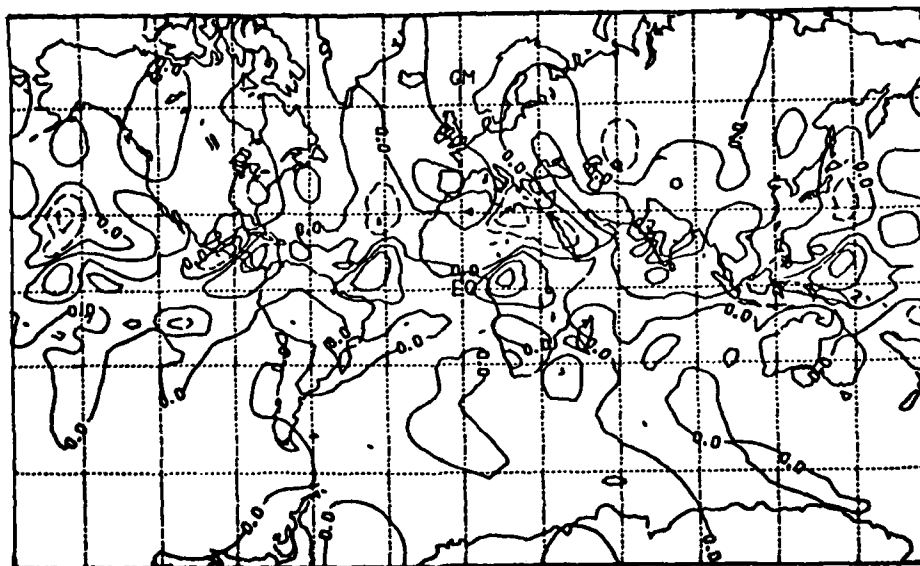
Figure 88. Two-level model no-mountain 27th day 200 mb
            meridional divergent velocity component (m s^{-1}).
            Contour interval is 1 m s^{-1}. Dashed lines repre-
            sent negative values.

of about 100 mb thickness. Since the TLPEM can only resolve a 340 mb layer in the upper portion of the model, the resulting divergent outflows in the model should be about a third of the real data case.

The computed meridional divergent velocity components in the model appear to reflect the tropical heating with magnitudes between 1 and 2 ms^{-1} to the north and 0 to -1 ms^{-1} to the south of the heat sources. Figure 87 is representative of the divergent meridional wind for days 5 to 24. Two examples of the zonal average meridional wind components for days 24 and 30 are given in Table II.

As previously stated after day 24, the amplitude of the baroclinic waves in the northern hemisphere grows very rapidly. This is to be expected since the vertical shear between the two levels is about 45 ms^{-1} at 30°N and 65 ms^{-1} at 18°N. By day 27, the baroclinic waves have grown considerably and the meridional (Figure 88) and zonal (Figure 89) divergent wind fields reflect this fact.

Of special interest are the areas of southerly divergent meridional flow of magnitude 2-3 ms^{-1} which originate in the deep tropics (around 4°S). These flows appear to be superimposed on the Hadley type outflows and part of the southern extension of the baroclinic wave activity. This can be inferred by comparing the 27th day 200 mb height field (Figure 90) and Figure (88). Several other comparisons at different times yield similar correlations between baroclinic wave activity and locally strong tropical areas of divergent outflow. These tropical divergent flows, which appear to be induced by the baroclinic wave activity, originate in small localized areas of divergence near 6 to 10°S. The divergence in these regions
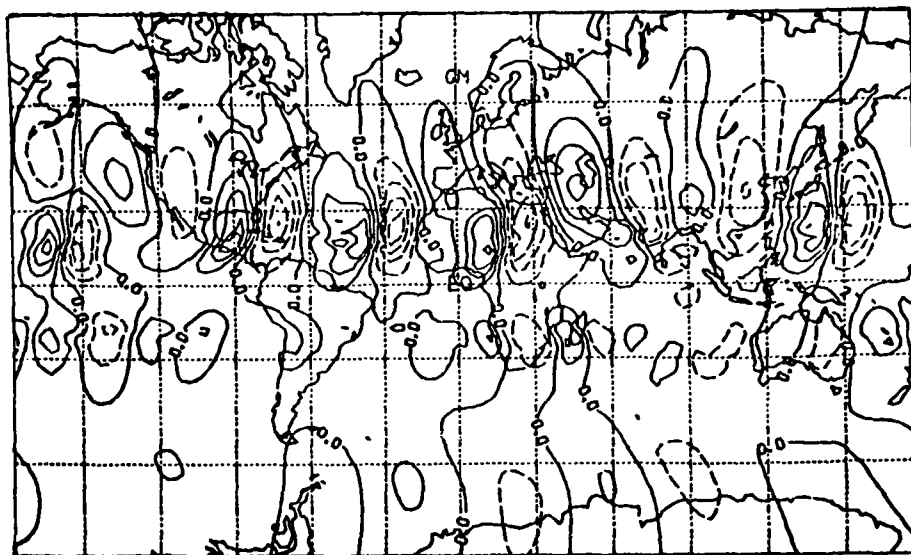
Figure 89. Two-level model no-mountain 27th day 200 mb zonal divergent velocity component (m s^{-1}). Contour interval is 1 m s^{-1}. Dashed lines represent negative values.
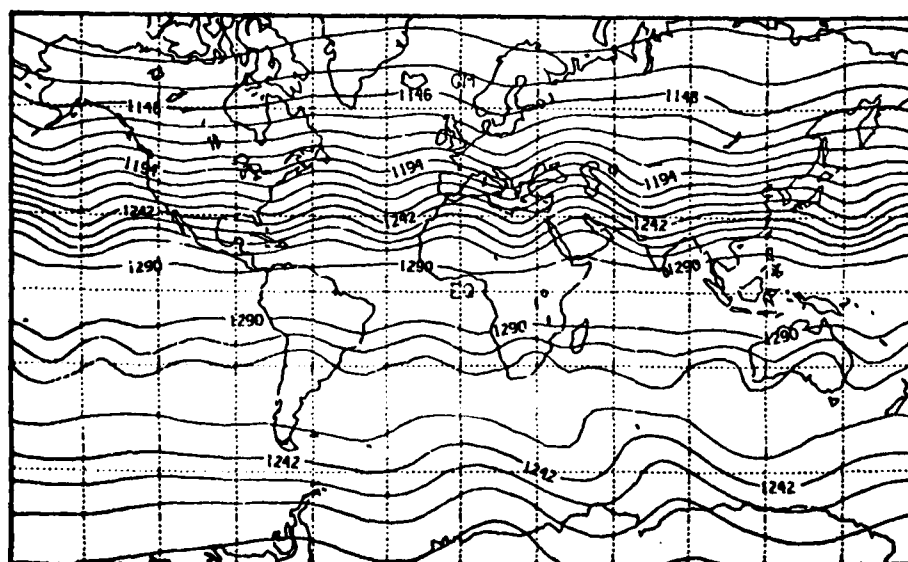
Figure 90. Two-level model no-mountain 27th day 200 mb height field (dm). Contour interval is every 12 dm.

TABLE II

The zonal average meridional velocity component

Latitude	Day 24		Day 30	
	200 mb	~700 mb	200 mb	~700 mb
84N	0.0	-0.0	0.0	-0.0
80N	0.0	0.0	0.1	-0.0
76N	0.0	-0.0	0.1	0.0
72N	0.0	0.0	0.1	-0.0
68N	0.0	0.0	0.1	-0.0
64N	0.1	0.0	0.2	-0.1
60N	0.1	0.0	0.1	-0.0
56N	0.1	0.0	0.1	0.0
52N	0.1	-0.0	0.3	-0.1
48N	0.1	-0.0	0.5	-0.2
44N	0.2	-0.0	0.5	-0.2
40N	0.2	-0.1	0.3	-0.1
36N	0.2	-0.0	-0.0	0.1
32N	0.2	-0.0	-0.2	0.1
28N	0.1	-0.0	-0.1	0.1
24N	0.2	-0.0	0.0	-0.0
20N	0.2	-0.0	-0.0	0.0
16N	0.3	-0.1	0.1	-0.1
12N	0.5	-0.3	0.5	-0.3
8N	0.8	-0.4	0.9	-0.6
4N	0.8	-0.5	1.0	-0.7
0	0.8	-0.4	1.2	-0.8
4S	0.4	-0.2	0.8	-0.6
8S	0.0	0.0	0.3	-0.2
12S	-0.3	0.2	-0.1	-0.0
16S	-0.3	0.2	-0.1	-0.0
20S	-0.2	0.1	-0.2	0.1
24S	-0.1	0.1	-0.2	0.1
28S	-0.1	0.0	-0.2	0.1
32S	-0.1	0.0	-0.2	0.1
36S	-0.1	0.0	-0.2	0.1
40S	-0.1	0.0	-0.2	0.1
44S	-0.0	-0.0	-0.1	0.0
48S	-0.0	-0.0	-0.1	0.0
52S	-0.0	-0.0	-0.1	0.0
56S	-0.0	0.0	0.1	-0.1
60S	-0.0	-0.0	0.3	-0.2
64S	-0.0	-0.0	0.2	-0.1
68S	-0.0	-0.0	0.1	-0.1
72S	-0.0	0.0	-0.0	0.0
76S	-0.0	0.0	-0.2	0.1
80S	-0.0	-0.0	-0.1	0.1
84S	-0.0	0.0	-0.1	0.1

appears to be more locally compensated than the larger divergent areas which appear to be in response to the large scale tropical heating patterns.

These locally large divergences (approximately $4 \times 10^{-6} s^{-1}$) could enhance the local precipitation and thus lead to more tropical latent heat release. The present modeling experiments do not allow for any feedback between baroclinic waves and the tropical heating disturbances. Figure 88 does suggest that some feedback may be of importance and this might be an area for future study.

Comparing the three-day average 200 mb zonal velocity component (Figure 86) with the DST data time average 200 mb zonal wind (Figure 10) one can see that the two-level model northern hemisphere jet maxima are displaced slightly to the south of the jets in the real data case. Also, there are many more jet maxima in the model case than in the NHW DST data. In the model zonal average wind, there is a definite wavenumber six pattern. This is reasonable considering the shortness of the averaging period and that wavenumber six would be one of the first waves to become baroclinically unstable.

In the model case the strongest average jet is north of, and slightly downstream of the maximum heating (see Figure 79). This jet has no apparent counterpart in the DST data. The next strongest jet produced by the model flows across Japan and this jet corresponds to the most active jet in the 200 mb average DST data zonal wind field. There is also another maximum in the jet north of, and slightly downstream of the heated area over the Amazon basin. This jet is displaced slightly east of the 200 mb jet off the east coast

of the United States given in Newell et al. (1972).

The next set of experiments is designed to test the short range (1-3 day) effect on the model atmosphere by "pulsing" (enhancing) or "unpulsing" (reducing) a given area of tropical heating. The "pulse" consists of adding 3°K day^{-1} to both the lower and upper forcing functions (Figures 79 and 80) in the local area of the Amazon basin. Figure 91 gives an example of the resulting forcing for the upper layer of the model. The "unpulse" subtracts 3°K day^{-1} from the forcing functions in the upper and lower levels in the same region as in the pulse case. Figure 92 shows the resulting unpulse forcing function for the upper layer.

The pulsed region in Figure 91 represents a very active convective case where about 2 cm day^{-1} of rain falls in the central core of the region. The unpulsed region in Figure 92 represents an inactive convective case where at most 1/2 cm day^{-1} of rain falls in the central core of the region. The pulsed and reduced forcing functions were turned on at the start of day 25 and were left constant for a six-day integration. These two forcing functions represent changes in the tropical rainfall pattern that are probably within the observed variability.

The 200 mb divergent wind fields at the end of the 27th day for both the pulsed and unpulsed cases are given in Figures 93 through 96. The divergent meridional velocity component is stronger in the pulsed region (Figure 93) while in the unpulsed region, the flow has switched from outflow to inflow (Figure 94). The same conclusion can also be drawn for the zonal divergent components
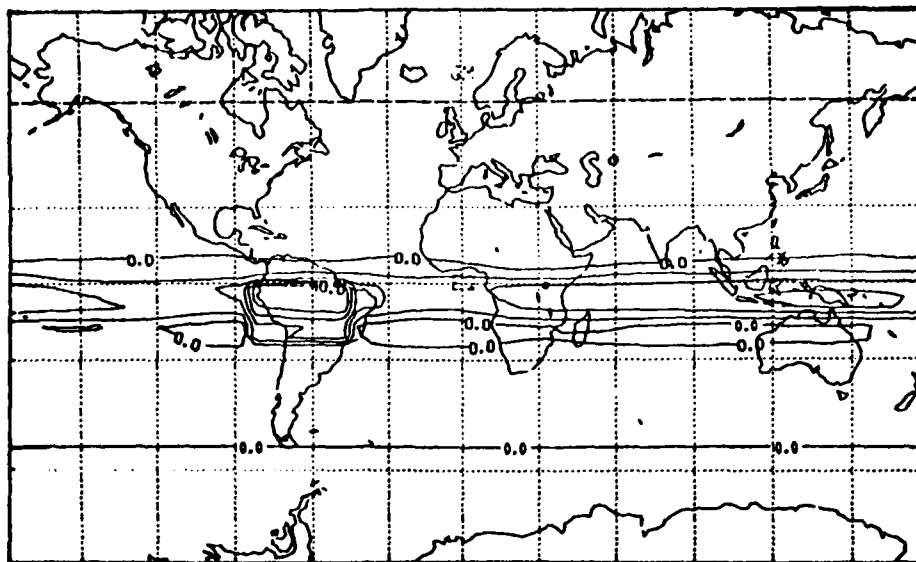
Figure 91. NHW total diabatic forcing function for upper level
with 3°K day^{-1} pulse over Amazon basin. Contour
interval is .5°K with labels scaled by 10.
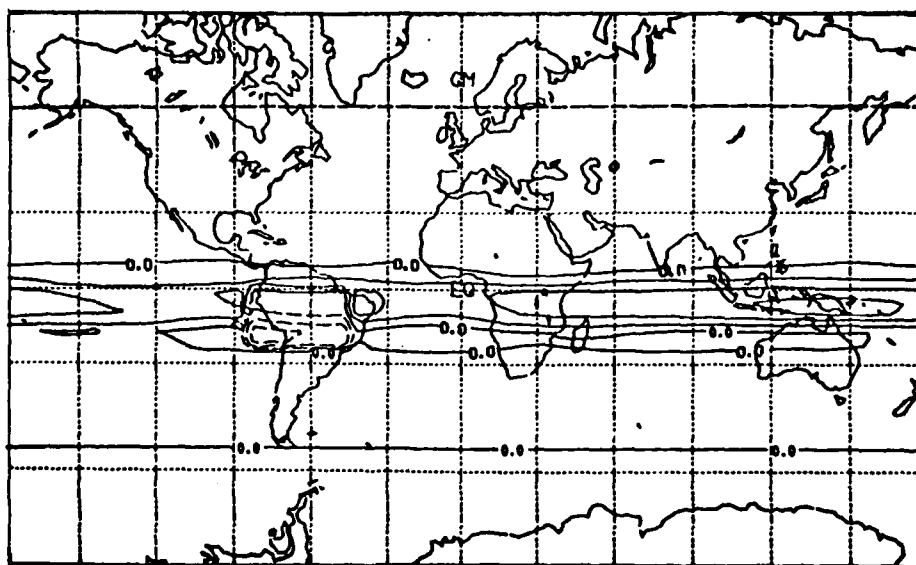
Figure 92. NHW total diabatic forcing function for upper level
with 3°K day^{-1} reduction over the Amazon basin.
Contour interval is .5°K with labels scaled by 10.
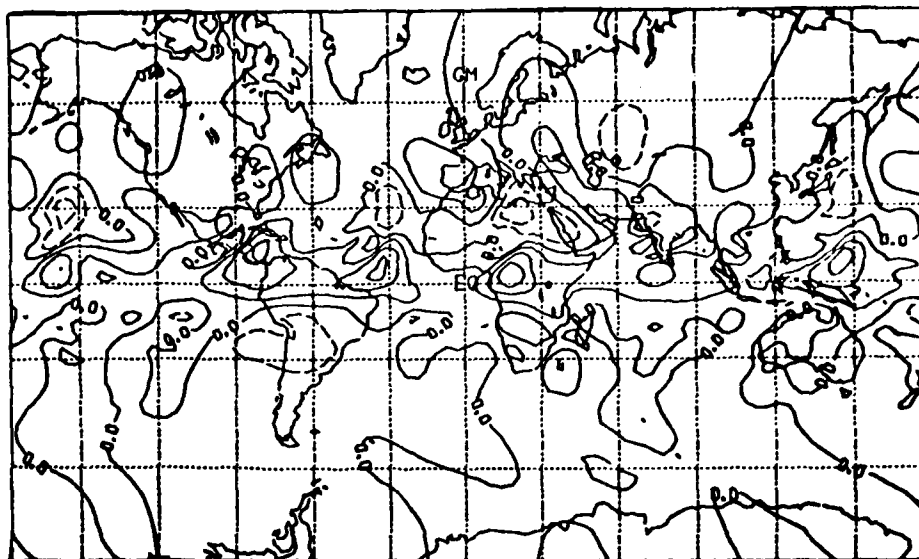
Figure 93. Two-level model no-mountain 27th day pulsed 200 mb meridional divergent wind component (m s^{-1}). Contour interval is 1 m s^{-1} with dashed lines representing negative values.
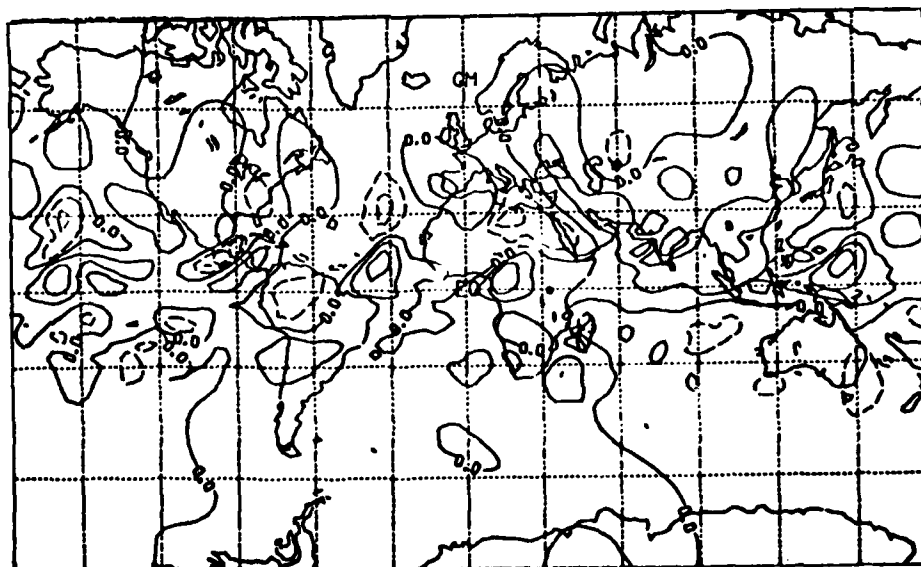
Figure 94. Two-level model no-mountain 27th day unpulsed 200 mb meridional divergent wind component (m s^{-1}). Contour interval is 1 m s^{-1} with negative contours dashed.

(Figures 95 and 96).

To further quantify the effect of the pulse and the unpulse on the subtropical jet streams of both the winter and summer hemispheres the 200 mb zonal wind components at the end of the 27th day are presented in Figures 97 - 99. Figure 97 shows the result of the three-day pulse while Figure 99 gives the result for the three-day unpulse. Figure 98 is the control for day 27 in which the original forcing function is left unchanged. The 200 mb subtropical jet just to the north of the pulsed area has changed substantially when compared to the two other cases. To better discern the actual change, the difference of the pulse and unpulse cases for the 200 mb zonal wind component is given in Figure 100. The maximum change in the NHW subtropical jet is about 14 m/sec and located at $(60^{\circ}W, 26^{\circ}N)$. Difference fields for the pulse and control case or for the control case and the unpulse case are very similar with about 1/2 the strength, suggesting that the changes in the 200 mb zonal wind field are almost linear in response to the heating. The pulsed (approximately) 700 mb zonal wind field is given in Figure 101, while the unpulsed (700 mb) zonal wind field is given in Figure 102. The change in the zonal wind field at the lower level (700 mb) of the model between the pulse and unpulse cases is given in Figure 103. At the (700 mb) layer, the pulsing causes a local deceleration of the tropical easterlies.

The 200 mb kinetic energy fields for the unpulsed and pulsed cases are given in Figures 104 and 105, respectively. The kinetic energy difference field (pulsed minus unpulsed) is given in Figure
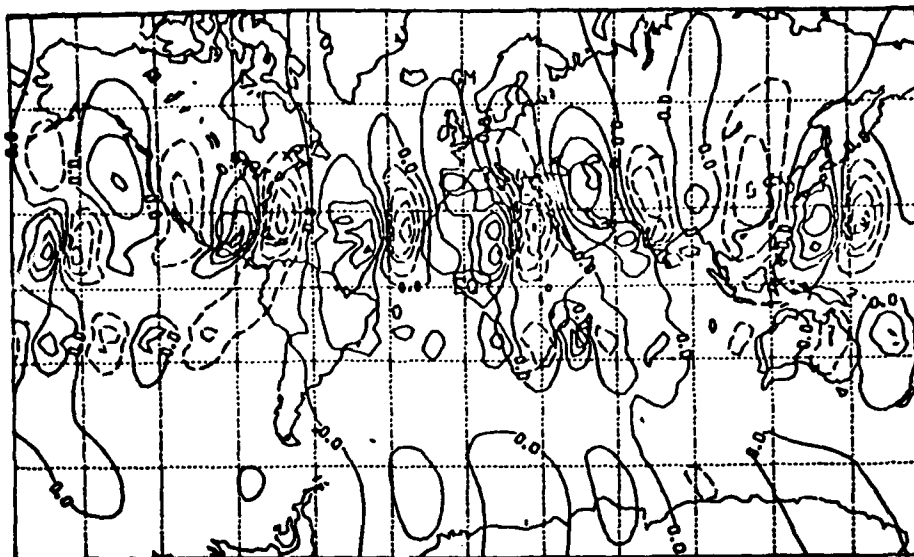
Figure 95. Two-level model no-mountain 27th day pulsed 200 mb zonal divergent wind component (m s^{-1}). Contour interval is 1 m s^{-1} with negative contours dashed.
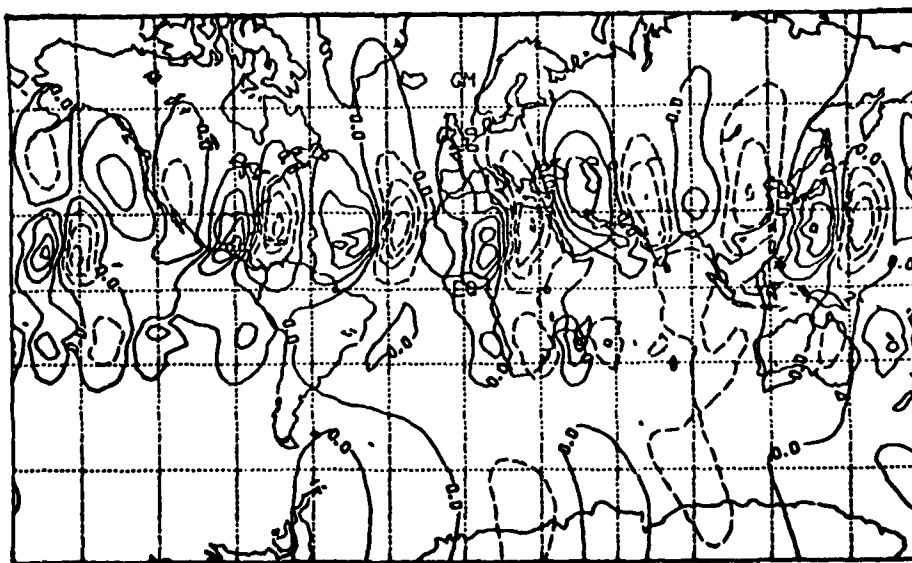
Figure 96. Two-level model no-mountain 27th day unpulsed 200 mb zonal divergent wind component (m s^{-1}). Contour interval is 1 m s^{-1} with negative contours dashed.
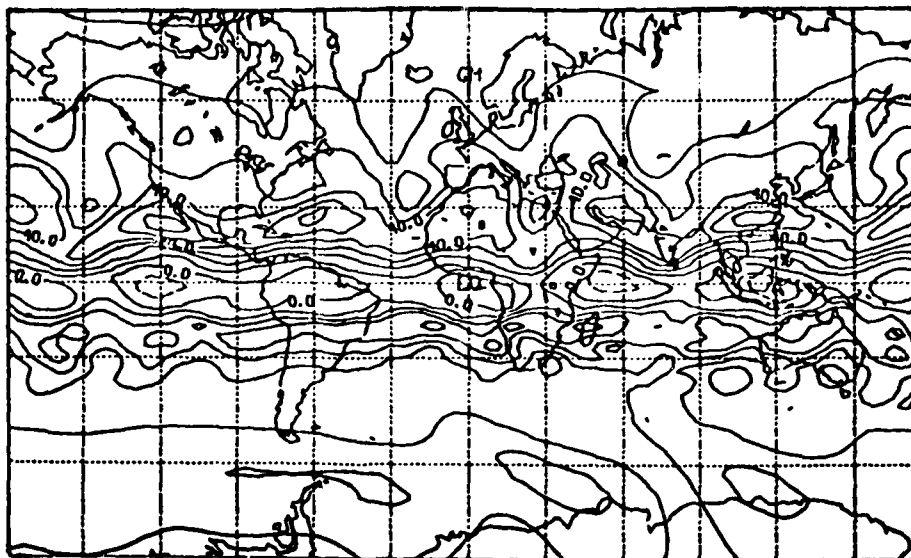
Figure 97. Two-level model no-mountain 27th day pulsed 200 mb
zonal wind component (m s^{-1}). Contour interval of
10 m s^{-1} with negative contours dashed.
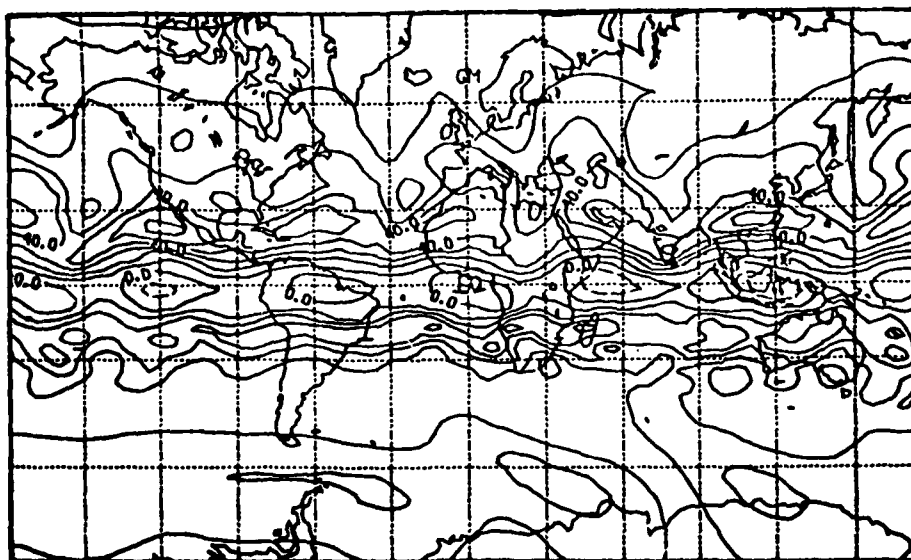
Figure 98. Two-level model no-mountain 27th day 200 mb zonal
wind component (m s^{-1}). Contour interval of
10 m s^{-1} with negative contours dashed.
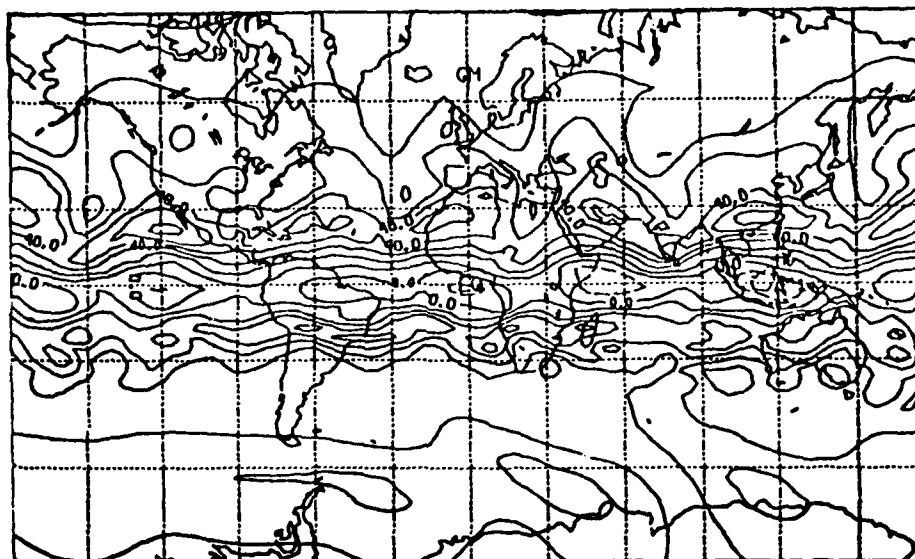
Figure 99.   Two-level model no-mountain 27th day 200 mb unpulsed
             zonal wind component (m s^{-1}). Contour interval of
             10 m s^{-1} with negative contours dashed.
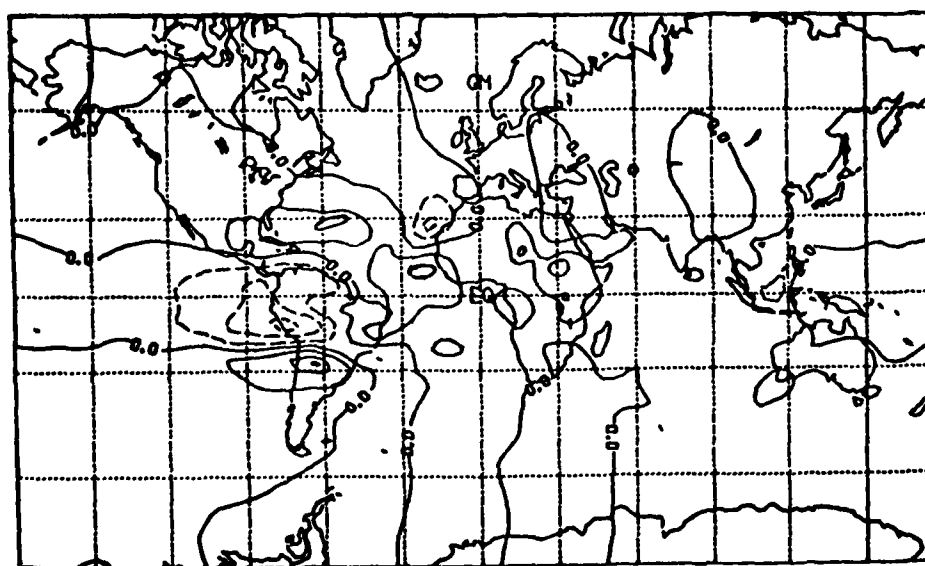
Figure 100. Two-level model no-mountain 27th day (pulse minus
             unpulse) 200 mb zonal component of velocity dif-
             ference field (m s^{-1}). Contour interval of 5 m s^{-1}
             and negative contours dashed.
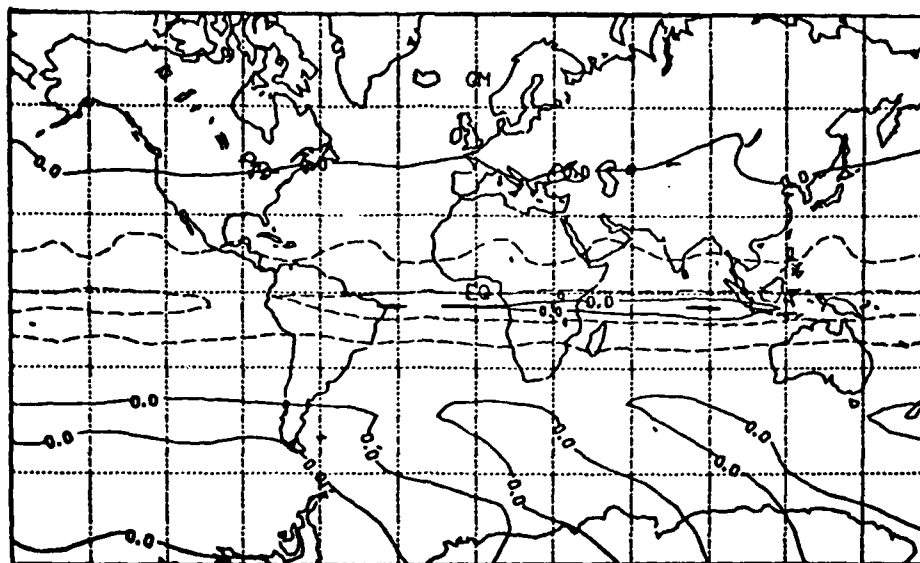
Figure 101.   Two-level model no-mountain 27th day lower level
              unpulsed zonal wind component (m s^{-1}). Contour
              interval of 10 m s^{-1} with negative contours dashed.
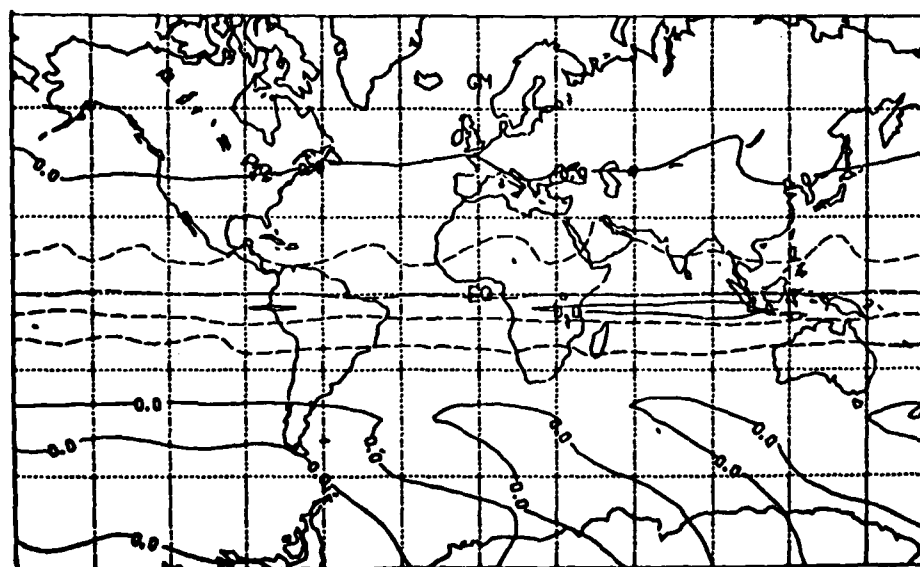
Figure 102.   Two-level model no-mountain 27th day lower level
              pulsed zonal wind component (m s^{-1}). Contour
              interval of 10 m s^{-1} with negative contours dashed.
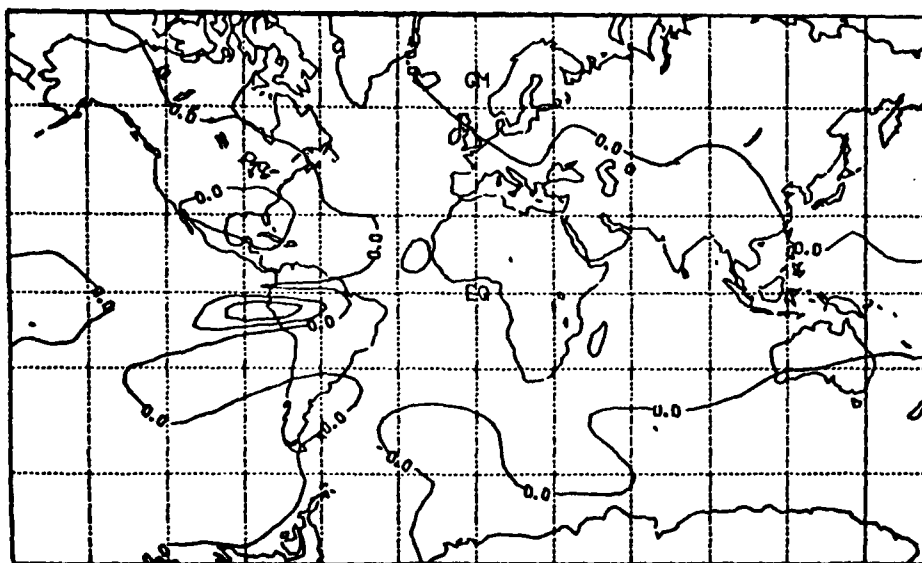
Figure 103. Two-level model no-mountain 27th day (pulse minus unpulse) lower level zonal component of velocity difference field (m s^{-1}). Contour interval of 5 m s^{-1}.
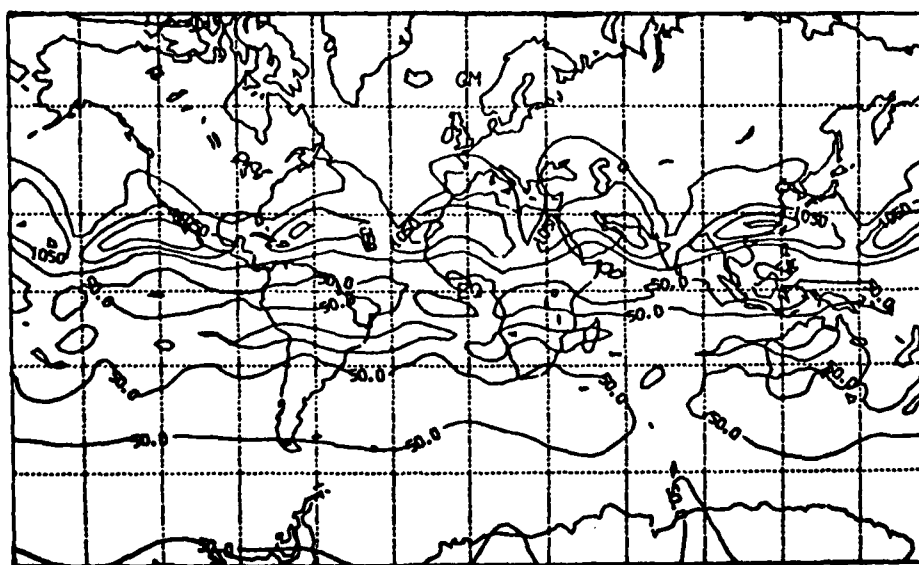
Figure 104. Two-level model no-mountain exeriment 27th day 200 mb unpulsed kinetic energy (m^{2}s^{-2}). Contour interval is 500 m^{2}s^{-2}.
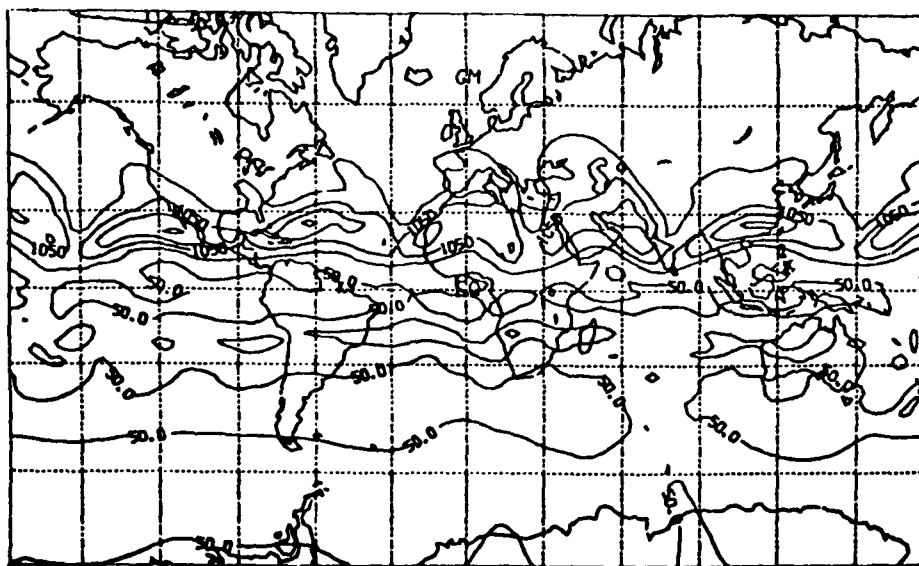
Figure 105. Two-level model no-mountain experiment 27th day 200 mb pulsed kinetic energy (m^2s^{-2}). Contour interval is 500 m^2s^{-2}.
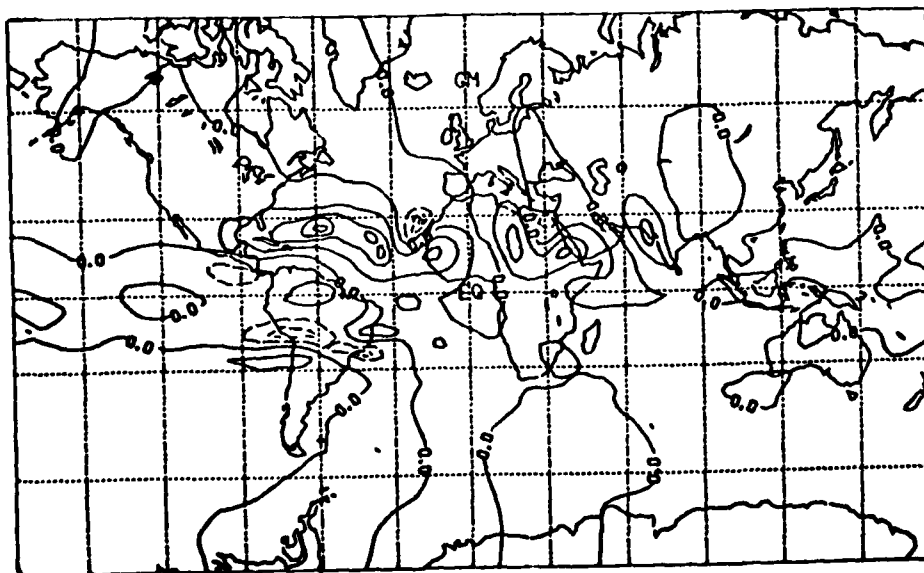
Figure 106. Two-level model no-mountain experiment 27th day 200 mb (pulse minus unpulse) kinetic energy (m^2s^{-2}) difference. Contour interval of 150 m^2s^{-2} with negative contours dashed.

106. Again, as in the 200 mb zonal wind field, the changes appear to be substantial to the north of the pulsed region. The maximum change in the northern hemisphere occurs at $57.5^{\circ}W$, $26^{\circ}N$ and has a value of about 650 m^2s^{-2}. This represents about 40% change as compared to the 200 mb unpulsed kinetic energy maximum. About a 20% change in the kinetic energy with respect to the unpulsed maximum value has been propagated downstream to just beyond $60^{\circ}E$ in a matter of only three days. This rapid downstream propagation is probably accomplished by the baroclinic waves through the β effect.

The 200 mb temperature difference (Figure 107) at the 27th day of integration between the pulse and unpulse seems to partially sub-stantiate the notion set forth in Chapters 1 and 2 that tropical latent heating is realized locally but is transported outward by the divergent motion field and realized when the outflows finally subside. Locally heated areas as large as $5^{\circ}K$ exist at $22^{\circ}N$ and $26^{\circ}S$, while in the pulsed region, the temperature difference is 0 to $-1^{\circ}K$. Since the local meridional divergent flows actually reverse for the unpulse case and flow into the tropical areas, it might be possible to generate sufficient warming due to tropical subsidence to warm the unpulsed case slightly more than the diabatically forced pulsed case.

The actual 200 mb temperature fields for the pulsed and unpulsed cases at day 27 are given in Figures 108 and 109. Comparing these fields with the height fields for the pulsed (Figure 110) and un-pulsed (Figure 111) cases, one can see that typical wintertime tem-perature and pressure patterns exist in the northern hemisphere. The summer hemisphere flows and temperature gradients are much weaker.

123
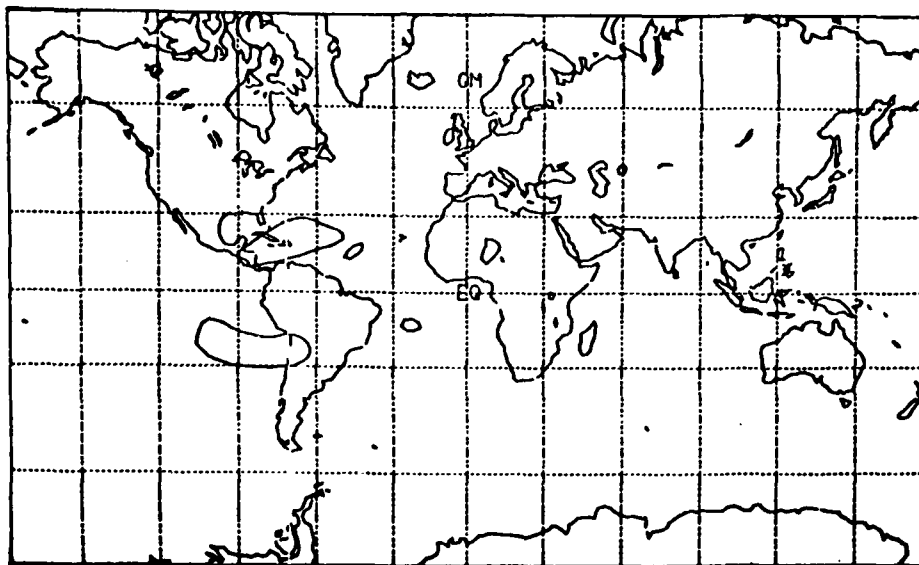
Figure 107. Two-level model no-mountain experiment 27th day 200 mb
temperature difference field (pulse minus unpulse)
(°K). Only isolines on chart are for 2.5°K.
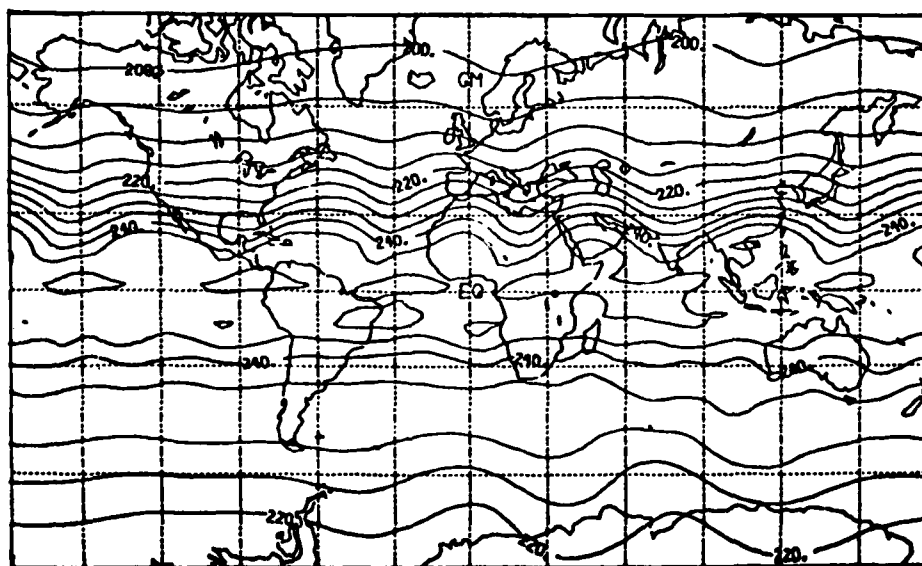
Figure 108. Two-level model no-mountain experiment 27th day
200 mb pulsed temperature field (°K). Contour
interval is 5°K.
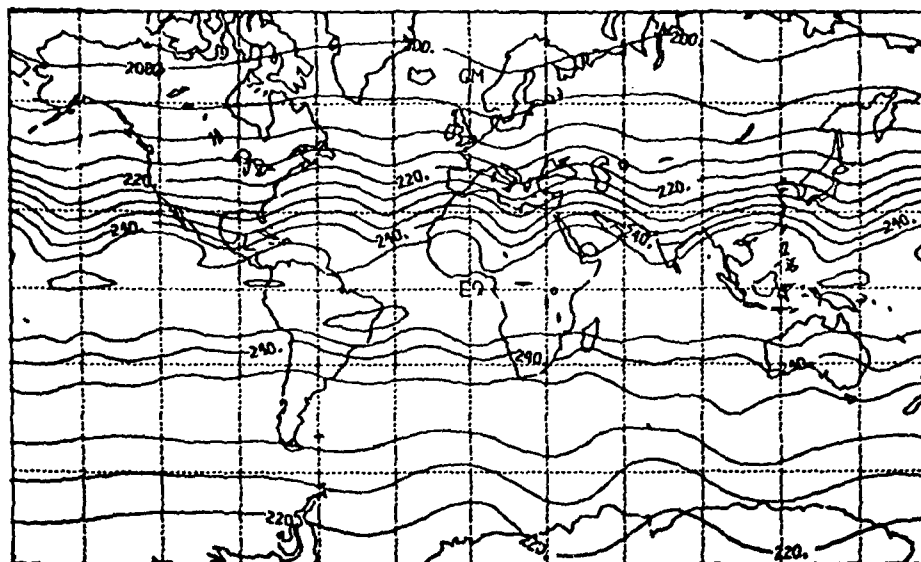
Figure 109. Two-level model no-mountain experiment 27th day 200 mb unpulsed temperature field (°K). Contour interval is 5°K.
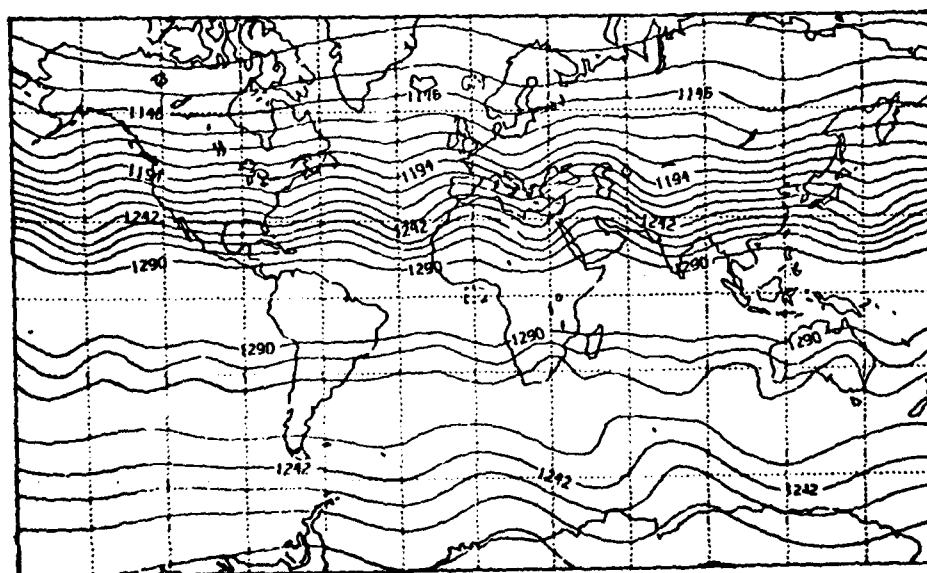
Figure 110. Two-level model no-mountain experiment 27th day 200 mb pulsed height field (dm). Contour interval is 12 dm.
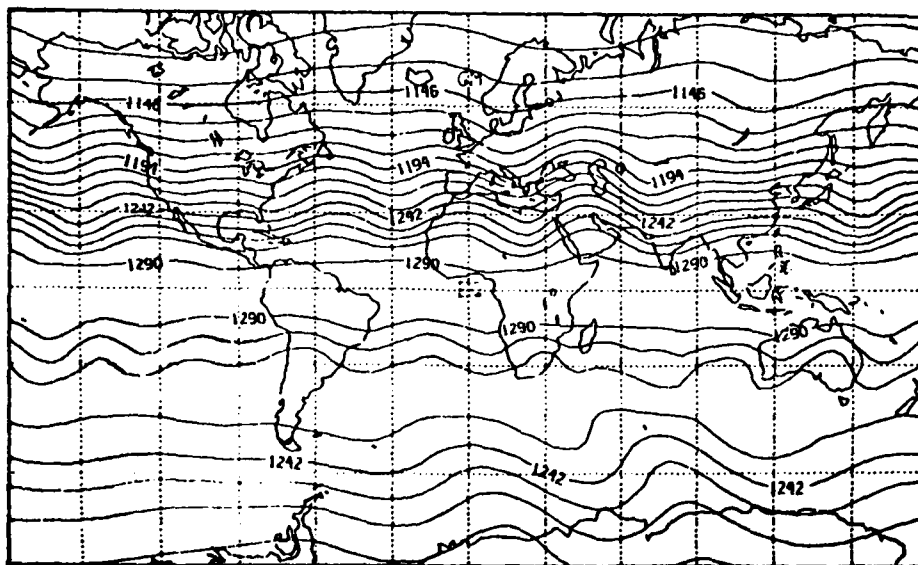
Figure 111.   Two-level model no-mountain experiment 27th day 200 mb
unpulsed height field (dm). Contour interval is 12 dm.
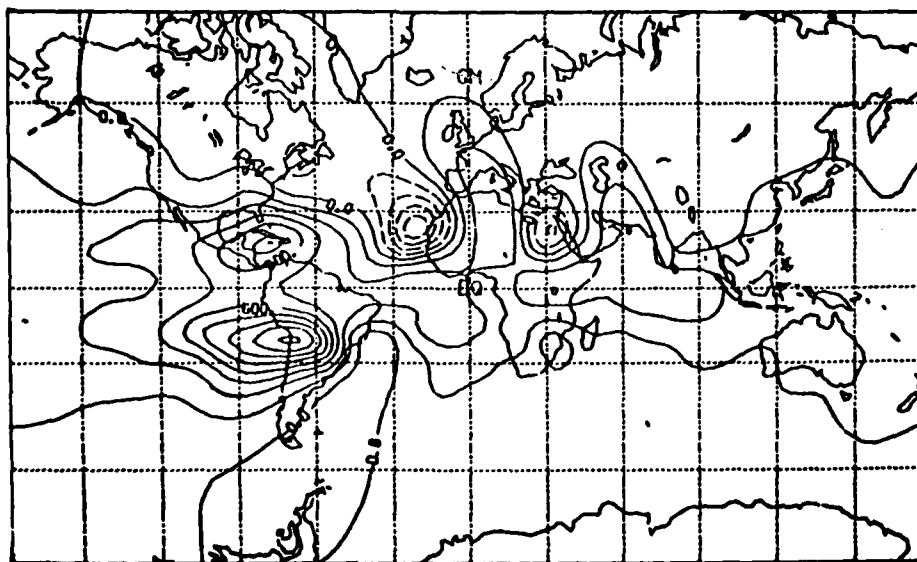
Figure 112.   Two-level model no-mountain experiment 27th day 200 mb
height field difference (Φ=gz) (pulse minus unpulse)
(m^2s^{-2}). Contour interval is 150 m^2s^{-2}).

This is to be expected since the zonal average forcing function (see Figure 76) has a much weaker latitudinal gradient of cooling in the summer hemisphere.

Comparing the pulsed (Figure 110) and unpulsed (Figure 111) 200 mb height fields, one can find very little difference in the overall structures. The only slight difference which can be detected is that the gradient in the pulsed case near Cuba is tighter. The difference of the pulsed and unpulsed 200 mb $\Phi=(gz)$ fields is given in Figure 112. The corresponding maximum height change is about 80 m in the northern hemisphere and 120 m in the southern hemisphere. One inference that might be drawn here is that a small change in the height field in tropical and subtropical latitudes can yield a substantial change in the kinetic energy. One might also be tempted to say that strongly heated tropical areas play a minor role in the positioning of the ultra-long wave troughs and ridges. But before making this statement, it is important to verify the percentage of change in the ultra-long wave patterns due to tropical heating differences.

Baumhefner (1978) uses longitude-time plots (Hovmöller diagrams) of the 500 mb height field to help quantify the forecasting skills of several different forecast models. To determine the accuracy of the ultra-long wave forecast of a given model, both the actual data and model forecast for the 500 mb level were decomposed into their respective wavenumbers using Fourier analysis. Then wavenumbers 1 through 3 for both the observed data and the forecast height fields were reconstituted to form ultra-long wave 500 mb

height fields (Φ_{1-3}). At a given latitude, these fields are plotted on Hovmöller diagrams. The difference between the observed data and the forecast models' results is also plotted on a Hovmöller diagram. Thus, using these types of difference fields for several different models, it is possible to discern the relative error in the uitra-long waves between the different forecast models.

As previously stated in the introduction, Baumhefner and Downey (1977) found that the GISS model produced better three-day ultra-long wave forecasts than the NMC and NCAR models. The Hovmöller diagrams of Baumhefner (1978) at 40°N of Φ_{1-3} show an amplitude of about 200 m in all of the forecasts and the observed data. One example shows that at the end of a three-day forecast, the GISS model error is about 60 m while the NMC model error is between 110 and 120 m. Thus, the error in the NMC model is almost two times as large as the error in the GISS model and about half of the total amplitude of the ultra-long waves themselves. The surprising fact is that the GISS model only forecasts the ultra-long waves with at most 60 m more accuracy. Yet Baumhefner and Downey (1977) point out that the main reason for the GISS model's slightly better overall forecasting skill lies in its ability to forecast the ultra-long waves with greater accuracy. In fact, a synoptician would be hard-pressed to discern a 60 m height change in the ultra-long waves on a typical 500 mb forecast chart. Thus, one could conclude from these arguments that small changes in the total height field that occur mainly in the ultra-long wave part of the spectrum during the course of a given forecast period could produce large differences in the final forecast.

Now in order to interpret our results using these techniques, one may note that there was approximately a 60 m error difference in the ultra-long wave forecasts between the best and worst forecasts of the model comparisons given in Baumhefner (1978). Since the GISS model includes tropical convective heating and the NCAR and NMC models do not, one could hypothesize that one of the reasons for the 60 m relative error in the ultra-long waves is due at least partially to tropical convective heating. The 60 m relative error represents about 30% of the total amplitude in the ultra-long waves. This 30% amplitude difference will be used as a benchmark for determining the relative importance of several tropical forcing experiments, like the pulsed and unpulsed comparisons of this section.

In the present study, one means of determining the effects of different tropical type heatings within the context of the two-level model is to utilize the pulsed and unpulsed forcing functions. This type of experiment has already been presented in this subsection for the NHW case with no mountains. In the next two subsections, similar experiments for the NHW and SHW cases with mountains will be presented. Yet another way of looking at the same set of experiments is to let the unpulsed case locally represent the set of all models, like the NMC and NCAR models, which do not include tropical convective heating. The pulsed case may then be taken to represent locally the set of models which do include tropical convective heating, like the GISS model. The analog is, of course, somewhat liberally made since the TLPEM with its simple parameterization of physical processes cannot be exactly compared to the more complex models, like the

GISS, NMC and NCAR models. The comparison is only given as another vehicle to help the reader in interpreting the results of this chapter.

As previously stated, the difference in the 200 mb total height fields for the pulsed and unpulsed cases is given in Figure 112. The largest height difference in Figure 116 at 30^ON is only 50 m. However, this is fairly sizeable compared to the actual long wave amplitude of the present model. For both the pulsed and unpulsed cases, Hovmöller diagrams of the ultra-long wave structure (Φ_{1-3}) at the 200 mb model level have been computed from day 24 to day 27. These diagrams are presented in Figures 113 to 130. Since the isopleth intervals vary from chart to chart, the results should be interpreted carefully.

In comparison of the results of these diagrams with the ones presented in Baumhefner (1978), one can see that the total magnitude in the ultra-long waves of the two-level model at 42^ON is about one-fourth of the 40^ON values given by Baumhefner (1978) for the observed data. This deficiency of general circulation models that have been started from rest and not from observed data has been pointed out by Pratt (1978).

Pratt (1978) finds (for the ultra-long waves) that the NCAR model 500 mb height variances are typically one-fourth of the actually observed 500 mb height variances. Since the variance in the height varies like the square of the actual height, the NCAR model will probably predict only about half of the observed amplitude in the ultra-long waves. Thus, from Pratt's results, it is to be
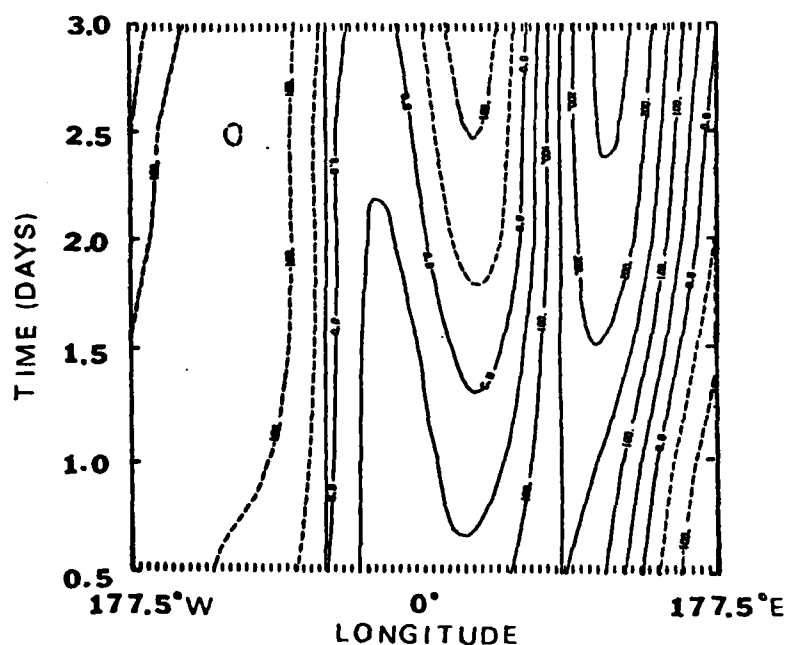
Figure 113. Hovmöller diagram for the 200 mb unpulsed geopotential
$(\Phi_{1-3})(m^2 s^{-2})$ at 42°S for days 24.5 to 27 with longi-
tude at the base (X axis) from 177.5°W on the left to
177.5°E on the right. The tic marks in the horizontal
represent a 5° longitude separation with the line
through the left center representing the longitude
center of the unpulsed forcing. The vertical axis
represents time, increasing upward. The tic marks
along the vertical axis represent 12-hour intervals.
The contour interval is 50 $m^2 s^{-2}$ with dashed lines
representing negative values.
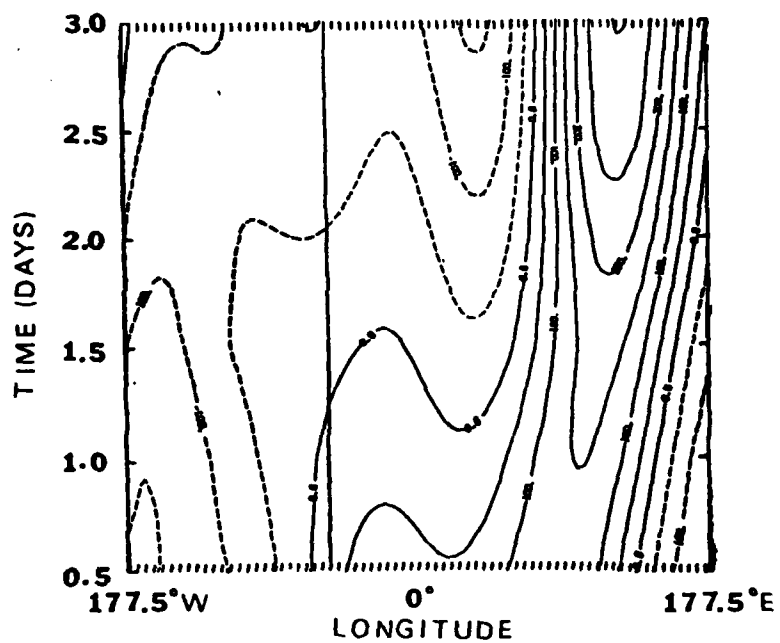
Figure 114. Same as 113 but for 24.5 to 27 day pulsed geopotential (Φ_{1-3}) field.
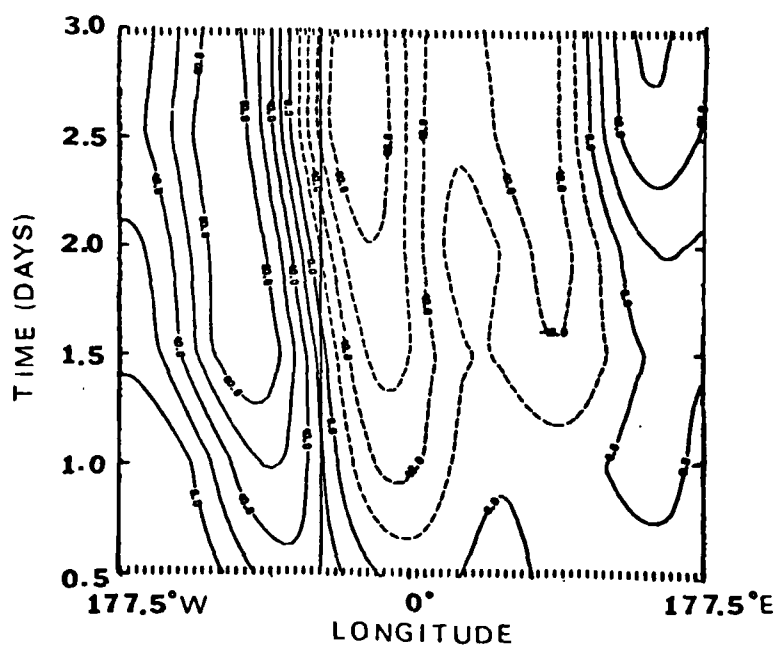
Figure 115. Same as 113 but for 24.5 to 27 day geopotential
(Φ_{1-3}) difference (pulsed minus unpulsed).
Contour interval is 20 $m^2 s^{-2}$.
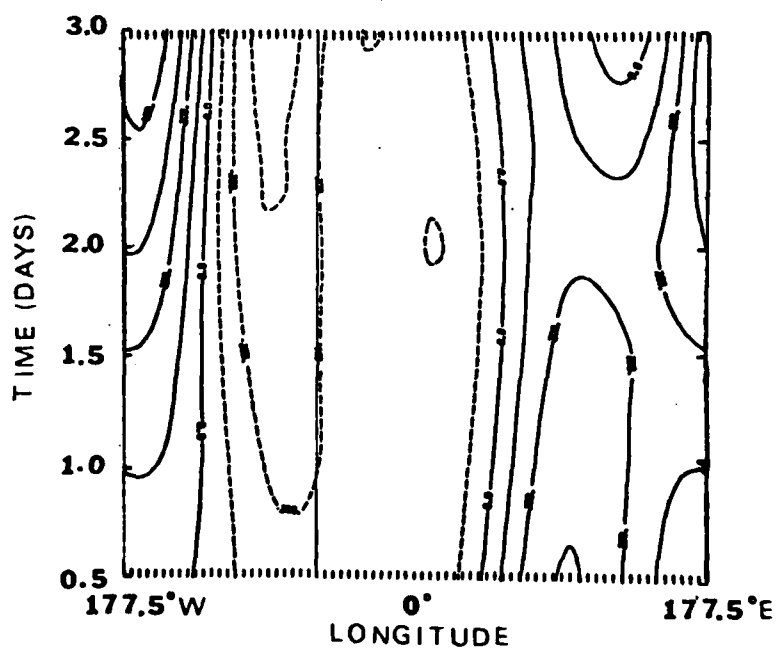
Figure 116. Same as 113 but for unpulsed geopotential (Φ_{1-3}) field at
$30^0 S$ for days 24.5 to 27. Contour interval is 100 $m^2 s^{-2}$.

Figure 117. Same as 113 except for pulsed geopotential (Φ_{1-3}) field at 30°S for days 24.5 to 27. Contour interval is 90 m^2s^{-2}.
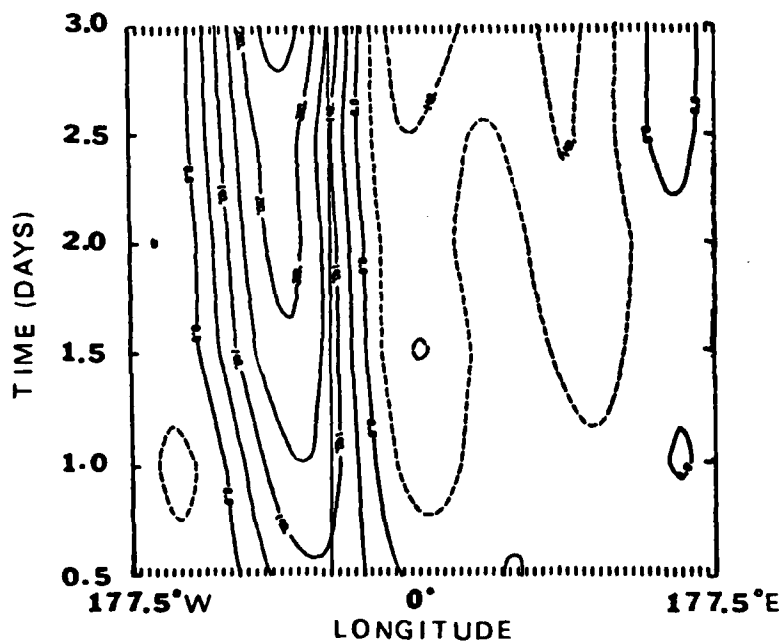
Figure 118. Same as 113 but for geopotential (Φ_{1-3}) field difference (pulsed minus unpulsed) at 30°S for days 24.5 to 27. Contour interval is 70 m^2s^{-2}.
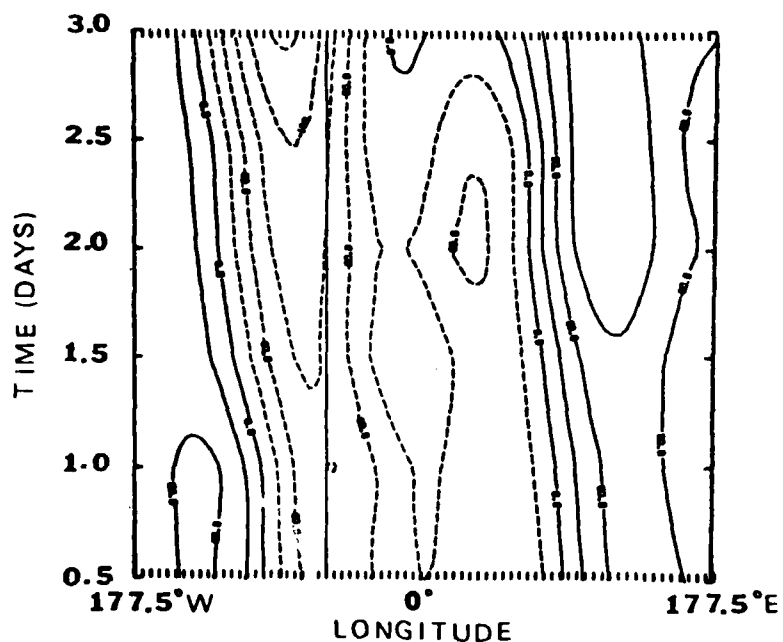
Figure 119. Same as 113 but for unpulsed geopotential (Φ_{1-3}) field
at 10°S for days 24.5 to 27. Contour interval is
40 m^2s^{-2}.
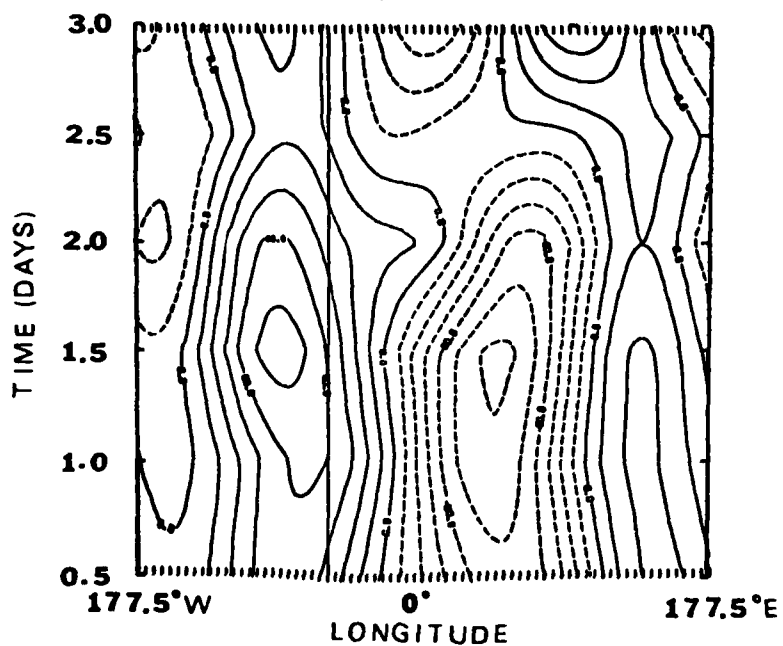
Figure 120. Same as 113 but for pulsed geopotential (Φ_{1-3}) field at
10°S for days 24.5 to 27. Contour interval is 20 m^2s^{-2}.
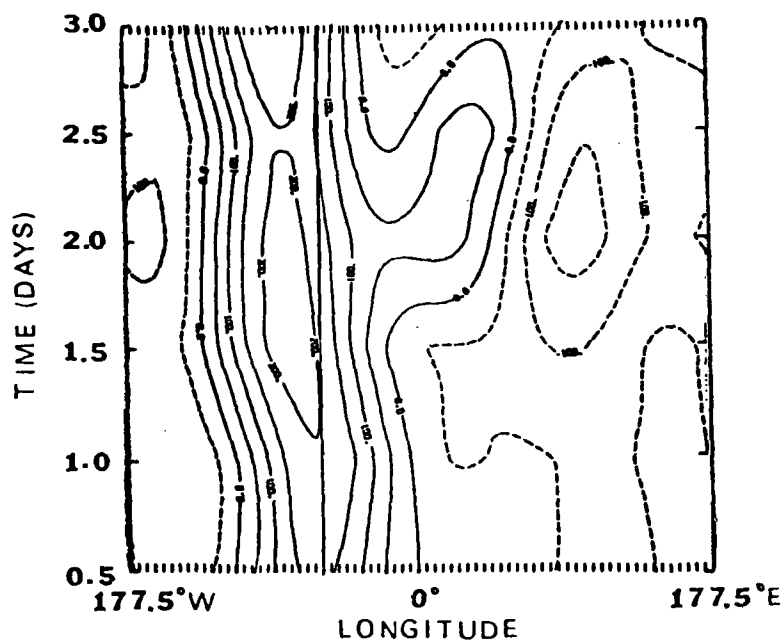
Figure 121. Same as 113 but for geopotential (Φ_{1-3}) field difference (pulsed minus unpulsed) at 10^{0}S for days 24.5 to 27. Contour interval is 50 $m^2 s^{-2}$.
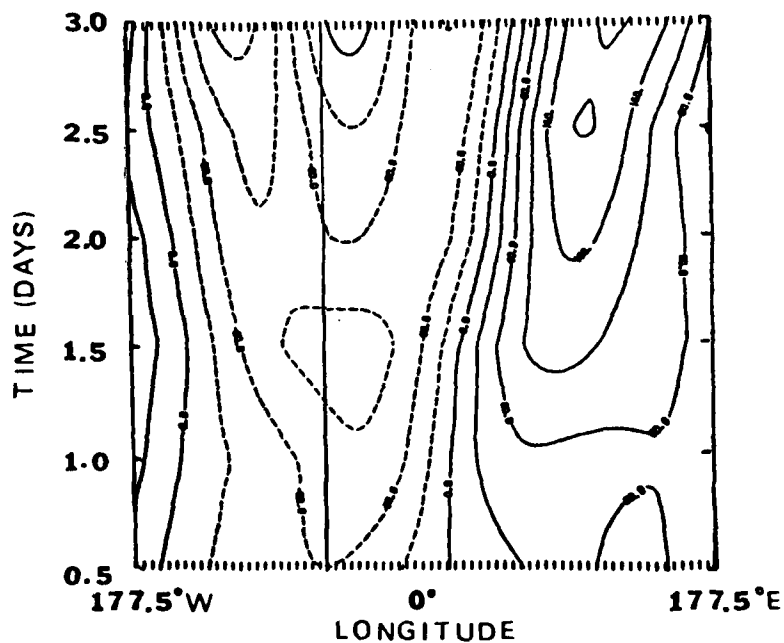
Figure 122. Same as 113 but for unpulsed geopotential (Φ_{1-3}) field at $10\,^{0}$N for days 24.5 to 27. Contour interval is 40 $m^2 s^{-2}$.
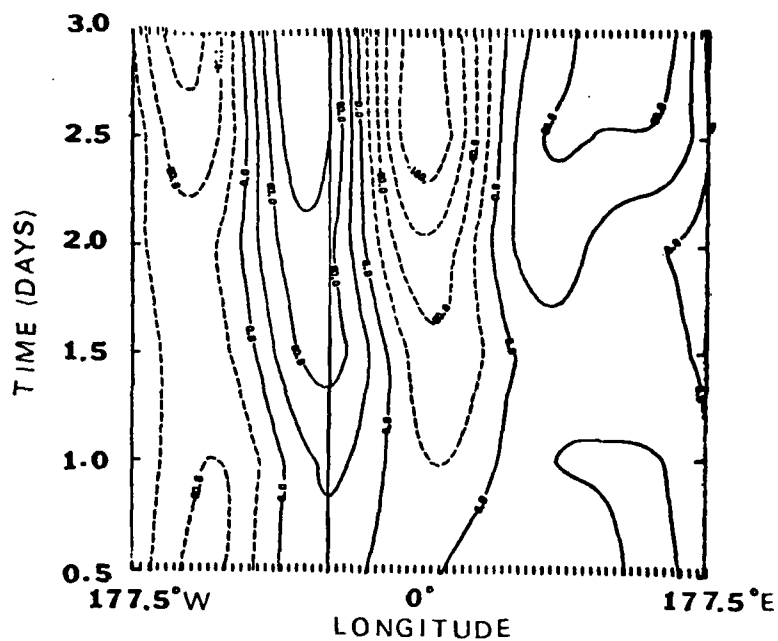
Figure 123. Same as 113 but for pulsed geopotential (Φ_{1-3}) field at 10^0N for days 24.5 to 27. Contour interval is 40 $m^2 s^{-2}$.
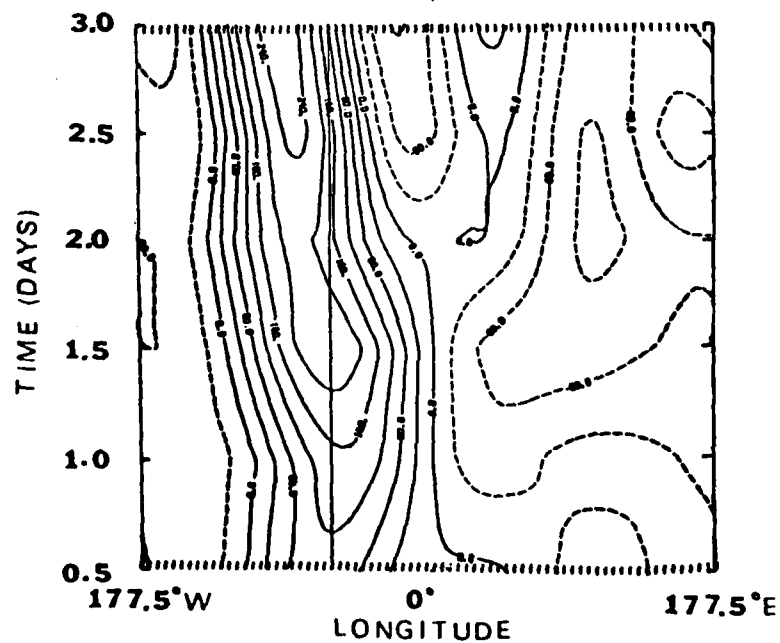
Figure 124. Same as 113 but for geopotential (Φ_{1-3}) field difference (pulsed minus unpulsed) at 10^0N for days 24.5 to 27. Contour interval is 40 $m^2 s^{-2}$.
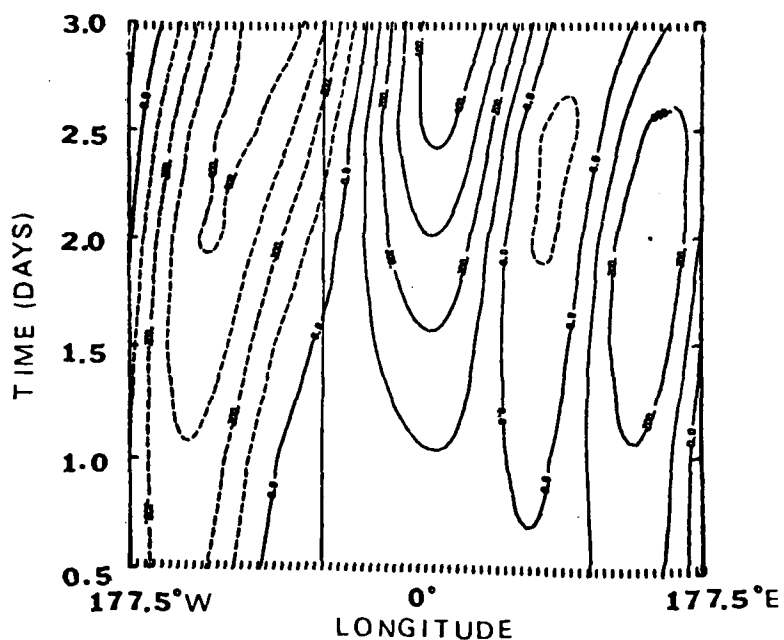
Figure 125. Same as 113 but for unpulsed geopotential (Φ_{1-3}) field at 30°N for days 24.5 to 27. Contour interval is 100 m²s⁻².
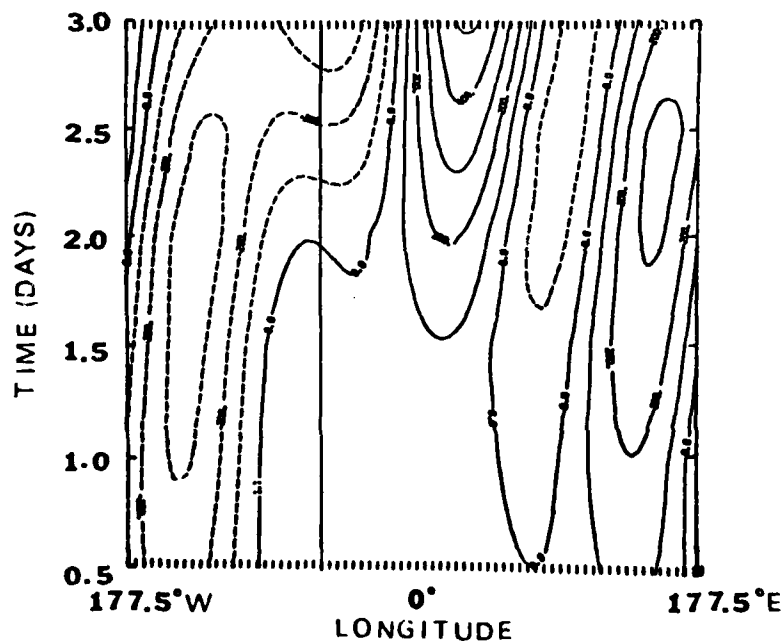
Figure 126. Same as 113 but for pulsed geopotential (Φ_{1-3}) field at 30°N for days 24.5 to 27. Contour interval is 100 m²s⁻².

138
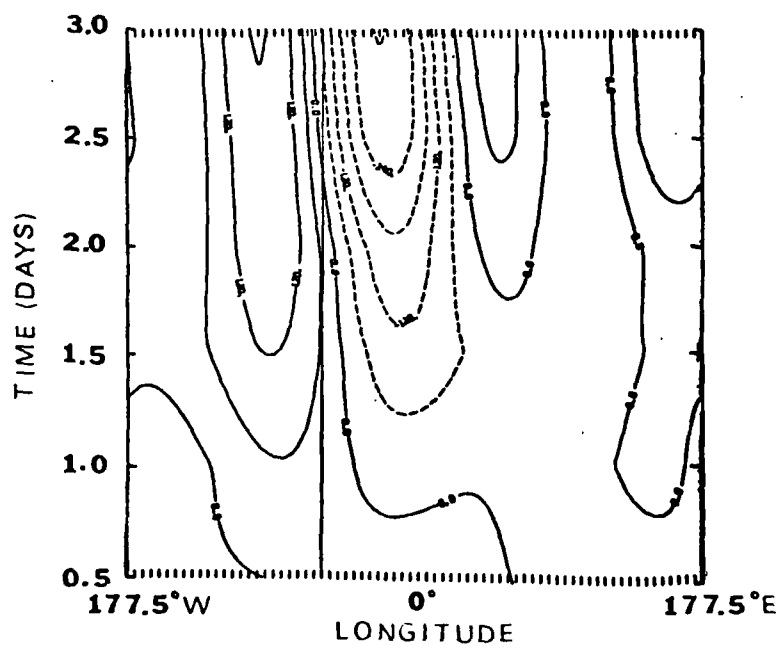
Figure 127. Same as 113 but for geopotential (Φ_{1-3}) field differ-
ence (pulsed minus unpulsed) at 30°N for days 24.5 to
27. Contour interval is 60 m^2s^{-2}.
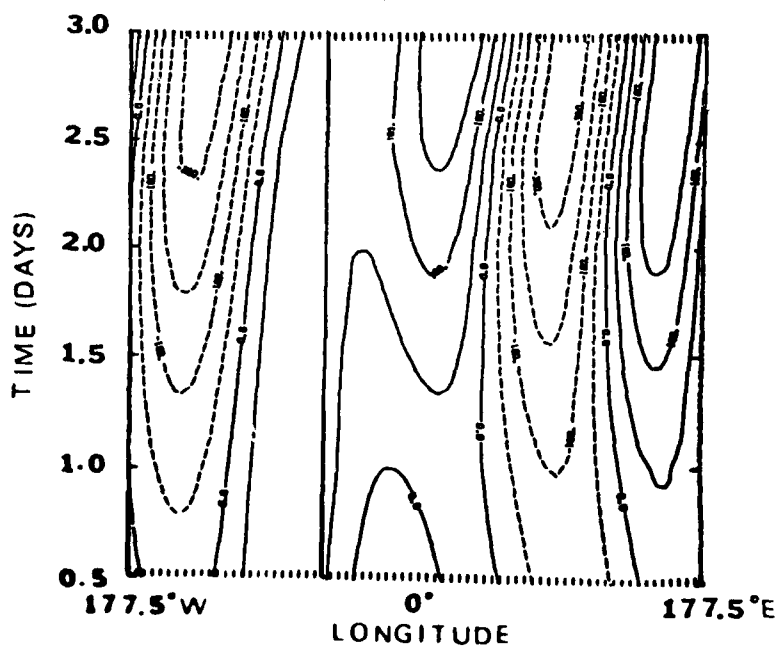
but for unpulsed geopotential (Φ_{1-3}) field at
to 27 Contour interval is 90 m^2s^{-2}.
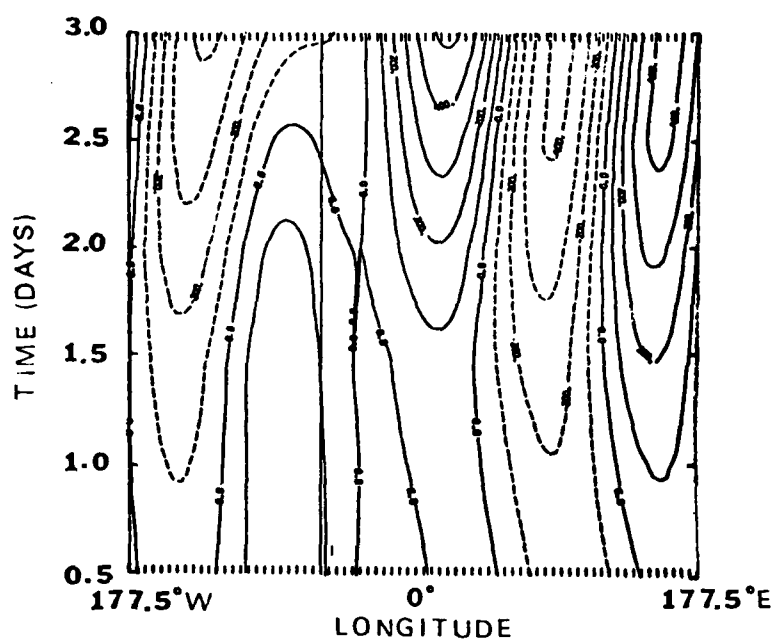
Figure 129. Same as 113 but for pulsed geopotential (Φ_{1-3}) field at 42°N for days 24.5 to 27. Contour interval is 100 $m^2 s^{-2}$.
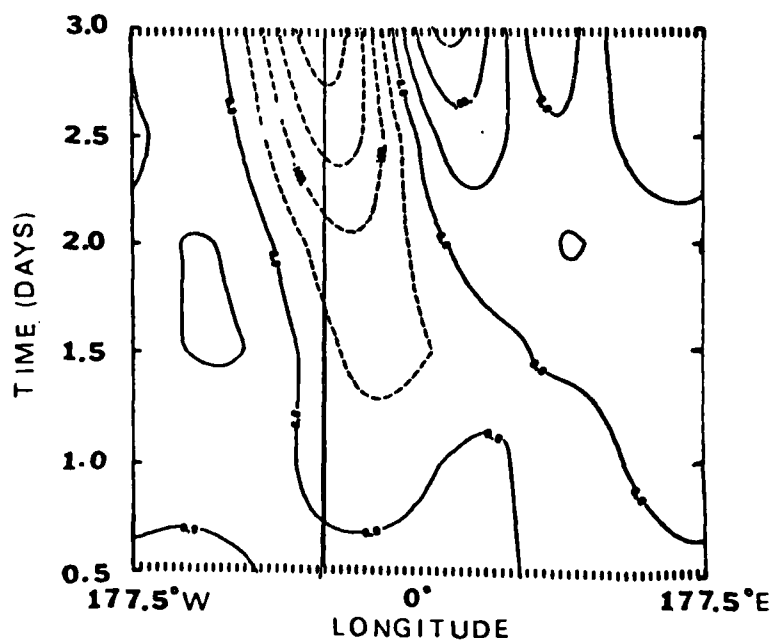
Figure 130. Same as 113 but for geopotential (Φ_{1-3}) field difference (pulsed minus unpulsed) at 42°N for days 24.5 to 27. Contour interval is 50 $m^2 s^{-2}$.
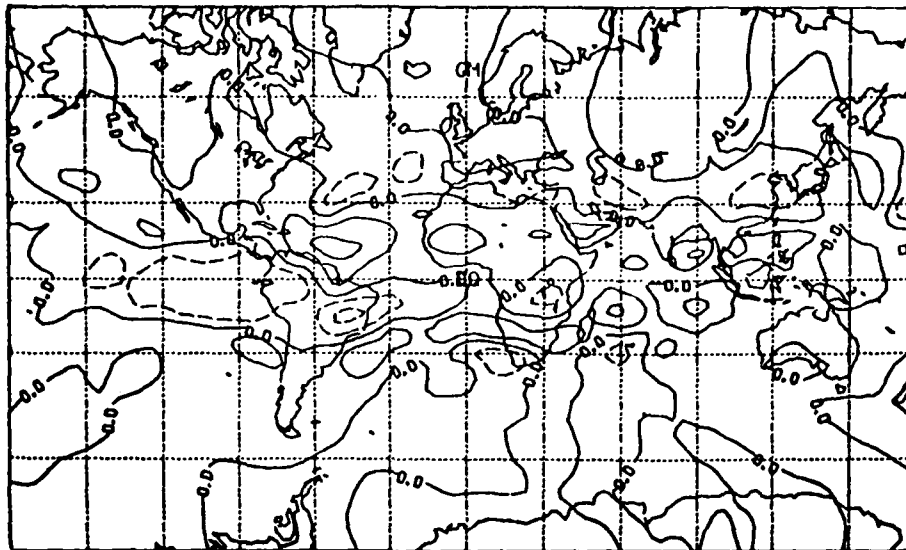
Figure 131. Two-level model no-mountain experiment 30th day 200 mb
zonal wind difference field (pulsed minus unpulsed)
(ms^{-1}). Interval is 10 ms^{-1} with negative contours
dashed.
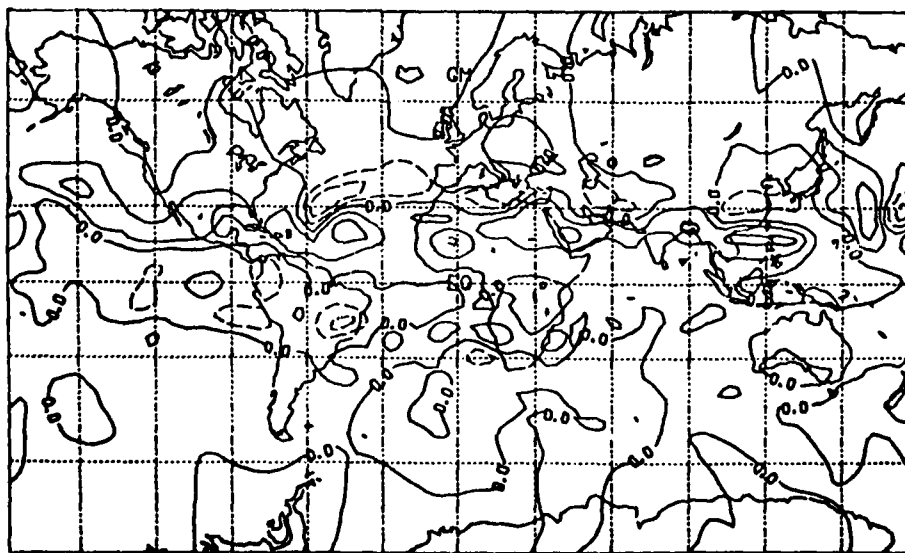
Figure 132. Two-level model no-mountain experiment 30th day 200 mb
kinetic energy difference (pulsed minus unpulsed)(m^2s^{-2}).
Contour interval is 300 m^2s^{-2} with negative contours dashed.
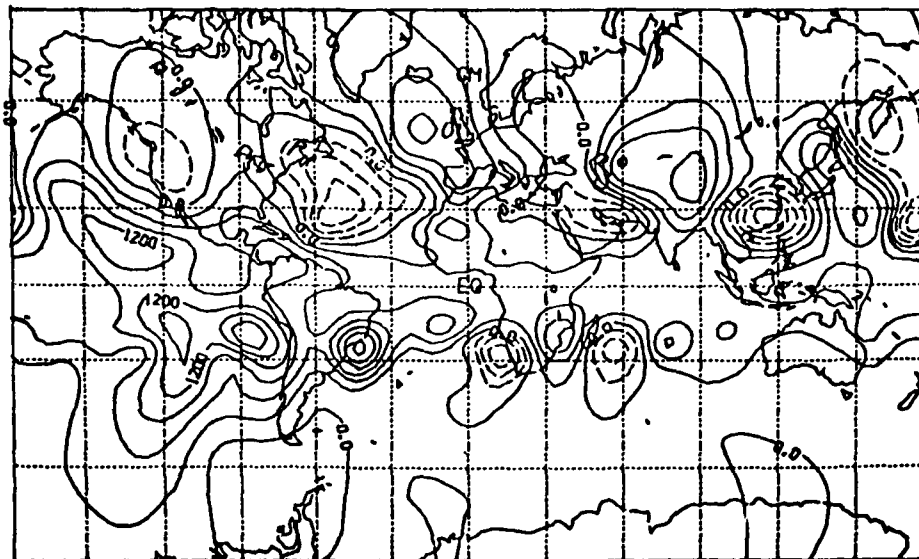
Figure 133. Two-level model no-mountain experiment 30th day 200 mb geopotential field difference (pulsed minus unpulsed) $(m^2 s^{-2})$. Contour interval is 300 $m^2 s^{-2}$ with negative contours dashed.
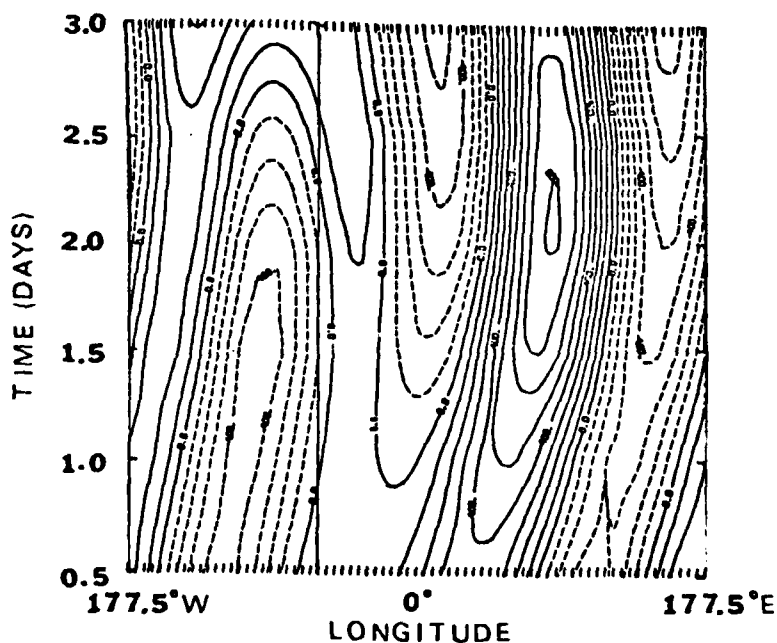
Figure 134. Same as 113 but for unpulsed geopotential (ϕ_{1-3}) field at 42°N for days 27.5 to 30. Contour interval is 100 $m^2 s^{-2}$.

expected that the present model would predict smaller than observed ultra-long wave height amplitudes. The two-level model's coarse vertical resolution probably leads to the rest of the amplitude discrepancies. The ratio of the different fields to the actual amplitude fields for the pulsed and unpulsed cases at a given latitude is perhaps a better measure of model sensitivity than the actual amplitude in the ultra-long waves. As previously stated, if this ratio nears 30%, then the change in the model ultra-long wave structure due to tropical heatings is significant.

There is a substantial change ($\geq$ 26%) in the amplitudes of the 200 mb ultra-long waves at all of the given latitudes of Figures 113 to 130. The percent change at each latitude along with the maximum amplitudes in the pulsed and unpulsed cases are given in Table III. The actual changes in the ultra-long wave pattern seem to lie mainly in the longitude belt where the pulse and unpulse are applied. But by the time the change in the 200 mb ultra-long wave height field reached 42^oN it has been displaced to the east (probably due to the coriolis effect) by about 40° longitude. At 42^oN there is a stronger ultra-long wave trough in the pulsed case than in the unpulsed case near 65^oW with a stronger ultra-long wave ridge for the pulsed case downstream at about 15^oE.

The difference fields between the pulsed and unpulsed cases after the sixth day of steady forcing (30th day of integration) for the 200 mb zonal wind component, the 200 mb kinetic energy, and the 200 mb geopotential are given in Figures 131 - 133. These difference fields represent the overall changes in the structure of the

TABLE III

The actual maximum ultra-long wave 200 mb height amplitudes with the percent change in the amplitudes due to the "pulsed" and "unpulsed" forcing in the absence of mountains.

Latitude	Maximum "pulsed" amplitude (m^2/sec^2)	Maximum "unpulsed" amplitude (m^2/sec^2)	Maximum Difference (m^2/sec^2)	% Change
42°S	300	250	80	26%
30°S	360	400	350	88%
10°S	120	200	200	100%
10°N	160	200	240	>100%
30°N	500	400	300	60%
42°N	500	360	200	40%

upper layer of the two-level model that are induced as a consequence of localized tropical heating differences that have existed for a six-day period. By the sixth day of the test, there are substantial changes in the 200 mb zonal wind component (Figure 131) throughout the entire substropical region (both northern and southern hemispheres). To the north of the pulsed and unpulsed region there is a 25 ms^{-1} difference (pulsed minus unpulsed) in the 200 mb zonal wind located at 55W, 14N.

The sixth day 200 mb kinetic energy difference field (Figure 132) shows that the main kinetic energy differences no longer lie poleward of the pulsed and unpulsed regions as was the case at the end of the 27th day (Figure 106). The kinetic energy has been distributed (probably by the baroclinic waves through the β effect)

throughout the northern hemisphere subtropical region. After six days, the energy due to a very active single monsoon scale convectively heated region is felt throughout the subtropical regions of both hemispheres.

The geopotential difference field (Figure 133) at the end of the sixth day also shows that the changes due to the steady pulsed and unpulsed disturbances has been spread over a wide area. The Hovmöller diagrams for the 200 mb pulsed, unpulsed and difference fields at 42^ON (Figures 134 - 136) are included in order to show the differences in the midlatitude ultra-long wave structure of the winter hemisphere that can occur from a strongly heated and weakly heated local tropical area. After six days of integration, the percent change in the amplitude of the ultra-long waves is almost 50% of the total amplitude. This change is definitely significant.

Finally, it appears from these experiments, that the subtropical and midlatitude ultra-long waves of both hemispheres can be substantially impacted by changes in local large scale tropical heating areas. In the next two subsections, the effects of various tropical heating profiles in the presence of mountains for the NHW and SHW cases are studied.

5.5 Experiment 2, NHW Forcing with Mountains

This experiment consists of two parts. The first part is a 25-day integration of the model with variable tropical heating in the presence of mountains. Along with the long-term integration, several other shorter term (3-6 day) pulsed and unpulsed experiments were also carried out.
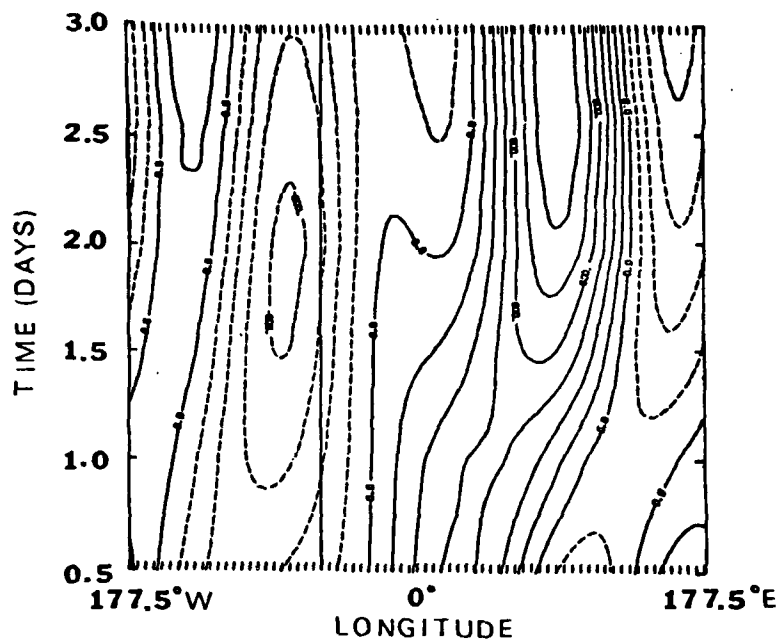
Figure 135.   Same as 113 but for pulsed geopotential (Φ_{1-3}) field at 42°N for days 27.5 to 30.   Contour interval of 200 m^2s^{-2}.
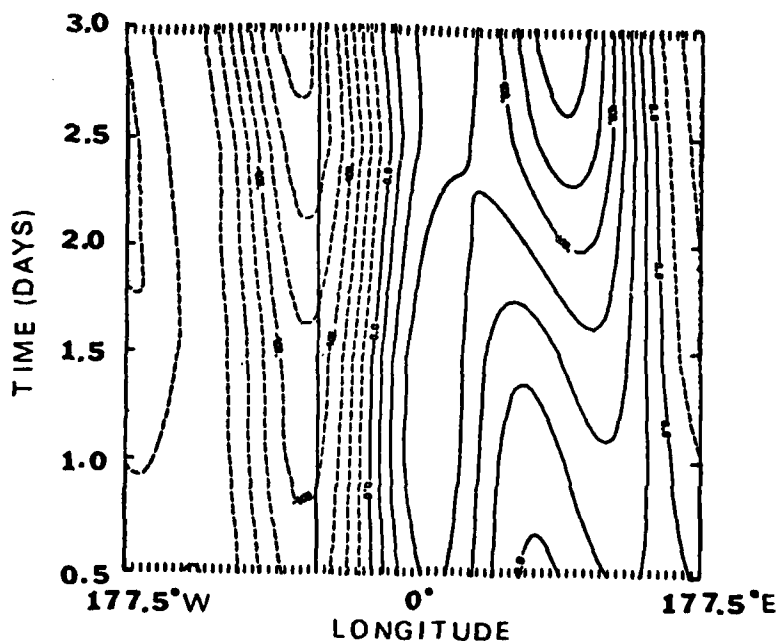
Figure 136.   Same as 113 but for geopotential (Φ_{1-3}) field difference (pulsed minus unpulsed) at 42°N for days 27.5 to 30. Contour interval is 100 m^2s^{-2}.

The second part also includes mountains and utilizes the same zonal average heating as the first part, but with no tropical variability. This case is designed to test the long term flow sensitivity to variability in the tropical heating.

5.5.1 Longitudinally variable tropical heating

The first case utilizes the diabatic forcing functions Q_1 and Q_3 given in Figures 137 and 138. These forcing functions were derived using the techniques given in Section 5.2 with r taken from Table I and $\alpha=1$. A value of $\alpha=1$ implies the full variability in the tropical heating pattern as deduced from the mean precipitation fields of Shutz and Gates (1972).

A similar case with $\alpha=\frac{1}{2}$ and mountains was also carried out. The results of this case were very similar to the $\alpha=1$ case and are not presented here.

Figure 139 shows the terrain field, Z_s, used for all the mountain integrations. This terrain field is also utilized by the 4° latitude by 5° longitude GISS GCM from 60^OS and 60^ON. Poleward of 60^OS and 60^ON, the terrain values were set to zero. This was done to avoid any possible problems due to high terrain (Antarctica and Greenland) near the poles.

The model is initialized for all cases with the atmosphere at rest and a constant temperature of 230^OK for the upper level. The lower level temperature was constrained to insure that the finite difference approximation to the static stability (Eq. 59) had the same initial value ($S = -.062^O$K mb^{-1}). To accomplish this, Eq. (59) was solved for T_3.
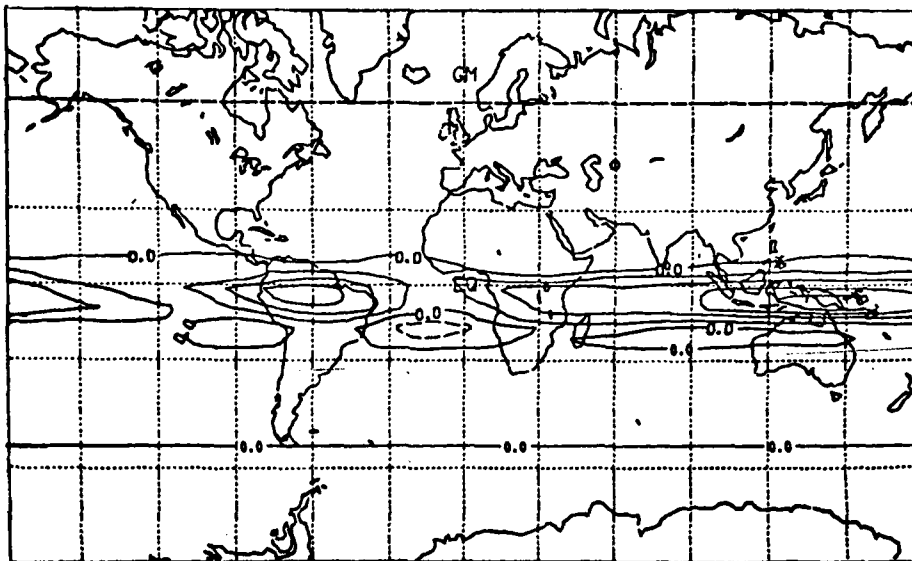
Figure 137. NHW total diabatic forcing function (Q) for upper level with α=1. Isolines every $1^{o}K$ day^{-1}. Contour labels scaled by 10.
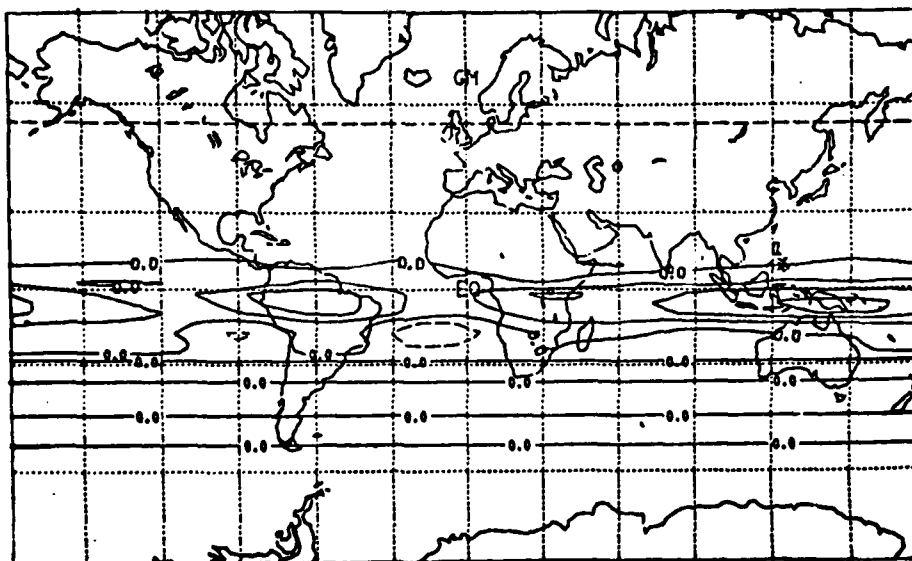
Figure 138. NHW total diabatic forcing function (Q) for lower level with α=1. Isolines $1^{o}K$ day^{-1}. Contour labels scaled by 10.

148
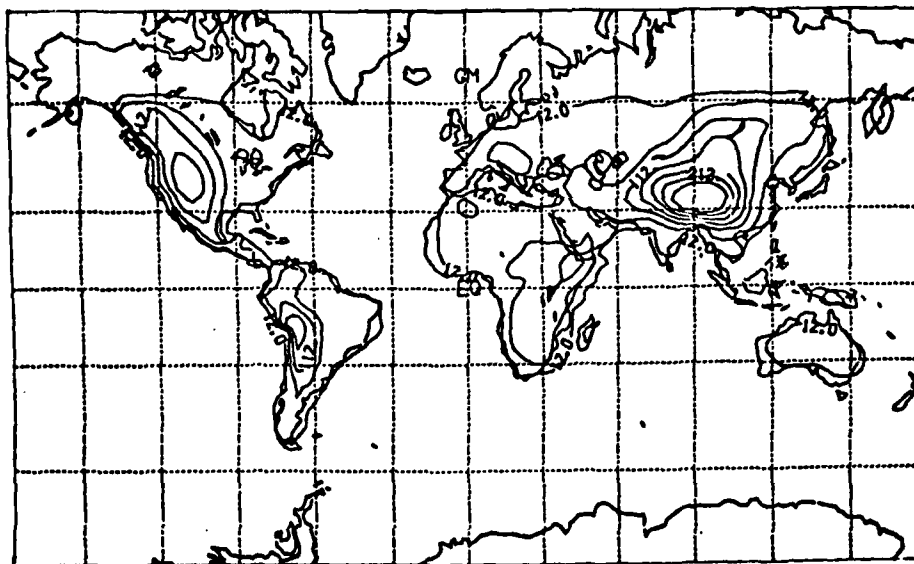
Figure 139. Actual terrain heights used for mountain integrations of two-level model (dm). Contour interval is 50 dm.
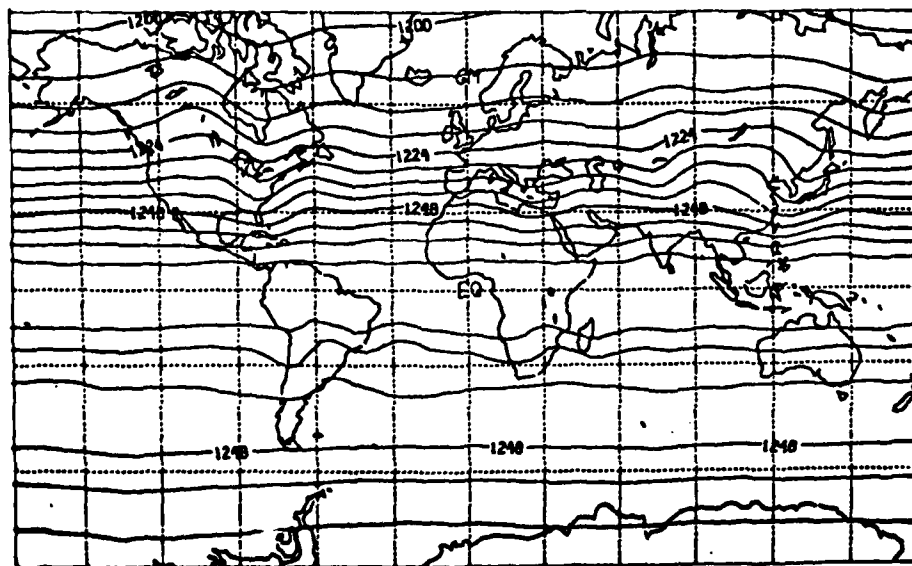
Figure 140. Two-level model, mountain NHW variable tropical heating experiment 200 mb 10.5 day height field (dm). Contour interval is 6 dm.

$$T_3 = T_1 \frac{(1+E)}{1-E} + S \frac{P_3-P_1}{1-E} \tag{60}$$

where S = -.062 and

$$E = (P_3-P_1)R / (2 \bar{P}_2 c_p) . \tag{61}$$

The initial value surface pressure, P_s, was computed from the hydrostatic equation assuming a mean temperature of 285^oK for the temperature between the lower level and the surface (Eq. (62) below).

$$P_s = P_0 e^{-(\Phi_s-\Phi_0)/R\bar{T}} \tag{62}$$

where P_0 = 1000 mb, T = 285° and Φ_0 = (111 m) g.

The results of a longitudinally variable tropical heating NHW ^5-day integration will be presented first. These will then be compared to the results from the 25-day NHW integration using no longitudinally variable heating. Finally, the short term effect on the ultra-long waves of pulsing or unpulsing the tropical longitudinally variable heating pattern will be discussed.

The zonally uniform flow pattern that existed in the 30-day, no mountain experiment (previous subsection) until the onset of baroclinically unstable waves (day 24) is not visible in any of the mountain experiments. As can be seen from the 10.5 day height field (Figure 140) for the longitudinally variable tropical heating, the mountains of both hemispheres force definite waves in the flow.

By the 17th day of integration in the variable tropical heating case, baroclinically unstable waves appear to be growing at the expense of the mean flow. Thus, the 17th day 200-mb height field

(Figure 141) contains transient waves.

At day 23, the 200 mb height field (Figure 142) shows three distinct high amplitude ridges at higher latitudes with several shorter waves visible in midlatitudes and subtropics. There are several subtropical type jets in both hemispheres visible in the 23rd day 200 mb zonal wind field (Figure 143) and 200 mb kinetic energy field (Figure 144). Comparing the 23rd day 200 mb kinetic energy field (Figure 144) and the diabatic forcing function (Figure 137) the areas of maximum kinetic energy in the northern hemisphere seem to be north of and slightly downstream of the maximum areas of tropical heating and also downstream of the two major mountain ranges.

To better determine the areas of highest short term average 200 mb zonal wind, a five-day average from days 20 to 25 (over ten 12-hour periods) was computed (Figure 145). The six-wave pattern visible in the 200 mb subtropical jet of the first experiment (Figure 86) has been replaced by a definite two or weaker three-wave pattern in the average 200 mb flow fields for this experiment. The strongest 200 mb northern hemisphere jet is southeast of Japan and near $26^{o}N$. This jet is slightly to the south and displaced by about 30° to the east of the 200 mb zonal average wind fields of Figure 10 and Plate 3.19 of Newell et al. (1972). The next strongest five-day average 200 mb jet is located north of the Amazon basin and is slightly to the south and downstream of the 200 mb average jet position given in Newell et al. (1972).

There is another area of stronger 200 mb westerly flow from
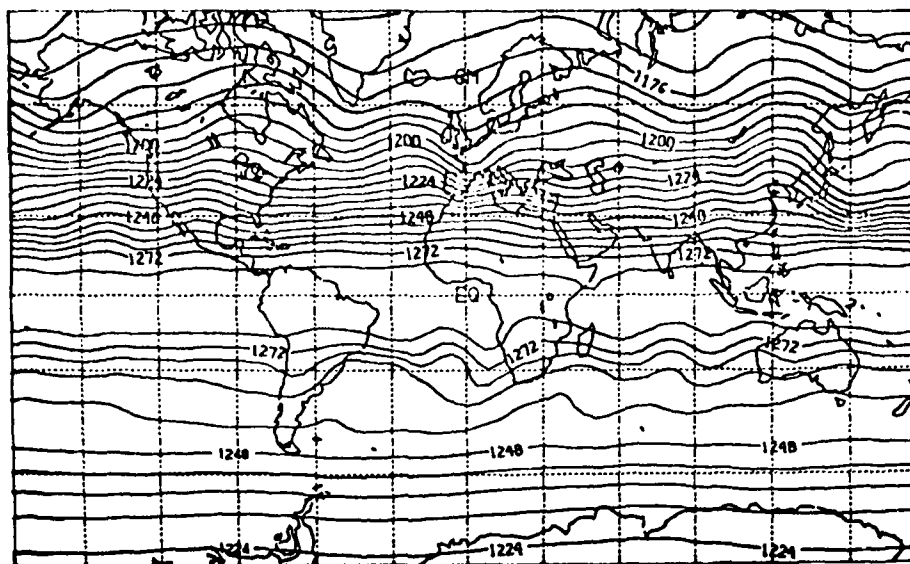
Figure 141. Two-level model, mountain NHW variable tropical heating experiment 200 mb 17th day height field (dm). Contour interval of 6 dm.
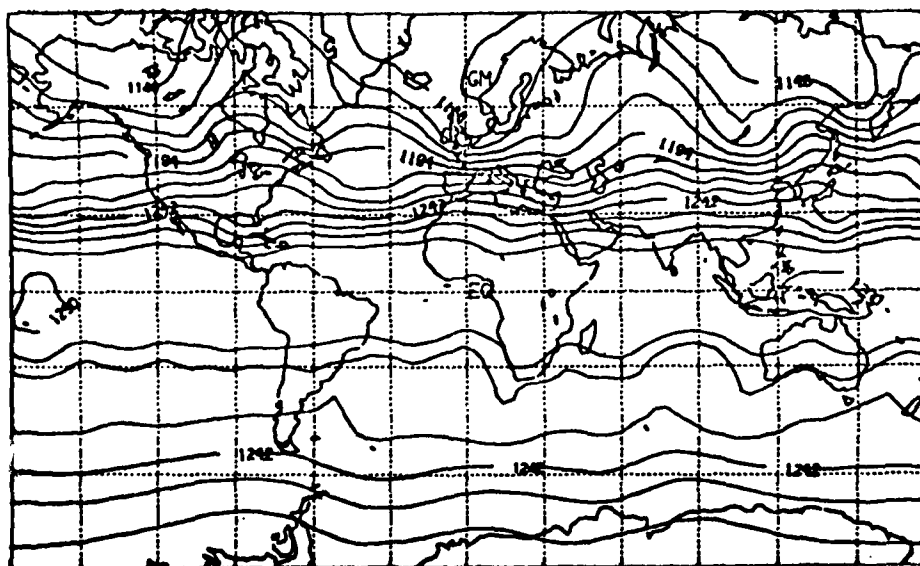
Figure 142. Two-level model, mountain NHW variable tropical heating experiment 200 mb 23rd day height field (dm). Contour interval is 12 dm.
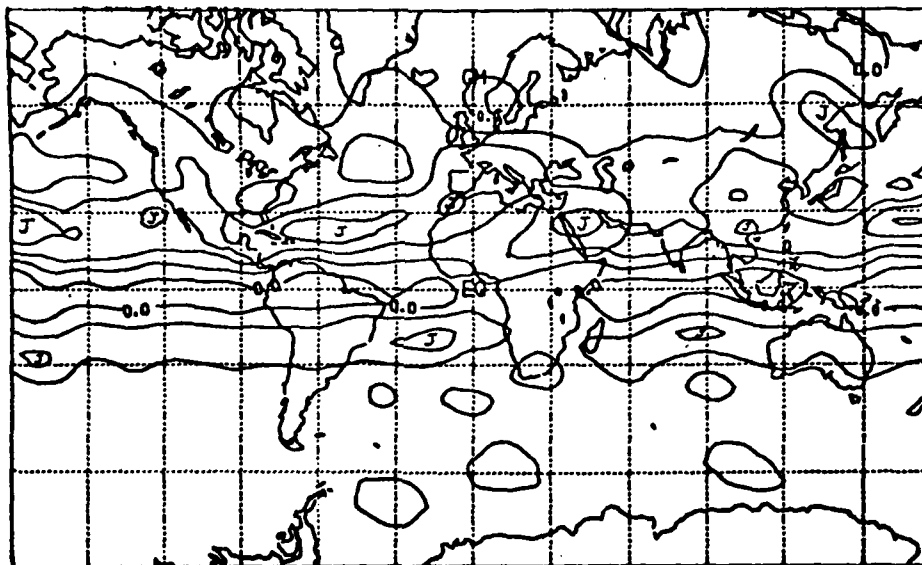
Figure 143. Two-level model, mountain NHW variable tropical heating experiment 200 mb 23rd day zonal wind component (ms^{-1}). Contour interval is 15 ms^{-1}.
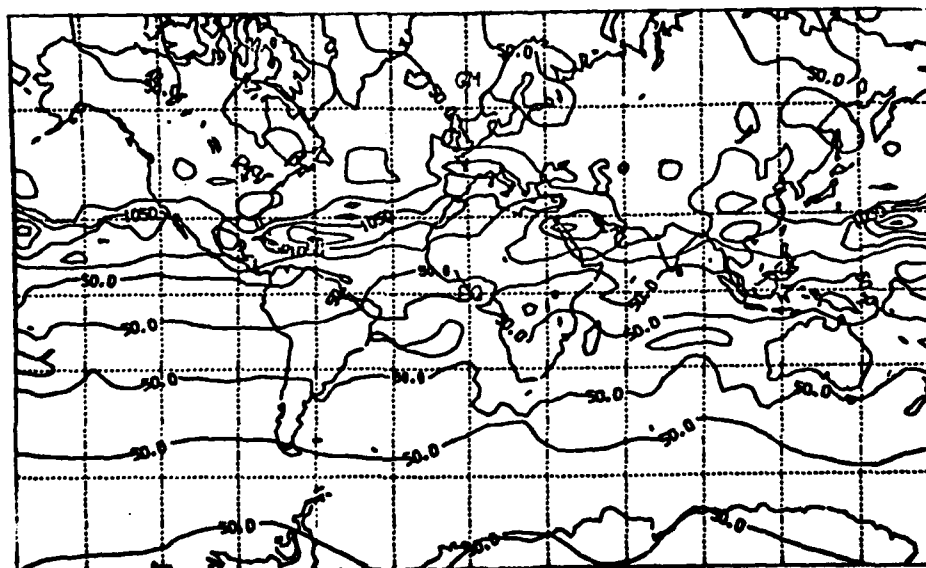
Figure 144. Two-level model, mountain NHW variable tropical heating experiment 200 mb 23rd day kinetic energy (m^2s^{-2}). Contour interval of 500 m^2s^{-2}.

Figure 145. Two-level model, mountain NHW variable tropical heating experiment 200 mb 5-day average (days 20-25) zonal wind component (ms^{-1}). Contour interval of 10 ms^{-1} with negative contours dashed.

Figure 146. Two-level model, mountain NHW variable tropical heating experiment 200 mb 25th day height field (dm). Contour interval is 12 dm.

eastern Africa to the Asian coast which is displaced slightly to the east of the comparable area given in Newell et al. (1972).

The 200 mb five-day average tropical easterlies are in a more narrow equatorial band than in the longer term average data set of Newell et al. (1972) and of Figure 10 of this study. The southern hemisphere five-day average 200 mb zonal wind field is quite zonal in nature with weaker jet maxima than in the northern hemisphere. These jets are much closer to the equator but located in almost the same longitudinal belts as the 200 mb average zonal wind field given in Figure 10.

Overall, the short term average zonal wind field produced from the simplified longitudinally variable tropical forcing function in the presence of mountains is much more realistic than the wind field produced with a similar forcing function but in the absence of mountains (Figure 86). Thus, a tentative conclusion based on these two-level model results is that mountains play an important role in determining the positioning of the 200 mb subtropical jet streams.

In a recent study by Grose and Hoskins (1979) smoothed terrain features in a steady state linearized version of the shallow water equations linearized about the observed 200 mb flow on the spherical earth were found to produce realistic large scale flow patterns. Thus, the present results are not surprising.

For completeness, the 25th day 200 mb height field (Figure 146) and the 25th day 200 mb meridional velocity component (Figure 147) are given. These figures show both midlatitude and subtropical wave activity whose strength appears to be within the realm of real
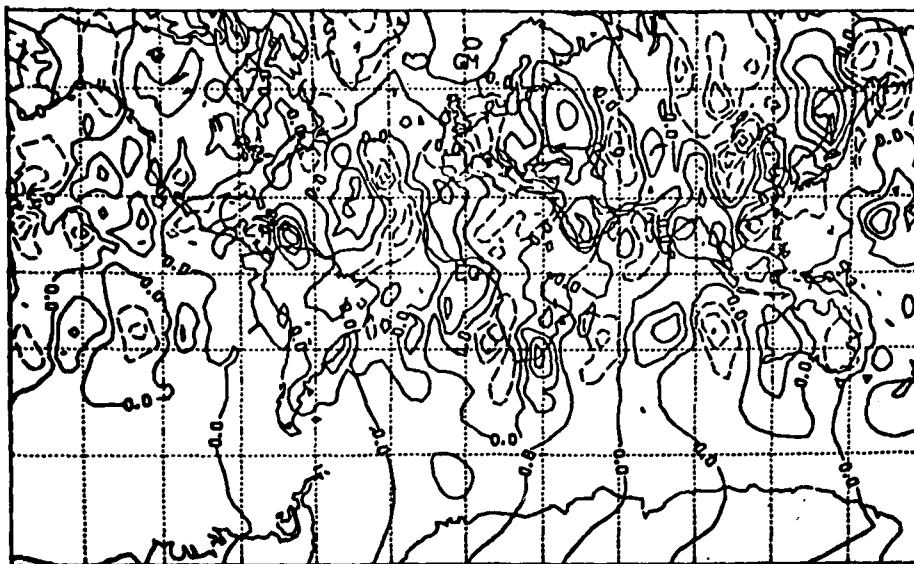
Figure 147. Two-level model, mountain NHW variable tropical heating experiment 200 mb 25th day meridional velocity component (ms^{-1}). Contour interval is 10 ms^{-1} with negative contours dashed.
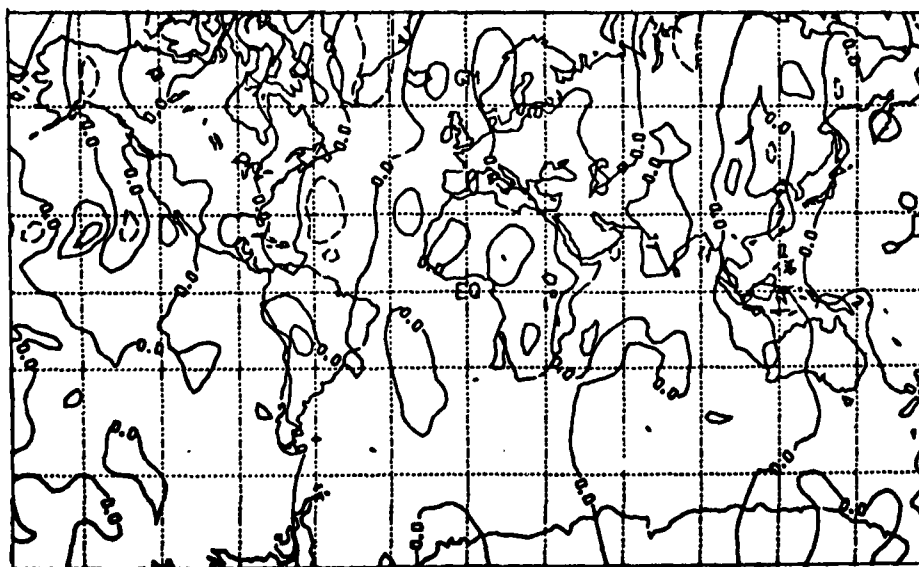
Figure 148. Two-level model, mountain NHW variable tropical heating experiment 200 mb 20th day zonal divergent wind component (ms^{-1}). Contour interval is 2 ms^{-1} with negative contours dashed.

atmospheric data.

As noted in the first experiment, the divergent wind fields come into a rapid steady state with the tropical forcing. The 200 mb zonal (Figure 148) and meridional (Figure 149) divergent wind fields for day 20 are fairly representative of the divergent wind fields in the deep tropics for the entire integration with the exception that the divergent flows that appear coupled with the baroclinic waves propagate along with the waves. An example of a deep tropical divergent outflow that appears coupled with the baroclinic wave activity can be seen in Figure (149) near 150°W and 15°N.

The zonal mean divergent wind for days 20 and 23 are given in Table IV. The magnitude of the Hadley cell does appear to be similar to the no-mountain integration (Table II) and, as previously noted, smaller than the observed values given in Newell et al. (1972). The northern extent of the Hadley cell and the Ferrel cell circulation appear to exist further north in the mountain case (Table IV). This is more realistic when compared to observed values.

5.5.2 Longitudinally uniform tropical heating

To better determine the role of longitudinally variable tropical heating in the presence of mountains, another 25-day integration was performed with the zonal average forcing function given in Figure 75. This case was identical to the one just reported in all other respects except that the longitudinally variable part of the forcing is removed. The mountain case with longitudinally variable tropical heating will be referred to as (MV) and the mountain case with no longitudinal variability in the heating will be referred to as (NV).
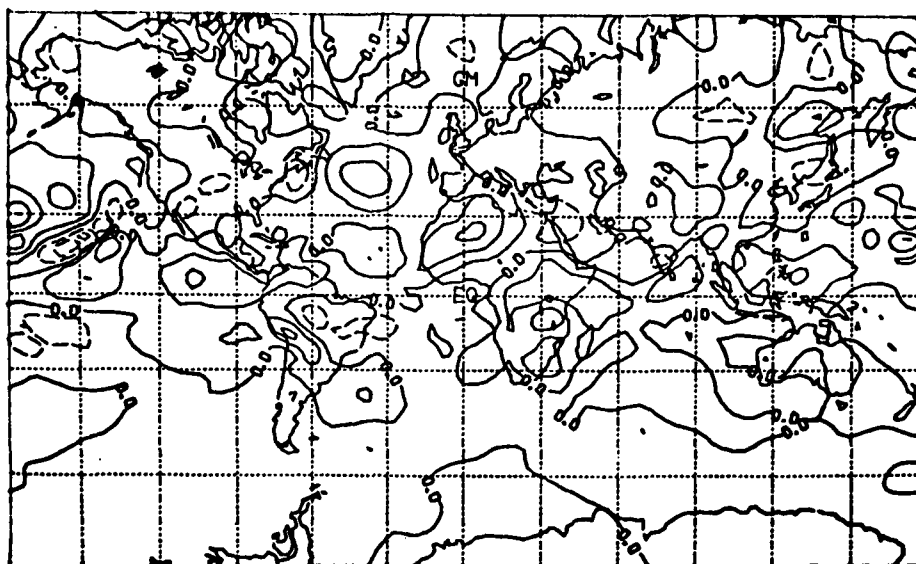
Figure 149. Two-level model, mountain NHW variable tropical heating
experiment 200 mb 20th day meridional divergent wind
component (ms^{-1}). Contour interval is 1 ms^{-1} with nega-
tive contours dashed.
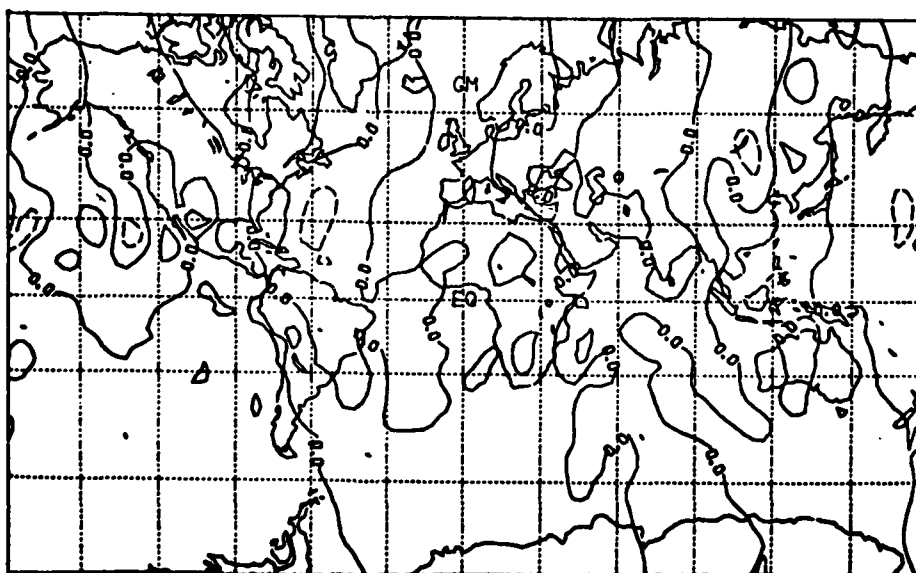
Figure 150. Two-level model, mountain NHW uniform tropical heating
experiment 200 mb 20th day zonal divergent wind compo-
nent (ms^{-1}). Contour interval is 2 ms^{-1} with negative
contours dashed.

TABLE IV

The zonal average meridional velocity component, mountain case

Latitude	Day 20		Day 30	
	200 mb	~700 mb	200 mb	~700 mb
84N	-0.0	0.0	0.1	-0.0
80N	0.1	-0.1	0.3	-0.1
76N	0.2	-0.1	0.3	-0.1
72N	0.1	-0.1	0.2	-0.0
68N	-0.0	0.0	0.1	-0.0
64N	-0.0	0.0	0.2	-0.1
60N	-0.2	0.1	0.2	-0.0
56N	-0.3	0.2	-0.0	0.1
52N	-0.3	0.2	-0.1	0.1
48N	-0.1	0.1	-0.0	0.0
44N	-0.1	0.1	-0.1	-0.0
40N	0.0	0.2	-0.1	0.2
36N	0.2	0.2	0.1	0.2
32N	0.1	0.1	0.2	0.2
28N	0.2	-0.1	0.1	0.1
24N	0.1	-0.0	0.3	-0.2
20N	0.2	-0.0	0.4	-0.2
16N	0.2	-0.1	0.6	-0.3
12N	0.5	-0.2	0.8	-0.5
8N	0.7	-0.4	1.0	-0.6
4N	0.7	-0.4	1.0	-0.7
0	0.5	-0.2	0.9	-0.6
4S	0.1	0.0	0.6	-0.5
8S	-0.3	0.2	0.2	-0.2
12S	-0.7	0.5	-0.0	-0.1
16S	-0.5	0.3	-0.0	-0.0
20S	-0.3	0.0	0.3	-0.4
24S	-0.3	0.1	0.3	-0.3
28S	-0.2	0.1	0.3	-0.4
32S	-0.2	0.1	0.1	-0.2
36S	-0.1	0.1	0.0	-0.0
40S	-0.1	0.1	-0.1	0.0
44S	-0.0	0.0	-0.0	0.0
48S	-0.1	0.0	-0.0	-0.0
52S	-0.1	0.1	-0.0	0.0
56S	-0.2	0.1	-0.0	0.0
60S	-0.2	0.1	-0.0	0.0
64S	-0.1	0.0	-0.0	0.0
68S	-0.2	0.1	-0.0	0.0
72S	-0.2	0.1	-0.0	0.0
76S	-0.2	0.1	0.1	-0.0
80S	-0.3	0.1	0.1	-0.0
84S	-0.1	0.1	-0.0	0.0

The 20-day 200 mb zonal (Figure 150) and meridional (Figure 151)
divergent wind components for the NV case are very similar to the
divergent winds from the MV case. The only difference is that the
divergent flows in the MV case are slightly larger (.5 to 1 ms^{-1}) in
the areas of greater relative heating.

The 20 to 25-day 200 mb zonal wind component (Figure 152) seems
to show a three-wave pattern in the jet stream. There are two
stronger jets of almost equal magnitude (~50 ms^{-1}) located to the
north of the Amazon basin and near the international date line. Two
weaker areas of just over 40 ms^{-1} exist across northern Africa and
over India.

Comparing Figure 145 (MV five-day average zonal wind) with
Figure 152 (NV five-day average zonal wind), the two figures appear
quite similar. The 200 mb jet north of Australia and associated
with the strongest heating in the MV case appears to be about 10°
longitude closer to the observed jet position of Newell et al. (1972)
than the corresponding jet in the NV case. This jet also appears to
be 10 to 20 ms^{-1} stronger in the MV case.

To better ascertain the differences in the 200 mb subtropical
jet patterns, the difference field (Figure 153) at day 25 was com-
puted between the MV and NV 200 mb zonal wind fields. As can be seen
from the difference field, the subtropical jets appear to be closer
to the equator for the MV case. The main areas of difference occur
where the heating is most variable. Overall, the differences are
substantial, with the maximum differences being about 30 ms^{-1} (approx-
imately 40% of the total magnitude). The 200 mb kinetic energy
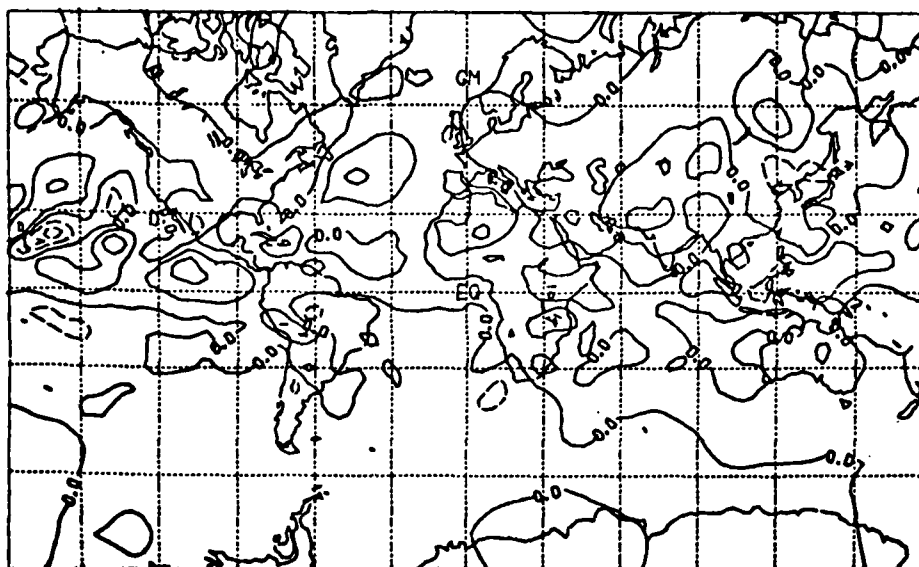
Figure 151. Two-level model, mountain NHW uniform tropical heating experiment 200 mb 20th day meridional divergent wind component (ms^{-1}). Contour interval is 1 ms^{-1} with negative contours dashed.
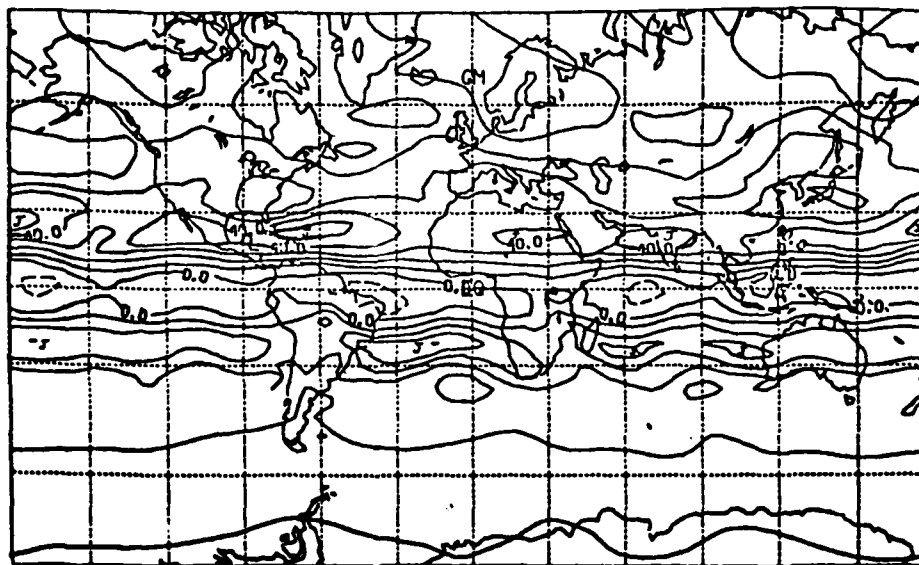
Figure 152. Two-level model, mountain NHW uniform tropical heating experiment 200 mb 5-day average (days 20-25) zonal wind component (ms^{-1}). Contour interval of 10 ms^{-1} with negative contours dashed.
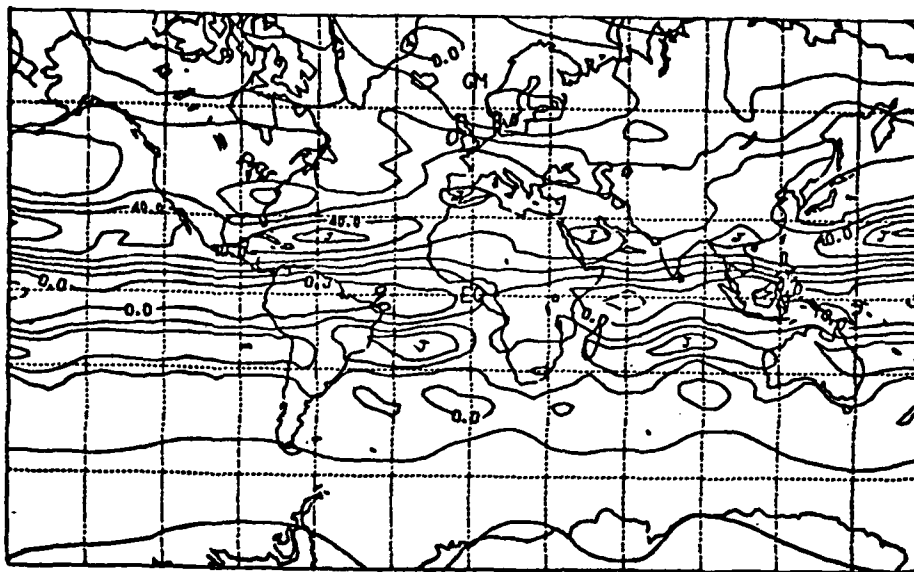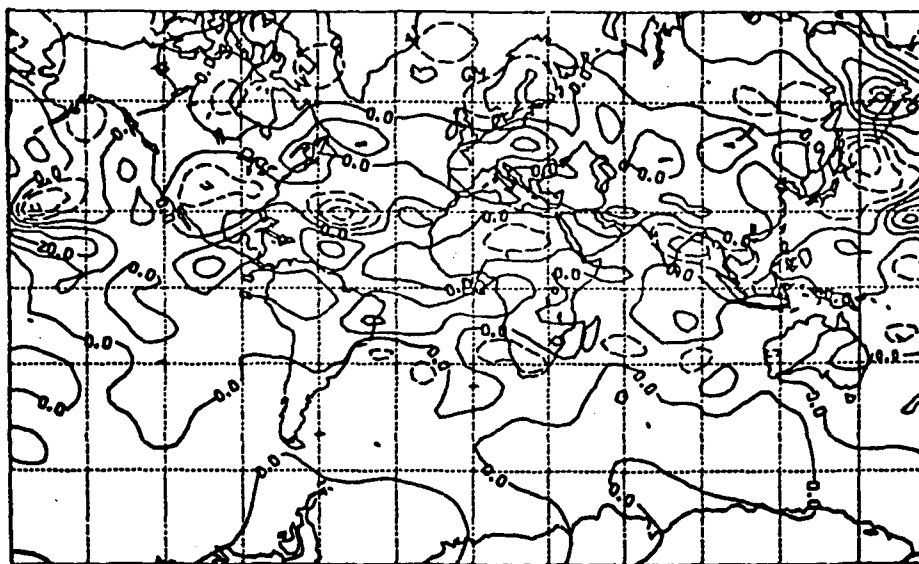
Figure 153.   Two-level model, mountain NHW 200 mb 25th day zonal wind
component difference field (variable tropical heating
minus uniform tropical heating) (ms^{-1}).   Contour interval
is 10 ms^{-1} with negative contours dashed.
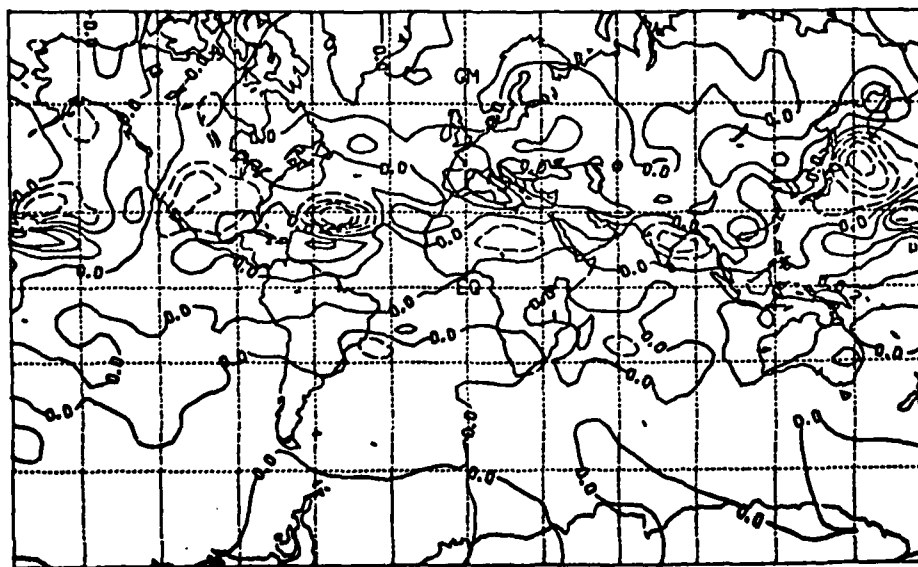
Figure 154.   Two-level model, mountain NHW 200 mb 25th day kinetic
energy difference field (variable tropical heating minus
uniform tropical heating) (m^2s^{-2}).   Contour interval is
300 m^2s^{-2} with negative contours dashed.

difference field (Figure 154) is very similar to the 200 mb zonal wind difference field. Again the changes in the kinetic energy appear to be substantial near the strongly heated regions. The strongest change near the international date line is almost 50% of the highest 200 mb value of kinetic energy in the MV case (Figure 144).

The 200 mb height field for the 25th day is given in Figure 155. The difference field of Φ (MV case minus the NV case) at day 25 is shown in Figure 156. The major differences between the MV and NV cases occur in the northern hemisphere. The largest differences occur to the north and east of Australia in the subtropics and midlatitudes of the northern hemisphere.

In summary, it appears that the mountains to a large degree determine the positioning of the subtropical and midlatitude jet streams in the two-level model. But the intensity of these preferred areas for jet information seems to be significantly modified by large scale variabilities in the tropical heating patterns.

5.5.3 Pulsed heating experiments

The next case deals with the short-term effects (3-6 days) of pulsing or unpulsing the convective area over the Amazon basin. Starting at day 17 of the MV integration, the unpulse and pulse were turned on with the same magnitude and in the same areas as previously discussed in the last subsection. The pulsed forcing function is given in Figure 157 and the unpulsed forcing function is given in Figure 158.
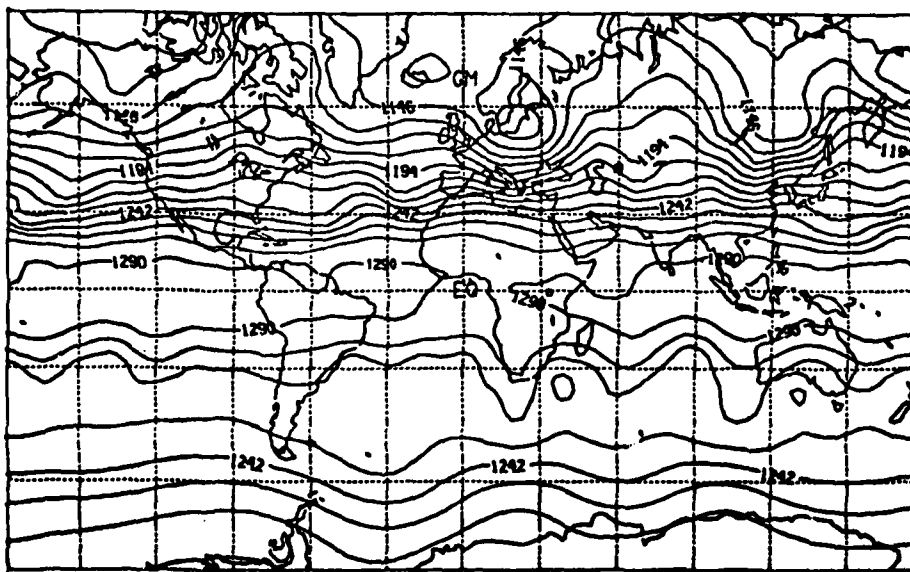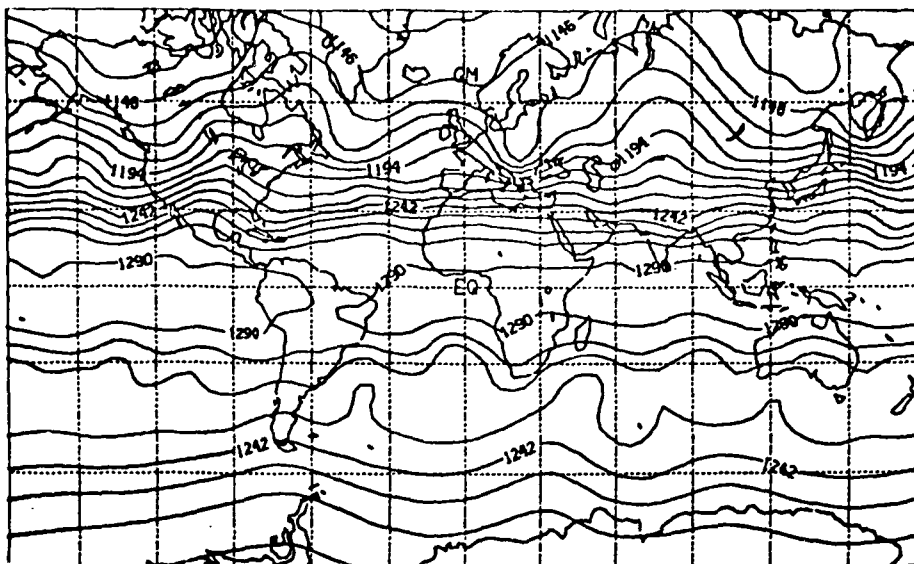
Figure 155.   Two-level model, mountain NHW uniform tropical heating
200 mb 25th day height field (dm).   Contour interval
is 12 dm.
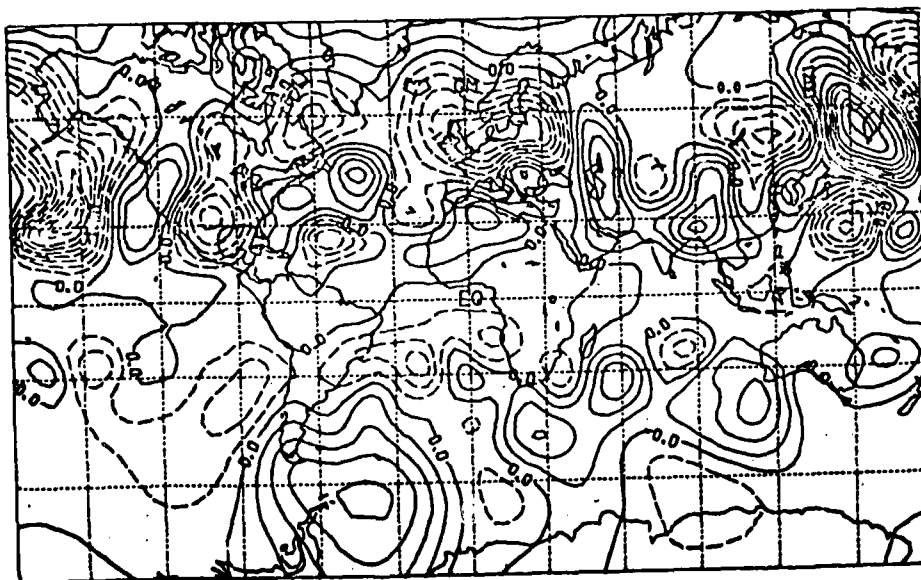
Figure 156.   Two-level model, Mountain NHW 25th day 200 mb geopotential
field difference (variable tropical heating minus uniform
tropical heating) $(m^2 s^{-2})$.   Contour interval is $300\,m^2 s^{-2}$
with negative contours dashed.

Figure 157. NHW total pulsed diabatic forcing function (Q) for upper
level with $\alpha=1$. Isolines every $1^{O}K$ day^{-1}. Contour
labels scaled by 10.

Figure 158. NHW total unpulsed diabatic forcing function (Q) for
upper level with $\alpha=1$. Isolines every $1^{O}K$ day^{-1}. Con-
tour labels scaled by 10.

The three-day average 200 mb zonal component of the wind field for the three-day pulse and unpulse are given in Figures 159 and 160, respectively. The difference field (pulsed minus unpulsed) for the 20th day is given in Figure 161. The maximum difference in the northern hemisphere of 9 ms^{-1} is located at 75°W and 26°N. The difference field for the 20th day (pulsed minus unpulsed) zonal wind component at the lower level (a sigma surface) is given in Figure 162. In the lower level, the change is confined mainly to the pulsed/ unpulsed region.

The 200 mb kinetic energy difference between the pulsed and unpulsed case is given in Figure 163, while the 200 mb pulsed and unpulsed kinetic energies are given in Figures 164 and 165, respectively.

The maximum northern hemisphere difference in the kinetic energy for the mountain case is about 60% of the maximum response reported for the no-mountain case (see Figure 106). Subjective evaluation of individual mountain case fields suggests that the energy change in the northern hemisphere is more spread out and not as localized as compared to the no-mountain case.

The change in the 200 mb geopotential field ($\Phi=gz$) at the 20th day between the pulsed/umpulsed cases is given in Figure 166. Comparing Figure 166 with the three-day 200 mb geopotential change ($\Phi=gz$) of the no-mountain case (Figure 112) one finds that in the region of and just to the north of the pulsing, the two figures are almost identical. The wavenumber 6 pattern near 30°N that is visible in the no-mountain case (Figure 112) is less evident in the mountain
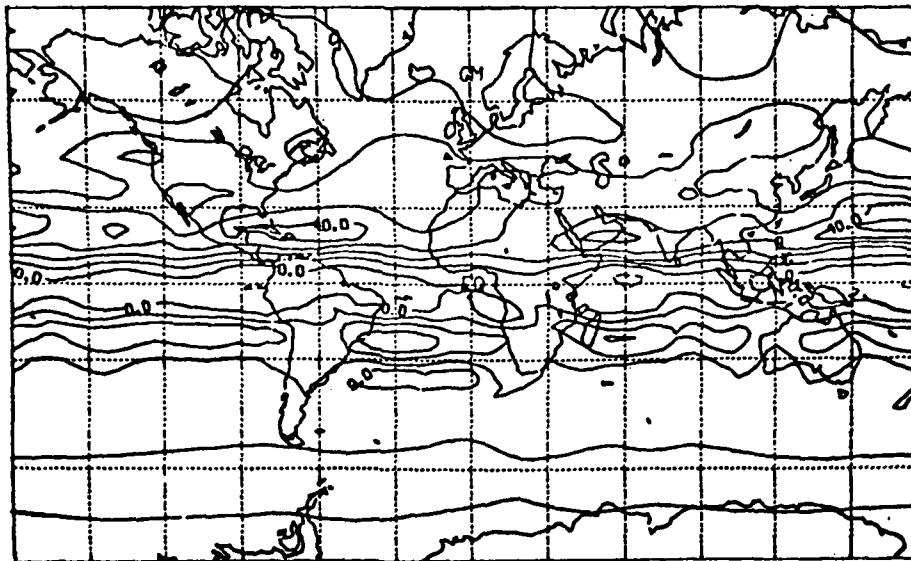
Figure 159. Two-level model, mountain NHW variable tropical heating 200 mb 3-day average (days 17.5-20) pulsed zonal wind field (ms^{-1}). Contour interval is 10 ms^{-1} with negative contours dashed.
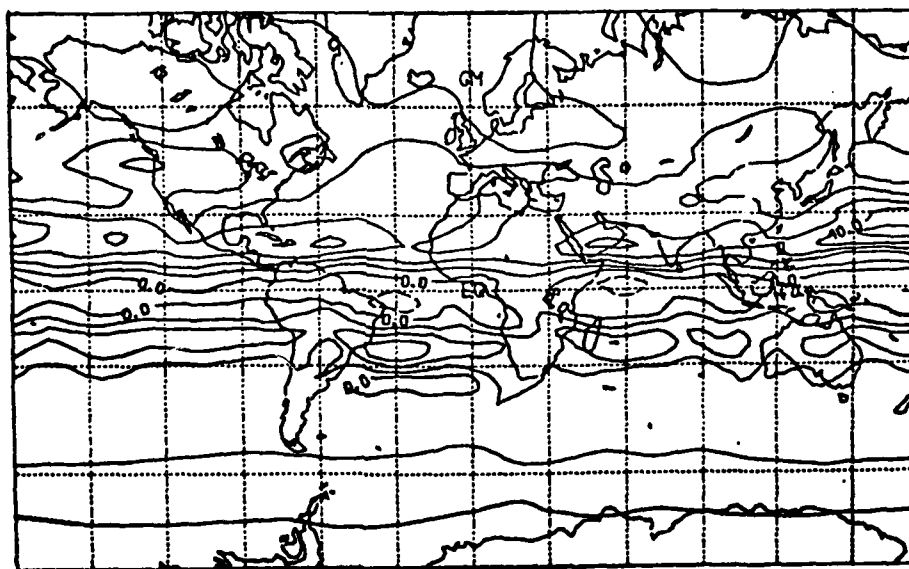
Figure 160. Two-level model, mountain NHW variable tropical heating 200 mb 3-day average (days 17.5-20) unpulsed zonal wind field (ms^{-1}). Contour interval is 10 ms^{-1} with negative contours dashed.

Figure 161.   Two-level model, mountain NHW variable tropical heating
200 mb 20th day zonal wind difference field (pulsed
minus unpulsed) (ms^{-1}). Contour interval is 5 ms^{-1}
with negative contours dashed.
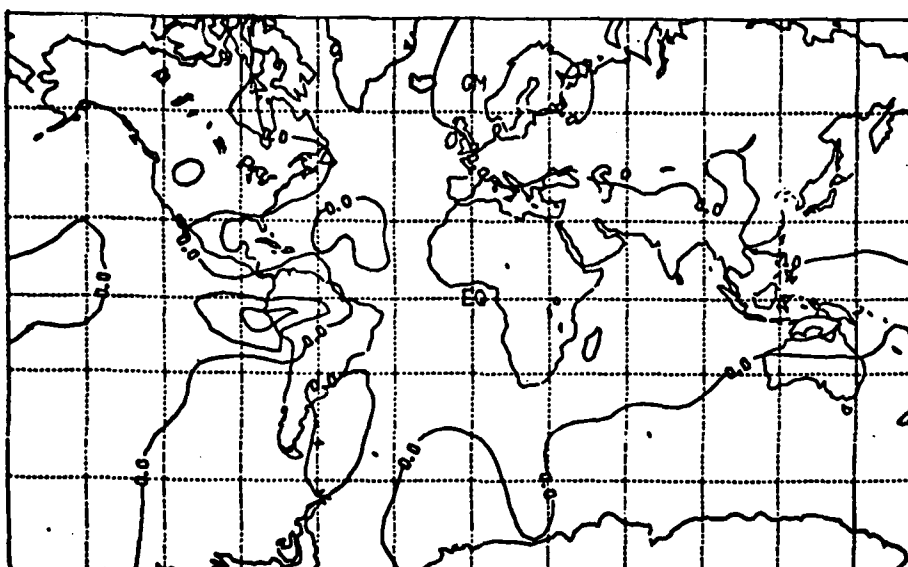
Figure 162.   Two-level model, mountain NHW variable tropical heating
20th day lower level zonal wind difference field (pulsed
minus unpulsed) (ms^{-1}). Contour interval is 5 ms^{-1}
with negative contours dashed.

Figure 163. Two-level model, mountain NHW variable tropical heating 200 mb 20th day kinetic energy difference field (pulsed minus unpulsed) (m^2s^{-2}). Contour interval is 150 m^2s^{-2} with negative contours dashed.

Figure 164. Two-level model, mountain NHW variable tropical heating 200 mb pulsed 20th day kinetic energy (m^2s^{-2}). Contour interval is 500 m^2s^{-2}.
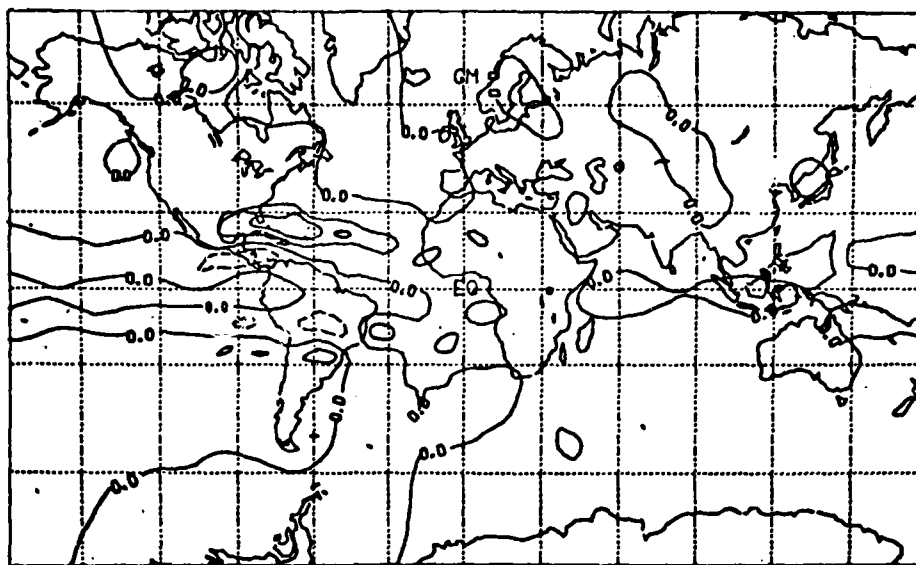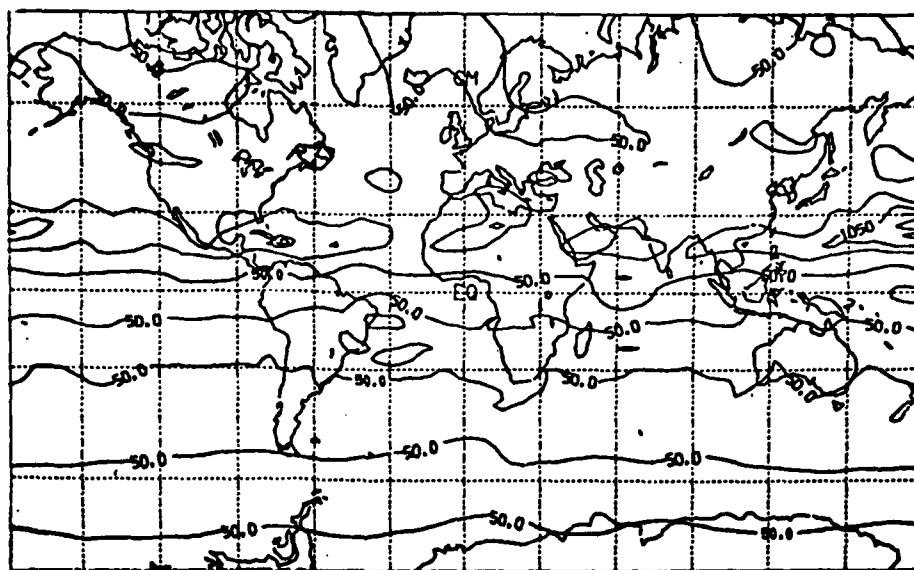
Figure 165. Two-level model, mountain NHW variable tropical heating 200 mb unpulsed 20th day kinetic energy (m^2s^{-2}). Contour interval is 500 m^2s^{-2}.
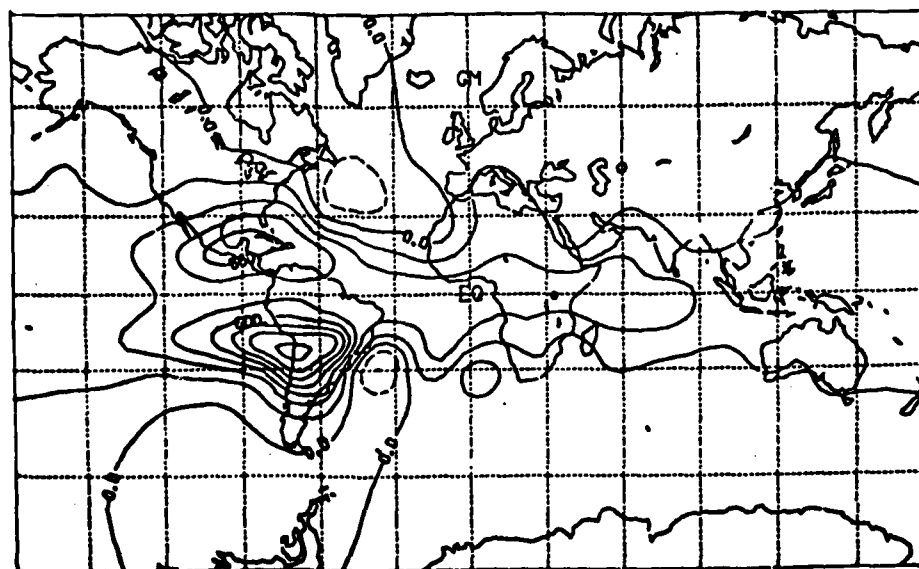
Figure 166. Two-level model, mountain NHW variable tropical heating 200 mb 20th day geopotential difference field (pulsed minus unpulsed) (m^2s^{-2}). Contour interval is 150 m^2s^{-2} with negative contours dashed.

case (Figure 166). This suggests that the baroclinic wave activity
in the no-mountain case is stronger than that in the mountain case.
This may explain why the energy in the no-mountain case is propa-
gated downstream in a more concentrated manner (β effect), while the
energy in the mountain case is more dispersed.

In order to measure the relative importance of the above three-
day 200 mb height change with respect to changes in the ultra-long
waves, Hovmöller diagrams of Φ_{1-3} from day 17.5 to day 20 for the
pulsed, unpulsed and differences (unpulsed minus pulsed) were com-
puted at $30^{o}S$, $10^{o}S$, $10^{o}N$, $30^{o}N$ and $42^{o}N$. These diagrams are given
in Figures 167-181. Table V summarizes the maximum amplitudes in
the ultra-long waves for the pulsed and unpulsed cases along with the
maximum percent change in Φ_{1-3} caused by the pulsed and unpulsed
steady forcing.

The percent change in the ultra-long waves in the mountain case
at $42^{o}N$ is 18%, while in the no-mountain case it was 40%. Thus the
effect of heating in this model in the presence of mountains can only
explain about half of the total 30% error in the amplitudes of the
ultra-long waves between the GISS GCM and the NMC model.

The mountains in the two-level model force much larger ampli-
tudes in the ultra-long waves. From a comparison of Tables III and
V one can see that the maximum amplitudes in the ultra-long waves
double for the mountain case, while the maximum differences between
the pulsed and unpulsed cases remain almost the same. Thus, the
heating effect between the no-mountain and mountain experiments does
not change appreciably, while the mountains force much higher

Figure 167. Same as 113 but for 17.5 to 20-day NHW mountain unpulsed geopotential field (Φ_{1-3}) at 30°S. Contour interval is 90 m^2s^{-2}.

Figure 168. Same as 113 but for 17.5 to 20-day NHW mountain pulsed geopotential field (Φ_{1-3}) at 30°S. Contour interval is 100 m^2s^{-2}.

Figure 169. Same as 113 but for 17.5 to 20 day NHW mountain geopotential difference field Φ_{1-3} (unpulsed minus pulsed) at 30°S. Contour interval is 70 m^2s^{-2}.

Figure 170. Same as 113 but for 17.5 to 20-day NHW mountain unpulsed geopotential field (Φ_{1-3}) at 10°S. Contour interval is 50 m^2s^{-2}.

Figure 171. Same as 113 but for 17.5 to 20-day NHW mountain pulse geopotential field (ϕ_{1-3}) at 10°S. Contour interval is 40 m^2s^{-2}.

Figure 172. Same as 113 but for 17.5 to 20-day NHW mountain geopotential difference field ϕ_{1-3} (unpulsed minus pulsed) at 10°S. Contour interval is 50 m^2s^{-2}.
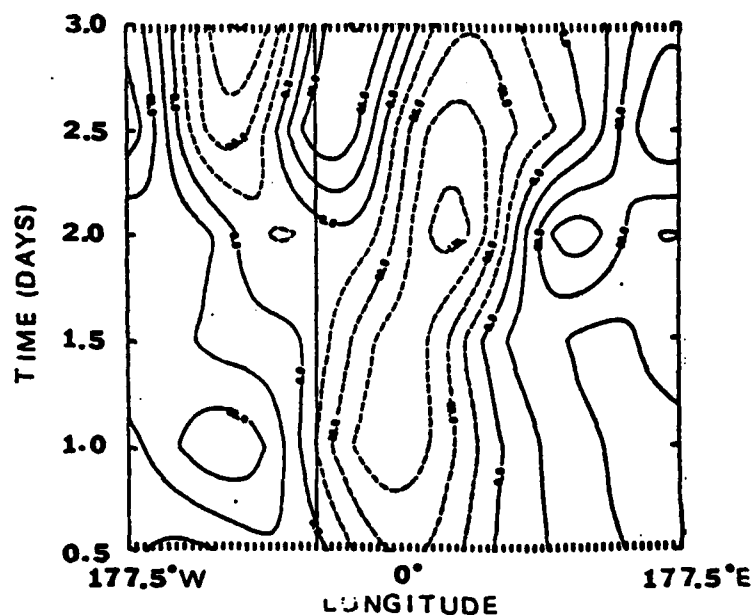
Figure 173. Same as 113 but for 17.5 to 20-day NHW mountain unpulsed geopotential field (ϕ_{1-3}) at 10°N. Contour interval is 50 $m^2 s^{-2}$.
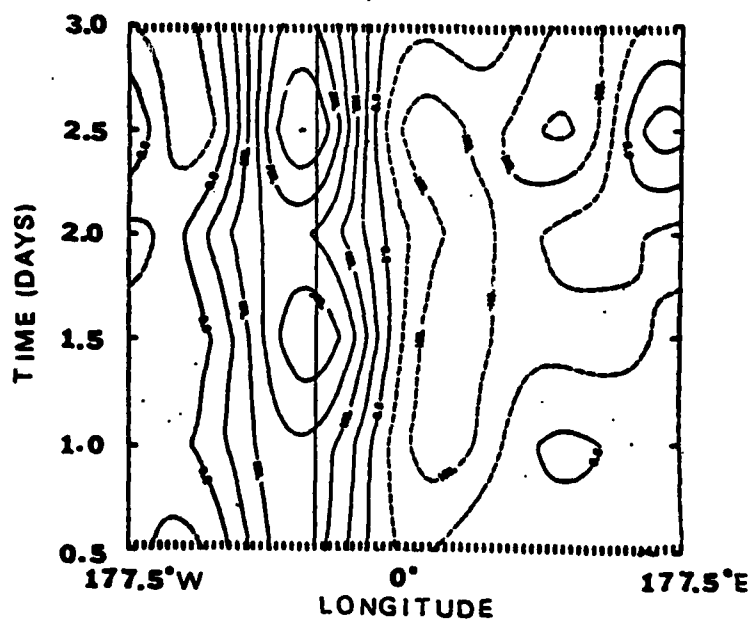
Figure 174. Same as 113 but for 17.5 to 20-day NHW mountain pulsed geopotential field (ϕ_{1-3}) at 10°N. Contour interval is 30 $m^2 s^{-2}$.
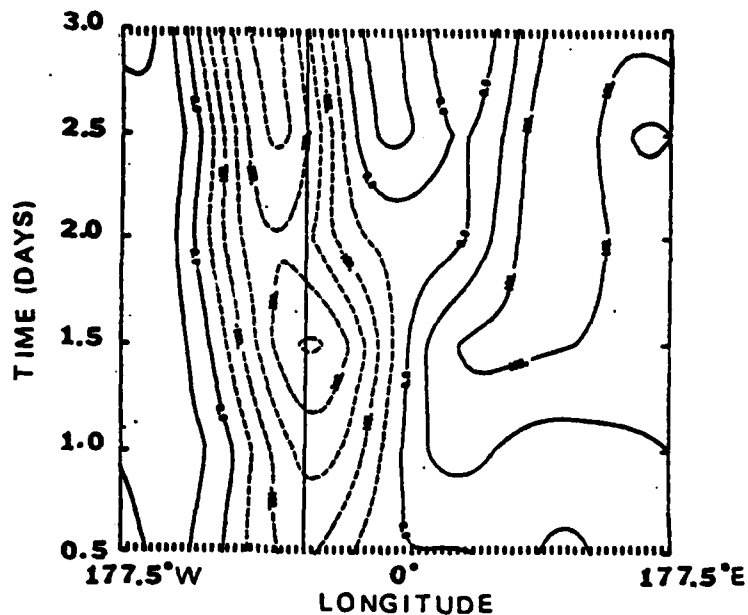
Figure 175. Same as 113 but for 17.5 to 20-day NHW mountain geopotential difference field ϕ_{1-3} (unpulsed minus pulsed) at 10°N. Contour interval is 50 m^2s^{-2}.
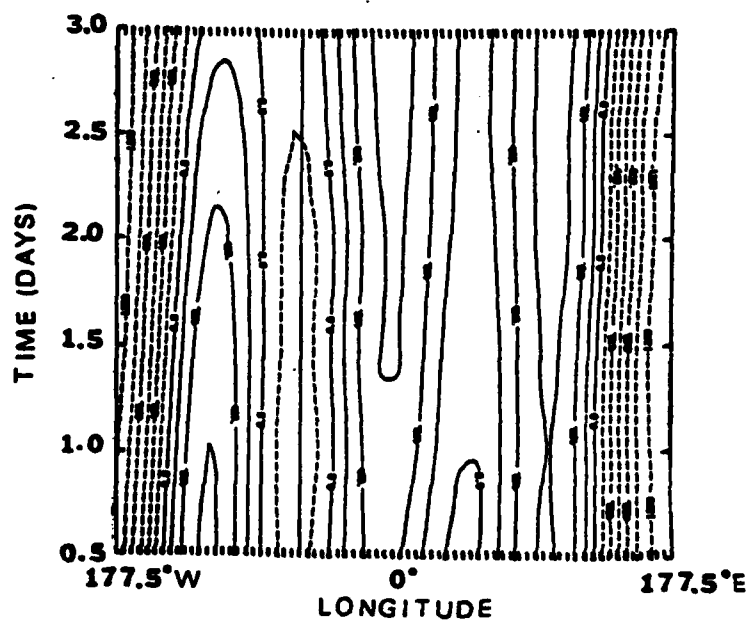
Figure 176. Same as 113 but for 17.5 to 20-day NHW mountain unpulsed geopotential field (ϕ_{1-3}) at 30°N. Contour interval is 200 m^2s^{-2}.
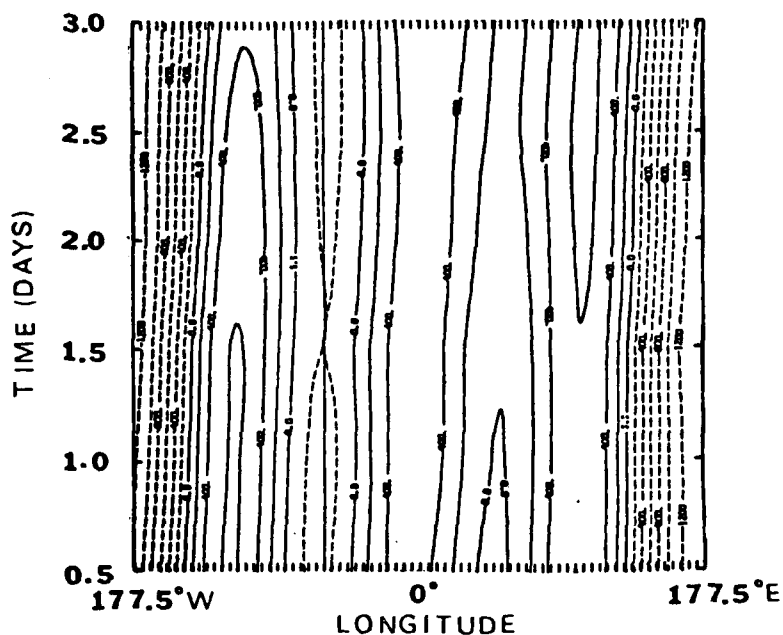
Figure 177. Same as 113 but for 17.5 to 20 day NHW mountain pulsed geopotential field (Φ_{1-3}) at $30°N$. Contour interval is 200 m^2s^{-2}.
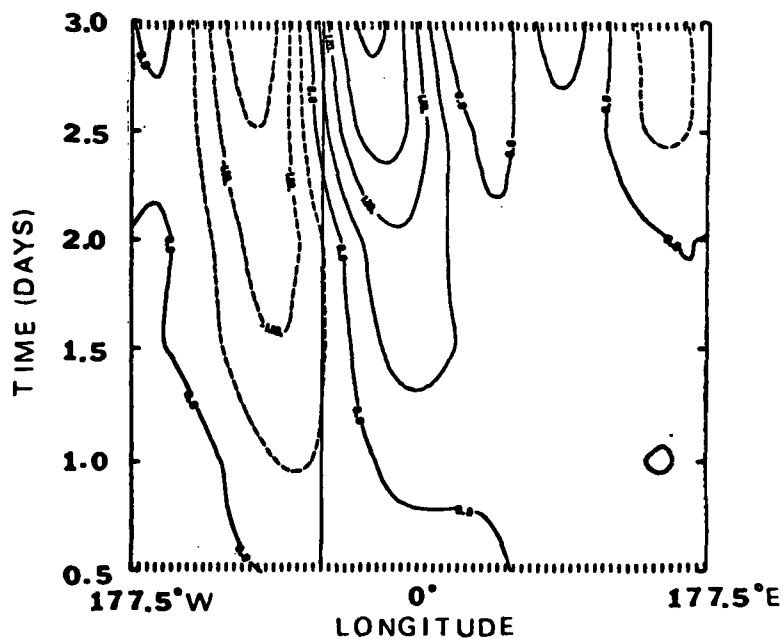
Figure 178. Same as 113 but for 17.5 to 20 day NHW mountain geopotential difference field Φ_{1-3} (unpulsed minus pulsed) at $30°N$. Contour interval is 60 m^2s^{-2}.
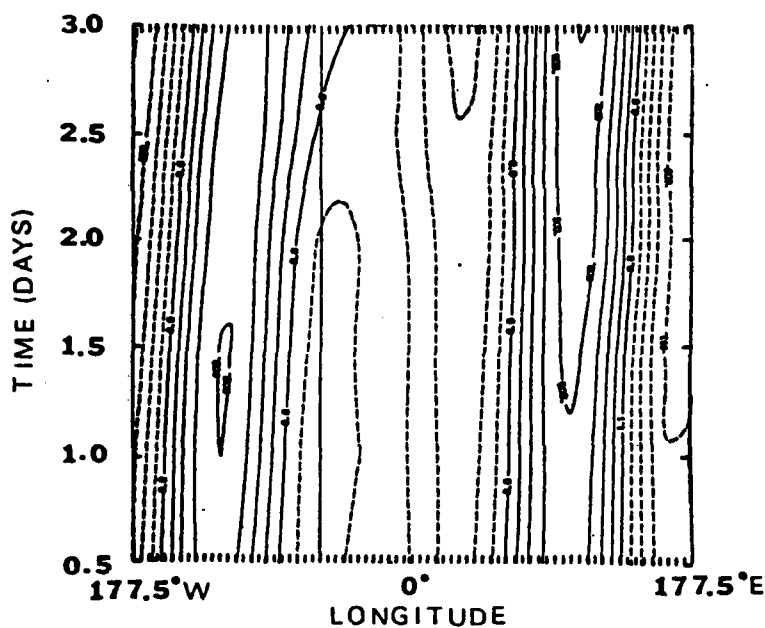
Figure 179. Same as 113 but for 17.5 to 20 day NHW mountain unpulsed geopotential field (Φ_{1-3}) at 42°N. Contour interval is 200 m^2s^{-2}.
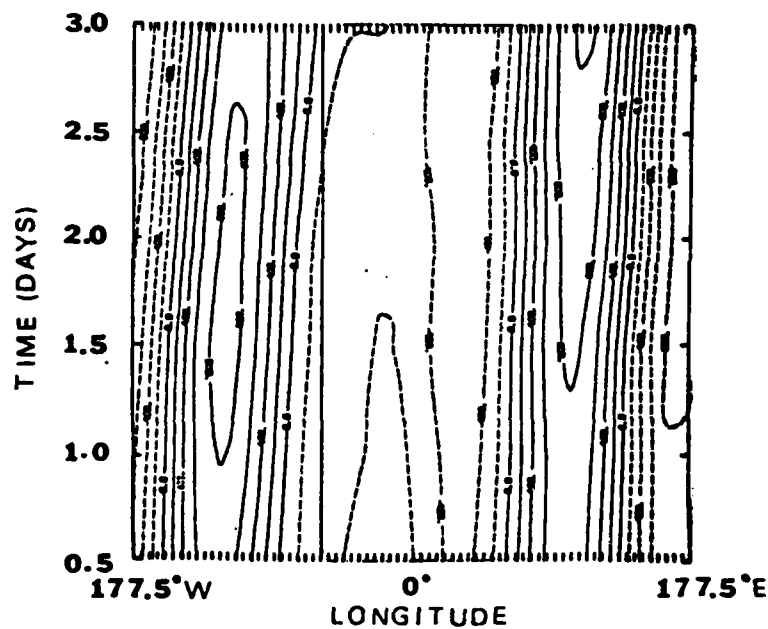
Figure 180. Same as 113 but for 17.5 to 20 day NHW mountain pulsed geopotential field (Φ_{1-3}) at 42°N. Contour interval is 200 m^2s^{-2}.
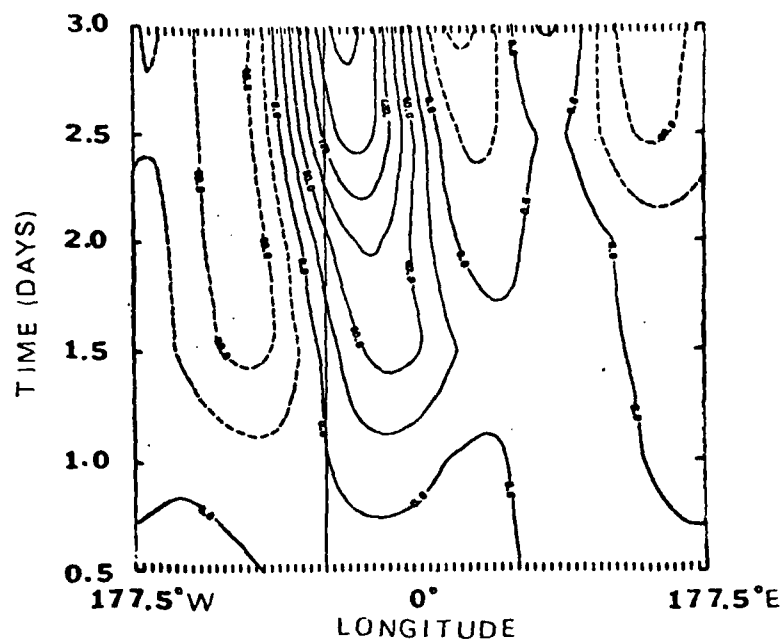
Figure 181. Same as 113 but for 17.5 to 20 day NHW mountain geopo-
tential difference field Φ_{1-3} (unpulsed minus pulsed)
at 42°N. Contour interval is 30 $m^2 s^{-2}$.
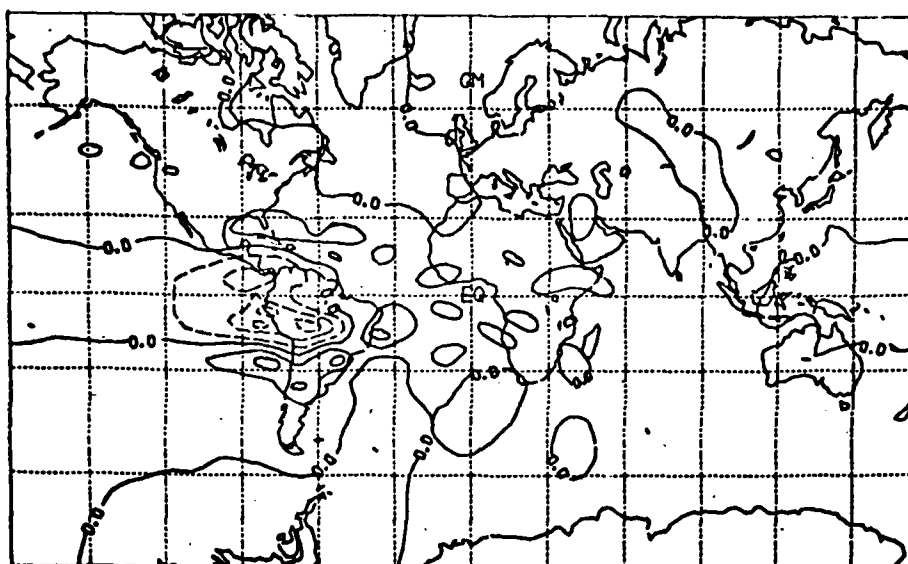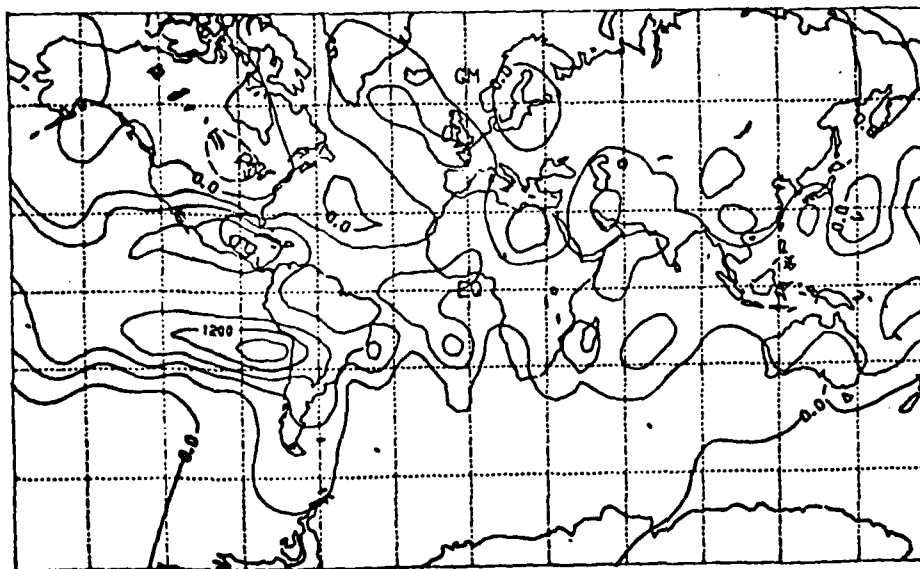

Figure 182. Two-level model mountain NHW variable tropical heating
200 mb 23rd day geopotential difference field (pulsed
minus unpulsed) ($m^2 s^{-2}$). Contour interval is 300 $m^2 s^{-2}$
with negative contours dashed.

TABLE V

Same as Table III but for the NHW mountain
pulsed and unpulsed cases

Latitude	Maximum "pulsed" amplitude	Maximum "unpulsed" amplitude	Maximum Difference	% Change
		Day 17.5 - 20		
30°S	400	360	350	88%
10°S	200	250	250	100%
10°N	120	300	250	83%
30°N	1200	1200	240	20%
42°N	1000	1000	180	18%
		Day 20.5 - 23		
30°N	1200	1200	320	26%
42°N	1000	1000	350	35%

amplitudes in the ultra-long waves.

The fact that mountains tend to force more amplitude into the
ultra-long waves is to be expected. The mountain forcing in the two-
level model should be fairly well resolved, since this effect is
essentially equivalent barotropic. The tropical heating effect in
the two-level model may not be as well resolved, since this process
involves mass overturnings coupled with a strong inflow at the bottom
and a strong outflow at the top. The strongest inflows and outflows
are focused in about 150 mb layers at the bottom and top of the real
atmosphere (see Newell et al., 1972, Table 3.3). In the two-level

model, the lower and upper layers are much thicker. Thus, future study is suggested in order to determine if the percent amplitude change in the ultra-long waves forced by the pulsed and unpulsed tropical heatings will increase in a higher vertical resolution (at least four levels) model.

The pulsed and unpulsed tests just reported were carried out for three more days to the 23rd day of integration. The 200 mb geopotential ($\Phi=gz$) difference field at the sixth day of pulsing and unpulsing is given in Figure 182. The Hovmöller Φ_{1-3} diagrams for the unpulsed, pulsed and difference fields (unpulsed minus pulsed) from day 20.5 to day 23 at 30^ON and 42^ON are given in Figures 183-188. Table V summarizes the results of these figures. Again, the percent change in the amplitude of the ultra-long waves from pulsing and unpulsing in the mountain case is reduced (35% to 50% at 42^ON) when compared to the no-mountain case.

The final case to be presented in this section was conducted to determine the effect of not including tropical heating or cooling ($Q=0$) in the two-level model on a three-day forecast. This test was designed to simulate a simplification of the present NMC models in a crude fashion.

To accomplish the above test, the zonal heating function (Q_z) at each level was set to zero from 22^OS to 10^ON. The model was then integrated for three days starting at day 20 with the initial fields taken from the MV 20th day case.

The kinetic energy at day 23 for the zero tropical heating (ZT) case is shown in Figure 189. Comparing this figure and the kinetic
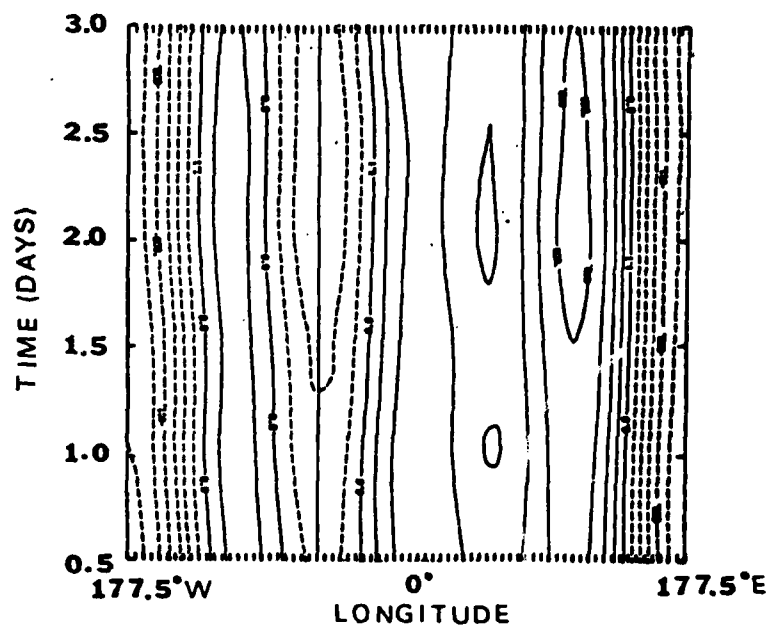
Figure 183. Same as 113 but for 20.5 to 23 day NHW mountain un-
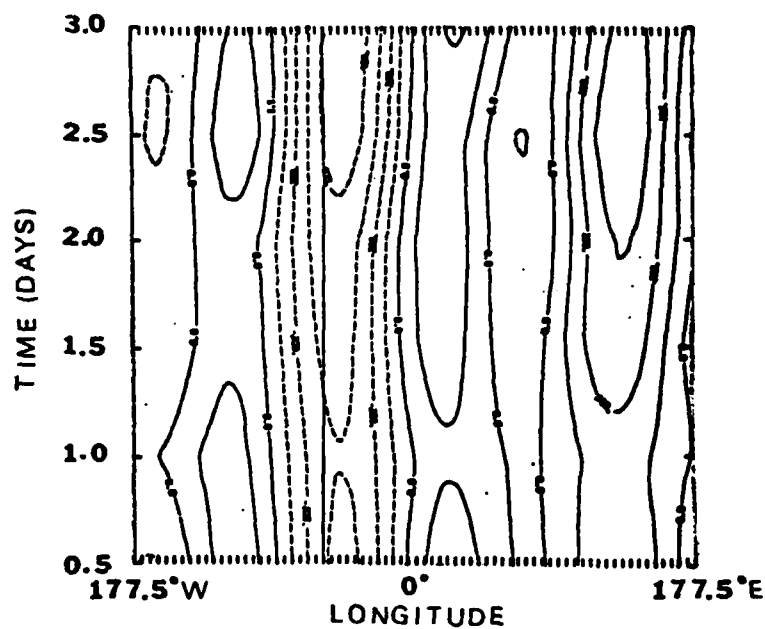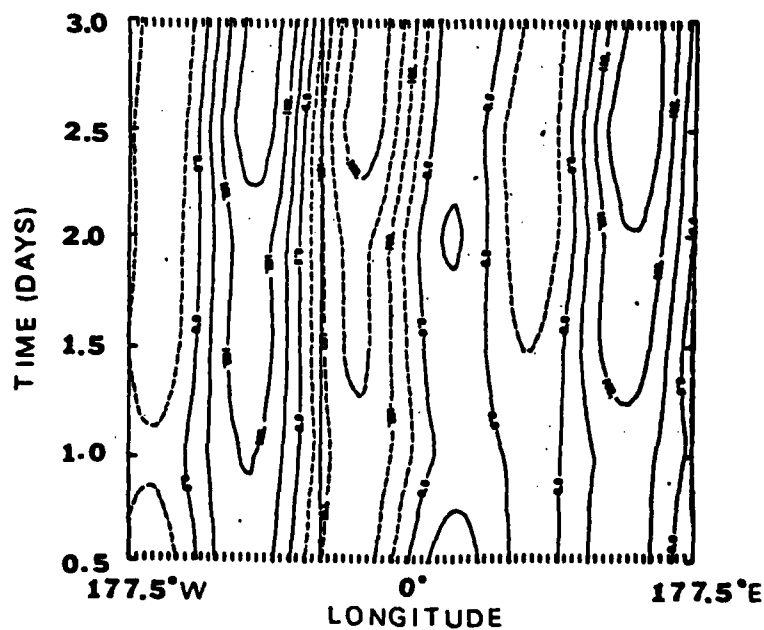pulsed geopotential field (ϕ_{1-3}) at 30°N. Contour
interval is 200 m^{2}s^{-2}.
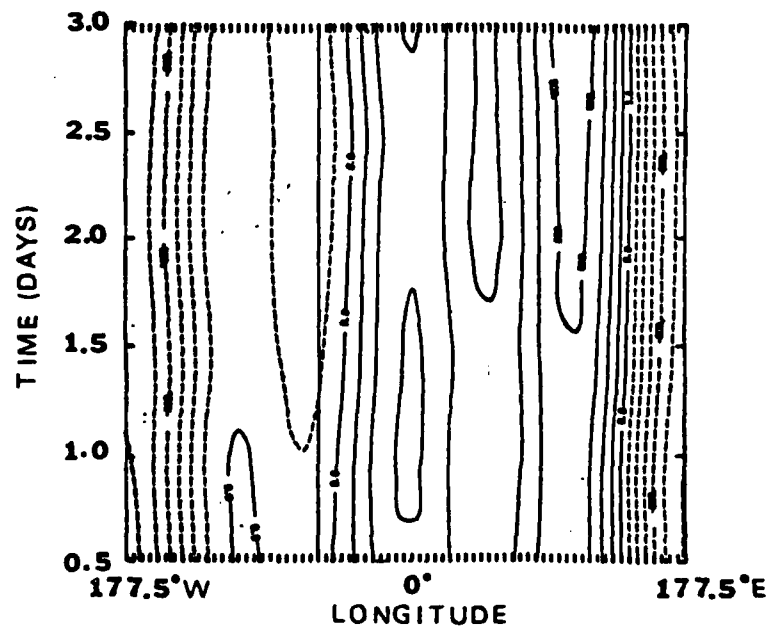
Figure 184. Same as 113 but for 20.5 to 23 day NHW mountain pulsed
geopotential field (ϕ_{1-3}) at 30°N. Contour interval
is 200 m^{2}s-^{2}.
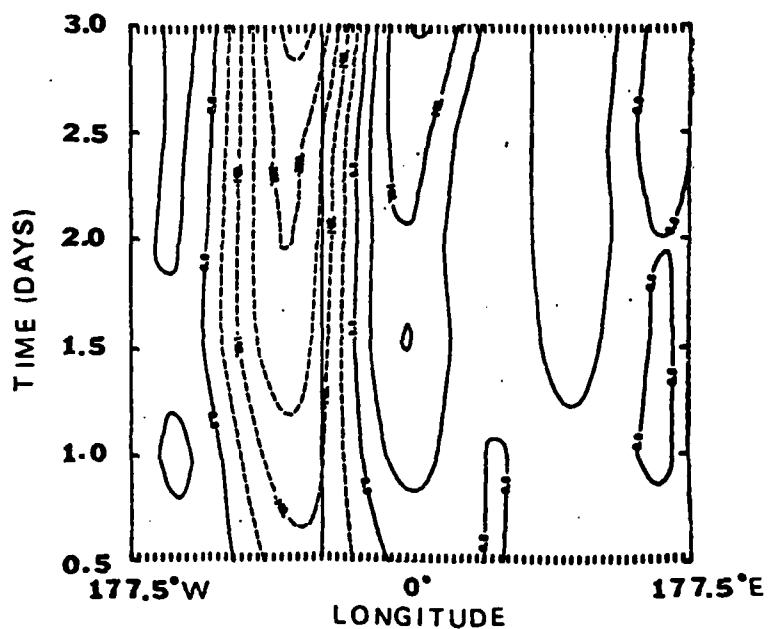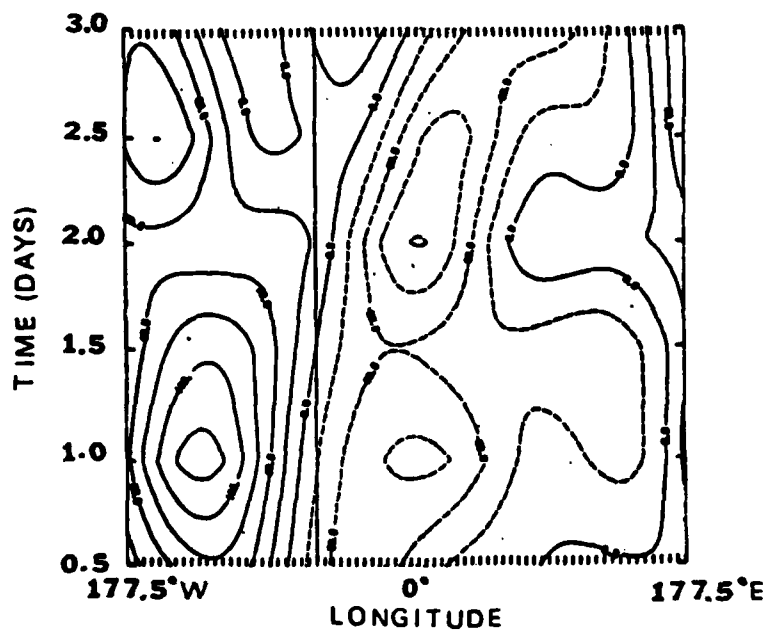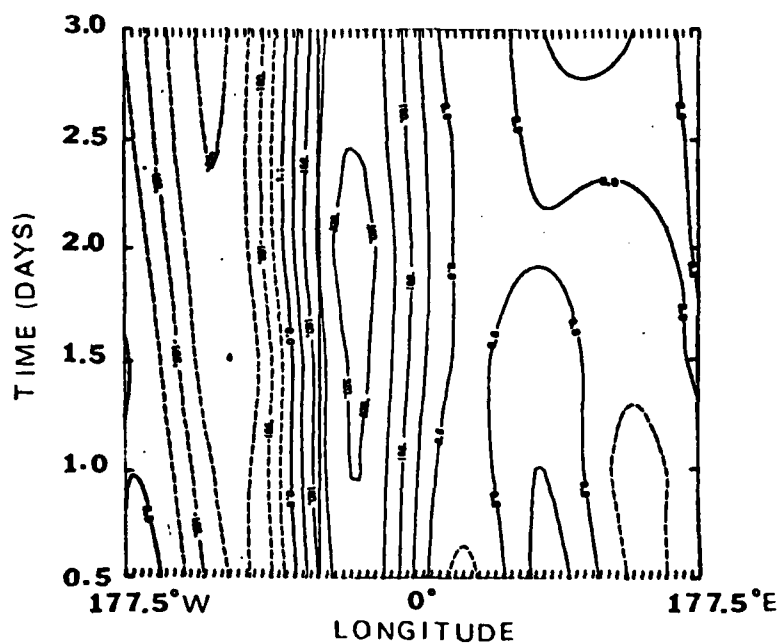
Figure 185. Same as 113 but for 20.5 to 23 day NHW mountain geopotential difference field Φ_{1-3} (unpulsed minus pulsed) at 30°N. Contour interval is 80 m^2s^{-2}.
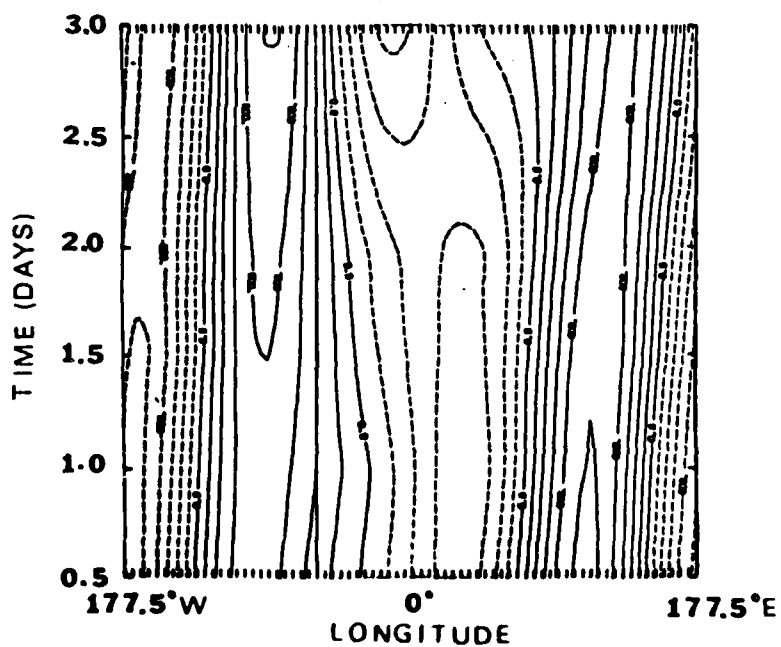
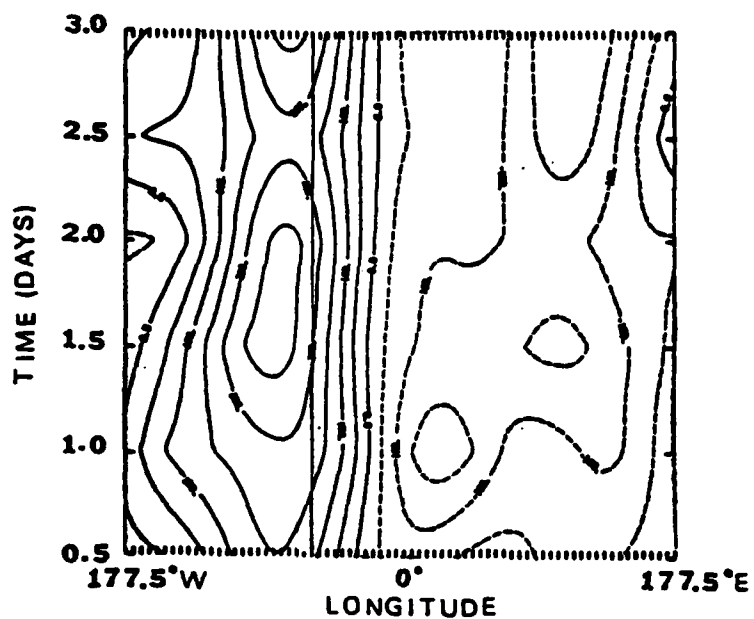Figure 186. Same as 113 but for 20.5 to 23 day NHW mountain unpulsed geopotential field (Φ_{1-3}) at 42°N. Contour interval is 200 m^2s^{-2}.
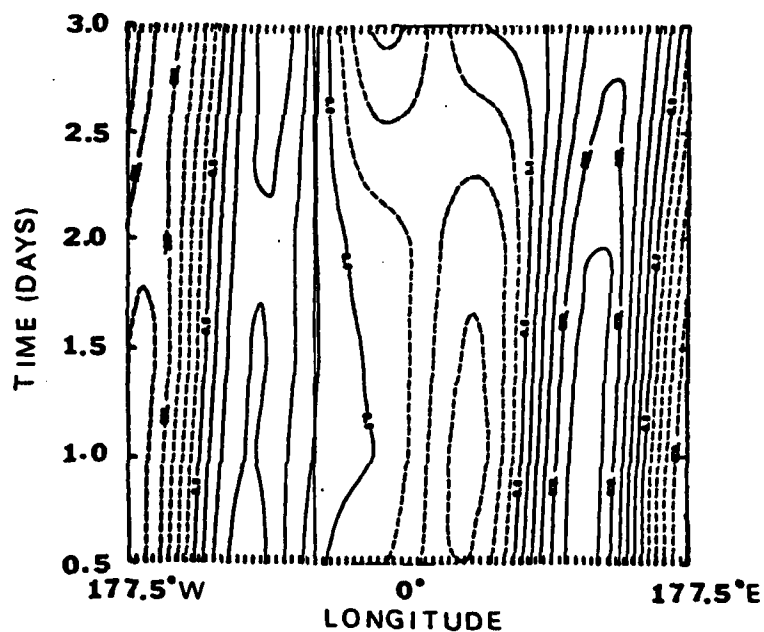
Figure 187. Same as 113 but for 20.5 to 23 day NHW mountain pulsed geopotential field (Φ_{1-3}) at 42°N. Contour interval is 200 m^2s^{-2}.
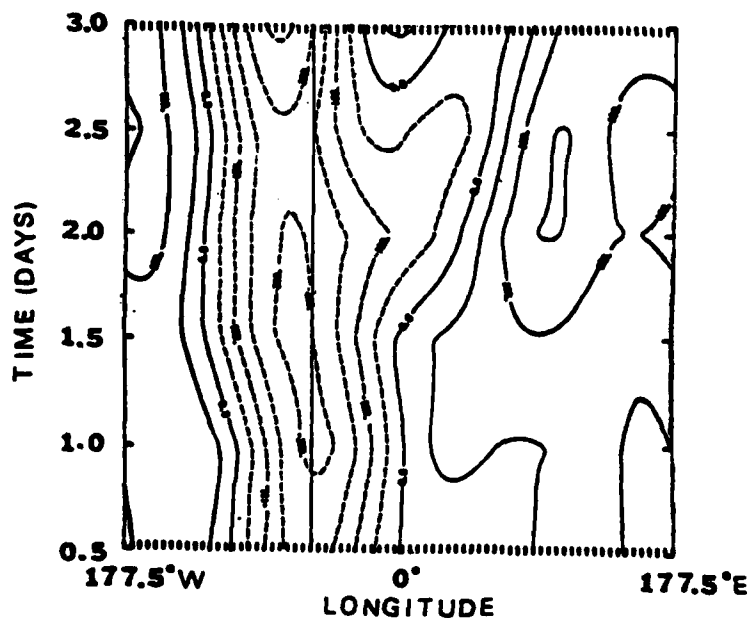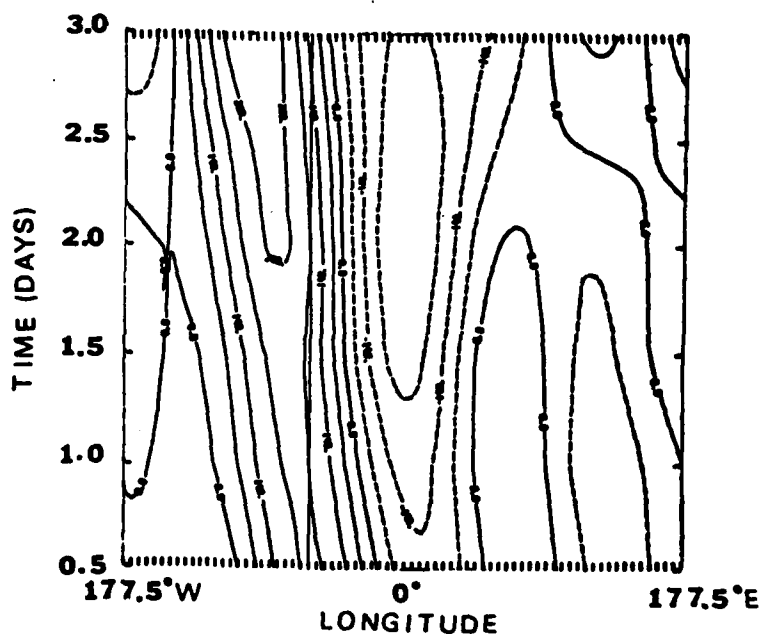

Figure 188. Same as 113 but for 20.5 to 23 day NHW mountain geopotential difference field (Φ_{1-3}) (unpulsed minus pulsed) at 42°N. Contour interval is 70 m^2s^{-2}.
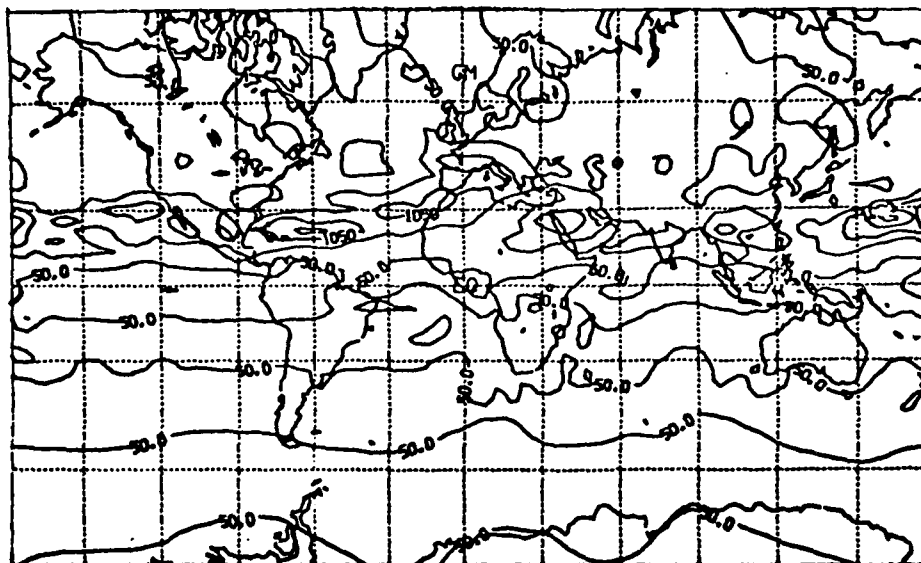
Figure 189. Two-level model mountain NHW zero tropical heating 200 mb 23rd day kinetic energy (m^2s^{-2}). Contour interval is 500 m^2s^{-2}.
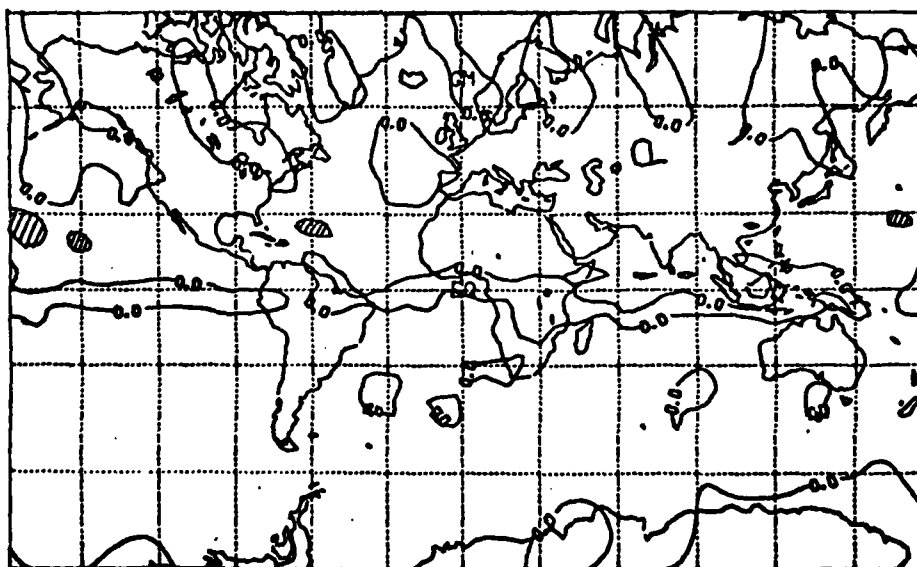
Figure 190. Two-level model mountain NHW 200 mb 23rd day kinetic energy difference (variable tropical heating minus zero tropical heating)(m^2s^{-2}). Contour interval is 300 m^2s^{-2}.

energy for the MV case at day 23 (Figure 144) one can see that the areas of strongest kinetic energy in the northern hemisphere are reduced in the ZT case. The difference field between the MV and ZT cases (Figure 190) shows a change in the kinetic energy in the jets of more than 300 m^2s^{-2} in the two regions of strongest jet maxima (north Australia and north of South America).

The geopotential difference is given in Figure 191 and the Hovmöller diagrams of Φ_{1-3} for the ZT case, MV case and difference (MV minus ZT) given at 30°S, 10°S, 10°N, 30°N and 42°N from day 20.5 to day 23 in Figures 192-206. The Hovmöller diagram maximum results are summarized in Table VI.

As can be seen from Table VI, the percent change in the amplitude of the ultra-long waves is 10% of the actual amplitude at 42°N.

TABLE VI

Same as Table III except for the NHW variable tropical heating case versus the zero tropical heating case from day 20.5 to day 23

Latitude	Maximum MV amplitude (m^2s^{-2})	Maximum zero tropical heating amplitude (m^2s^{-2})	Maximum difference (m^2s^{-2})	% Change
30°S	500	500	100	20%
10°S	150	150	120	80%
10°N	150	200	120	60%
30°N	1200	1200	200	17%
42°N	1000	1000	100	10%
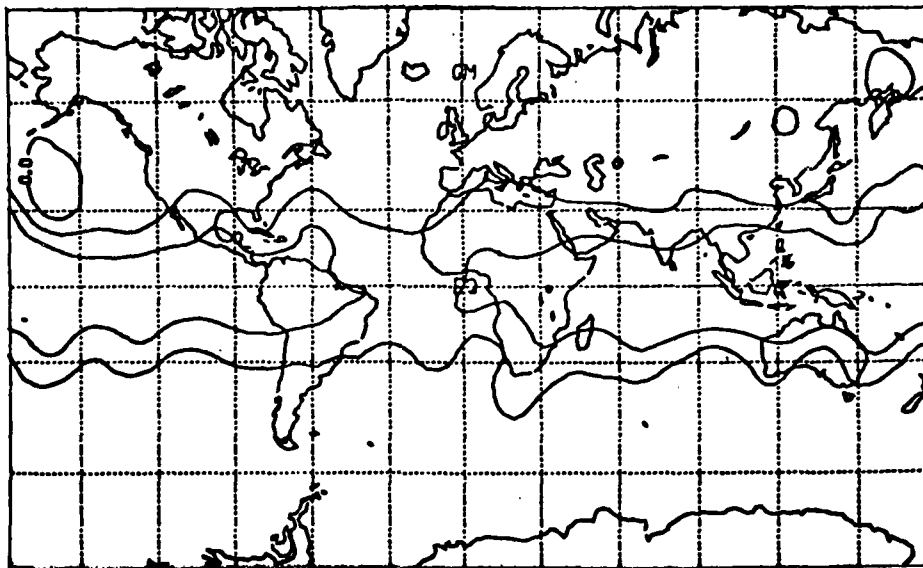
Figure 191. Two-level model mountain NHW 200 mb 23rd day geopotential difference field (variable tropical heating minus zero tropical heating)(m^2s^{-2}). Contour interval is 300 m^2s^{-2}.
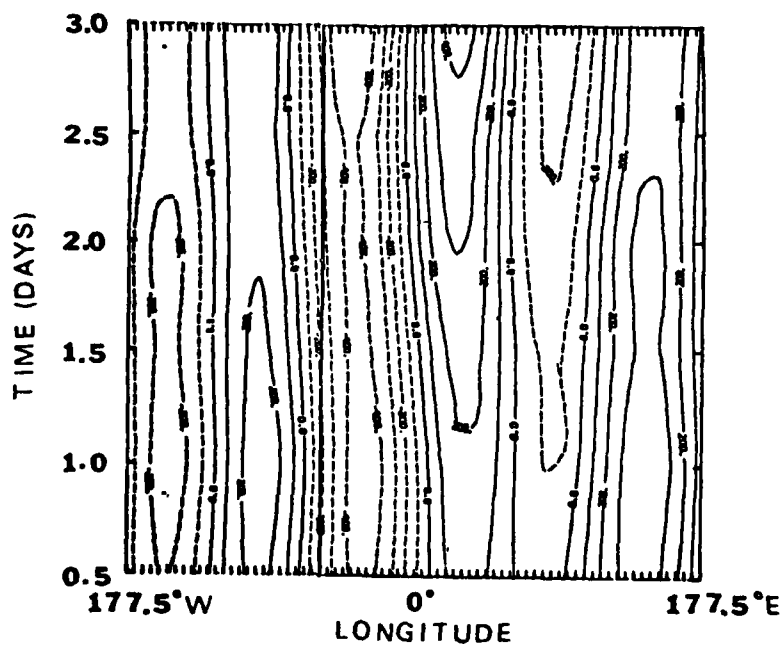
Figure 192. Same as 113 but for 20.5 to 23 day NHW mountain zero tropical heating geopotential field (ϕ_{1-3}) at 30°S. Contour interval is 100 m^2s^{-2}.
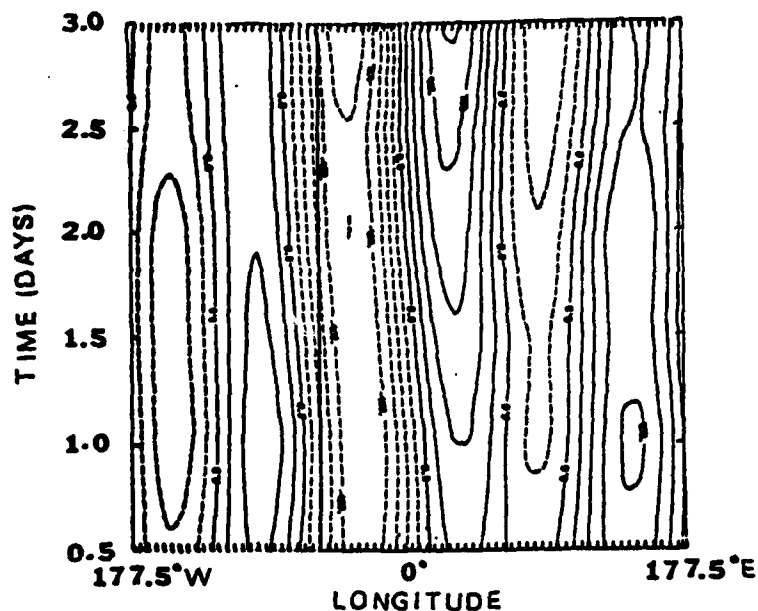
Figure 193. Same as 113 but for 20.5 to 23 day NHW mountain variable tropical heating geopotential field (ϕ_{1-3}) at 30°S. Contour interval is 100 m^2s^{-2}.
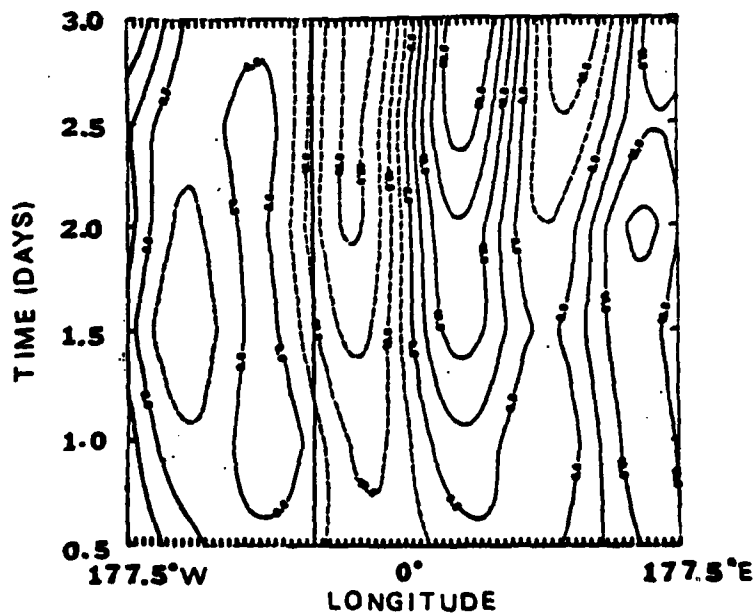
Figure 194. Same as 113 but for 20.5 to 23 day NHW mountain geopotential (ϕ_{1-3}) difference field (variable tropical heating minus zero tropical heating) at 30°S. Contour interval is 30 m^2s^{-2}.
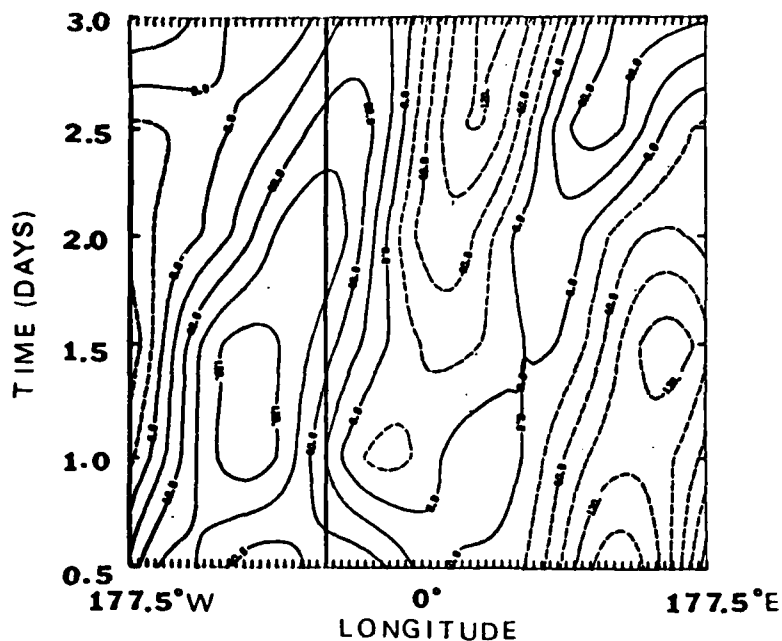
Figure 195. Same as 113 but for 20.5 to 23 day NHW mountain zero tropical heating geopotential field (ϕ_{1-3}) at 10^0S. Contour interval is 30 m^2s^{-2}.
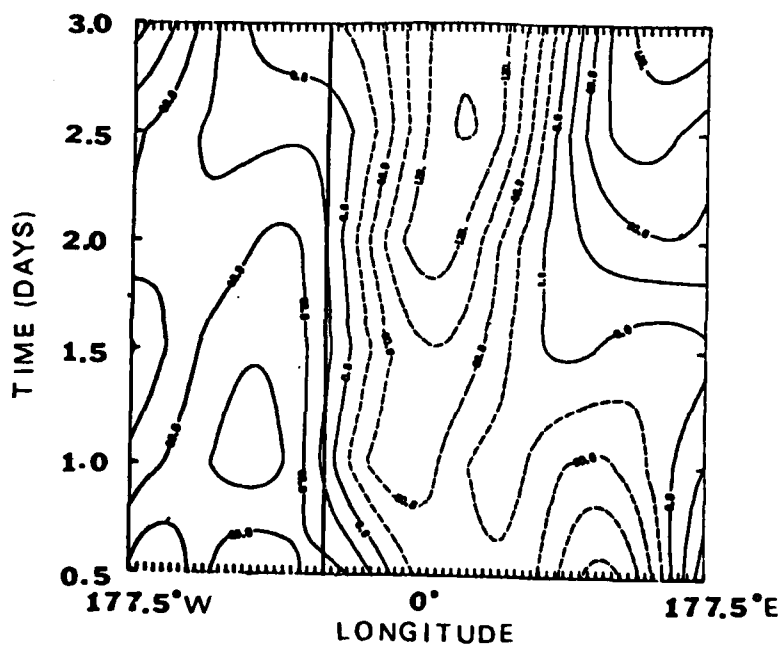
Figure 196. Same as 113 but for 20.5 to 23 day NHW mountain variable tropical heating geopotential field (ϕ_{1-3}) at 10^0S. Contour interval is 30 m^2s^{-2}.
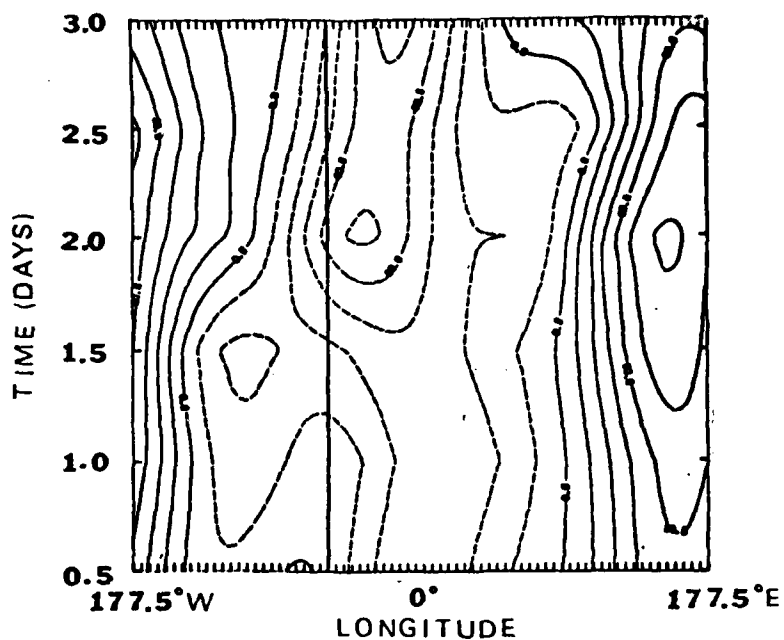
Figure 197. Same as 113 but for 20.5 to 23 day NHW mountain geopoten-
tial difference field (ϕ_{1-3})(variable tropical heating
minus zero tropical heating) at 10°S. Contour interval
is 20 m^2s^{-2}.
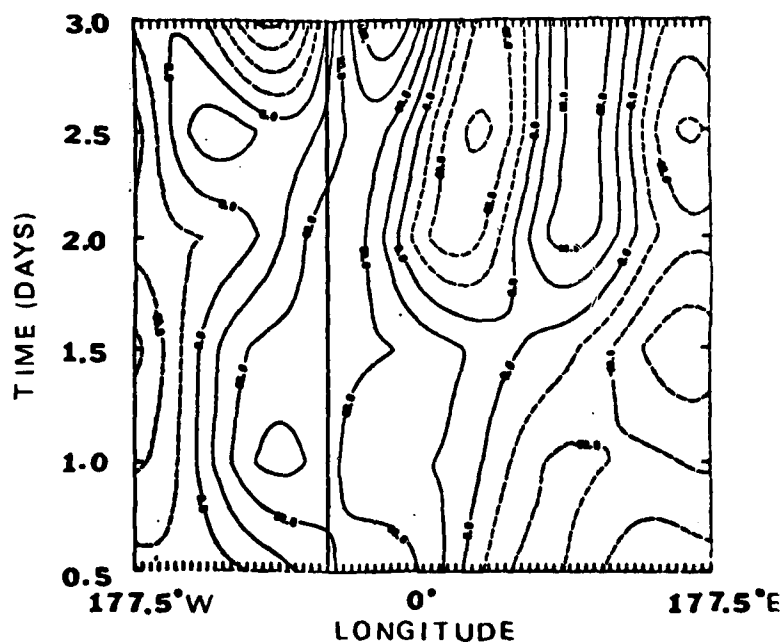
Figure 198. Same as 113 but for 20.5 to 23 day NHW mountain zero
tropical heating geopotential field (ϕ_{1-3}) at 10°N.
Contour interval is 40 m^2s^{-2}.
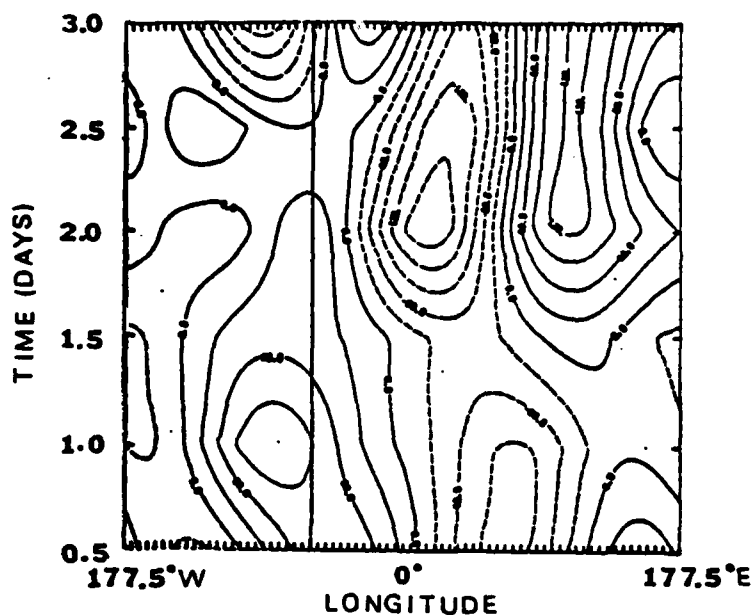
Figure 199. Same as 113 but for 20.5 to 23 day NHW mountain variable tropical heating geopotential field (ϕ_{1-3}) at 10°N. Contour interval is 30 m^2s^{-2}.
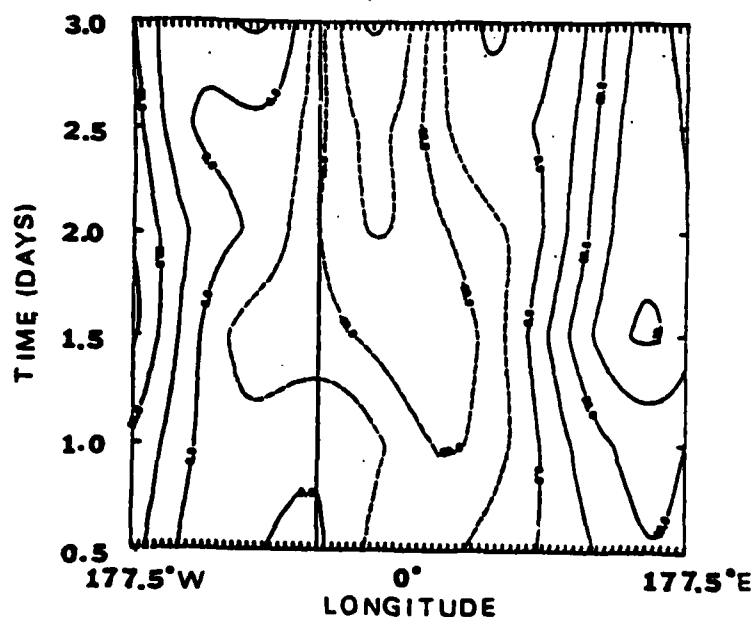
Figure 200. Same as 113 but for 20.5 to 23 day NHW mountain geopotential (ϕ_{1-3}) difference field (variable tropical heating minus zero tropical heating) at 10°N. Contour interval is 30 m^2s^{-2}.
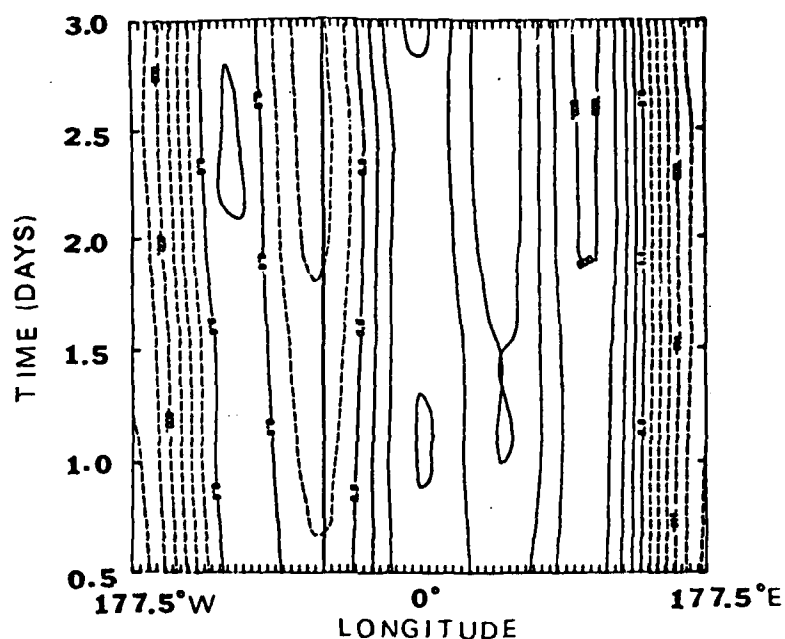
Figure 201. Same as 113 but for 20.5 to 23 day NHW mountain zero tropical heating geopotential field (Φ_{1-3}) at 30°N. Contour interval is 200 m^2s^{-2}.
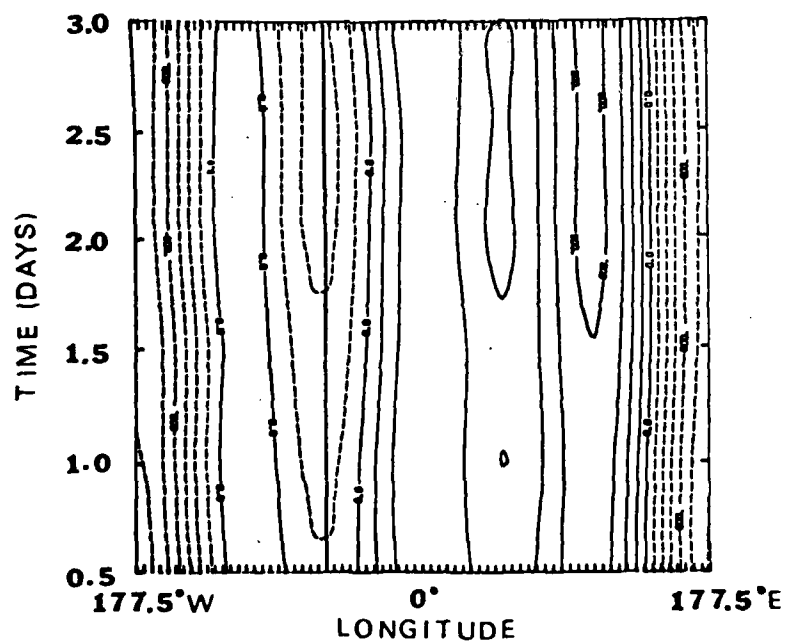
Figure 202. Same as 113 but for 20.5 to 23 day NHW mountain variable tropical heating geopotential field (Φ_{1-3}) at 30°N. Contour interval is 200 m^2s^{-2}.
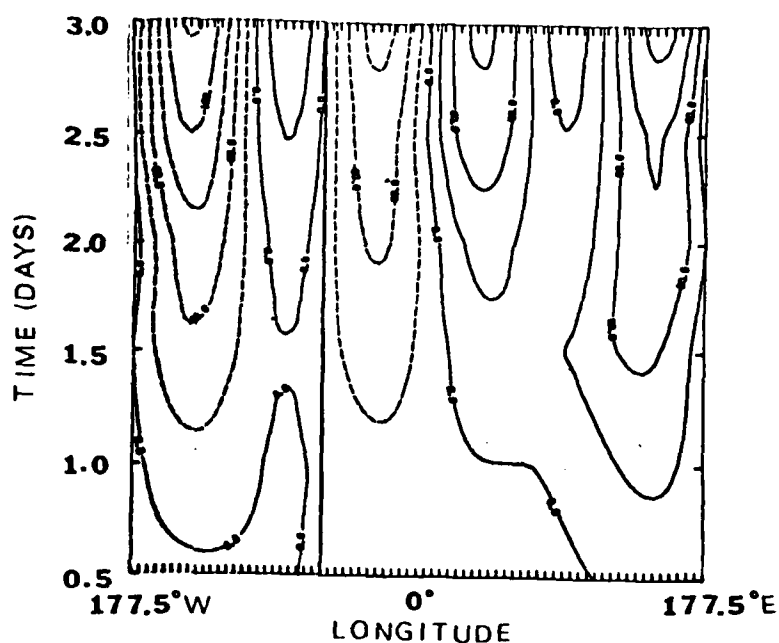
Figure 203. Same as 113 but for 20.5 to 23 day NHW mountain geopotential (Φ_{1-3}) difference field (variable tropical heating minus zero tropical heating) at 30°N. Contour interval is 40 $m^2 s^{-2}$.
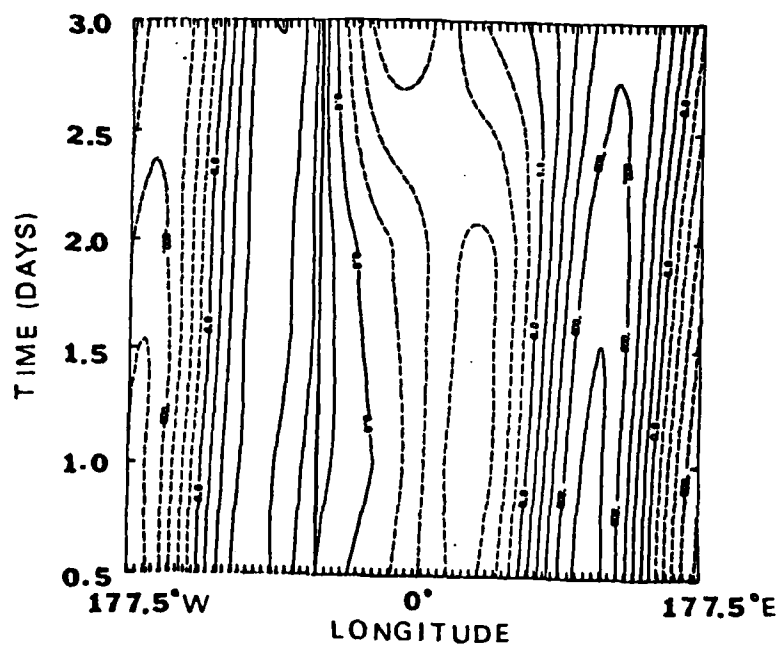
Figure 204. Same as 113 but for 20.5 to 23 day NHW mountain zero tropical heating geopotential field (Φ_{1-3}) at 42°N. Contour interval is 200 $m^2 s^{-2}$.
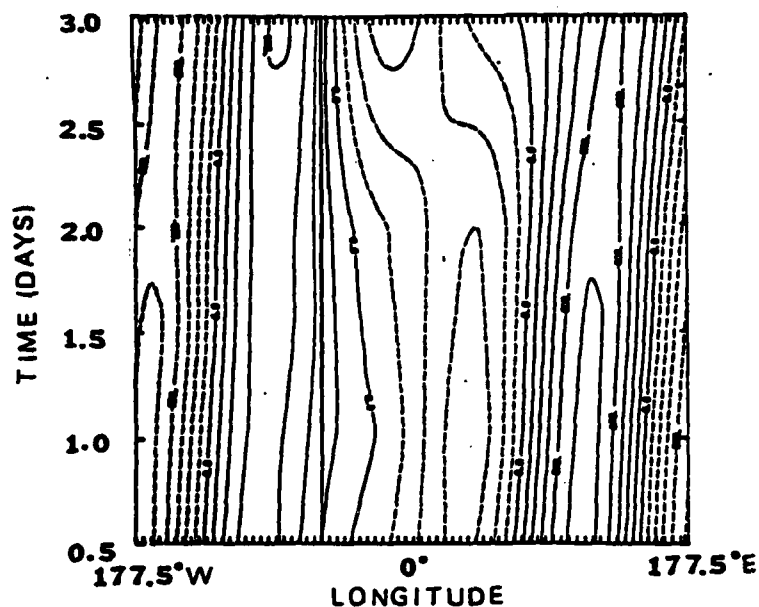
Figure 205. Same as 113 but for 20.5 to 23 day NHW mountain variable tropical heating geopotential field (ϕ_{1-3}) at 42°N. Controu interval is 200 m^2s^{-2}.
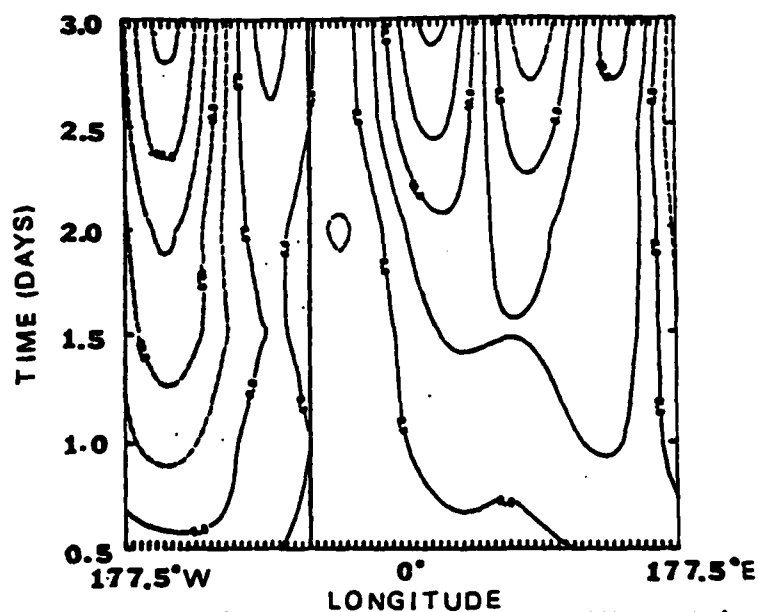
Figure 206. Same as 113 but for 20.5 to 23 day NHW mountain geopotential (ϕ_{1-3}) difference field (variable tropical heating minus zero tropical heating) at 42°N. Contour interval is 20 m^2s^{-2}.

Thus, this experiment suggests that 1/3 of the error in the ultra-long waves between the GISS GCM and the NMC model might be explained by tropical heating. This comparison was carried out for the cases with zero tropical heating and tropical heating remaining at the mean value with the highest precipitation values on the order of 1.5 cm day^{-1}. Thus relating this to forecasts made by the NMC model, if the convection in an area becomes enhanced during a three-day forecast by about 1 cm day^{-1} of rain, then the forecast difference in the long waves between the enhanced case and the actual model results could be significant. This statement is based on two aspects of the two-level model that have become evident in the course of this study. First, the model outflows respond almost immediately (within 12 hours) at large distances ($\geq$2000 km) to changes in the tropical heating pattern. Next, the intensity of the response appears to be directly proportional to the change in the tropical heating.

In concluding this section, it is important to note that the mountains of the northern hemisphere play a major role in the forcing of the ultra-long waves in the two-level model. Also, the various tropical forcing functions were found to affect the ultra-long wave structure of the subtropics and midlatitudes in a lesser amount as compared to the mountain forcing. But, even though the tropical heating did not account for the entire error in the forecast suggested by Baumhefner (1978) (30% ultra-long wave amplitude error difference between the GISS and NMC models), it does account for at least 1/3 of the difference at 42°N and possibly more if the actual tropical forcings are larger than the mean forcing used in the two

level model during the forecast period. As previously mentioned, the effect of tropical heating in the presence of mountains needs to be further quantified in a higher resolution model to determine whether the effect of tropical heating on the ultra-long waves will be increased when the heating effect is better resolved.

5.6 Experiment 3, SHW Forcing with Mountains

This experiment consists of three main cases. Cases one and two are SHW integrations (25 days) to determine the effects of longitudinally variable versus longitudinally uniform tropical heating over the long term in the two-level model. The last case consists of pulsing and unpulsing the Indian monsoonal area to study the short range effect on the model results of the different forcings. The longitudinally variable tropical heating case will be referred to as (SHV) and the uniform heating case as (SHN).

5.6.1 Longitudinally variable tropical heating

The diabatic forcing functions used for the SHV case at the upper and lower levels are given in Figures 207 and 208, respectively. These forcing functions were derived as discussed in the beginning of this chapter.

The initialization was exactly as specified in Section 5.5, the only difference in the two cases being the forcing.

By the 10th day, the 200 mb height field (Figure 209) for the SHV case is quite zonal with the exception of a lee wave trough downwind of the Andes Mountains and another smaller trough downwind of Africa. The height field at the end of the 25th day (Figure 210) no
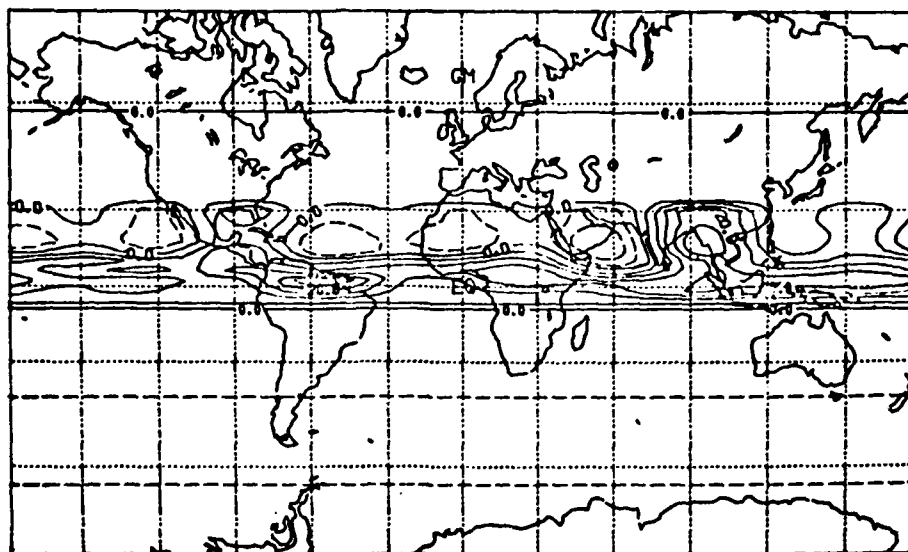
Figure 207. SHW total diabatic forcing function (Q) for upper level
with α=1.   Isolines every ½°K day⁻¹. Contour labels
scaled by 10.
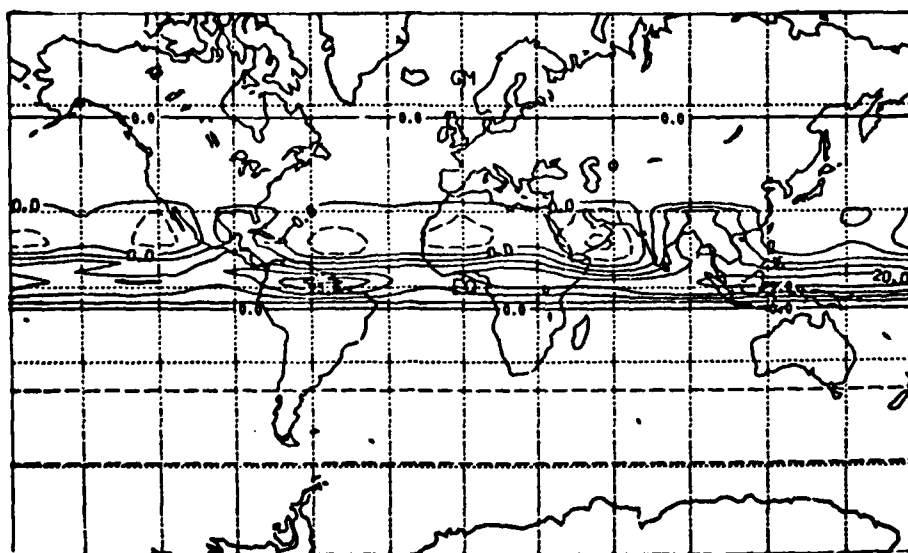
Figure 208. SHW total diabatic forcing function (Q) for lower level
with α=1.   Isolines every ½°K day⁻¹. Contour labels
scaled by 10.

Figure 209. Two-level model, mountain SHW variable tropical heating experiment 200 mb 10 day height field (dm). Contour interval is 6 dm.

Figure 210. Two-level model, mountain SHW variable tropical heating experiment 200 mb 25th day height field (dm). Contour interval of 6 dm.

longer shows a definite response to the mountains as is expected.
The field is composed of a broad range of waves and appears to be
within the realm of atmospheric observation.

The 200 mb zonal (Figure 211) and meridional (Figure 212) com-
ponents of the velocity at the 25th day for the SHV case show that
strong southern hemisphere midlatitude and subtropical wave activity
is definitely present by this time. The 200 mb meridional divergent
wind field (Figure 213) also reflects the wave activity in the south-
ern hemisphere. Again, as in the NHW cases, the divergent flows due
to the baroclinic waves are superimposed upon the larger scale diver-
gent outflows from the most strongly heated areas in the summer hemi-
sphere. A divergent outflow from the most strongly heated region to
the north and west of Australia of -2 ms^{-1} is clearly visible in
Figure 213. Table VII gives the 25th day zonal average meridional
wind at the upper and lower levels of the model.

5.6.2 Longintudinally uniform tropical heating

The 200 mb meridional divergent component of the velocity at the
25th day for the SHN case is given in Figure 214. The divergent out-
flow regions shown in this figure are somewhat different from those
of Figure 213. For example, the area of strongest monsoonal outflow
to the north and west of Australia in Figure 213 is much weaker in
Figure 214.

The five-day average 200 mb zonal wind fields (over days 20 to
25) for the SHN and SHV cases are given in Figures 215 and 216. The
SHN 200 mb zonal wind (Figure 215) and the SHV 200 mb zonal wind
(Figure 216) appear quite similar in the southern hemisphere. There
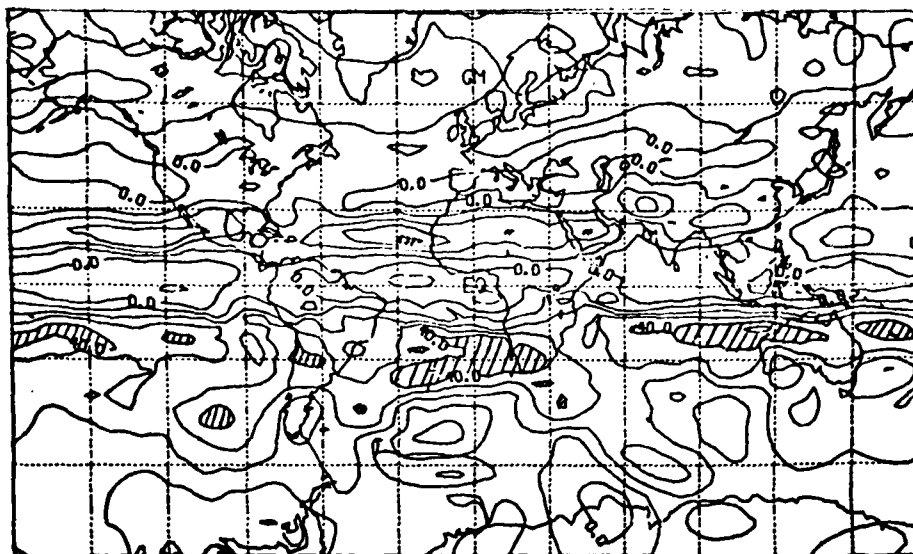
Figure 211. Two-level model, mountain SHW variable tropical heating
experiment 200 mb 25th day zonal wind component (ms^{-1}).
Contour interval is 10 ms^{-1}.
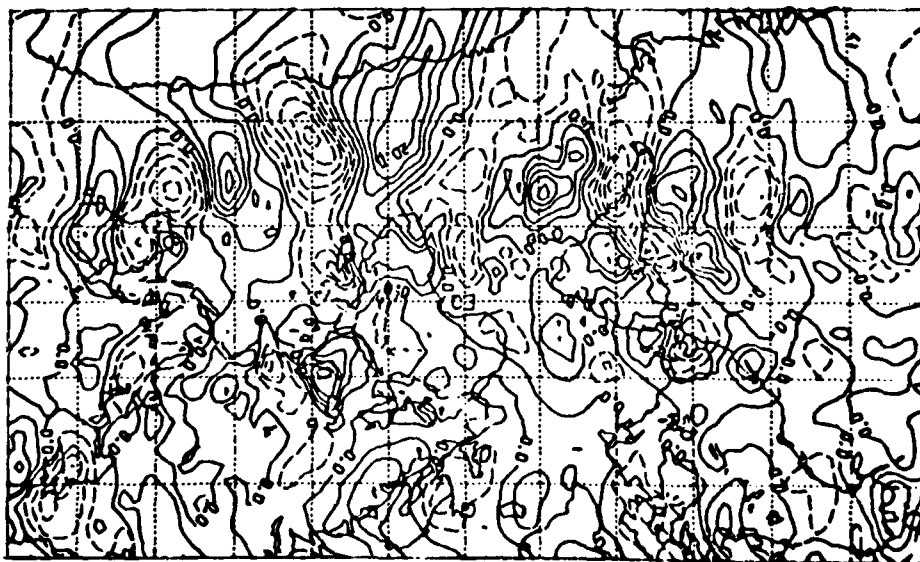
Figure 212. Two-level model, mountain SHW variable tropical heating
Experiment 200 mb 25th day meridional velocity component
(ms^{-1}). Contour interval is 5 ms^{-1} with negative contours
dashed.
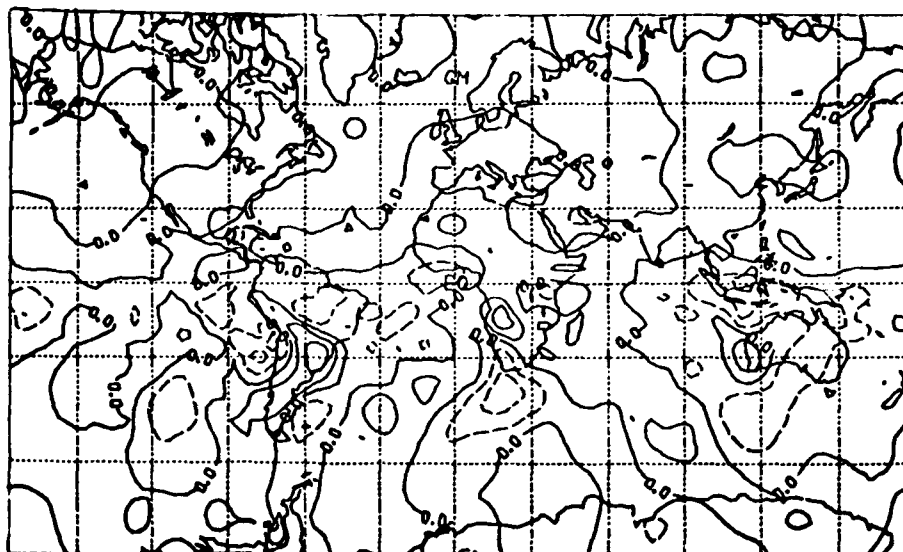
Figure 213. Two-level model, mountain SHW variable tropical heating experiment 200 mb 25th day meridional divergent wind component (ms^{-1}). Contour interval is 1 ms^{-1} with negative contours dashed.
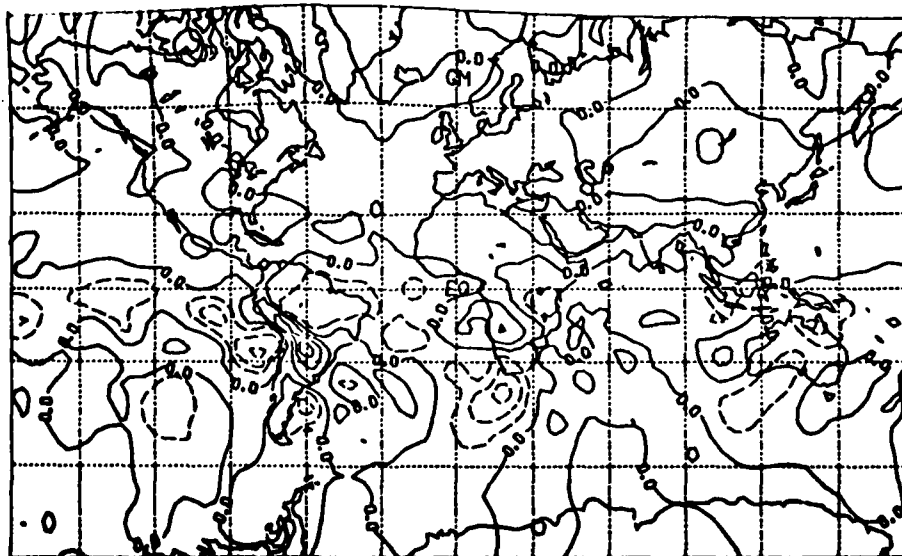
Figure 214. Two-level model, mountain SHW uniform tropical heating experiment 200 mb 25th day zonal divergent wind component (ms^{-1}). Contour interval is 1 ms^{-1} with negative contours dashed.
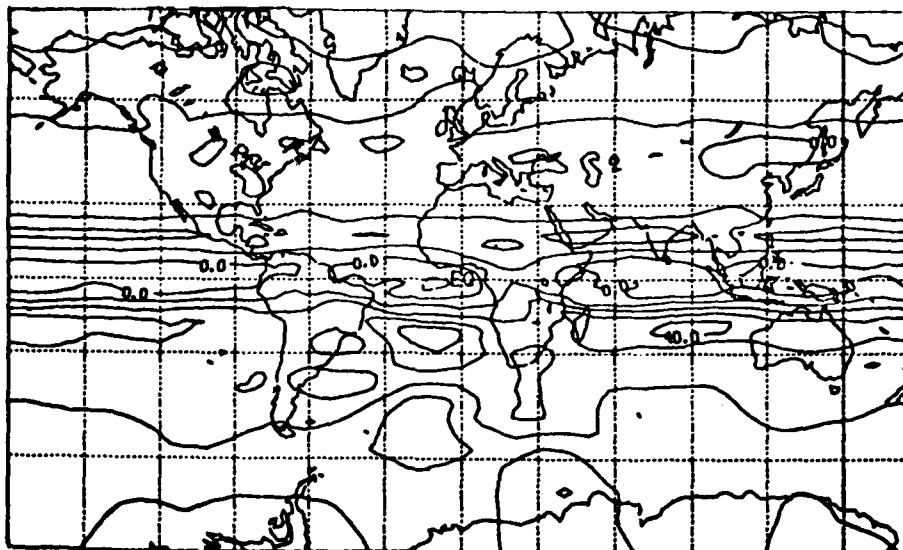
Figure 215. Two-level model, mountain SHW uniform tropical heating
experiment 200 mb 5-day average (days 20-25) zonal wind
component (ms^{-1}). Contour interval is 10 ms^{-1} with
negative contours dashed.
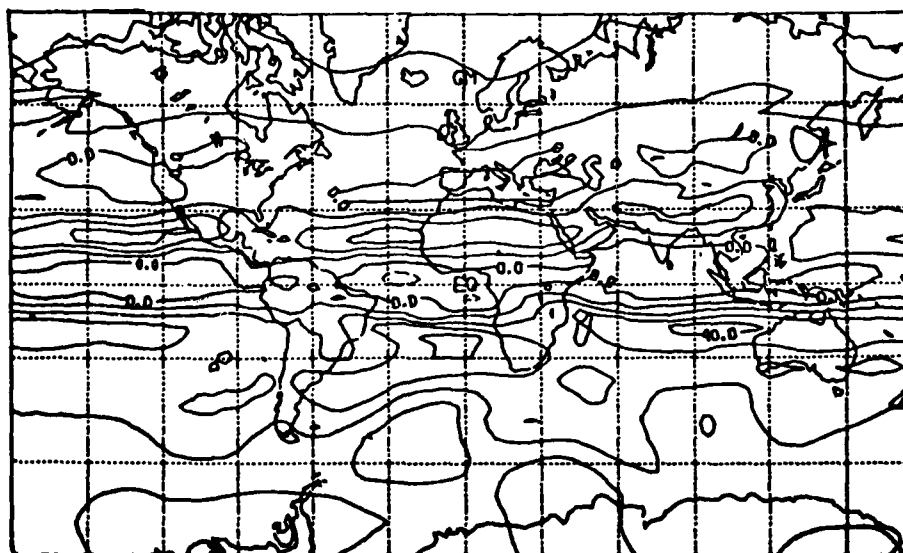
Figure 216. Two-level model, mountain SHW variable tropical heating
experiment 200 mb 5-day average (days 20-25) zonal wind
component (ms^{-1}). Contour interval is 10 ms^{-1} with
negative contours dashed.

TABLE VII

The Zonal Average Meridional Velocity Component for SHW Experiment

Latitude	200 mb	~700 mb
	Day 25	
84N	0.0	-0.0
80N	0.0	-0.0
76N	0.2	-0.1
72N	0.2	-0.1
68N	0.0	0.0
64N	-0.1	0.1
60N	-0.1	0.1
56N	0.0	0.0
52N	0.2	-0.0
48N	0.2	-0.1
44N	0.3	-0.2
40N	0.2	-0.1
36N	0.2	-0.1
32N	0.1	-0.1
28N	0.1	-0.1
24N	0.2	-0.1
20N	0.2	-0.2
16N	0.3	-0.3
12N	0.3	-0.3
8N	0.1	-0.2
4N	-0.1	-0.0
0	-0.6	0.3
4S	-0.7	0.4
8S	-0.8	0.3
12S	-0.5	0.2
16S	-0.3	0.0
20S	-0.2	-0.0
24S	-0.2	-0.1
28S	-0.1	-0.1
32S	-0.1	-0.0
36S	-0.1	-0.1
40S	-0.1	-0.0
44S	-0.2	0.0
48S	-0.3	0.1
52S	-0.2	0.0
56S	0.0	-0.1
60S	0.1	-0.1
64S	0.2	-0.1
68S	0.0	-0.0
72S	-0.1	0.1
76S	-0.1	0.0
80S	-0.1	0.1
84S	-0.1	0.0

are two jets; one near Australia and the other downwind of South
America, of equal magnitude in both figures. The better 200 mb jet
positions as compared to Newell et al. (1972) Plate 3.19 and Figure
26 appear to be given in the SHV case zonal wind field.

In the northern hemisphere, the 200 mb jets of the SHV case
occur much too close to the equator, although the longitudinal posi-
tioning of these jets is in fair agreement with the jets given in
Figure 26. The SHN northern hemisphere 200 mb zonal wind field
(Figure 215) has mainly a zonal structure with much weaker jets than
the SHV case.

In the observed 200 mb SHW average zonal wind fields given in
Newell et al. (1972) and Figure 26 the strongest jet (50 ms^{-1} or
greater) is located across Australia near 30°S. The SHV and SHN
experiments produce jets near Australia with similar magnitudes. The
reason for this is not entirely clear, but it could be partially in
response to the heating field used in the SHV case (Figures 207 and
208). These forcing functions may have too much uniform structure
near the equator where the largest zonal average heatings occur.

The 25th day difference field of 200 mb zonal wind fields (SHV
minus SHN) is given in Figure 217. Here the main differences in
response to the heating lie in the northern hemisphere, although the
two main 200 mb jet areas in the southern hemisphere are about
10 ms^{-1} stronger in the SHV case. The kinetic energy difference
field is given in Figure 218 and is quite similar to the zonal wind
difference field.

The 200 mb geopotential (Φ=gz) difference field is given in
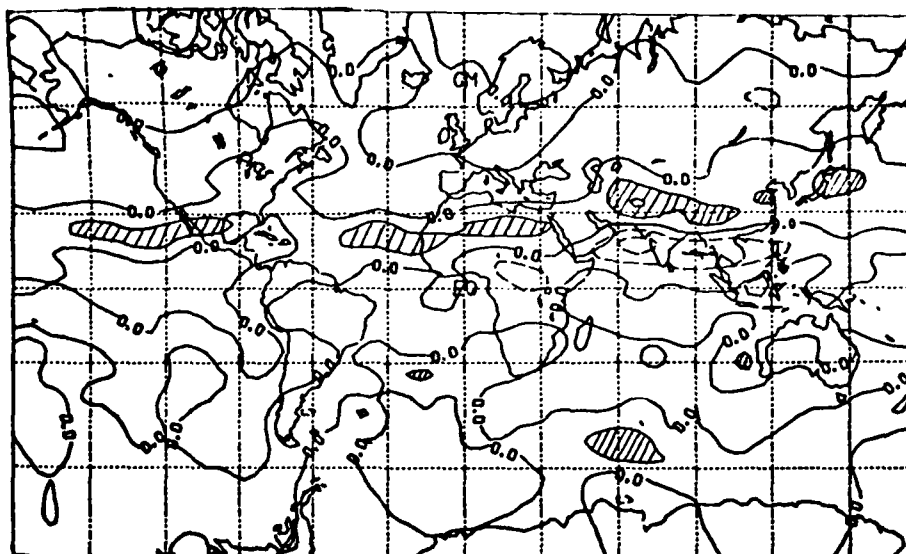
Figure 217. Two-level model, mountain SHW 200 mb 25th day zonal wind component difference field (variable tropical heating minus uniform tropical heating)(ms^{-1}). Contour interval is 10 ms^{-1} with negative contours dashed.
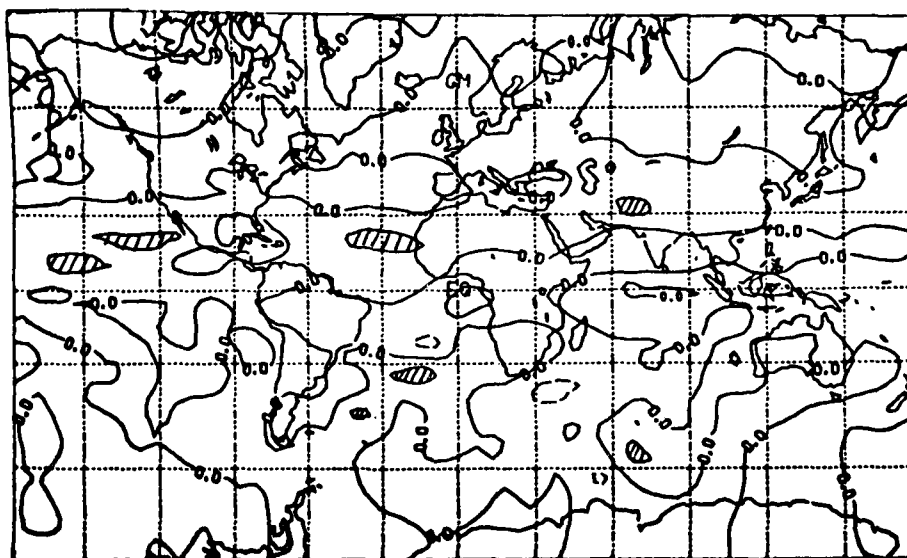
Figure 218. Two-level model, mountain SHW 200 mb 25th day kinetic energy difference field (variable tropical heating minus uniform tropical heating)(m^2s^{-2}). Contour interval is 300 m^2s^{-2} with negative contours dashed.

Figure 219. This field is a sensitive measure to changes in the heating pattern. The largest changes in the southern hemisphere occur basically to the south of the more strongly heated areas. The actual SHN and SHV height fields are given in Figures 220 and 221. The changes in the 200 mb height field due to differences in the heating mainly occur in the intensity rather than the positioning of the large scale features. This suggests, as previously postulated for the NHW case, that mountains may play some role in focusing the energy provided by the tropical heat sources. This point must remain relatively speculative and deserves further study since the only real mountain barrier of the southern hemisphere is the relatively narrow Andes.

5.6.3 Pulsed heating experiments

The next case studies the changes in the flow patterns of the model induced by unpulsing and pulsing the Indian monsoonal area in the northern hemisphere. The upper level of the pulsed and unpulsed forcing functions is given in Figures 222 and 223, respectively.

The pulsed and unpulsed forcing regions in the SHW case are located further from the equator than the NHW experiment pulsed and unpulsed regions. In the SHW case, the pulsing is centered at $20^{\circ}N$ while in the NHW case it is centered near $10^{\circ}S$ (see Figure 91).

In the analysis presented in Paegle (1978) where a two-level model (with constant coriolis parameter f) is diabatically forced, it is found that for larger values of f (where the Rossby radius of deformation $\lambda=(c/f)$ is smaller) that the divergent response to the diabatic forcing is diminished. Thus from Paegle's study and others,
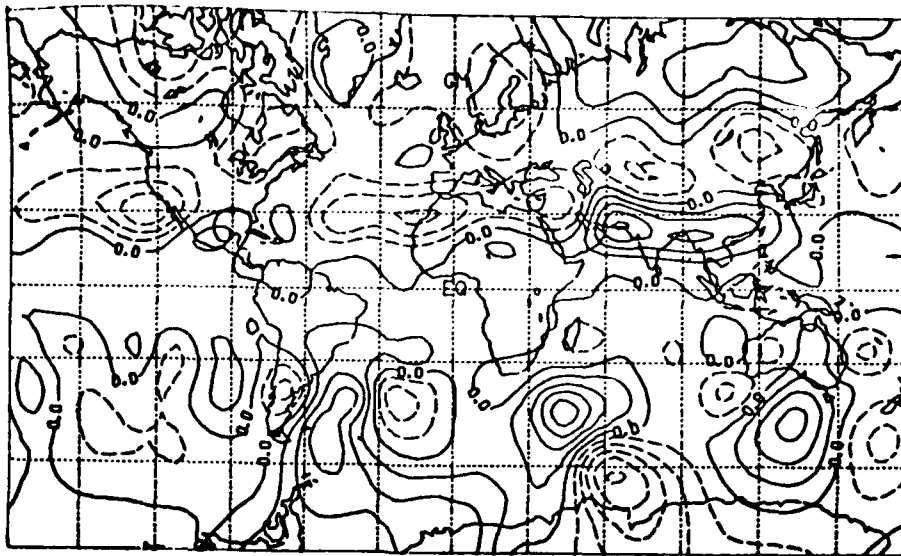
Figure 219. Two-level model, mountain SHW 25th day geopotential field difference (variable tropical heating minus uniform tropical heating)(m^2s^{-2}). Contour interval is 300 m^2s^{-2} with negative contours dashed.
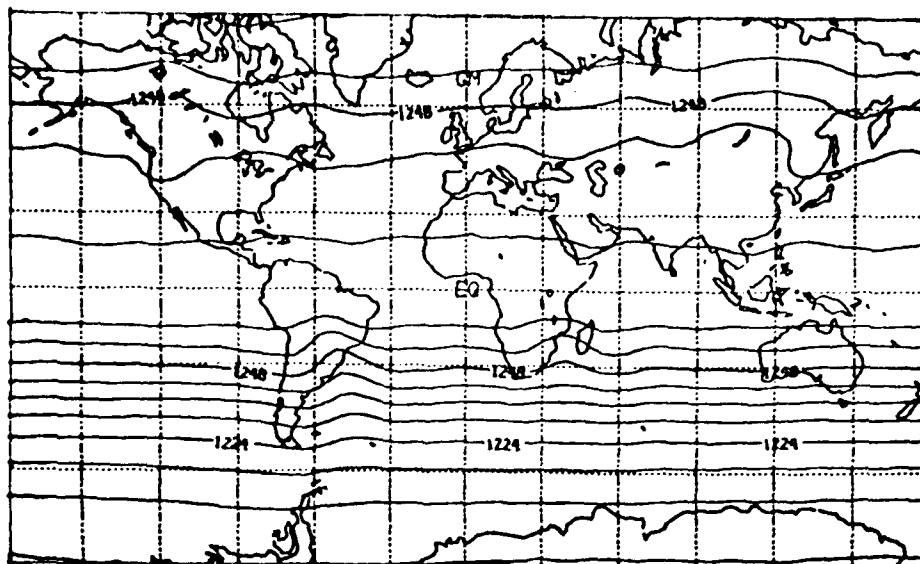

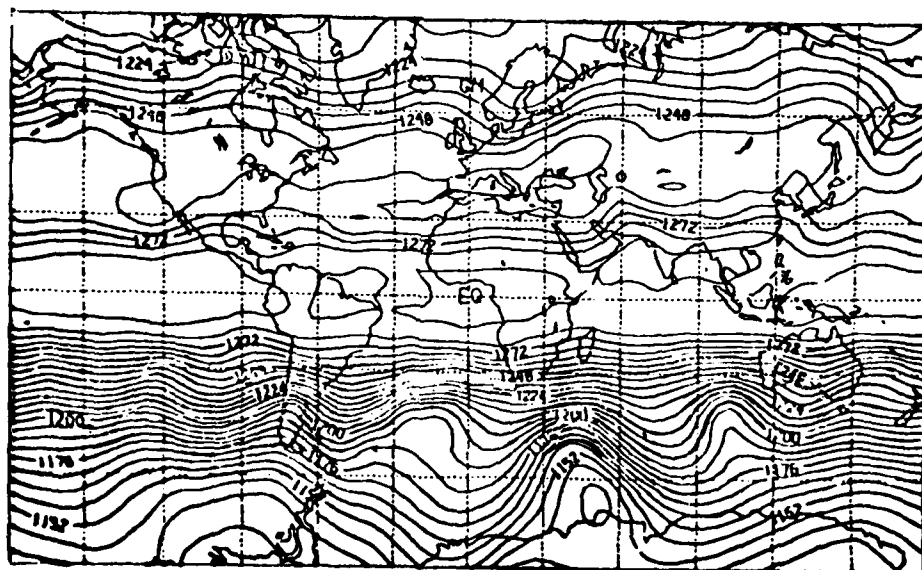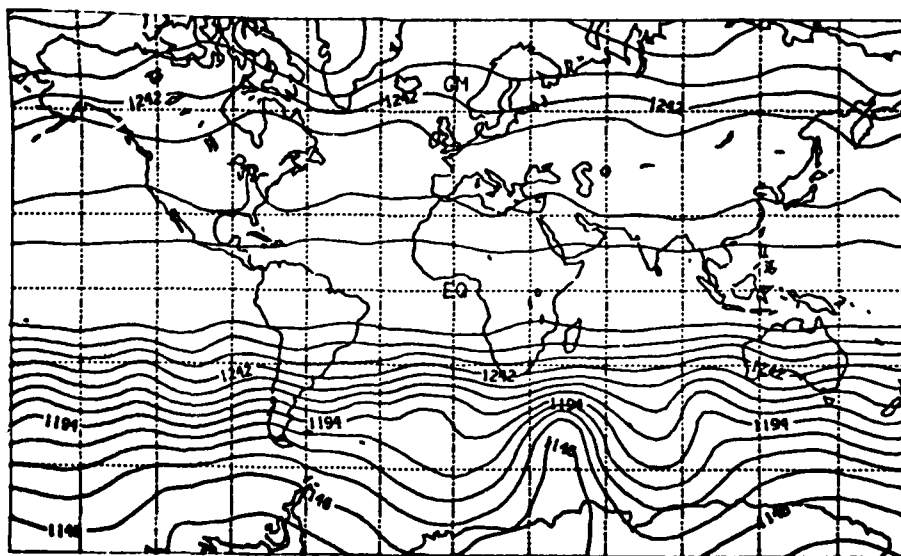Figure 220. Two-level model, mountain SHW uniform tropical heating 25th day height field (dm). Contour interval is 12 dm.

Figure 221. Two-level model, mountain SHW variable tropical heating experiment 200 mb 25th day height field (dm). Contour interval is 12 dm.

Figure 222. SHW total pulsed diabatic forcing function (Q) for upper level with $\alpha=1$. Isolines every 1^0K day^{-1}. Contour labels scaled by 10.

Figure 223. SHW total unpulsed diabatic forcing function (Q) for upper level with $\alpha \approx 1$. Isolines every $1^{\circ}K$ day^{-1}. Contour labels scaled by 10.

Figure 224. Two-level model, mountain SHW variable tropical heating 200 mb unpulsed 25th day kinetic energy ($m^2 s^{-2}$). Contour interval is 500 $m^2 s^{-2}$.

a larger portion of the energy of the SHW large scale pulsing (centered at 20°N) might be expected to go into the rotational part of the flow in the northern hemisphere. And, conversely, a lesser portion of the kinetic energy change should occur in the southern hemisphere of the NHW experiments. Comparing subsequent diagrams with Figure 163 (the 200 mb NHW kinetic energy difference field, pulsed minus unpulsed) appears to verify the point.

The 25th day, 200 mb kinetic energies for the unpulsed and pulsed SHW cases are given in Figures 224 and 225, respectively, while the 25th day, 200 mb kinetic energy difference field is given in Figure 226. Two main areas of kinetic energy increase can be seen. One corresponds to the pulsed/unpulsed region while the other is to the south of the pulsed/unpulsed region and in the southern hemisphere. The maximum 200 mb kinetic energy difference in the northern hemisphere is about 380 m^2s^{-2} while in the southern hemisphere the change is approximately 260 m^2s^{-2}. Thus as previously postulated, more of the kinetic energy appears to go into the local rotational field near 20°N than is propagated into the southern hemisphere.

The 200 mb zonal wind difference field after three days of steady pulsing and unpulsing (day 25) is given in Figure 227. As previously noted, a sizeable portion of the acceleration difference does appear to go into the rotational part of the flow in the northern hemisphere. But there are still two areas of acceleration in the southern hemisphere near Australia of maxima 7 and 8 ms^{-1}.

The 200 mb divergent meridional velocity component (Figure 228) for the pulsed case at day 25 (three days after pulsing) shows a
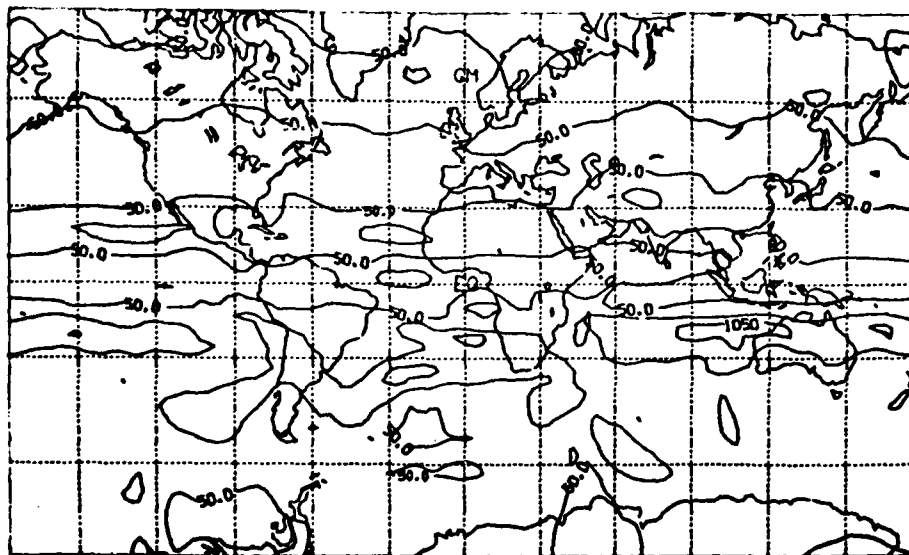
Figure 225. Two-level model mountain SHW variable tropical heating 200 mb pulsed 25th day kinetic energy (m^2s^{-2}). Contour interval is 500 m^2s^{-2}.
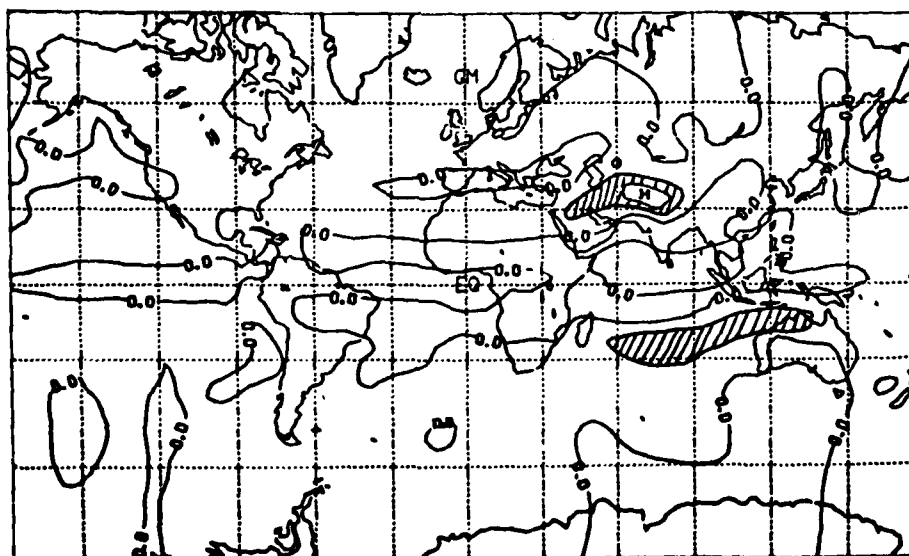
Figure 226. Two-level model, mountain SHW variable tropical heating 200 mb 25th day kinetic energy difference field (pulsed minus unpulsed)(m^2s^{-2}). Contour interval is 150 m^2s^{-2} with negative contours dashed.
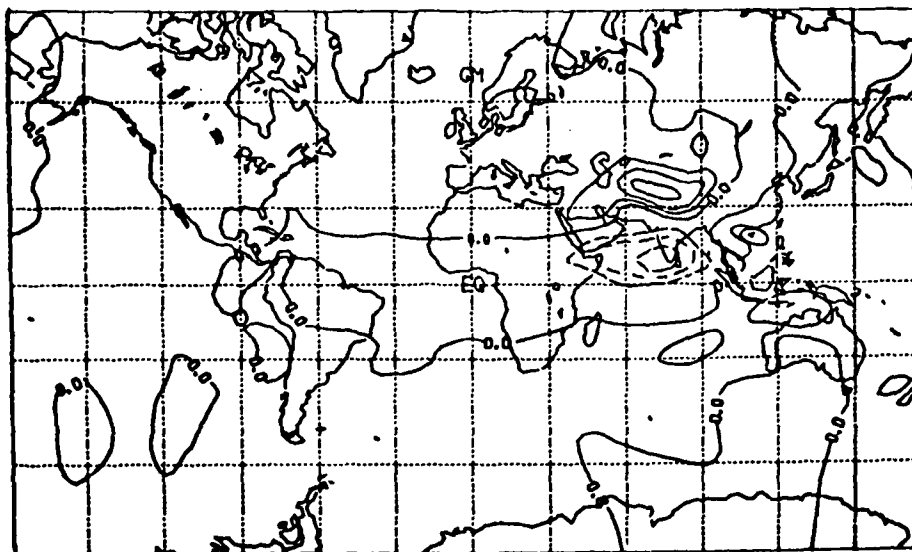
Figure 227. Two-level model, mountain SHW variable tropical heating 200 mb 25th day zonal wind difference field (pulsed minus unpulsed)(ms^{-1}). Contour interval is 5 ms^{-1} with negative contours dashed.
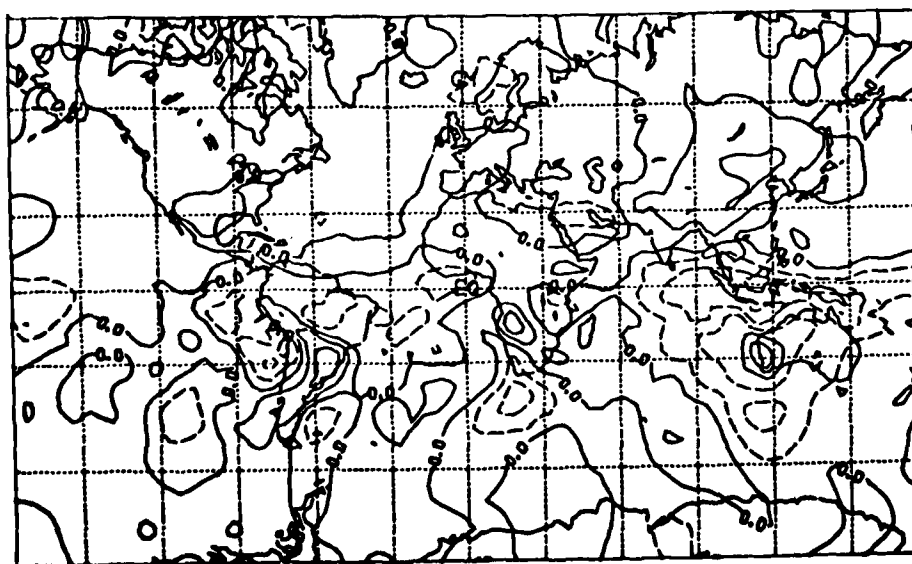
Figure 228. Two-level model, mountain SHW variable tropical heating 200 mb pulsed 25th day meridional divergent wind field (ms^{-1}). Contour interval is 1 ms^{-1} with negative contours dashed.

substantial response in the divergent flow field to the south and north of the pulsed area. The 25th day 200 mb unpulsed divergent meridional component (Figure 229) shows a local reversal in the divergent flow in the unpulsed area.

The difference in the 200 mb geopotential field ($\Phi=gz$) at the 25th day is given in Figure 230. The response in the vicinity of the pulsed/unpulsed region of this field is almost identical to the response in the pulsed/unpulsed region of the NHW mountain case (Figure 116).

To determine if the small change in the total height for the southern hemisphere given in Figure 230 is significant when compared to the amplitude in the ultra-long waves, Hovmöller diagrams of Φ_{1-3} for the unpulsed, pulsed and difference fields were computed. These diagrams are given at $42^\circ S$, $30^\circ S$, $10^\circ S$, $10^\circ N$, $30^\circ N$ and $42^\circ N$ in Figures 231 through 248. The results of these figures are summarized in Table VIII.

The relative effect of the three-day heating on the ultra-long waves in the SHW case with mountains appears stronger at $42^\circ S$ than in the NHW mountain case at $42^\circ N$ (26% change versus 18% change). This difference is due mainly to the fact that the mountains in the northern hemisphere force higher amplitudes in the ultra-long wave patterns In fact, comparing Tables III (no mountain NHW experiment), V (mountain NHW experiment), and VIII (mountain SHW experiment) the maximum difference in the amplitudes of the ultra-long waves in response to pulsed and unpulsed heatings are very similar (except for $30^\circ N$ of the SHW case) in comparison of the same seasons in opposite hemispheres.
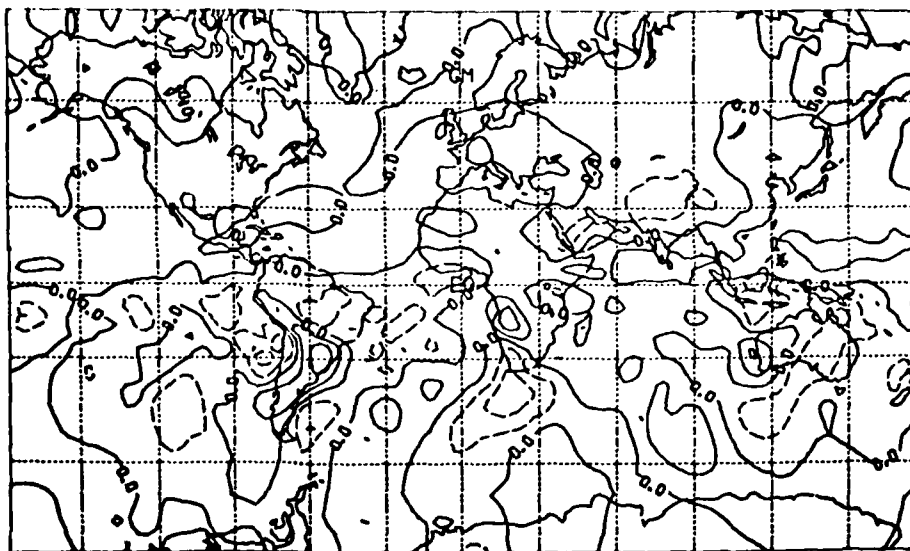
Figure 229. Two-level model, mountain SHW variable tropical heating 200 mb unpulsed 25th day meridional divergent wind field (ms^{-1}). Contour interval is 1 ms^{-1} with negative contours dashed.

Figure 230. Two-level model, mountain SHW variable tropical heating 200 mb 25th day geopotential difference field (pulsed minus unpulsed)(m^2s^{-2}). Contour interval is 150 m^2s^{-2} with negative contours dashed.
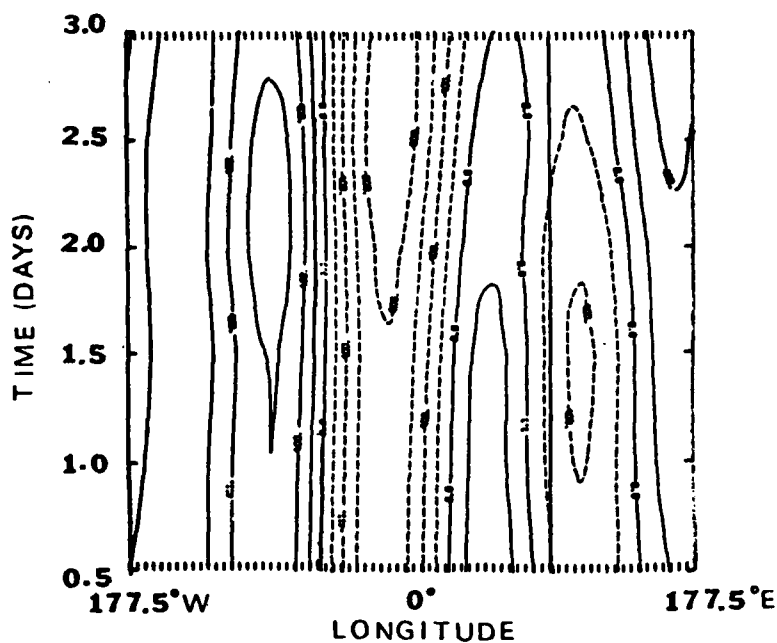
Figure 231. Same as 113 but for 22.5 to 25 day SHW mountain unpulsed geopotential field (ϕ_{1-3}) at 42°S. Contour interval is 200 m^2s^{-2}.
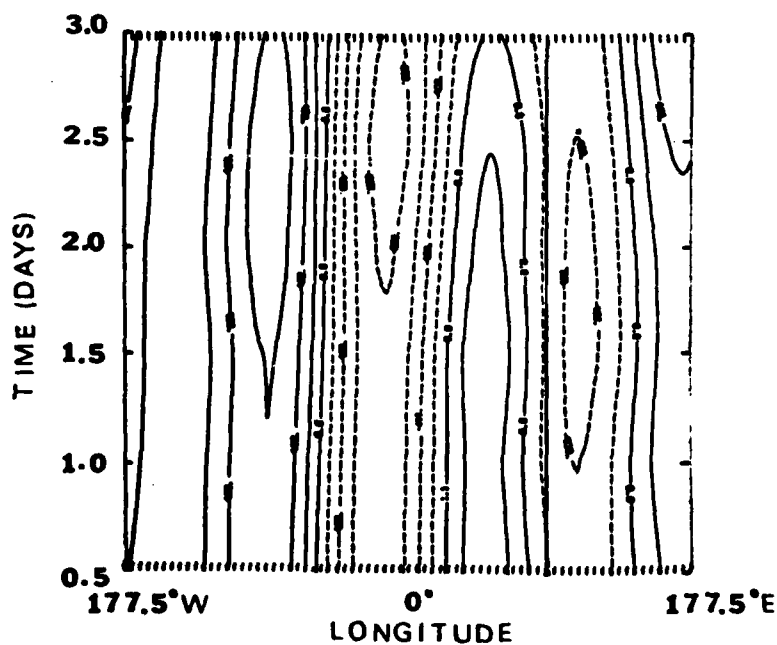
Figure 232. Same as 113 but for 22.5 to 25 day SHW mountain pulsed geopotential field (ϕ_{1-3}) at 42°S. Contour interval is 200 m^2s^{-2}.
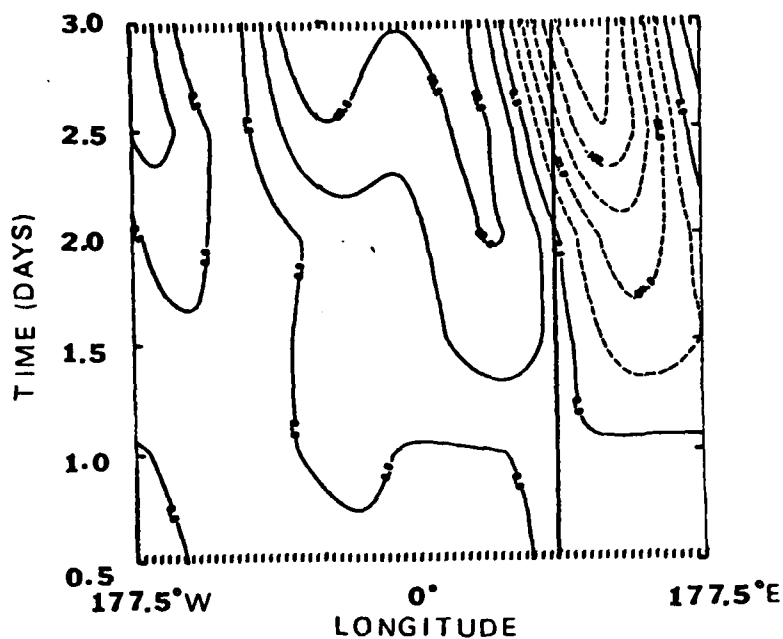
Figure 233. Same as 113 but for 22.5 to 25 day SHW mountain geopotential difference field (Φ_{1-3}) (pulsed minus unpulsed) at 42°S. Contour interval is 40 m^2s^{-2}.

Figure 234. Same as 113 but for 22.5 to 25 day SHW mountain unpulsed geopotential field (Φ_{1-3}) at 30°S. Contour interval is 100 m^2s^{-2}.

Figure 235. Same as 113 but for 22.5 to 25 day SHW mountain pulsed
geopotential field (Φ_{1-3}) at 30°S. Contour interval is
200 $m^2 s^{-2}$.

Figure 236. Same as 113 but for 22.5 to 25 day SHW mountain geopo-
tential difference field (Φ_{1-3}) (pulsed minus unpulsed)
at 30°S. Contour interval is 60 $m^2 s^{-2}$.

Figure 237. Same as 113 but for 22.5 to 25 day SHW mountain unpulsed geopotential field (Φ_{1-3}) at 10^0S. Contour interval is 60 m^2s^{-2}.

Figure 238. Same as 113 but for 22.5 to 25 day SHW mountain pulsed geopotential field (Φ_{1-3}) at 10^0S. Contour interval is 30 m^2s^{-2}.

Figure 239. Same as 113 but for 22.5 to 25 day SHW mountain geopo-
tential difference field (Φ_{1-3}) (pulsed minus unpulsed)
at 10°S. Contour interval is 40 m^2s^{-2}.

Figure 240. Same as 113 but for 22.5 to 25 day SHW mountain unpulsed
geopotential field (Φ_{1-3}) at 10°N. Contour interval is
40 m^2s^{-2}.

Figure 241. Same as 113 but for 22.5 to 25 day SHW mountain pulsed geopotential field (Φ_{1-3}) at 10^{0}N. Contour interval is 40 m^2s^{-2}.

Figure 242. Same as 113 but for 22.5 to 25 day SHW mountain geopotential difference field (Φ_{1-3}) (pulsed minus unpulsed) at 10^{0}N. Contour interval is 60 m^2s^{-2}.
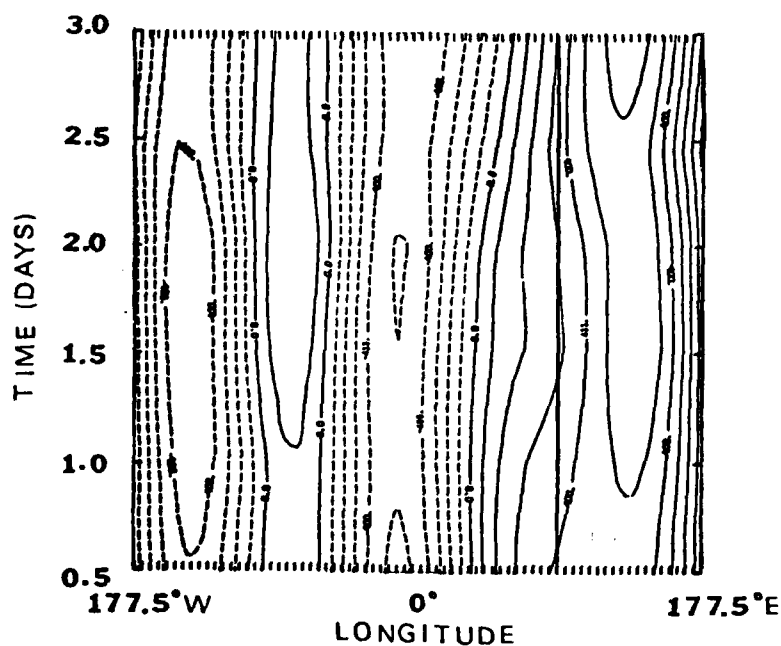
Figure 243. Same as 113 but for 22.5 to 25 day SHW mountain unpulsed geopotential field (Φ_{1-3}) at 30°N. Contour interval is 100 m^2s^{-2}.
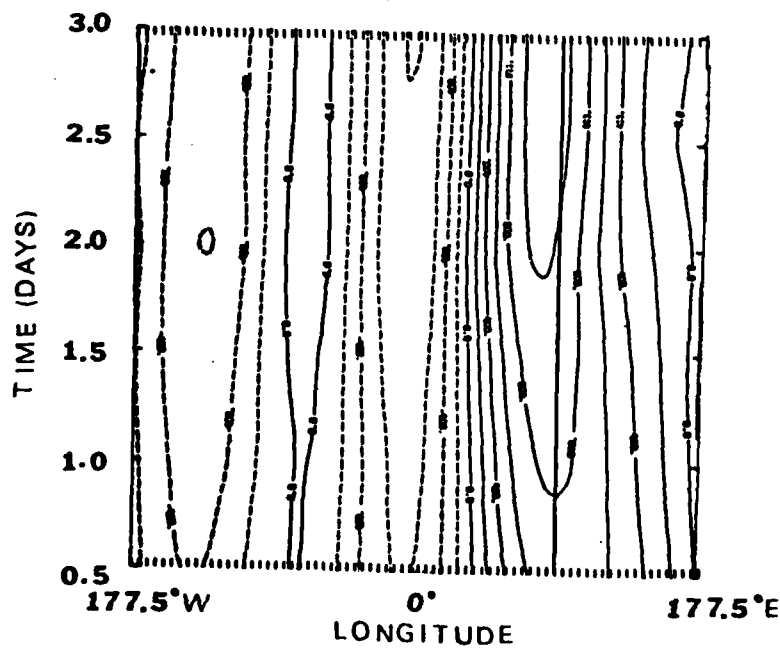
Figure 244. Same as 113 but for 22.5 to 25 day SHW mountain pulsed geopotential field (Φ_{1-3}) at 30°N. Contour interval is 200 m^2s^{-2}.
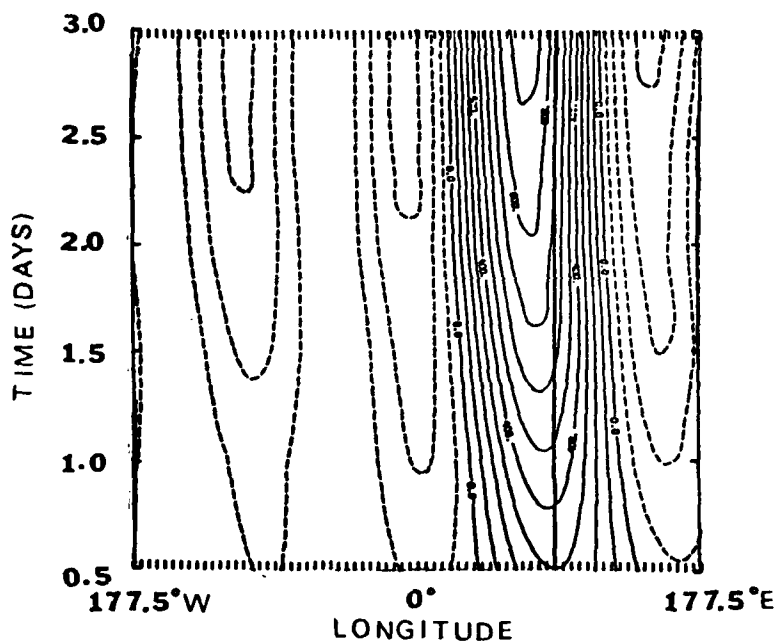
Figure 245. Same as 113 but for 22.5 to 25 day SHW mountain geopotential difference field (Φ_{1-3}) (pulsed minus unpulsed) at 30°N. Contour interval is 100 $m^2 s^{-2}$.
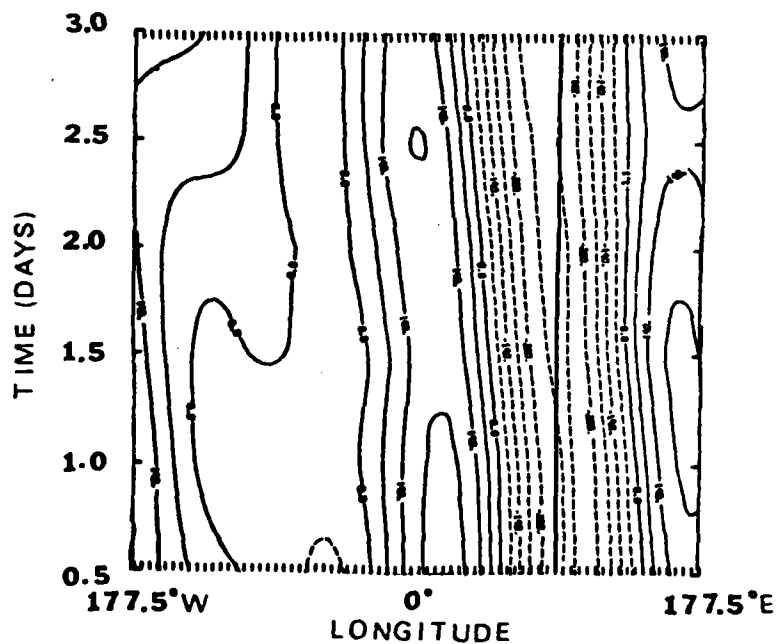
Figure 246. Same as 113 but for 22.5 to 25 day SHW mountain unpulsed geopotential field (Φ_{1-3}) at 42°N. Contour interval is 70 $m^2 s^{-2}$.
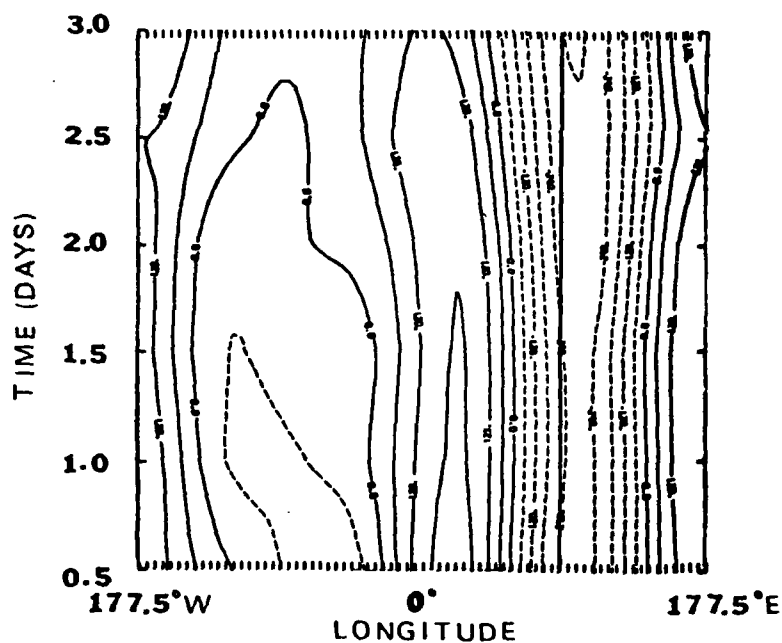
Figure 247. Same as 113 but for 22.5 to 25 day SHW mountain pulsed geopotential field (Φ_{1-3}) at 42°N. Contour interval is 60 m^{2}s^{-2}.
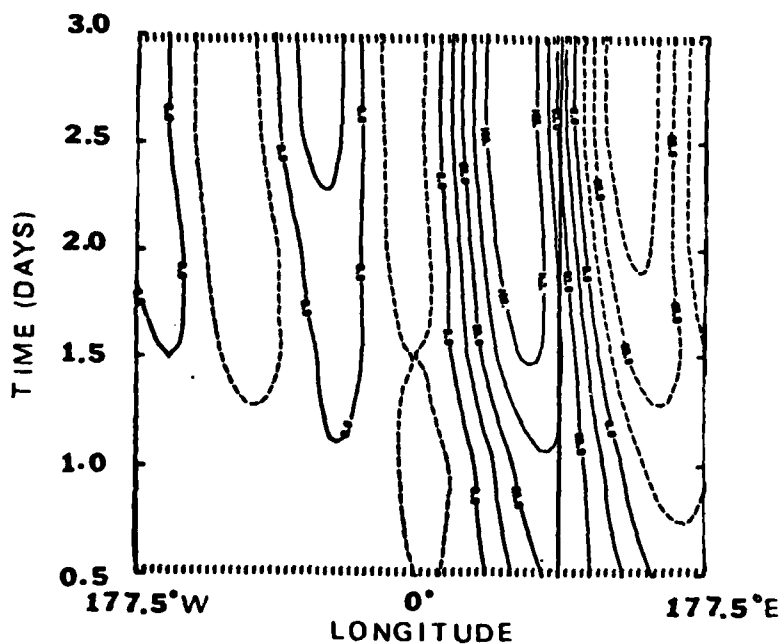
Figure 248. Same as 113 but for 22.5 to 25 day SHW mountain geopotential difference field (Φ_{1-3}) (pulsed minus unpulsed) at 42°N. Contour interval is 40 m^{2}s^{-2}.

TABLE VIII

Same as Table III but for the SHW mountain pulsed and unpulsed cases

Latitude	Maximum pulsed amplitude $(m^2 s^{-2})$	Maximum unpulsed amplitude $(m^2 s^{-2})$	Maximum Difference $(m^2 s^{-2})$	% Change
Days 22.5 - 25				
42°S	800	800	200	25%
30°S	900	800	240	26%
10°S	150	240	200	83%
10°N	160	200	300	150%
30°N	1000	600	900	90%
42°N	300	350	160	46%
Days 25.5 - 28				
42°S	1000	1000	420	42%
30°S	1000	700	280	28%

The 200 mb (28th day) height fields after six days of steady pulsing and unpulsing are given in Figures 249 and 250, respectively. The 200 mb height difference field for these two fields is given in Figure 251. Again, considering the different positions of the pulsings, this field is very similar to the height difference field after six days of pulsing in the NHW case (see Figure 182). The Hovmöller diagrams (unpulsed, pulsed and difference) for the sixth day of pulsed/unpulsed forcing at 42°S and 30°S are given in Figures 252 through 257. These diagrams are also summarized in Table VIII.
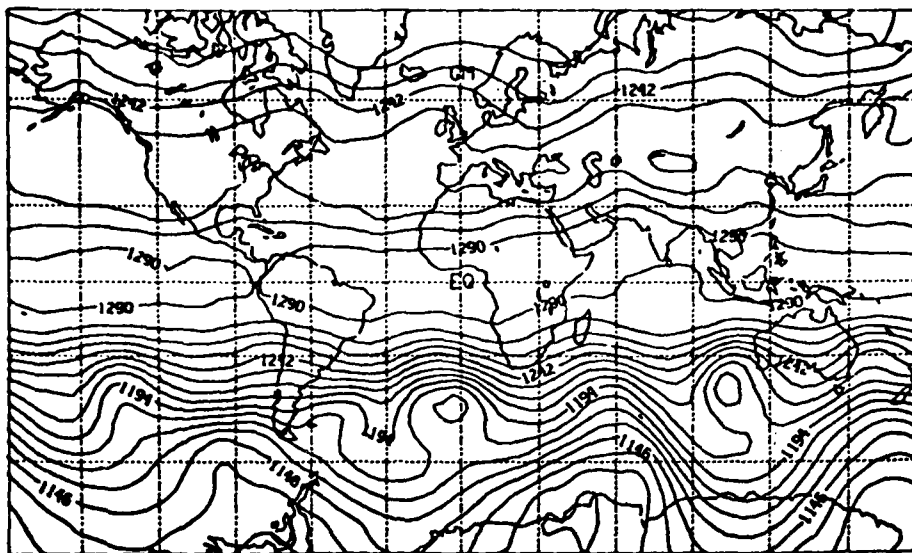
Figure 249. Two-level model, mountain SHW variable pulsed tropical heating experiment 200 mb 28th day height field (dm). Contour interval is 12 dm.
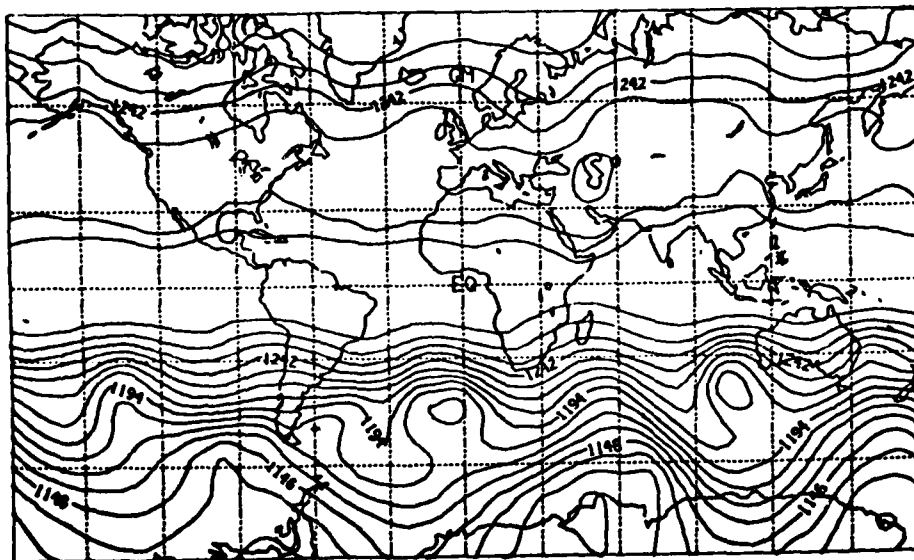
Figure 250. Two-level model mountain SHW variable unpulsed tropical heating experiment 200 mb 28th day height field (dm). Contour interval is 12 dm.
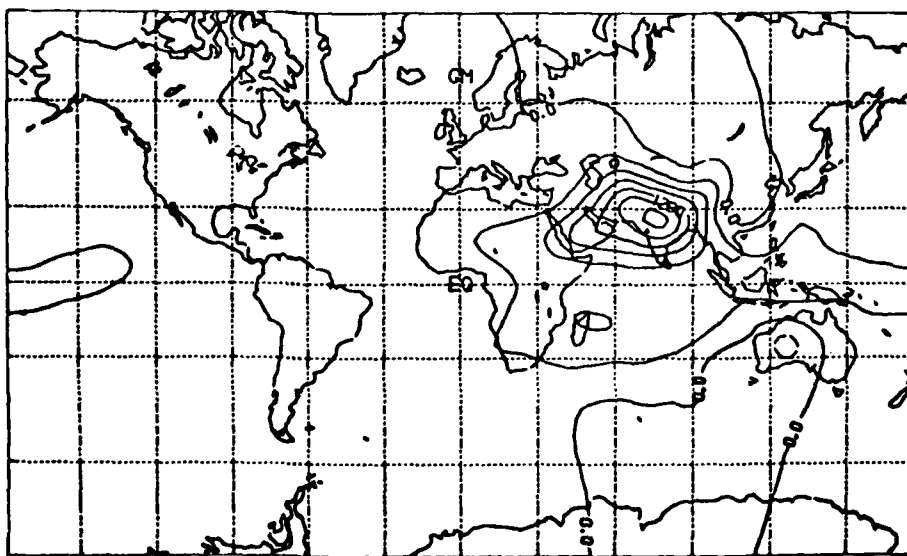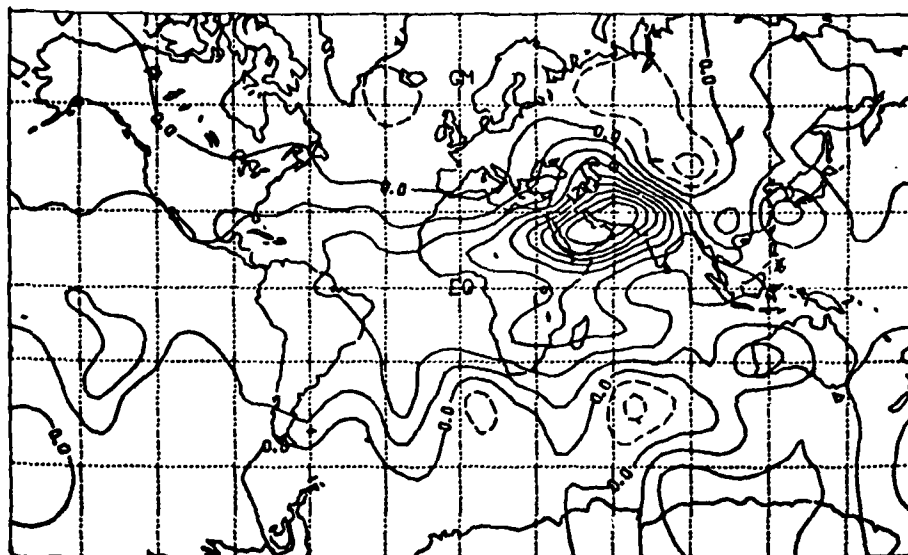
Figure 251. Two-level model mountain SHW variable tropical heating 200 mb 28th day geopotential difference field ($\Phi=gz$) (pulsed minus unpulsed)(m^2s^{-2}). Contour interval is 300 m^2s^{-2} with negative contours dashed.
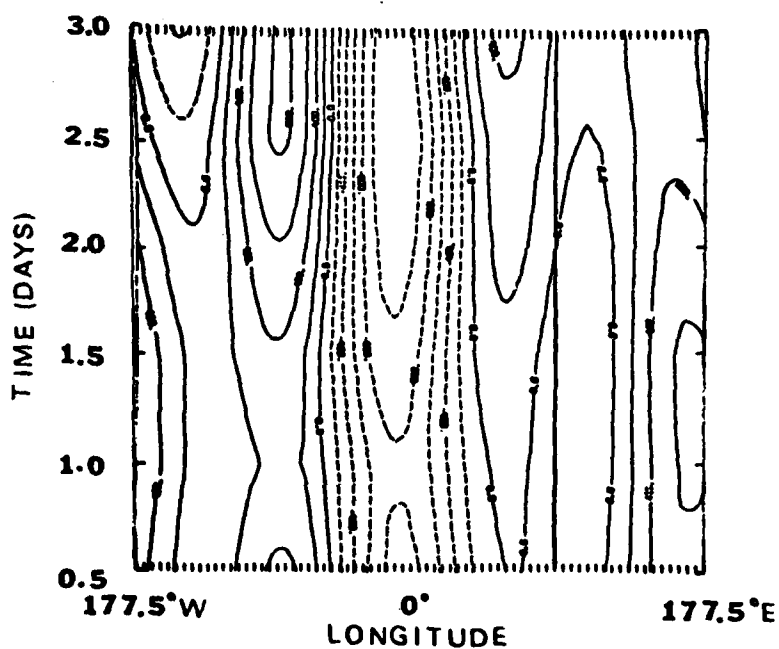
Figure 252. Same as 113 but for 25.5 to 28 day SHW mountain unpulsed geopotential field (Φ_{1-3}) at 42°S. Contour interval of 200 m^2s^{-2}.
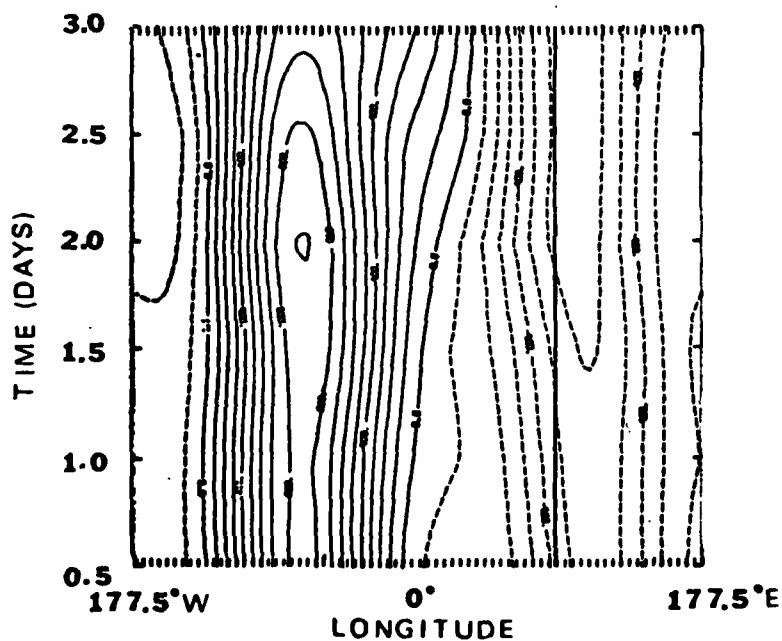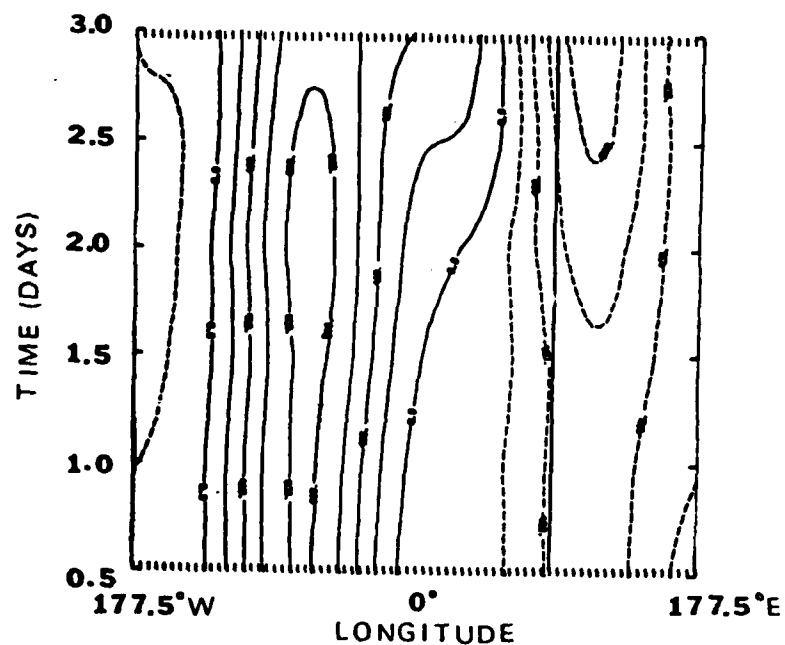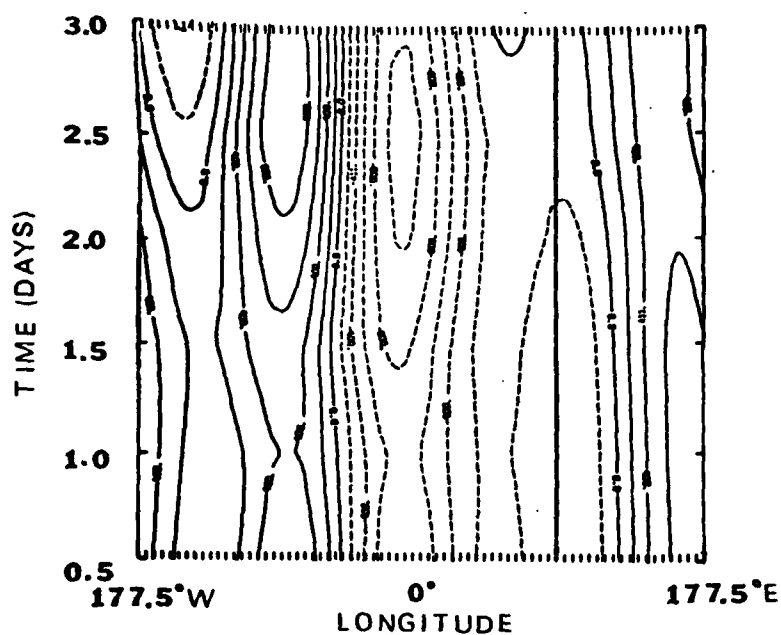
Figure 253. Same as 113 but for 25.5 to 28 day SHW mountain pulsed geopotential field (ϕ_{1-3}) at 42°S. Contour interval of 200 m^2s^{-2}.
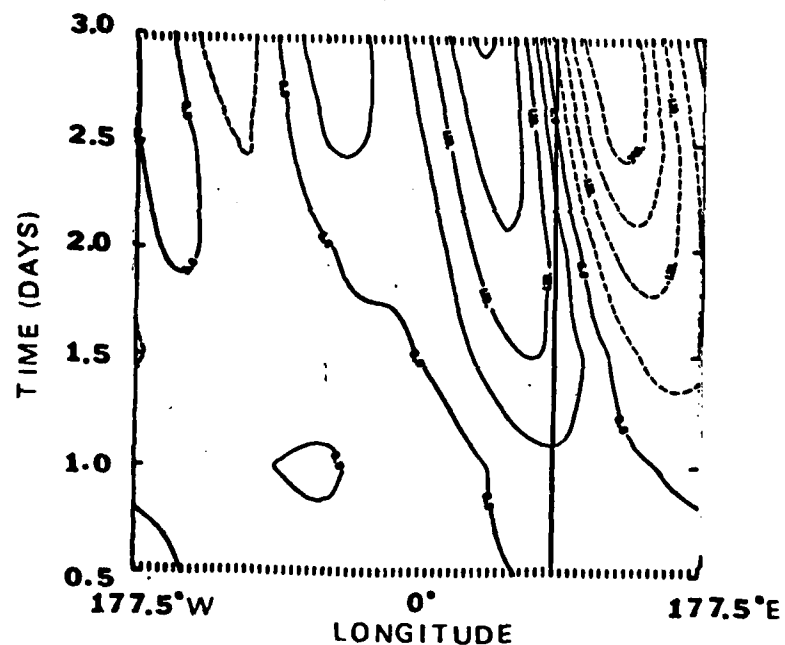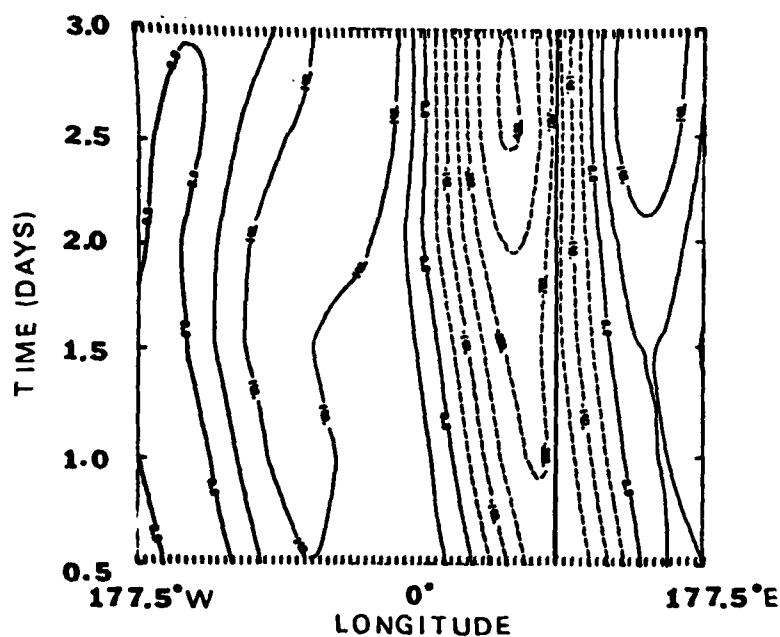

Figure 254. Same as 113 but for 25.5 to 28 day SHW mountain geopotential difference field (ϕ_{1-3}) (pulsed minus unpulsed) at 42°S. Contour interval is 70 m^2s^{-2}.
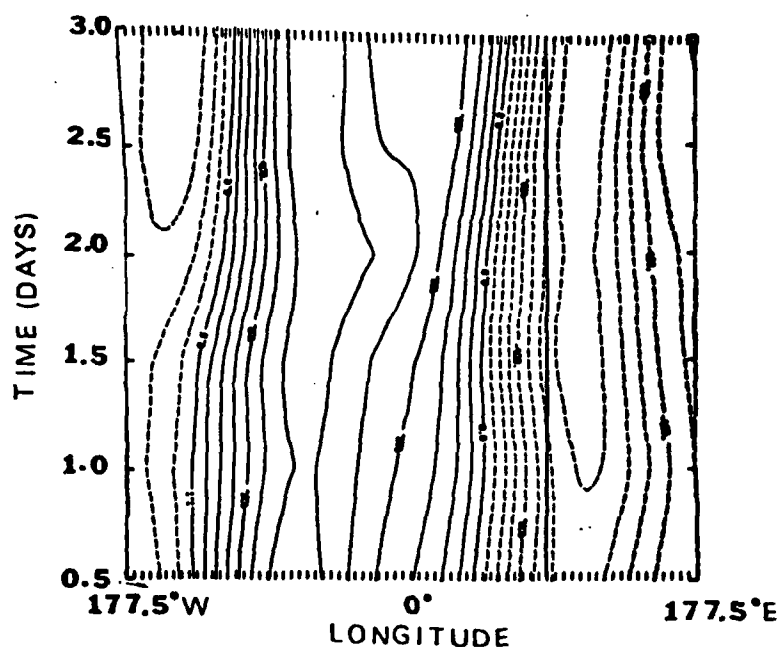
Figure 255. Same as 113 but for 25.5 to 28 day SHW mountain unpulsed geopotential field (Φ_{1-3}) at 30°S. Contour interval is 100 m^2s^{-2}.
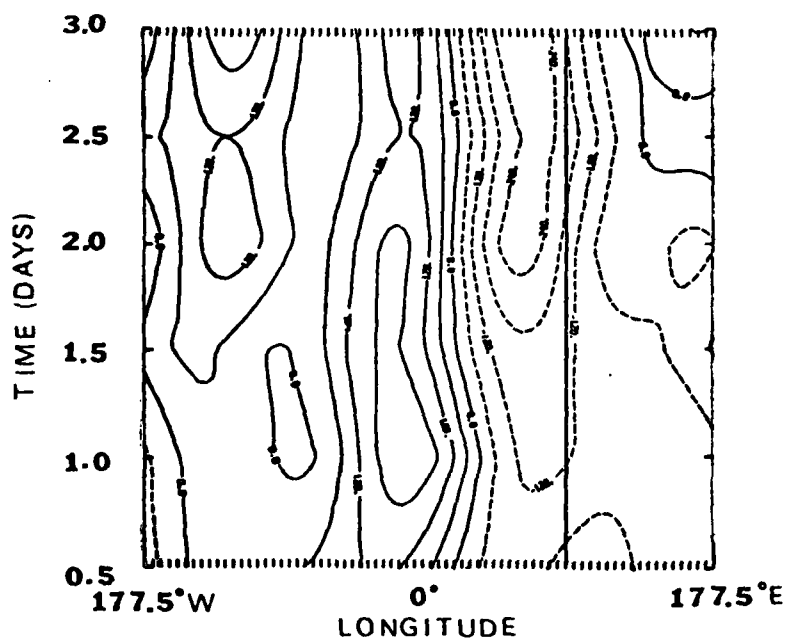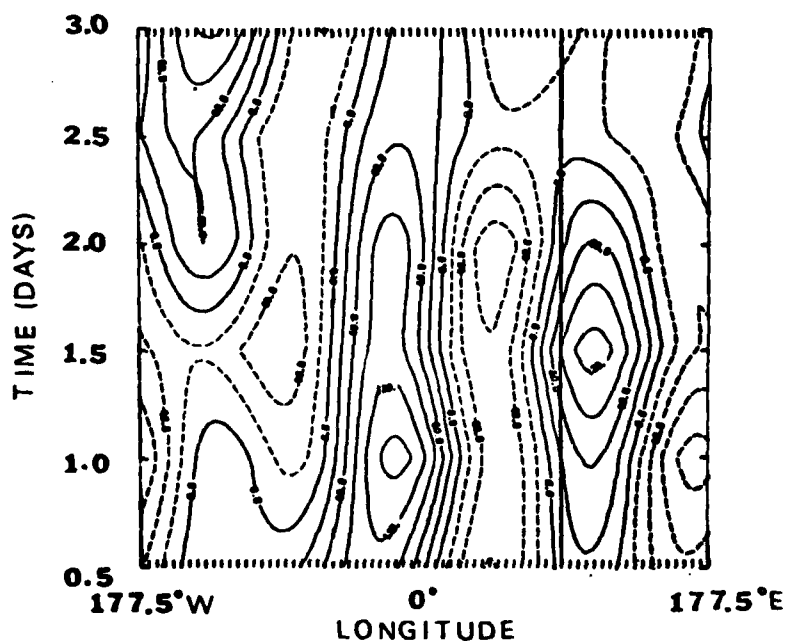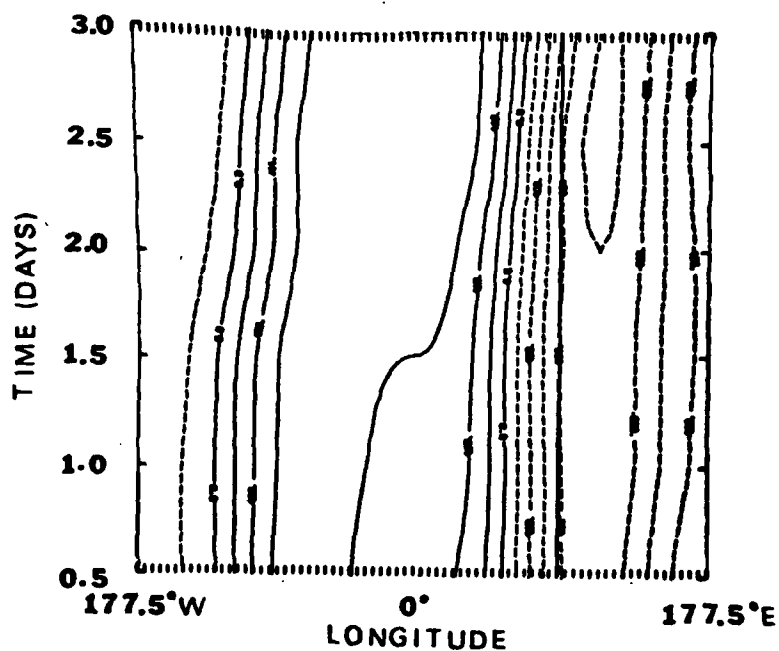

Figure 256. Same as 113 but for 25.5 to 28 day SHW mountain pulsed geopotential field (Φ_{1-3}) at 30°S. Contour interval is 200 m^2s^{-2}.
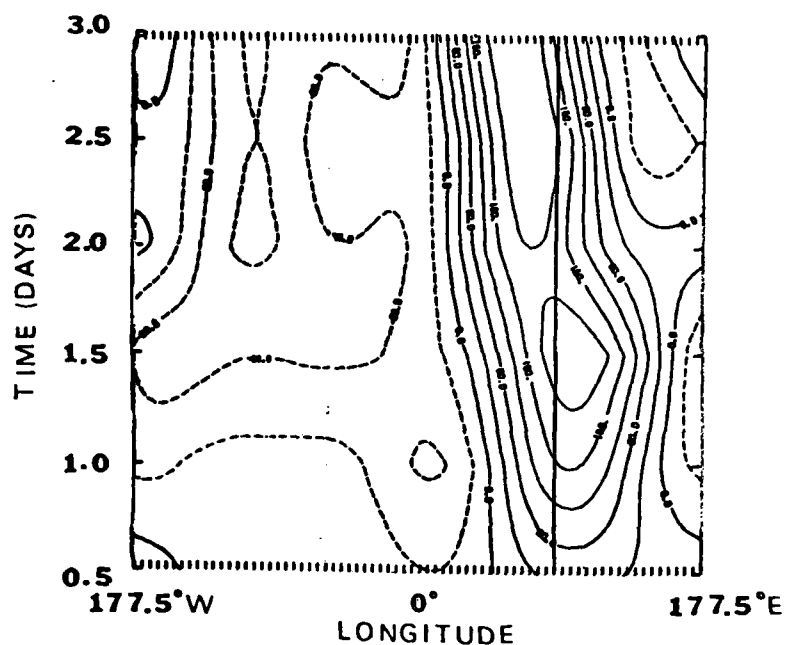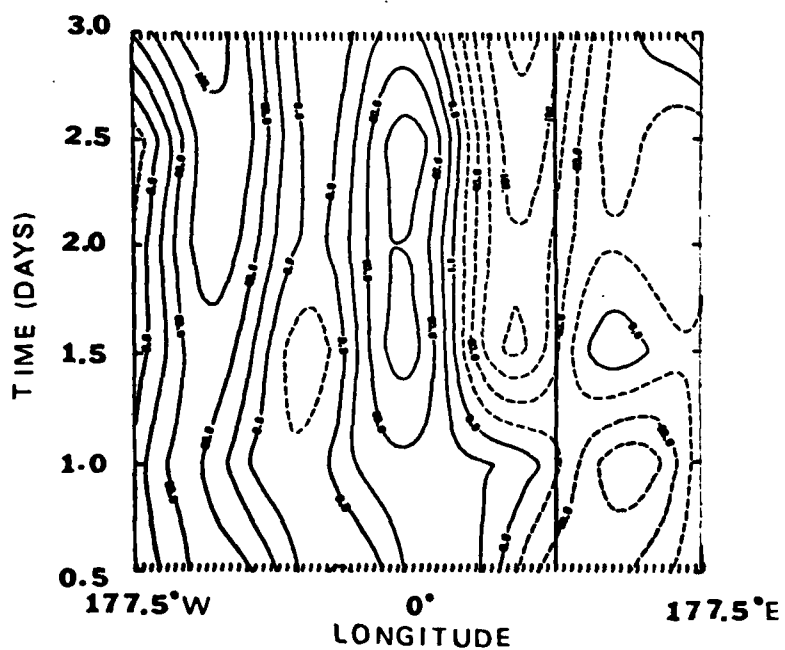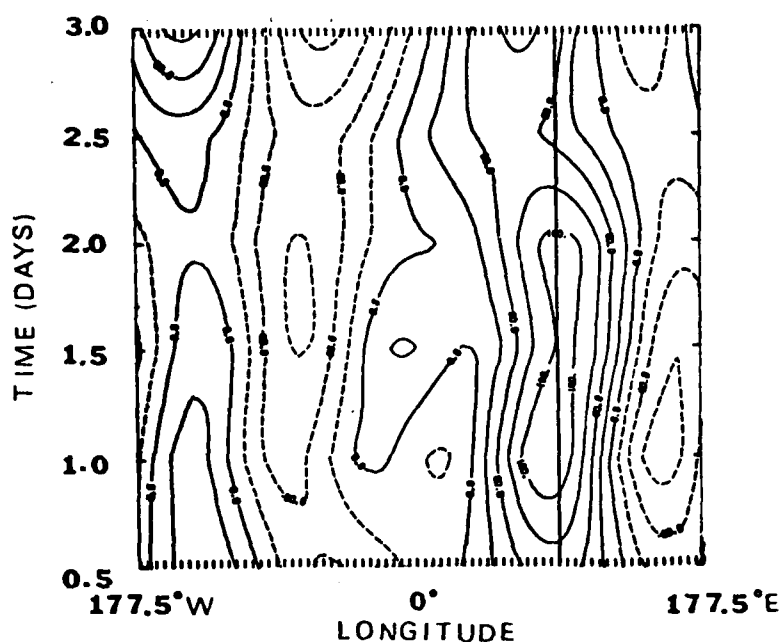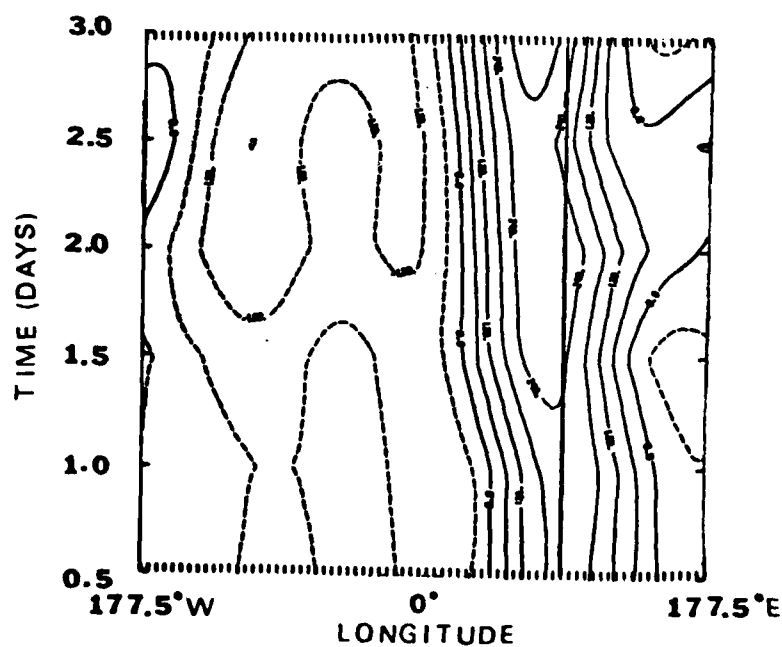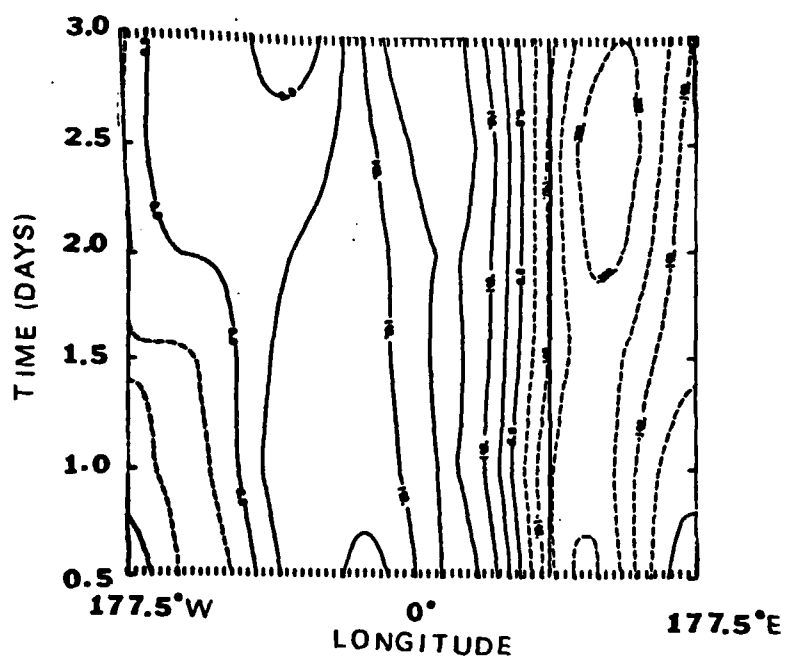
Figure 257. Same as 113 but for 25.5 to 28 day SHW mountain geopotential difference field (Φ_{1-3}) (pulsed minus unpulsed) at 30^0S. Contour interval is 70 m^2s^{-2}.

In concluding this section, it is of interest to note that the changes in the ultra-long wave geopotential amplitude in the southern hemisphere due to a three-day northern hemisphere pulsed/unpulsed forcing are definitely substantial ($\geq 25\%$). Also, the Andes Mountains in this experiment do tend to force higher ultra-long wave amplitudes in the flow than just heating alone. This is inferred from the NHW no-mountain case where the amplitude of Φ_{1-3} at 42^ON has a maximum value of 500 m^2s^{-2} as compared to the maximum value at 42^OS of 1000 m^2s^{-2} for the SHW experiment with mountains. Table IX summarizes the maximum amplitudes for the three experiments in the winter hemisphere.

TABLE IX

Maximum amplitudes of Φ_{1-3} taken from the pulsed/unpulsed
tests given in the winter hemisphere midlatitudes

Latitude	NHW no mountains (m^2s^{-2})	NHW mountains (m^2s^{-2})	SHW mountains (m^2s^{-2})
30^ON	500	1200	
42^ON	500	1000	
30^OS			800
42^OS			750

CHAPTER 6

CONCLUDING REMARKS

6.1 Summary and Conclusions

The GISS DST data were found to be a consistent and reliable
data set when compared to previously documented data sets. During
the analysis of the GISS DST data an interesting correlation was
found to exist between the positioning of the 200 mb winter hemi-
sphere subtropical jets, the 200 mb tropical areas of divergent out-
flow, and the areas of highest column average relative humidities in
the tropics of the summer hemisphere. Strong 200 mb meridional
divergent outflows originated in the summer hemisphere tropical areas
where the maximum inferred precipitation existed and flowed into
areas where the winter hemisphere 200 mb subtropical jet was being
accelerated. These divergent outflows thus appear forced by the
strong tropical convectively heated areas which can initiate large
areas of positive divergence in response to the heating.

The subtropical and midlatitude jet streams possess pronounced
ultra-long wave features. Thus it appears from the DST data sets
that the ultra-long wave forecast error in the NMC model documented
by Leith (1974) and Baumhefner (1978) may be partially due to the
lack of tropical convective heating.

In an attempt to further quantify the above observations a
divergent barotropic model and a two-level primitive equation model

were utilized. The divergent barotropic model was locally forced in the tropics of the southern hemisphere (centered near 12°S). The magnitude and scale of the divergent forcings were inferred from the observed time averaged 200 mb divergences of the GISS DST NHW data. This 200 mb divergence appears to represent the upper level response of the atmosphere to strong convective heating.

The sources of divergence were found to force stronger subtropical jets in the winter hemisphere than in the summer hemisphere. Through barotropic model experiments with normal and reduced gravity, gravity waves were shown to be the main mechanism for the transport of energy away from the divergently forced areas. These waves were also found to propagate energy from the summer hemisphere tropics to the winter hemisphere subtropics in the presence of strong tropical easterly flow. Thus, the gravity wave modes do not appear to be trapped by tropical easterlies as are the Rossby wave modes.

This gravity wave propagation induces divergent outflows which originate in the summer hemisphere regions of forcing and flow into winter hemisphere areas of strongest subtropical zonal flow. These divergent outflows adjust rapidly (within one day's time) to changes in the summer hemisphere tropical forcing (pulsed cases) at distances on the order of 2000 to 3000 km.

The single most important conclusion to be drawn from the divergent barotropic forcing experiments is that for a barotropic atmosphere, tropical divergent forcing in one hemisphere can rapidly accelerate the jet stream of the opposite hemisphere in a matter of one to three day's time regardless of easterly or westerly tropical

flow.

In order to further quantify the effect of large scale convective heating (e.g., monsoon, ITCZ, etc.) on the subtropical and midlatitude ultra-long waves and the subtropical jet streams, several two-level baroclinic primitive equation model experiments were completed. These experiments included spatially variable long-term heating, spatially uniform long-term heating, mountains, no mountains, and short range pulses and unpulses for both the NHW and SHW seasons. The results of the individual cases are summarized in Chapter 5.

The overall results and conclusions of the tropical heating experiment can be summarized as follows. First, large scale tropical heatings were found to induce divergent outflows at large distances ($\geq$ 2000 km) in 12 to 24 hours. The divergent response was typically smaller than that observed in the GISS DST data and the reason for this seems to be the model's coarse vertical resolution. This explanation may not be the entire reason. Considering the role of the Rossby radius of deformation λ ($= c/f$) in the adjustment problem, the horizontal resolution of the model may also play a role. With such large scale resolution ($4^{o} \times 5^{o}$) the tendency may be for a larger portion of the energy to go into the local rotational part of the flow than would be the case for actual localized convective heating. If this is a problem, then at least some of the energy of the large scale heating functions would be put in the rotational part of the flow and thus be trapped in the summer hemisphere by the tropical easterlies.

Even with the crude resolution, tropical heating did tend to

force substantial changes (as compared to the 30% error amplitude difference between the GISS and NMC models ultra-long wave forecasts) in the subtropical and midlatitude ultra-long wave structure. Table X summarizes the percent change in the ultra-long waves at 42^0 latitude (for all the pulsed and unpulsed integrations, including the three-day simulation eliminating tropical heating). In the final analysis, the mountains force larger amplitudes in the wintertime ultra-long waves (for the two-level model) than the effects of tropical heating.

The mountains, to a large degree, anchor the position of the ultra-long waves and subtropical jets, while long and short term changes in heating mainly alter the magnitude in the ultra-long waves and jet patterns with only small changes in position ($10-15^0$ longitude).

Even though mountains may tend to force higher amplitudes in the ultra-long waves, the mountains are fixed features. Therefore, one is hard pressed to completely explain the high variability from year to year in the ultra-long wave features in terms of mountains only. The year to year wintertime variability in the ultra-long wave can be seen in the mean 700 mb height fields for January given (usually in the following April issue) in the Monthly Weather Review. Some years the mean trough in the Pacific lies near Japan (Jan 1976) while other years it is more in the central Pacific (Jan 1977). Some years a strong three-wave pattern exists while in others the pattern is dominated by wavenumber two. Changes like these in the ultra-long wave features can represent large changes in local climate features.

234

TABLE X

Summarized percent change in the amplitude of the ultra-long
waves due to the various pulsed/unpulsed regions

Latitude	% Change	
	NHW pulsed/unpulsed no mountains	
	Days 24.5 - 27	Days 27.5 - 30
42°N	40%	50%
30°N	60%	75%
	NHW pulsed/unpulsed mountains	
	Days 17.5 - 20	Days 20.5 - 23
42°N	18%	26%
30°N	20%	35%
	NHW variable heating/zero heating mountains	
	Days 20.5 - 23	
30°N	17%	
42°N	10%	
	SHW pulsed/unpulsed mountains	
	Days 22.5 - 25	Days 25.5 - 28
42°S	25%	42%
30°S	26%	28%

6.2 Future Study

The fact that large scale tropical convective heating in this coarse resolution model shows some definite changes in the ultra-long wave and subtropical jet magnitude is suggestive. However, it is premature to conclude from this study that these waves totally force the yearly variability in the ultra-long wave structure.

The results here must be placed in proper perspective and areas of further study can then be determined. One seemingly evident fact is that the two-level model resolves the vertical structure of the ultra-long wave heating poorly. The observed tendency of the real atmosphere to focus the heating and divergent outflows near 200 mb in a 100 to 150 mb layer cannot be resolved in the present model.

Another, and maybe more important, deficiency of the two-level model is the coarse horizontal resolution. The coarse resolution probably diminishes the amount of energy that goes into the gravity wave modes. Thus, the divergent portion of the flow which has been shown to correspond to areas of acceleration of the subtropical jet may be reduced.

To further determine the effects of long and short term tropical heating, a finer resolution model should be considered. This may prove difficult for if one simply halves the spacial resolution, the required computer time goes up by a factor of about 16 since the time step must also be reduced. The two-level version of the current model requires about 30 mintues of Cary 1 computer time to complete a five-day forecast, and this is a principal practical limitation.

REFERENCES

Arakawa, A. and Y. Mintz, 1974: The UCLA atmospheric general circulation model. Notes distributed at the Workshop 25 March - 4 April 1974, Dept. of Meteor., University of California, Los Angeles, California 90024.

Arakawa, A. and V. R. Lamb, 1977: Computational design of the basic dynamical processes of the UCLA General Circulation, edited by J. Chang. Methods in Computational Physics, Academic Press, New York, N.Y., 337 pp.

Baumhefner, D. P., 1977: A comparison of 6 wintertime forecasts of large scale flow from several numerical weather prediction models. Proc. 1977 Stanstead Seminar, Lennoxville, Quebec (available from McGill University, Montreal, Quebec).

Baumhefner, D. P. and P. Downey, 1978: Forecast intercomparisons from three numerical weather prediction models. Mon. Wea. Rev., 106, 1245-1279.

Bjerknes, V., 1919: Wetlervorhersage. Meteor. Z., Braunschweig, 36, 68 pp.

Blackmon, M., J. M. Wallace, N. Ch.Lau and S. L. Mullen, 1977: An observational study of the Northern Hemisphere wintertime circulation. J. Atmos. Sci., 7, 1040-1053.

Charney, J. G. and A. Eliassen, 1949: A numerical method for predicting the perturbation of the middle latitude westerlies. Tellus, 1, 38-54.

Charney, J. G., R. Fjortoft and J. von Newman, 1950: Numerical integration of the barotropic vorticity equations. Tellus, 2, No. 4, 237-254.

Grose, W. L. and B. J. Hoskins, 1979: On the influence of orography on large-scale atmospheric flow. J. Atmos. Sci., 36, No. 2, 223-234.

Hantel, M. and H. Badder, 1978: Diabatic heating climatology of the zonal atmosphere. J. Atmos. Sci., 35, No. 7, 1180-1189.

Hastenrath, S., 1976: Variations in low-latitude circulation and extreme climate events in the tropical Americas. J. Atmos. Sci., 2, 202-215.

Hastenrath, S., 1978: On modes of tropical circulation and climate anomalies. J. Atmos. Sci., 12, 2222-2231.

Hoskins, B. J., 1973: Stability of the Rossby-Haurwitz waves. Quart. J. Roy. Meteor. Soc., 99, 723-745.

Hoskins, B. J., A. J. Simmons and D. G. Andrews, 1977: Energy dispersion in a barotropic atmosphere. Quart. J. Roy Meteor. Soc., 103, 553-567.

Houghton, D. D., 1968: Derivation of the elliptic condition for the balance equation in spherical coordinates. J. Atmos. Sci., 25, 927-928.

Julian, P. R. and R. M. Chervin, 1978: A study of the southern oscillation and Walker circulation phenomenon. Mon. Wea. Rev., 106, No. 10, 1433-1451.

Krishnamurti, T. N., 1961: The subtropical jet stream of winter. J. Meteor., 18, 172-191.

_____, 1971a: Observational study of the tropical upper tropospheric motion field during the Northern Hemisphere summer. J. Appl. Meteor., 10, 1066-1096.

_____, 1971b: Tropical east-west circulations during the northern summer. J. Atmos. Sci., 28, 1342-1347.

Leith, C. E., 1974: Spectral statistical dynamical forecast experiments. Contributed paper to the International Symposium on Spectral Methods in Numerical Prediction, Copenhagen.

McGlasson, A. J., 1977: A study of the characteristics of the data systems test kinematics fields. Masters Degree Thesis, University of Utah, 69 pp.

Murakami, T., 1978: Regional energetics of the 200 mb summer circulations. Mon. Wea. Rev., 106, 614-628.

Newell, R. E., J. W. Kidson, D. G. Vincent and G. J. Boer, 1972: The General Circulation of the Tropical Atmosphere and Interactions with Extratropical Latitudes, Vols. 1 and 2. The MIT Press, 248, 371.

Oort, A. H. and E. M. Rasmusson, 1970: On the annual variation of the monthly mean meridional circulation. Mon. Wea. Rev., 90, No. 6, 423-442.

Paegle, J., 1978: The transient mass-flow adjustment of heated atmospheric circulations. J. Atmos. Sci., 35, 1678-1688.

Paegle, J. and J. N. Paegle, 1976a: On geopotential data and ellip-
ticity of the balance equation: A data study. _Mon. Wea. Rev.,_
_104,_ 1279-1288.

_____, 1976b: On the realizability of strongly divergent
supergradient flow. _J. Atmos. Sci.,_ _33,_ 2300-2307.

Paegle, J., J. N. Paegle, F. P. Lewis and A. J. McGlasson, 1979:
On the generation of large scale divergent winds and related
energetics. Accepted for publication by _Mon. Wea. Rev._

Phillips, N. A., 1957: A coordinate system having some special
advantages for numerical forecasting. _J. Meteor.,_ _14,_ 184-185.

_____, 1959: Numerical integration of the primitive equations
on the hemisphere. _Mon. Wea. Rev.,_ _86,_ 333-345.

Pratt, R. W., 1977: Comparison of planetary wave simulation in the
GFDL and NCAR general circulation models. _Proc. 1977 Stanstead_
Seminar, Lennoxville, Quebec (available from McGill University,
Montreal, Quebec).

Ramage, C. S., 1968: Role of a tropical "maritime continent" in the
atmospheric circulation. _Mon. Wea. Rev.,_ _96,_ 365-370.

Richardson, L. F., 1922: _Weather Prediction by Numerical Process._
Cambridge Univ. Press, London, 236 pp. Reprinted by Dover.

Robert, A., 1965: The behavior of planetary waves in an atmospheric
model based on spherical harmonics. Publication in Meteorology
No. 77, McGill University, Montreal, Canada.

Rossby, C. G., 1938: On the mutual adjustment of pressure and
velocity distribution in certain simple current systems, II.
J. Marine Res., (Sears Foundation), 239-263.

_____, 1940: Planetary flow patterns in the atmosphere. _Quart._
J. Roy. Meteor. Soc., _66,_ 68-87.

Rountree, P. R., 1976a: Tropical forcing of atmospheric motions in
a numerical model. _Quart. J. Roy. Meteor. Soc.,_ _102,_ 583-605.

_____, 1976b: Response of the atmosphere to a tropical Atlantic
Ocean temperature anomaly. _Quart. J. Roy. Meteor. Soc.,_ _102,_
607-625.

Sadler, J. C., 1975: The upper tropospheric circulation over the
global tropics. Hawaii Institute of Geophysics, University
of Hawaii, UHMET-75-05, 35 pp.

Schutz, C. and W. L. Gates, 1972: Supplemental global climatic data: January. Advanced Research Projects Agency, Rep. R-Ji5/1-ARPA, Rand Corporation, Santa Monica, 41 pp.

Smagorinsky, J., 1953: The dynamical influence of large-scale heat sources and sinks on the quasi-stationary mean motions of the atmosphere. Quart. J. Roy. Meteor. Soc., 79, 342-366.

Sommerville, R. C. J., P. H. Stone, M. Halem, J. E. Hansen, J. S. Hogan, L. M. Druyan, G. Russel, A. A. Lacis, W. J. Quirk and J. Tenenbaum, 1974: The GISS model of the global atmosphere. J. Atmos. Sci., 31, 84-117.

van Loon, H., J. J. Taljaard, R. L. Jenne and H. L. Crutcher, 1971: Climate of the upper air: Southern Hemisphere. Vol. II, Zonal Geostrophic Winds. NCAR TN/STR-57 and NAVAIR 50-1C-56, National Center for Atmospheric Research, Boulder, Colorado, 43 pp.

Webster, P. J., 1972: Response of the tropical atmosphere to local, steady forcing. Mon. Wea. Rev., 100, 518-541.

VITA

NAME	Fred Park Lewis
BIRTHPLACE	Cottonwood, Arizona
BIRTHDATE	March 2, 1949
HIGH SCHOOL	Alchesay High School Whiteriver, Arizona
UNIVERSITIES	University of Arizona Tucson, Arizona 1967-1972 University of Utah Salt Lake City, Utah 1972-1973 1976-1979
DEGREES	B.S., 1971 University of Arizona Tucson, Arizona B.S., 1973 University of Utah Salt Lake City, Utah
HONORARY SOCIETIES	Phi Beta Kappa Phi Kappa Phi Chi Epsilon Pi
PROFESSIONAL POSITION	Weather Officer United States Air Force
PUBLICATIONS	"On the Generation of Large Scale Divergent Flow," 1977, with Jan Paegle and Allan J. McGlasson. Proc. 1977 Stanstead Seminar, Lennoxville, Quebec (available from McGill University, Montreal, Quebec). "On the Generation of Large Scale Divergent Winds and Related Ener- getics," accepted for publication by Mon. Wea. Rev., with Jan Paegle, Julia N. Paegle and Allan J. McGlasson.